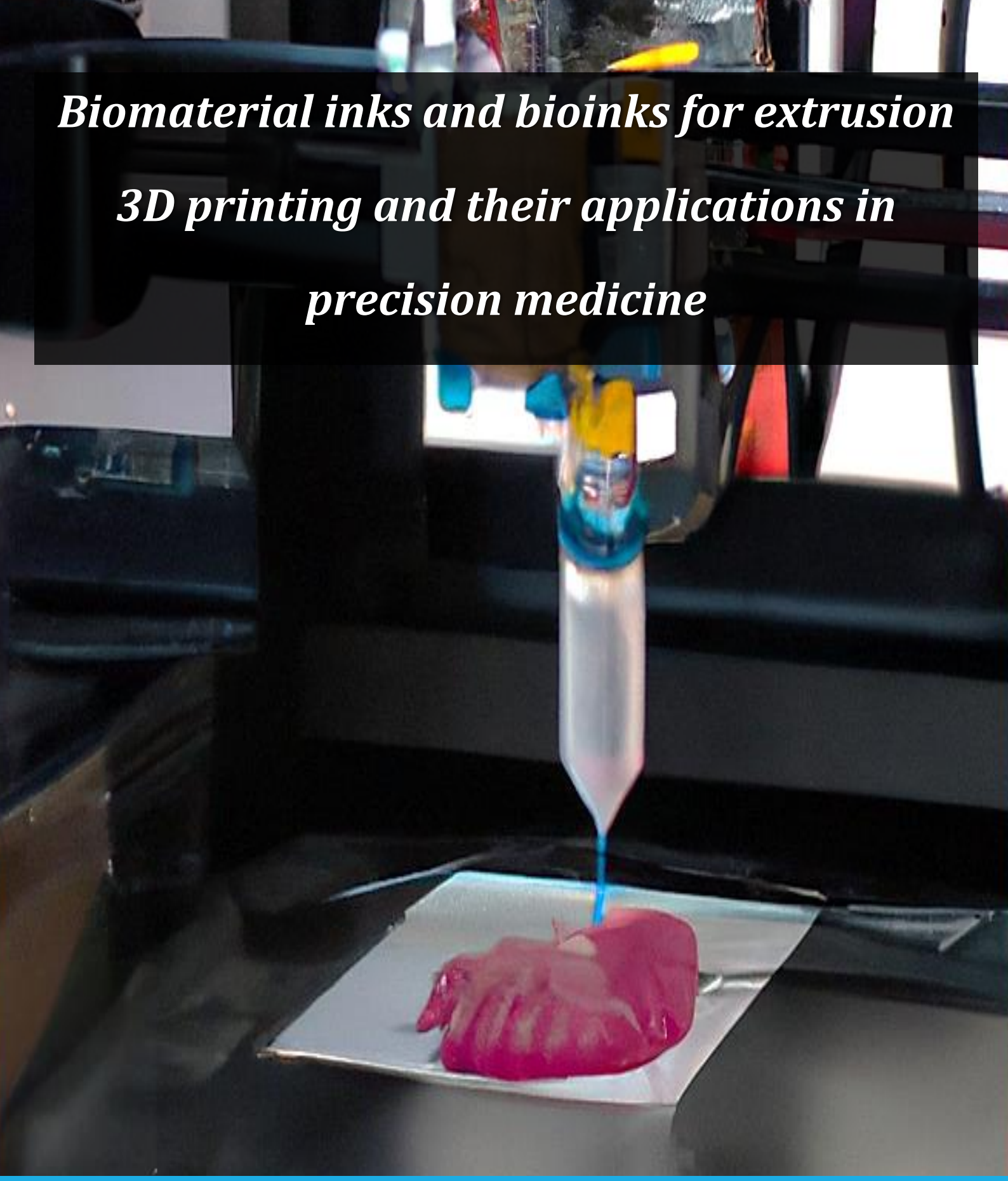

Biomaterial inks and bioinks for extrusion 3D printing and their applications in precision medicine

Raquel Olmos Juste

Donostia-San Sebastián, 2022

UPV EHU

Biomaterial inks and bioinks for extrusion 3D printing and their applications in precision medicine

PhD dissertation presented by

RAQUEL OLMOS JUSTE

Supervised by

Dr. ARANTXA ECEIZA and Dr. NAGORE GABILONDO

Donostia-San Sebastián, December 2022

ACKNOWLEDGEMENTS

En primer lugar, me gustaría dar las gracias a mis directoras, la Dr. Arantxa Eceiza y la Dr. Nagore Gabilondo por haberme dado la oportunidad profesional de desarrollar esta tesis doctoral y unirme a su grupo durante estos cuatro años.

Por otro lado, quisiera agradecer al Ministerio de Ciencia e Innovación, a la Agencia Estatal de Investigación (MCIN/AEI) /10.13039/501100011033 y al Fondo Social Europeo "FSE invierte en tu futuro" por la financiación percibida en la ayuda BES-2017-080624 para la realización de esta tesis doctoral. También me gustaría agradecer a la Universidad del País Vasco (UPV/EHU) por su apoyo económico.

Así mismo, me gustaría agradecer a los Servicios Generales de Investigación (SGIker) de la UPV/EHU por el apoyo técnico durante esta tesis y por facilitarme el acceso a los recursos e instalaciones. Más concretamente, a las unidades de Macroconducta-Mesoestructura-Nanotecnología y Microscopía Analítica y de Alta Resolución en Biomedicina tanto por su apoyo técnico como humano.

También me gustaría agradecer tanto al Dr. Raúl Pérez Jiménez del CIC nanoGUNE como a la Dra. Sandra Camarero Espinosa del Instituto Polymat por darme la oportunidad de colaborar y realizar parte del trabajo de esta tesis doctoral en sus respectivos grupos de investigación, lo cual me ha permitido crecer tanto personal como profesionalmente.

Además, quiero agradecer a la Dra. Ana Alonso Varona y su equipo del departamento de Biología Celular e Histología de la Facultad de Medicina de la UPV/EHU por su ayuda y disposición para realizar los ensayos de biocompatibilidad.

Del mismo modo, me gustaría también agradecer a todos mis compañeros del GMT por su cariño y apoyo durante estos 4 años, además de a todos los compañeros con los que he tenido el placer de trabajar tanto en el grupo de Nanobiotecnología del CIC nanoGUNE como del grupo BioSmarTE del Instituto Polymat.

Finalmente, quiero dar las gracias a mi familia y amigos por su apoyo incondicional durante estos cuatro años.

SUMMARY

This study is focused on the development of biomaterial inks and bioinks suitable for 3D printing technology and their applicability in the field of personalized medicine. Extrusion 3D printing represents a multidisciplinary technology that is generating high interest in healthcare area for tailoring treatments to individual patients. The engineering and development of advanced biomaterials with specific rheological characteristics for this technology, with biocompatible character and more environmentally friendly, are in the spotlight of the pharmaceutical industry.

In the first place, three commercial polymers such as alginate, an aqueous polyurethane dispersion and cellulose nanoentities have been analyzed and characterized. In addition, cellulose nanocrystals have been obtained via enzymatic hydrolysis based on a method developed in previous studies. These water-based polymeric materials will constitute the base of the developed inks, by either mixing the polymers or acting as single-component inks.

After the preparation and rheological characterization of the all single-component and multicomponent inks, the 3D printed samples were processed using different techniques in order to maintain their three-dimensional structure and thus, obtaining forms with either porous or compact structures. These printed samples were characterized for their subsequent evaluation as potential drug delivery systems or scaffold materials for tissue engineering, among other biomedical applications.

The inks based on alginate and nanocellulose allowed the addition of different drugs to their formulations, creating customizable devices for controlled release. On the other hand, bioinks based on alginate and polyurethane containing living cells were developed for 3D bioprinting in order to obtain scaffolds with the proper characteristics for neo-cartilage formation.

In addition, 3D printed customizable mesh implants for groin hernia repair, made of alginate and polyurethane and capable to release antibiotics *in situ,* were developed.

RESUMEN

El presente estudio está enfocado al desarrollo de tintas y biotintas aptas para la tecnología de impresión 3D y su aplicabilidad en el campo de la medicina personalizada. La ingeniería y desarrollo de materiales avanzados con características reológicas específicas para esta tecnología, que resulten respetuosos con el medio ambiente y presenten propiedades biocompatibles suponen una gran revolución en el sector de la salud.

En primer lugar, en este trabajo se han analizado y caracterizado tres polímeros comerciales como son el alginato, una dispersión acuosa de poliuretano y nanoentidades de celulosa. Además, se han obtenido nanocristales de celulosa vía hidrólisis enzimática en base a un método desarrollado en estudios anteriores. Dichos materiales poliméricos en base acuosa constituyen la base de las tintas desarrolladas, bien mediante la mezcla de dichos polímeros entre sí o actuando como tintas monocomponente.

Después de la preparación y caracterización reológica de todas las tintas, las muestras impresas en 3D se procesaron mediante diversas técnicas para el correcto mantenimiento de su estructura tridimensional obteniendo así piezas con estructuras porosas o compactas. Dichas piezas impresas fueron caracterizadas para su posterior evaluación como sistemas para liberación de fármacos o soporte para ingeniería de tejidos, entre otras aplicaciones biomédicas.

Las tintas desarrolladas en base a alginato y nanocelulosa permitieron la adicción de diferentes fármacos a sus formulaciones, creando dispositivos personalizables mediante impresión 3D que permitan su liberación de forma controlada. Por otro lado, se desarrollaron biotintas capaces de albergar células en base a alginato y poliuretano, con el fin de imprimir un soporte celular con las características idóneas para la formación de neo-cartílago articular *in situ*.

Además, en este estudio se desarrollaron implantes de mallas personalizables para la reparación de hernias inguinales a partir de alginato y poliuretano, capaces de liberar antibióticos *in situ,* mediante la tecnología de impresión 3D.

TABLE OF CONTENTS

Chapter 1

Introduction

CHAPTER 1 – Introduction

1. Introduction

1.1. Motivation

Nowadays medicine is moving towards the employment of customized treatments adaptable to individual necessities. The pursuit of these new personalized therapies impulses the demand of advanced technologies to cover specific requirements. Moreover, the increment of data collection and analysis of individual patients can provide precise information to design and develop tailor-made therapies.

In recent times, three-dimensional (3D) printing technology, also known as additive manufacturing, has gained high interest in healthcare due to the ability of fabrication of advanced and customizable objects, using non-cytotoxic materials. This versatile technique allows the layer-by-layer manufacturing of objects with predefined design, made by materials with specific characteristics. Those employed materials not only must present biocompatibility, but also ideally they should be extracted or synthesized causing the least possible impact on the environment. More concretely, in extrusion 3D printing water-based biopolymers are used, which present a suitable atmosphere for the integration of living cells and drugs, showing a great potential for biomedical applications. The development of suitable materials for this technology is considered as an important key question, since the extrusion printing process requires materials, called inks, with specific rheological behavior to achieve functional 3D constructs. The inks used for extrusion 3D printing are usually composed of water-based biomaterial blends, containing multiple components interacting one another to reach the required rheological character, but the pursuit of single-component inks has been arousing interest, since the presence of one type of material decreases the possibility of adverse reactions in the host body.

Biocompatible 3D constructs or living cellular scaffolds must be modified after being printed to retain the shape over a long period and thus, perform the predetermined functions. The need of new advanced carriers for controlling drug release focalized in specific areas, the pursuit of customizable implants and medical devices, as well as smart materials for cell support and tissue regeneration have increased the healthcare industry's interest in extrusion 3D printing technology as an innovative tool to meet the high demand of personalized therapies.

Therefore, in this work, inks suitable for extrusion 3D printing technology have been developed from biocompatible and environmentally friendly materials such as alginate, waterborne polyurethane dispersion and cellulose nanoentities. These biomaterials were

employed either alone or blended to achieve specific rheological properties to be 3D printed. Furthermore, customized devices were printed from the developed inks and then were tested for controlled drug release, as well as their capacity as supporting materials for tissue regeneration, among other medical applications.

1.2. State of the art

1.2.1. Precision medicine and customized therapies

In recent times, medicine is moving away from 'one size fits all' concept [1]. The increasing awareness about individual variation leads to the development of personalized therapies adjusted to specific needs and thus, to treat the patient as an individual. Clinical treatments are commonly designed for a particular disease, without taking into account individual patient requirements or limitations that could lead to inadequacy or infectivity of the treatment [2]. The administration of the same active compound at the same dosage to different individuals has shown varied responses or inefficacy in some cases [2,3]. Moreover, there are even drugs or stablished dosages that are harmful to certain groups of people [3], but taking into account individual variability it would be possible to predict how a person reacts to a specific treatment and design an alternative therapy adapted to particular requirements [4,5]. The common observation of patients with apparently the same clinical diagnosis or symptoms often exhibit different responses to the same treatment and consequently, they could be classified into subgroups and identify which ones will work for them based on their individual genetic and environmental predisposition (**Figure 1.1**) [5].

Personalized medicine is a field of pharmaceutics that is arousing high importance nowadays and consisting in the recompilation of each person's clinical history data, genetics and environmental information and thus, taking into account almost all individual sources of variability that might influence the disease treatment and prevention [3]. Advances in genomics, metabolomics or proteomic technologies are required for data collection, as well as other advanced methodologies are needed to develop personalized therapies based on precision medicine. A recent study has reported that the market for precision medicine in the European Union (EU) is estimated in 15.8 billion dollars, whereas in United States it will be more than 87 billion dollars by the year 2023 [6], indicating a very high increase in demand for these advanced technologies.

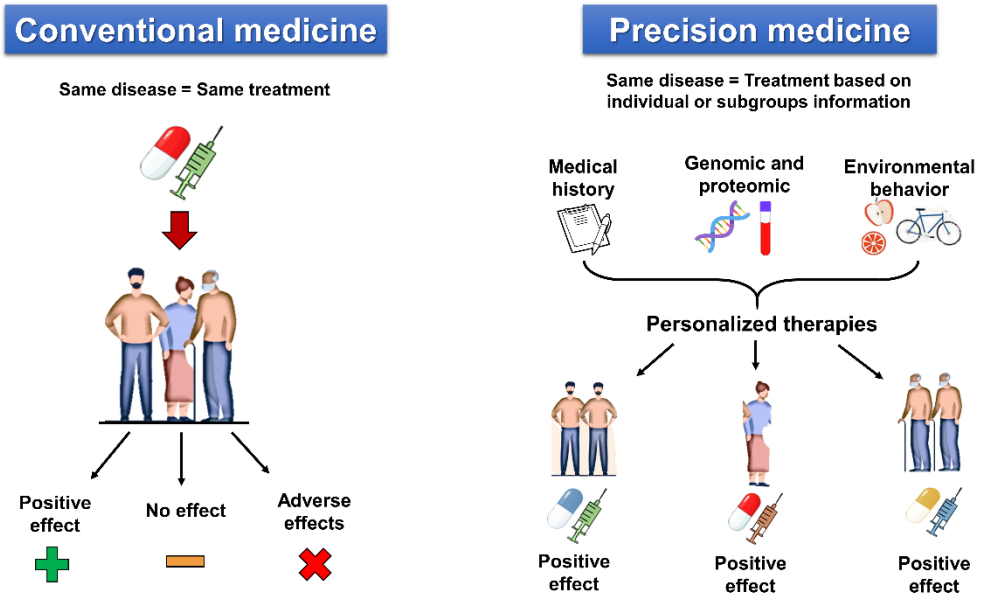

Figure 1.1 *Schematic overview of conventional medicine versus precision medicine.*

Engineering and biomedical engineering fields are in charge of the development of specific tools that can approach precision therapies and clinical solutions [7]. Some examples of the developed engineering tools applied in personalized medicine data collection are artificial intelligence and machine learning, being crucial in drug dosage determination and other specific analysis for individual patient. Other important technologies are related to gene sequencing, gene editing and nanomedicine, but one of the most relevant area that is currently arousing high interest in precision medicine is the biomaterials' field [6,7].

Advanced biomaterials' research enables the development of innovative product designs to target and treat a wide range of diseases [6]. New sophisticated biological and drug products will require advanced biomaterial-based devices to deliver them in order to obtain the desired effect in target site [6,8]. Biomaterials can play an important role as delivery vehicles to control cellular viability or as drug carrier. Additionally, 3D printing technology allowed the creation of biomaterial-based devices with complex morphologies and structures across many length scales to fit specifically the condition defect of the individual patient [9,10]. In healthcare and pharmaceutical industry, 3D printing can be employed to produce advanced medical devices to achieve tailored treatments and therefore, it shows high potential in the field of personalized medicine [11].

1.2.2. 3D printing technology in precision medicine

3D printing technology, formally known as additive manufacturing, consists in the layer-by-layer deposition of the material, creating complex structures engineered by computer-aided design (CAD) software, converting those prototypes into real physical objects [12,13]. These patterns are automatically transformed in sequential slides, and then a computer-controlled translation mechanism moves in X, Y and Z directions based on the designed pattern, depositing the material to fabricate objects in a succession of layers [14–16]. This technology was first introduced in 1980 and its use has increased significantly in recent years in industrial applications as well as in conventional every day, creating high socioeconomic impact [14,17]. In the medical sector, the 3D printing market size was valued at over 1.7 billion dollars in 2020 and is estimated to expand between 2021 and 2027 expecting to reach 7.1 billion dollars by then due to the high demand for customized 3D printed devices and implants [18]. According to Global Market Insights, in 2020 the percentage of 3D printing in health industry was 40 % and 30 % in North America and Europe, respectively, but the tendency is changing and the increment in Asian and Latin American regions are notably [18].

There are several types of 3D printers depending on physical and chemical characteristics of the employed materials and the industrial application of the obtained object [19]. One of the most employed is Fused Deposition Modelling (FDM) that consists in the fabrication layer-by layer of 3D structures by melting filaments made of pure thermoplastic polymers or a combination of different polymeric materials [13]. A printer-heated head melts the filament and deposits the material in a plane surface, cooling down rapidly and thus retaining the shape with high-resolution [14,20]. This technology is also used in pharmaceutical and healthcare industries [21,22], but the most employed and promising 3D printing method in precision medicine and biomedical field is extrusion 3D printing of biomaterials [23,24].

1.2.2.1. Extrusion 3D printing technology

Syringe extrusion 3D printing technology, also known as Direct Ink Writing (DIW), refers to the fabrication of complex 3D structures using semi-solid materials with specific rheological properties that could be extruded through nozzle and recover its shape afterwards [19]. The mechanism of this extrusion-based printer is similar to that explained previously for FDM, switching the printer-heating head for a syringe containing the material. This semi-solid material is pushed by a mechanical or pneumatic piston that applies enough force to extrude the material through a needle or nozzle, located in the

tip of the syringe. The material is progressively deposited on a bed or in a Petri dish, depositing the layers on top of one another, building the CAD prototype (**Figure 1.2**) [19,20]. The controlling system of the equipment automatically calculates the force, the amount of material needed and the number of layers depending on parameters such as printing speed, the diameter of the nozzle and the dimensions of the CAD model.

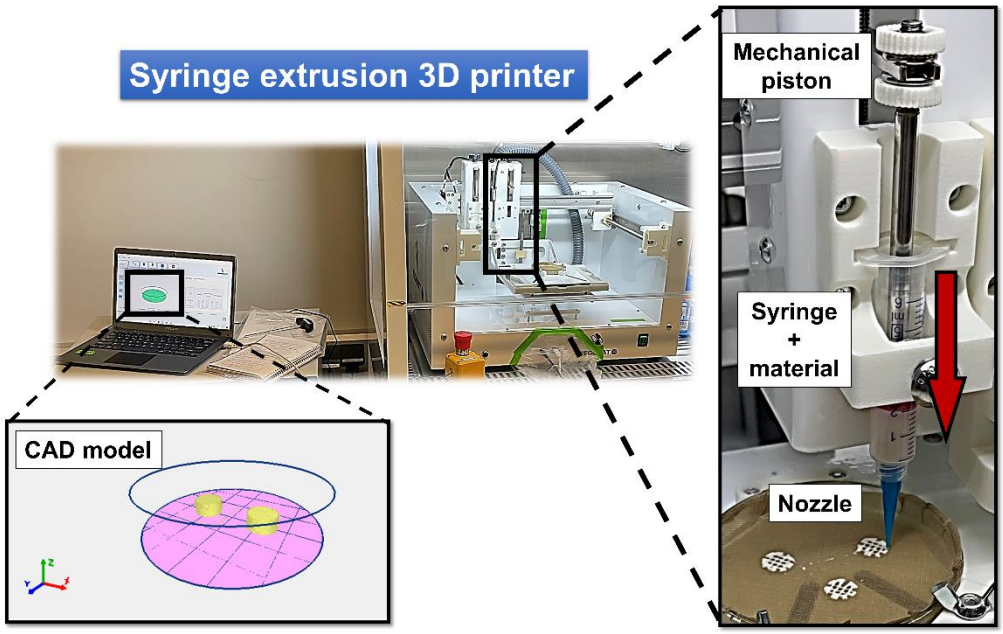

Figure 1.2. *Images of an extrusion 3D printer. From CAD model to material extrusion process.*

Syringe based technology occupied more than 40 % of the market share in 2020 and it is expected to triplicate its impact by the year 2027. One of the factors that influences this high market demand is the field of 3D bioprinting, which is expected to continue growing in the coming years, due to the healthcare and the pharmaceutical industry[18]. Indeed, Khaled et al. [25] carried out studies in which syringe extrusion 3D printing was employed as a tool for the manufacturing of polypills for the release of different drugs to treat type II diabetes, while Kolesky et al. [26] developed 3D printed constructs for the biofabrication of artificial vasculature for organs and tissues, demonstrating that this technology currently represents an emerging tool for healthcare industry.

1.2.2.2. Bioinks and biomaterial inks

The materials employed in extrusion 3D printing technology are known as inks, and they have to present specific rheological characteristics to achieve a suitable printing performance [27–29]. Inks used in the field of 3D printing for medical applications should be classified as bioinks, if they contain living cells dispersed in a water-based biomaterial,

and if the material does not carry living cells they are known as biomaterial ink [19,30]. Bioinks are commonly employed in 3D bioprinting for tissue regeneration applications [31] while biomaterial inks, which can contain drugs in their formulation [9], are often employed for advanced drug delivery [32]. This biomaterial inks can also be employed as scaffolds for the support of living cells seeded afterwards [33] (**Figure 1.3**).

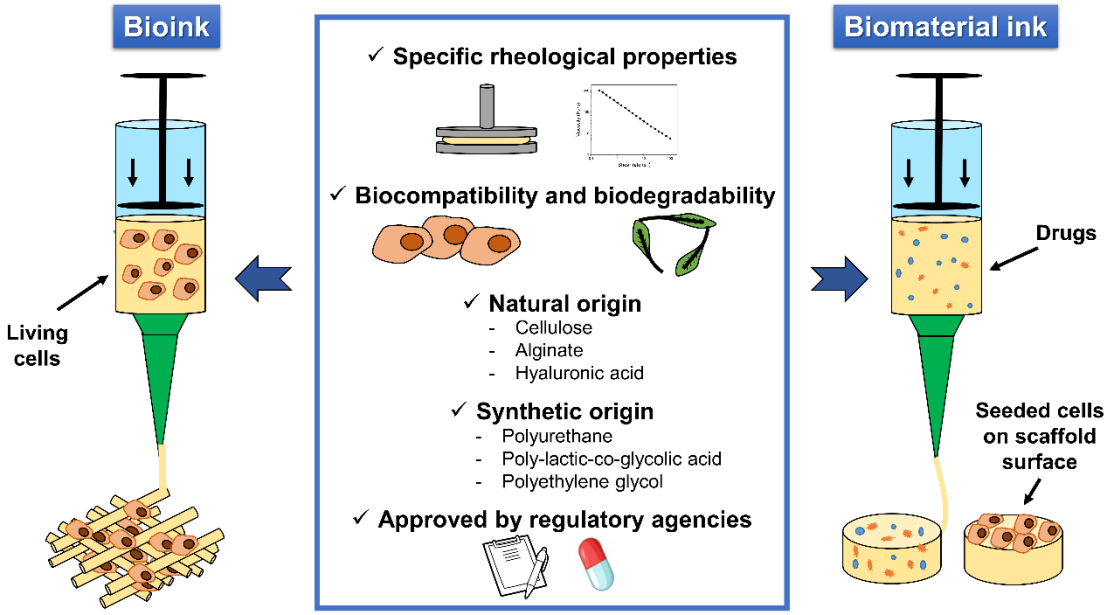

Figure 1.3. *Graphical representation of bioink and biomaterial ink concepts and their main characteristics.*

These bioinks and biomaterial inks are usually composed by polymeric biomaterials specifically developed to avoid cytotoxicity and undesirable inflammatory reactions from host body [34,35]. The employed biomaterials can be extracted from natural sources [36] or synthesized from different monomers [37], showing biocompatibility properties in all cases [38]. Some examples of the naturally occurring biomaterials are chitosan, hyaluronic acid (HA), alginate, cellulose, collagen, starch, gelatin or even extra cellular matrix (ECM) components [24,39]. Synthesized biomaterials such as poly-lactic-co-glycolic acid (PLGA), polyethylene glycol (PEG), acrylic copolymers based on poly(acrylate co-ethyl-methacrylic acid), known commercially as Eudragit ® [40], and polyurethane (PU) are also widely employed in extrusion 3D printing [9,37]. Regulatory agencies such as Food and Drug Administration (FDA) and European Medicines Agency (EMA) must approve their use in pharmaceutical and healthcare industries [41,42]. In 1989, the FDA approved the use of PLGA as injectable drug carrier [43] and recently HA and collagen as soft tissue fillers [41].

- *Rheological properties*

Extrusion efficiency and shape fidelity quality are highly dependent on rheological properties of the bioinks and biomaterial inks and therefore a careful design of the materials is required [35,44,45].

Rheological properties such as viscosity, yield stress, yield point and elastic modulus should be evaluated to determine the printing characteristics of the inks [45,46]. Bioinks and biomaterial inks for extrusion based 3D printing technology must present viscoelastic properties [47], shear thinning behavior and appropriate viscosity to form continuous and smooth filaments [46,48]. Besides, those inks have to show rapid viscosity recovery after passing through the nozzle to ensure shape fidelity of the printed samples [49], as well as enough elastic behavior to prevent structure collapse after printing [50].

During extrusion, the material behaves as a laminar fluid, showing resistance to flow under the application of a shear stress [51]. This resistance depends on the viscosity, which higher values usually implies high printing fidelity and shape accuracy [48]. However, high viscosity also gives rise to increased shear stress when the material passes through the nozzle, that in the case of bioinks containing cells can compromise their viability [52,53]. The main characteristics that determine the viscosity of inks are the molecular weight of the polymer and the concentration of their solutions [54].

Viscosity is defined as the ratio between the shear stress and the velocity gradient perpendicular to the plane of shear, called shear rate [51,55]. Fluids showing a linear relationship between the two are classified as Newtonian, whereas those that display deviations from linearity are known as non-Newtonian fluids [56]. Non-Newtonian fluids can be classified into pseudoplastic or dilatant [57,58]. Pseudoplastic behavior, also known as shear-thinning, displays a decrease of the shear stress as the shear rate increases, which will result in a decrease of viscosity [51]. Shear-thinning is the most common non-Newtonian fluid behavior that materials exhibit in extrusion 3D printing [59]. Dilatant behavior or shear-thickening typically shows an increase in viscosity, i.e. an increase in shear stress as the shear rate increases [60].

The assessment of the viscosity under a shear rate increment by means of rotational rheometry can provide information on the shear-thinning behavior [61] of the bioinks and biomaterial inks and thus, predict their printability window and allow the establishment of important printing parameters such as proper printing speed or nozzle diameter [36,45]. Mathematical models can approach experimental shear-thinning results to ideal material behavior [62,63]. There are several mathematical models to adjust experimental profiles, but power-law model is the most employed for non-Newtonian fluids [64] due to its

versatility to explain Newtonian, pseudoplastic and dilatant behaviors depending on their flow behavior index or n value [65,66], as it can be observed in **Figure 1.4**.

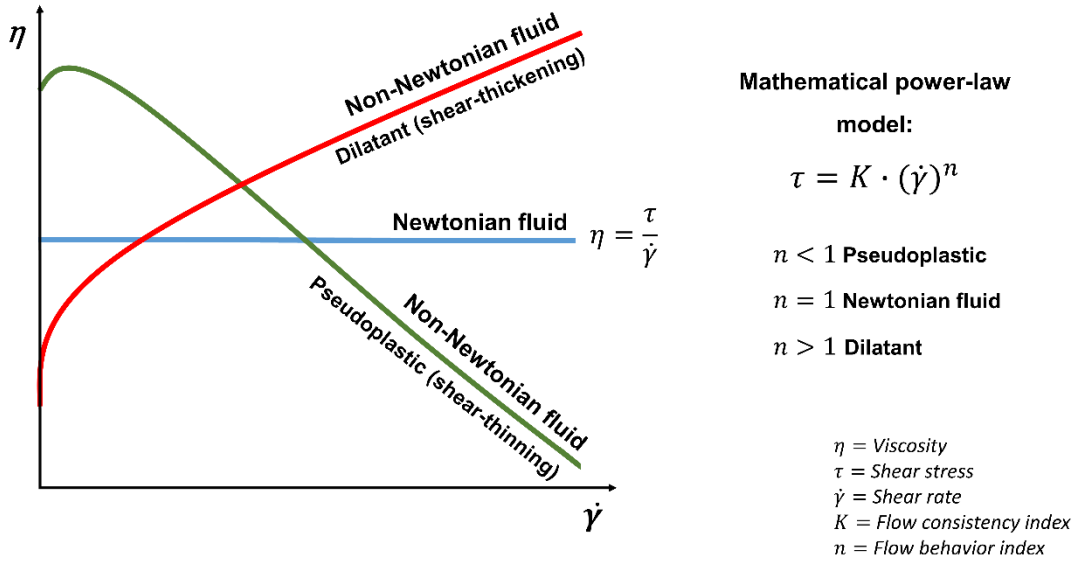

Figure 1.4. *Representation of the different material flow behaviors and mathematical power-law model.*

In extrusion 3D printing, shear-thinning behavior can be traduced in high initial viscosity at zero shear rate, when the bioink or biomaterial ink is placed into the syringe. Afterwards, the viscosity should decrease at high shear rates, when the material is passing through the nozzle. At this step, the material should flow with the minimal resistance, particularly in the presence of cells [29,45]. Finally, in a third stage, the viscosity must increase almost until initial values, recovering the structure when the shear rate is stopped after extrusion and thus, contributing to hold the printed shape [19,46,49] (**Figure 1.5**). It has been widely observed that higher initial viscosity values of the material demonstrate less possibility to structural collapse after printing [67,68]. On the other hand, the assessment of flow behavior index (n) and flow consistency index (K) from power-law adjustments of the different inks will help to predict their properties and suitability for extrusion-based 3D printing technology [69,70]. After extrusion, when the ink has been deposited on the surface, the internal forces of the material should oppose to collapse, showing elastic properties and consequently holding the printed shape [19,73].

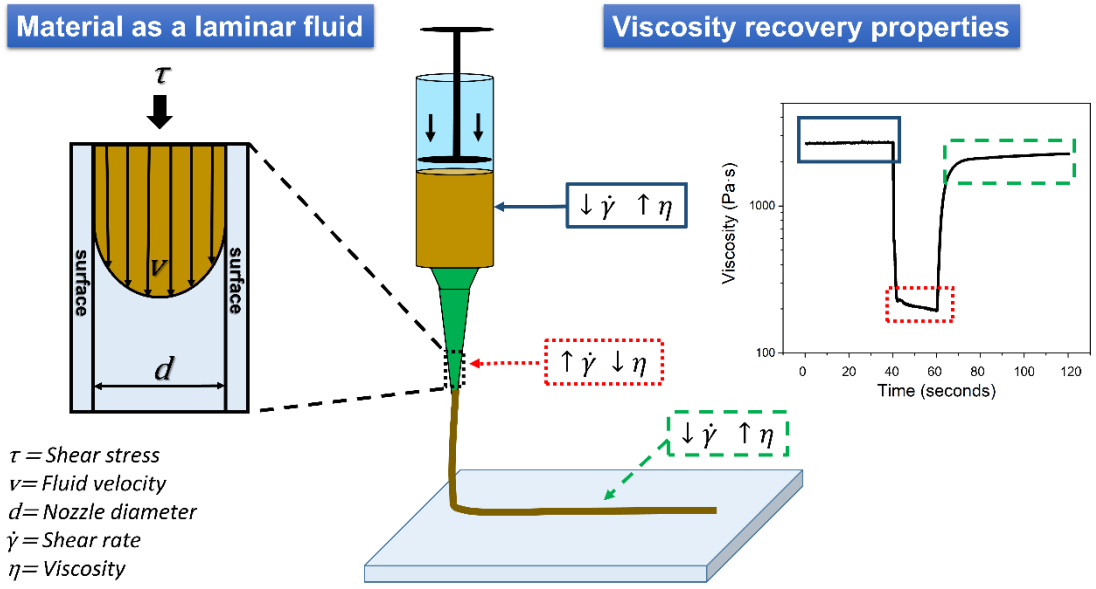

Figure 1.5. *Schematic representation of inks behavior during 3D printing process.*

Viscoelasticity is a property of the material that shows elastic behavior and viscous flow, which can be described by two parameters [74,75]. The storage modulus, also related to the elastic modulus and represented by G', is a parameter that represents the amount of energy stored by the material after the application of a stress [76] and therefore, it is related to its shape retention after 3D printing [77,78]. The loss modulus, also named viscous modulus and denoted by G'', represents the amount of energy dissipated by the material [76] and thus, this characteristic is related to viscous flow of the bioinks and biomaterial inks.

Shape fidelity and extrudability can also be correlated with yield stress and yield point, as well as with G' values [19,79]. Yield stress is defined as the pressure that has to be exceeded for starting the material flow [48,80]. It depends on the number and the strength of existing interactions between the molecules in the ink, which provides internal resistance to deformations and shape changes. For a proper material extrusion, the internal network should be broken under certain shear stress application, reaching the critical yield stress value and, hence, starting the flow [48]. Achieving this critical yield stress value is required for the viscosity to start to decrease. However, applied shear stress should be enough to reach the yield point stress value [45], which is defined as the stress value at the crossover point between G' and G''. According to the literature, it is the force needed for extrusion [81], allowing material flow through the nozzle. Storage modulus values are also an indicative of the amount of interactions among the polymer chains within the bioink or biomaterial ink [82]. The higher storage modulus, the higher

stiffness due to the presence of a highly structured network into the material, which will be traduced in shape retention [46,48]. Chen et al. [83] reported G' values from 1150 to 6909 Pa with a yield stress from 32 to 455 Pa and yield point values from 140 to 722 Pa for starch based inks suitable for extrusion 3D printing.

Bioinks or biomaterial inks presenting suitable initial viscosity, yield stress, yield point values and high elastic properties will show proper filament formation and material deposition on a surface after extrusion [19,84], being able to support their own weight and the subsequent layers on top achieving thus, proper-extrusion properties (**Figure 1.6**) [29].

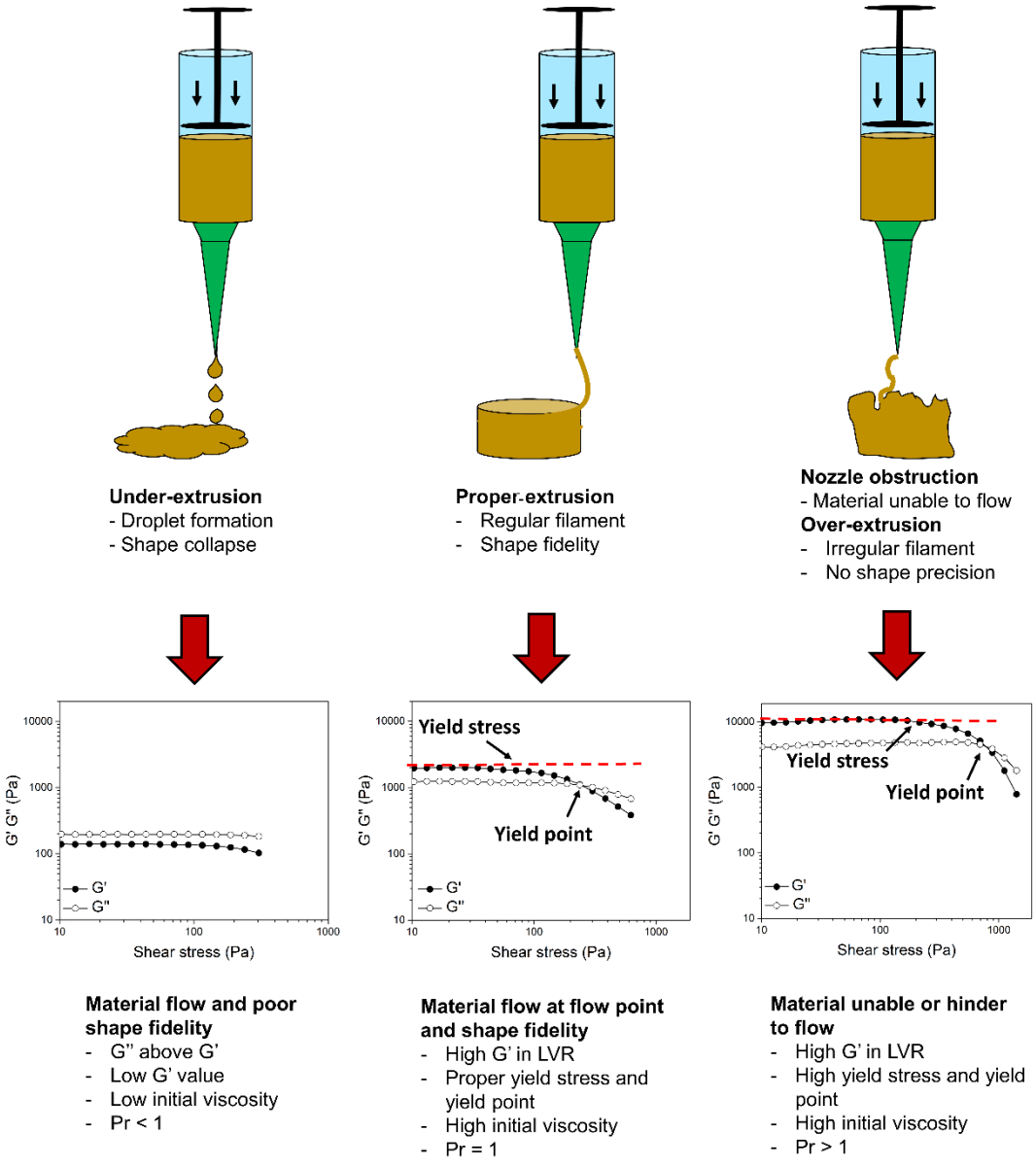

Figure 1.6. *Schematic representation of extrusion performance and correlation with rheological properties of the inks.*

Extrudability properties can be tested by the evaluation of filament uniformity in planar surfaces. Semi quantitative evaluation, based on the circularity of printed filaments and shape fidelity, was recently introduced by the printability index concept (Pr) [85]. When the inks present proper-extrusion properties the disposition of the deposited filaments present perfect square shape when filaments form 90 º and thus, Pr index is 1. On the contrary, bioinks or biomaterial inks that present low initial viscosity and loss modulus values higher than storage modulus under an increment of shear stress present under-extrusion properties [36]. This will be traduced in droplet formation after extrusion due to the material liquid state and collapse of the printed structure, presenting Pr index < 1 with circular and rounded shape when filament are deposited with an angle of 90 º. Finally, inks with high G' values, high yield stress and yield point values present difficulties to flow through the nozzle, or even can cause nozzle obstruction. In this case, the amount of molecular interactions within the material is such that the shear stress applied by the 3D printer system is not sufficient to overcome yield point value. This phenomenon is known as over-extrusion properties and it can be traduced as irregular filament formation presenting Pr values > 1 and unsuitable material deposition, which derives in imprecise shape reproduction [14,29,86].

Storage modulus and loss modulus of the bioinks and biomaterial inks are also typically assessed as a function of the frequency and deformation [46]. Those experiments provide information about the material behavior under oscillatory sweep measurements. The ratio between viscous modulus and elastic modulus (G''/G') as the angular velocity increases is known as loss tangent or tan δ [87], and it is related to printing resolution. When low tan δ values are measured, the material produces regular extrusion filaments indicating solid-like behavior while as tan δ values increase, the uniformity of the extrusion filaments is disrupted, forming droplets and showing liquid-like behavior [47]. Gao et al. [47] reported values of tan δ in the range of 0.25 to 0.45 for a suitable 3D printing performance of alginate-gelatin based inks, while Mazzocchi et al. [88] reported tan δ ranges from 0.29 to 0.33 for thiolated HA bioinks.

Rheological parameters of the bioinks and biomaterial inks are important to establish the proper printability window depending on employed biomaterials and their possible application field after 3D printing [45,70]. For the development of bioinks, which containing living cells, the rheological parameters should present enough viscosity and viscoelasticity to be successfully extruded and retain the desired shape, without compromising cell integrity [52,92,93]. However, biomaterial inks cover a wider printability window in which printing parameters and consequently, rheological properties are more flexible. As it can be observed in **Table 1.1**, initial viscosities in the range of

10^3 Pa·s are adequate to show good printability as well as G' values in the range of 10^3 Pa and tan δ values of 0.2. However, these printability windows often depend on the solid content and the amount of interactions between the biopolymer chains present in the inks [94].

Table 1.1. *Summary of rheological properties and printability window of suitable bioinks and biomaterial inks found in the literature.*

Bioink / Biomaterial ink	Viscosity Pa·s	n	K (Pa·s^n)	G' (Pa)	Yield stress (Pa)	Yield point (Pa)	Tan δ	Ref.
Alginate-gelatin	-	-	-	-	-	-	0.25-0.45	[47]
Starch-based	-	-	-	1.10^3-$7{\cdot}10^3$	32-455	140-722	-	[81]
GO-Alginate	$4{\cdot}10^3$	0.35	360	-	-	-	-	[72]
PU- cell laden	-	-	-	$4{\cdot}10^3$	-	-	-	[89]
Alginate-cellulose cell-laden	$1{\cdot}10^4$	-	-	$3{\cdot}10^3$	-	-	0.2	[90]
Alginate-cellulose	$5{\cdot}10^3$	0.39	787	-	-	-	-	[71]
Alginate-cellulose	$1.5{\cdot}10^3$	-	-	$4{\cdot}10^3$	-	-	0.15	[49]
Gelatin methacryloyl-gellan gum cell-laden	$1{\cdot}10^3$	-	-	-	48.2	-	-	[86]
PU-cellulose	$5{\cdot}10^3$	0.18	335	$3{\cdot}10^3$	94	$1{\cdot}10^3$	0.2	[91]

- *Inks composition*

Bioinks and biomaterial inks employed in extrusion 3D printing are mainly composed of polymeric biomaterials that present a great capacity to be suspended in aqueous solutions [95,96]. Water-based polymeric systems that compose bioinks should present flexibility, providing a suitable niche to host living cells [31]. However, this extra flexibility can give rise to problems for achieving functional 3D printing constructs [97]. Those constructs occasionally do not present suitable mechanical characteristics to retain the

printed shape for a long period and therefore, post-printing modifications such as freeze-drying or crosslinking are needed to overcome these challenges [98,99]. Freeze-drying technique is commonly used after 3D printing of water-based biomaterial inks in order to retain accurately the printed shape, creating nanoporous structures. This technique consists in the elimination of water from the 3D printed samples directly by sublimation, preserving the original dimensions and obtaining porous structures [100,101]. Besides, these porous structures show great swelling capacity, which can facilitate not only the release of many drugs and molecules of interest, but also enable the growth and proliferation of seeded cells into the porous matrix [100,102]. Crosslinking processes allow either the transformation of the polymer suspension into a gel-like structure or the stabilization of the printed shape, modifying their physicochemical characteristics [97,103]. The presence of specific chemical groups in the polymer structure enables the formation of a high viscosity gel-like material that could be maintained for a longer periods with the aid of crosslinking agents. Those crosslinking agents normally are small molecules that stablish covalent or non-covalent bonds among polymer chains [104].

Bioinks and biomaterial inks can be either single-component or multicomponent. Generally, single-component inks show poor viscosity and viscoelasticity to be correctly printed and retain the printed shape [105] and consequently, the mixture with other biopolymers that present larger molecular weight or nanoentities that interact with the polymeric structure can improve their rheological properties [106,107]. Multicomponent inks are composed of different polymeric systems that interacts one another by means of the entanglement of their polymer chains, or by the establishment of either physical or chemical interactions among their molecules [107,108]. Multicomponent inks widely employed for 3D printing technology are based on alginate blends [109,110]. Alginate water suspensions usually present poor viscoelastic characteristics to retain the printed shape, but when they are mixed with other high molecular weight biopolymers such as gelatin, HA or collagen, their rheological properties are adequate [111–113]. Moreover, the addition of nanoparticles to the alginate suspensions, either natural or synthetic, enables the modification of their rheological characteristics and therefore, expands their printability window [36,49,71].

Alginate is widely employed in extrusion 3D printing technology for biomedical applications due to its great capacity to form hydrogels and its biocompatible character that provides a suitable environment for cell proliferation [102,109]. Alginate is commonly extracted from the cell wall of some brown algae species such as *Laminaria hyperborea, Macrocystis pyrifera* or *Ascophyllum nodosum* [114], or it can also be obtained via bacterial synthesis from bacteria of *Pseudomonas* and *Azotobacter* genera [115]. This

biopolymer is composed of large chains of linear unbranched polysaccharides containing different amounts of 1,4′-linked β-D-mannuronic acid (M) and α-L-guluronic acid (G) subunits [116,117]. The chemical composition and the M/G sequence may vary widely between algae species and even among the different parts of the algae [118]. The ratio between M and G subunits influences their physicochemical properties, since alginate chains containing majority of G blocks provide stiffer structural conformations [118] while M blocks predominance shows high flexibility of the chains [119]. The large content of hydroxyl groups (-OH) along the whole polysaccharide structure allows the formation of hydrogen bonds among those hydroxyl groups and the water molecules and thus, its suspension in aqueous media [120,121]. All M and G subunits present in their structure a carboxyl group (-COOH) that can establish ionic interactions with cations. The bond between two carboxyl groups from alginate chains with a single divalent cation forms egg-box structures that promote the creation of a strong gel-like network, with higher affinity for G subunits than M [118,122,123]. Ca^{2+} ions are widely employed as crosslinker agent of alginate-based bioinks and biomaterial inks after 3D printing to retain the printed shape for a longer period [36,124] (**Figure 1.7**).

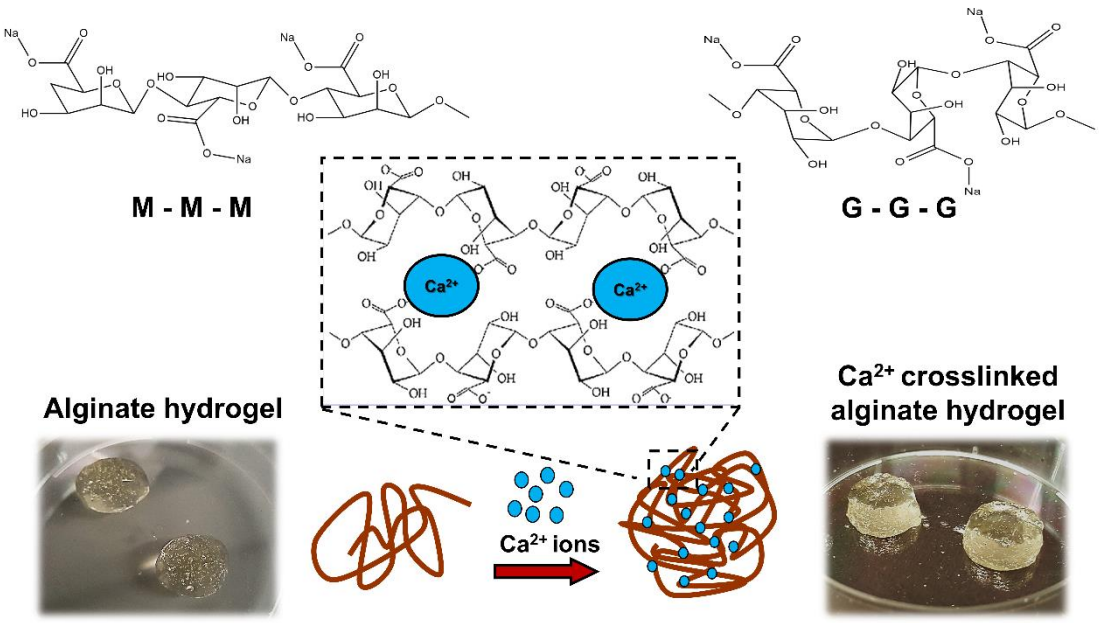

Figure 1.7. *Representation of M-M-M and G-G-G blocks of alginate and graphical representation of Ca^{2+} crosslinking process: formation of the egg-box structure when Ca^{2+} ions are added to an alginate solution.*

Other water-based polymers that are also widely used in extrusion-based 3D printing technology due to their suitable characteristics are waterborne polyurethanes. Polyurethanes (PU) are synthetic polymers commonly used for biomedical purposes due to its excellent biocompatibility as well as its great physical and mechanical properties.

Polyurethane family present tensile strength, large elasticity, and biocompatible character, characteristics that imitate successfully natural tissue mechanics. Therefore, they are widely employed as scaffolds for tissue engineering applications such as cartilage regeneration [125,126]. Besides, PUs are also used for manufacturing of medical devices and surgical instrumentation such as catheters, intra-aortic and gastric balloons or as a coating for breast implants, among others [127]. However, PUs are commonly synthetized using organic solvents, and the presence of those residual solvent in the final product can derive in a cytotoxic material. The recent development of waterborne polyurethane (WBPU) dispersions has created an environmentally friendly material in which organic solvents are replaced by water, overcoming possible cytotoxic reactions [128,129].

PUs and WBPU dispersions as well, are usually composed by two main blocks: the soft-segment, which is formed by a polyol, and the hard-segment that generally is composed by an isocyanate and a chain extender consisting on a low molecular weight diol. Besides, a covalently attached molecule containing ionic groups such as carboxylic, sulfonate, or quaternary ammonium salt, is incorporated as an emulsifier component. By this way, the hydrophilic character of the ionic groups allows the dispersion of the polyurethane in water enclosing the hydrophobic part in the core and thus, forming stable polyurethane nanoparticles (**Figure 1.8**) [129–132].

WBPU dispersions usually present strength and flexibility related to the hard and soft segments, respectively, as well as a structure with regular particle sizes, which allow the maintenance of the dispersion over time [129,132]. WBPU dispersions present other positive characteristics such as the combination of high solid content and high molecular weight with low viscosity [133]. Moreover, the presence of carboxylic groups in the outer part of the particle structure allow the crosslinking in the presence of divalent cations such as Ca^{2+} or Mg^{2+}, forming ionic interactions among the carboxylic groups from different particles and thus creating a 3D stiff network [134].

All of these characteristics make biodegradable WBPU dispersions good candidates for the manufacture of medical devices using extrusion 3D printing technology. Besides, non-degradable WBPU are also demanded in personalized medicine depending if the scaffold or implant requires to remain into human body for long time, performing a specific function [135]. WBPU can form part of the bioinks and biomaterial inks blended with other polymers such as sodium alginate, gelatin or HA that provide an increase of the viscosity of the neat WBPU dispersion [89,126,134].

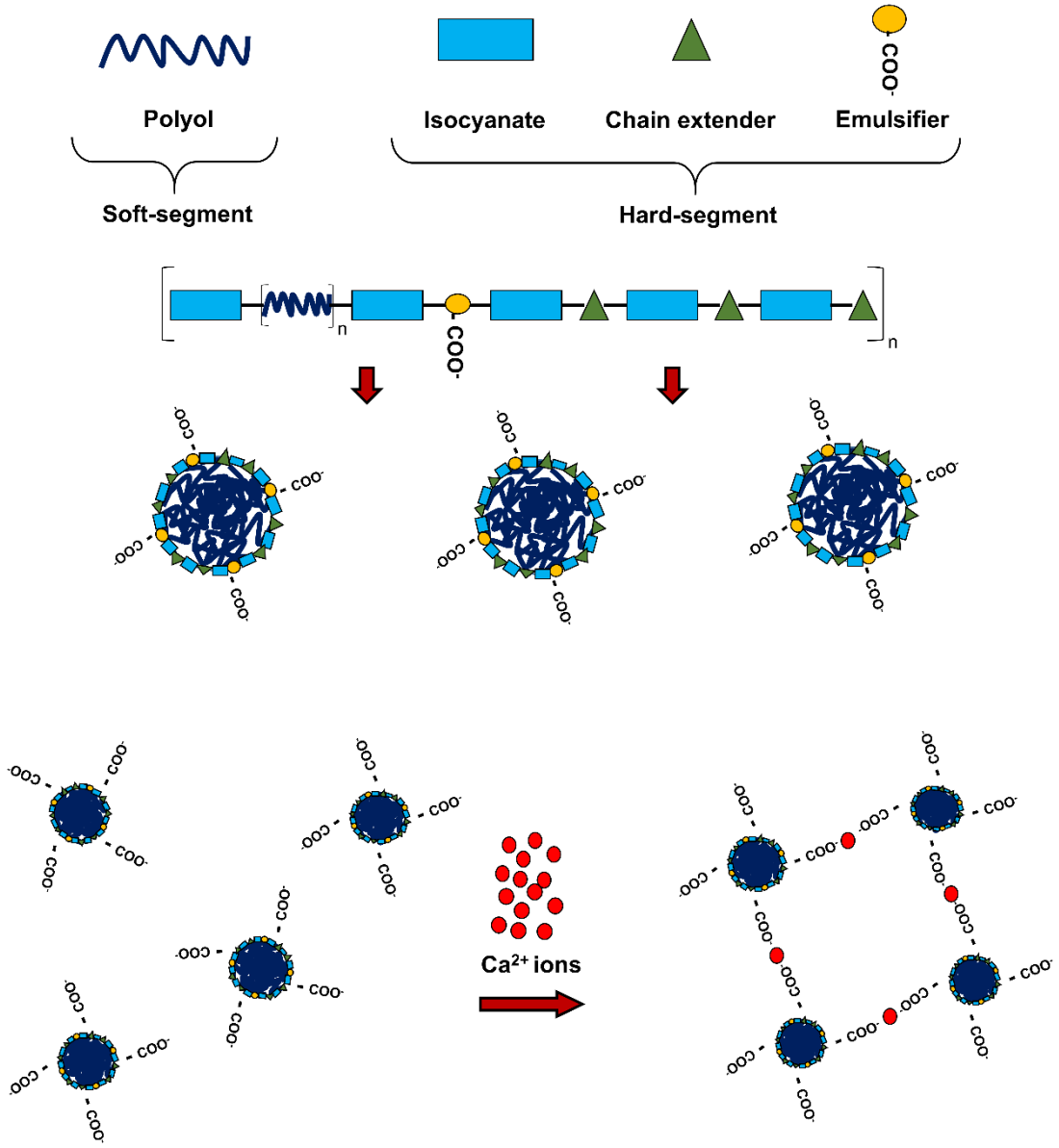

Figure 1.8. *Schematic representation of WBPU dispersion structure: from basic components to particle formation. Ca^{2+} ion crosslinking among particles forming a high-organized network.*

In reported studies carried out by Hung et al. [125], a WBPU dispersion was blended with hyaluronan at 2 wt. %, achieving an increase in the viscosity of the neat WBPU dispersion from 2.5 Pa·s to 10.2 Pa·s at 1 s^{-1}, and showing at 100 s^{-1} a viscosity of 2.7 Pa·s, and hence, shear-thinning behavior. In another work also reported by Hung et al. [128] a WBPU dispersion was mixed with polyethylene oxide (PEO) in a proper concentration among 22 and 26 wt. % to increase the viscosity at rest, achieving suitable printability.

Another common polymer employed in extrusion 3D printing for pharmaceutical and medical applications is cellulose. Cellulose is a natural biopolymer present in the cellular

wall of all plant cells performing a structural function and therefore, is one of the most abundant polymers on earth. It is commonly extracted from different wood species, but also it can be extracted from some species of bacteria, tunicates and algae [136]. Diverse cellulose forms such as cellulose nanoentities and functionalized cellulose structures are widely employed in the biomedical and pharmaceutical industry due to their biocompatible and biodegradable character [137,138].

Cellulose structure consists in long polysaccharide chains composed of D-glucose subunits linked by β-(1-4)-glycosidic bonds [139]. The hydrogen bonds formed between hydroxyl groups and oxygen from the different chains stabilizes the linkage among the different subunits and results in a linear structural configuration. Hydrogen bonds can also be formed among the hydroxyl groups from cellulose chains and water molecules, stabilizing the structure in aqueous environments.

Cellulose is widely known for its role as a reinforcement in different composites due to its great mechanical properties provided by a high crystalline structure [140,141], reporting Young's Modulus values up to 50 to 70 GPa and tensile strength values from 600 to 1200 MPa for cellulose nanofibers papers [142]. Cellulose fibers are composed by macrofibers, microfibers and elementary fibrils, which have specific regions that present highly ordered cellulose parts (crystalline) and other regions showing disordered structures, known as amorphous regions (**Figure 1.9**) [136,143].

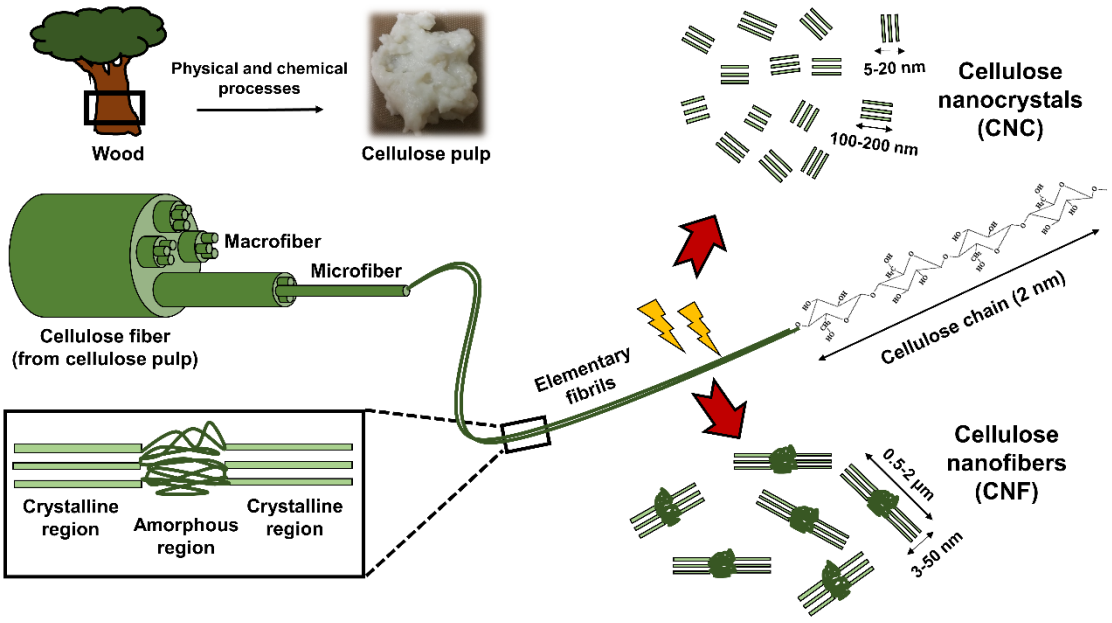

Figure 1.9. *Schematic representation of cellulose structure, CNC and CNF obtaining process from wood.*

Those elementary fibrils from cellulose pulp can be individualized by mechanical treatment, chemical oxidation or enzymatic treatment, giving rise to cellulose nanofibers (CNF) presenting sizes from 3 to 50 nm in diameter and from 0.5 to 2 μm in length, depending on the treatment intensity. Furthermore, treatments with strong acids such as sulfuric acid can hydrolyze the amorphous regions, producing the isolation of short rigid cellulose nanocrystals (CNC) with sizes from 5 to 20 nm in diameter and lengths among 100-200 nm [142,144,145]. However, those acid treatments can compromise the biocompatible character as well as the structural integrity of the cellulose by the incorporation of sulfate groups into CNC structure and providing high solubility in water. On the contrary, enzymatic hydrolysis processes to obtain CNCs have demonstrated to be less aggressive and thus, their biocompatible properties remaining unchanged [146–148]. In addition to being more environmentally friendly compared to acidic processes, the enzymatic hydrolysis process usually results in a higher polymerization degree of cellulose and consequently, in nanoentities with higher lengths, compared to those obtained by sulfuric acid hydrolysis. Endoglucanases are a type of enzymes that attack specifically in the amorphous regions in a random way, resulting in nanofibers in the crystalline form entwined with fibers in amorphous phase [149].

CNC and CNF are usually employed as rheological modifier and reinforcement of bioinks and biomaterial inks, improving viscosity and viscoelastic properties of multiple biomaterial blends [124,150]. Cellulose nanoentities normally do not present suitable properties to be single printed and therefore, they are typically blended with high molecular weight polymers that present inappropriate rheological characteristics, such as SA, HA, chitosan or WBPU dispersions, achieving inks with suitable characteristics for extrusion 3D printing technology. The nanoentities are just entangled within the long chains of the polymers or even establish hydrogen bonds among the hydroxyl groups from cellulose and other hydroxyl groups from the polymers, forming a complex network [71,151,152]. In a recent study carried out by Vadillo et al. [91] a biomaterial ink was developed by adding 0.5 wt. % of CNC to a WBPU dispersion, which increased the viscosity of the initial WBPU from $3 \cdot 10^3$ to $1 \cdot 10^4$ Pa·s, as well as the G' from $1 \cdot 10^3$ to $3 \cdot 10^3$ Pa was developed.

1.2.3. Applications of extrusion 3D printed scaffolds in precision medicine

Extrusion 3D printing technology has experienced a marked increment on healthcare field in recent times. Medical applications, involving extrusion 3D printed constructions, are an advantage over conventional therapies, including the development of personalized prostheses, implants and surgical models, as well as advanced drug

delivery carriers or customizable scaffolds for tissue engineering (**Figure 1.10**). These are some of the principal technological advantages of healthcare 3D printing, enhancing the industry progression of this advanced technology [153,154].

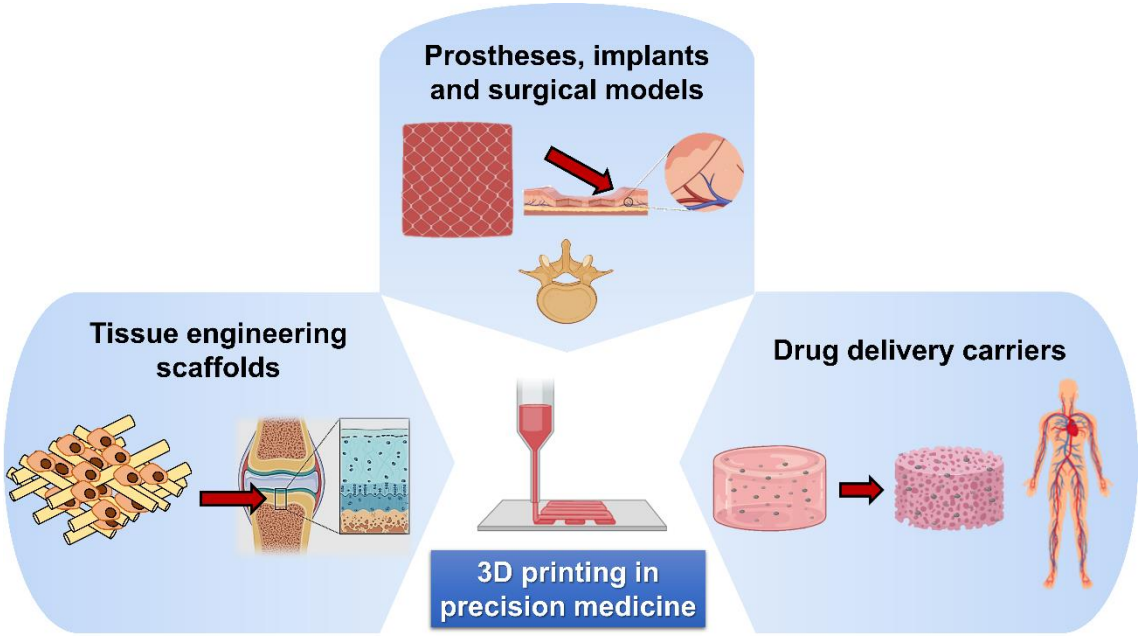

Figure 1.10. *Schematic overview of the principal applications of extrusion 3D printing technology in precision medicine: From mesh implants for skin and surgical models of vertebra to scaffolds for bone regeneration and drug delivery carriers.*

1.2.3.1. Personalized prostheses, implants and surgical models

The manufacturing of implants and prostheses by 3D printing technology has recently caused a great impact in the area of medical devices, satisfying the high demand for personalized therapies. 3D printing enables the manufacture of tailor-made products that cover individual needs depending on patient anatomy and condition [155,156].

The design and manufacturing of 3D printing medical implants and prostheses commonly start from digital images obtained by computed tomography (CT) or magnetic resonance imaging (MRI) from a specific injury or area of a patient. CAD technology recreates the 3D prototype using the images previously obtained and the tailor-made structures are fabricated layer by layer directed by the 3D printer system, following the specific CAD design [157,158].

The capacity to produce rapidly customized implants and prostheses through 3D printing overcomes persistent problems in orthopedics and surgery, providing implants that match site-specific mechanical and physical properties [156]. New orthopedic devices such as nylon meshes presenting lightweight, durability and water resistant properties

[159], medical instruments and devices such as nylon-based uretic stents and laparoscopic trocars, as well as personalized surgical implants for vaginal tissue reinforcement [160] have been successfully manufactured and developed through 3D printing. Those are great examples of how 3D printing technology can specifically cover and satisfy the market of personalized implants.

Moreover, surgical model structures from individual patients are highly demanded for diagnosis and treatment support [161]. The use of 3D printing models enables accurate diagnosis, a better evaluation and analysis of the injury, as well as the proper visualization of patient specific organ anatomy or defect. The use of these models during the preoperative planning increases the amount of information of the characteristics of a specific organ or anatomical area, reducing possible complications during surgery [156,162]. An example of this application is the 3D printing orbital models to be used in surgical procedures to help and recognize anatomical landmarks and thus, allow the accurate fixation of the required implant due to the difficulty of skull area visualization [163].

1.2.3.2. Carriers for drug delivery

Pharmaceutical industry is one of the principal fields in which personalized therapies are demanded. Solid oral dosage forms such as tablets or capsules are most recommended pharmaceutical products. However, those items occasionally do not have the desired positive effect or present negative effects in determined population groups. Pediatric population group usually require specific dose that varies according to the age and body weight of children, whereas large amount of different drugs are administrated for geriatric group population on a daily basis. Besides, both groups commonly present swallowing difficulties of conventional tablets [154,164]. Polypharmacy can be an alternative to traditional oral dosage forms by means of the development of poly-pills fabricated according to specific patient necessities using 3D printing technology [165]. Active pharmaceutical ingredients (API) and drugs are commonly incorporated and stabilized into the biomaterial inks before being 3D printed and thus, oral dosage forms can be designed to release the required dose for each patient [166]. It was concluded that customized 3D printed tablets containing a combination of the different drugs with the required individual dose are more accurate and safe for advanced age populations [154].

The 3D printing tablets containing one or more APIs with different properties can present different dissolution profiles in physiological media. Precise control over the release behavior of the APIs can be achieved depending on the selected materials to carry the

drugs, but also by the design of a specific geometry and internal structure of the printed tablet [156,167]. Internal structure modification processes are usually carried out after 3D printing of the constructs by means of post-printing processes [99]. These post-printing processes not only modulate the release pattern of the drugs but also stabilize the obtained 3D shape after printing.

Although solid oral dosage forms have been the most widely studied, 3D printing is also used to fabricate transdermal drug delivery systems in order to achieve a focalized release in a specific area [168,169]. This could be beneficial for the improvement of hydrophobic drug release in target site. Hydrophobic drugs usually present issues related to pharmacokinetics and bioavailability due to their low solubility in physiological conditions [170]. The fabrication of customizable drug carriers or patches for the localized release of hydrophobic drugs by means of encapsulation and stabilization into the biomaterial inks could be a form to overcome bioavailability problems [171,172].

1.2.3.3. Scaffolds for tissue engineering

Tissue regeneration field is focused on the development of new techniques to repair, regenerate and replace damaged tissues and organs, as well as the creation of *in vitro* 3D tissue models for better understanding of tissue ingrowth, broad visualization of a different disease stages and as a non-invasive tool for testing new drugs and cosmetic products [96,173].

The manufacturing of suitable 3D biological environments enabling cell-cell interactions and recreating the natural biological niches needed for suitable tissue ingrowth can be achieved through extrusion 3D printing technology. 3D bioprinting is the most popular technology for this complex application due to its low cost, high customization degree and capacity to print a wide range of biocompatible smart materials containing living cells and biological molecules into accurately designed constructs, which will provide structural support for the newly formed tissue [96,105,174]. The employed cells for this application can come from different sources, including established cell lines, primary cell cultures from individual patients or even stem cells. Successful tissue regeneration strongly depends on the interactions between cells and the cells with scaffold and therefore, the selected biomaterials should enable essential biological functions such as cell adhesion and migration, the diffusion of nutrients, oxygen and secreted products, as well as sufficient mechanical support over time [175,176]. Furthermore, in some cases, scaffolds should remain for a long period or degrade depending on the clinical scenario,

and therefore this is another important factor to keep in mind at the time of scaffold design.

Multilayer scaffold design enables to repair complex tissues such as skin, cartilage or bone, which have a high thickness and heterogeneous composition, a major challenge for monolayer scaffolds until now [177]. Moreover, the multilayer scaffold geometry influences a wide range of aspects such as porosity, mechanical properties and biological cell performance [178]. The obtained geometry of the scaffolds is determined by the position and orientation of the deposited filaments, and therefore, the space and direction among filaments will result in a broad range of pore sizes. Effective pore interconnection is an essential requirement to enable nutrient and oxygen transport to the cells and thus, scaffold design and geometry are the key factors to ensure tissue ingrowth [179,180].

In precision medicine, not only scaffolds should be designed according to better scenario for cell proliferation, but also in base of the damaged zone or specific injury from an individual patient [181]. Extrusion 3D printing technology enables a high grade of customization, fabricating constructs that match with the shape of damaged area providing a suitable biological environment for tissue ingrowth. Therefore, this technology is a key tool to enable faster solutions for tissue replacement in regenerative medicine [154,173,181].

1.3. General objectives

The main objective of this work has been the development of biomaterial inks and bioinks with suitable characteristics for extrusion 3D printing technology, as well as the subsequent analysis of the 3D printed constructs for their potential use in precision medicine as drug delivery carriers, customizable implants and scaffolds for tissue engineering. For that purpose, different alginate/WBPU/cellulose biomaterial blends were developed varying their solid contents on the ink formulations. Moreover, two single-component inks made of crosslinked alginate and enzymatically obtained CNCs (EnCNCs), respectively, were also developed and characterized. After the development and characterization of both inks and 3D printed scaffolds, their potential applications in precision medicine and biomedical field were also studied in each case.

Therefore, after a brief introduction to the state of the art of the principal topics of this work in Chapter 1, the specifications of the materials and reactants employed, as well as the full methodologies and techniques have been well described in Chapter 2. From this point, the work was divided as follows:

- In Chapter 3, the alginate, WBPU dispersion and the CNF employed throughout the study have been well characterized. Besides, the obtaining process of EnCNCs was also described.
- In Chapter 4, single-component inks from either alginate with different crosslinking degrees or EnCNCs with different solid contents were developed. The different inks and the suitable 3D printed constructs have been well characterized. Moreover, the potential biomedical applications of the printed scaffolds are tested.
- In Chapter 5, different alginate-CNF biomaterial inks with different CNF contents have been developed and characterized for extrusion 3D printing. The suitable inks were loaded with hydrophobic and/or hydrophilic drug models, and the subsequent 3D printed constructs were tested as tablets for controlled drug delivery.
- In Chapter 6, different alginate contents were added to WBPU dispersion to create five different biomaterial inks. 3D printed meshes have been created and their potential use as customizable implants for groin hernia repair was evaluated through mechanical and morphological analyses. Besides, the most promising ink was loaded with antibiotic for local release.
- In Chapter 7, five different A-WBPU blends were developed as bioinks for cartilage tissue regeneration applications. The rheological properties as well as the encapsulation and viability of the cells into the bioinks has been studied. The selected bioinks were 3D printed and the synthesis of specific cartilage molecules into the scaffolds was evaluated.

1.4. References

[1] Litman T. Personalized medicine: Concepts, technologies, and applications in inflammatory skin diseases. Apmis 2019;127:386–424. https://doi.org/10.1111/apm.12934.

[2] Schork NJ. Personalized medicine: Time for one-person trials. Nature 2015;520:609–611. https://doi.org/10.1038/520609a.

[3] Chan IS, Ginsburg GS. Personalized medicine: Progress and promise. Annu Rev Genomics Hum Genet 2011;12:217–44. https://doi.org/10.1146/annurev-genom-082410-101446.

[4] Duffy DJ. Problems, challenges and promises: Perspectives on precision medicine. Brief Bioinform 2016;17:494–504. https://doi.org/10.1093/bib/bbv060.

[5] König IR, Fuchs O, Hansen G, von Mutius E, Kopp M V. What is precision medicine? Eur Respir J 2017;50:1–12. https://doi.org/10.1183/13993003.00391-

2017.

[6] Aguado BA, Grim JC, Rosales AM, Watson-Capps JJ, Anseth KS. Engineering precision biomaterials for personalized medicine. Sci Transl Med 2018;10:1-10. https://doi.org/10.1126/scitranslmed.aam8645.

[7] Ho D, Quake SR, McCabe ERB, Chng WJ, Chow EK, Ding X. Enabling technologies for personalized and precision medicine. Trends Biotechnol 2020;38:497–518. https://doi.org/10.1016/j.tibtech.2019.12.021.

[8] Xu X, Jia Z, Zheng Y, Wang Y. Bioadaptability of biomaterials: Aiming at precision medicine. Matter 2021;4:2648–2650. https://doi.org/10.1016/j.matt.2021.06.033.

[9] Tappa K, Jammalamadaka U. Novel biomaterials used in medical 3D printing techniques. J Funct Biomater 2018;9:1-17. https://doi.org/10.3390/jfb9010017.

[10] dos Santos J, de Oliveira RS, de Oliveira T V., Velho MC, Konrad M V., da Silva GS, Deon M, Beck CR. 3D Printing and Nanotechnology: A Multiscale Alliance in Personalized Medicine. Adv Funct Mater 2021;31:1–35. https://doi.org/10.1002/adfm.202009691.

[11] Amekyeh H, Tarlochan F, Billa N. Practicality of 3D printed personalized medicines in therapeutics. Front Pharmacol 2021;12:1–15. https://doi.org/10.3389/fphar.2021.646836.

[12] Kang HW, Lee SJ, Ko IK, Kengla C, Yoo JJ, Atala A. A 3D bioprinting system to produce human-scale tissue constructs with structural integrity. Nat Biotechnol 2016;34:312–319. https://doi.org/10.1038/nbt.3413.

[13] Rocha VG, Saiz E, Tirichenko IS, García-Tuñón E. Direct ink writing advances in multi-material structures for a sustainable future. J Mater Chem A 2020;8:15646–15657. https://doi.org/10.1039/d0ta04181e.

[14] Jiang Z, Diggle B, Tan ML, Viktorova J, Bennett CW, Connal LA. Extrusion 3D printing of polymeric materials with advanced properties. Adv Sci 2020;7:1–32. https://doi.org/10.1002/advs.202001379.

[15] Saadi MASR, Maguire A, Pottackal NT, Thakur MSH, Ikram MM, Hart AJ, Ajayan, PM, Muhammad MR. Direct ink writing: A 3D printing technology for diverse materials. Adv Mater 2022;2108855:1–57. https://doi.org/10.1002/adma.202108855.

[16] Chia HN, Wu BM. Recent advances in 3D printing of biomaterials. J Biol Eng 2015;9:1–14. https://doi.org/10.1186/s13036-015-0001-4.

[17] Khan A, Mcmenamin P, Rozen W, Chae M. A comprehensive study on 3D printing technology. MIT Int J Mech Eng 2016;6:63–69.

[18] Global Market Insights. Healthcare 3D printing market size by product (Syringe based, Magnetic Levitation, Laser Based, Inkjet Based), By Technology (Fused Deposition Modelling (FDM), Selective Laser Sintering (SLS), Stereolithography), By Application (Biosensors, Medical Pharm) 2021:120. https://www.gminsights.com/segmentation/detail/healthcare-3D-printing-market. (jun. 2022)

[19] Schwab A, Levato R, D'este M, Piluso S, Eglin D, Malda J. Printability and shape fidelity of bioinks in 3D bioprinting. Chem Rev 2020;120:11028–11055. https://doi.org/10.1021/acs.chemrev.0c00084.

[20] Shah J, Snider B, Clarke T, Kozutsky S, Lacki M, Hosseini A. Large-scale 3D printers for additive manufacturing: design considerations and challenges. Int J Adv Manuf Technol 2019;104:3679–3693. https://doi.org/10.1007/s00170-019-04074-6.

[21] Park BJ, Choi HJ, Moon SJ, Kim SJ, Bajracharya R, Min JY, Han HK. Pharmaceutical applications of 3D printing technology: Current understanding and future perspectives. J Pharm Investig 2019;49:575–585. https://doi.org/10.1007/s40005-018-00414-y.

[22] Mathew E, Domínguez-Robles J, Stewart SA, Mancuso E, O'Donnell K, Larrañeta E, Lamprou DA. Fused deposition modeling as an effective tool for anti-infective dialysis catheter fabrication. ACS Biomater Sci Eng 2019;5:6300–6310. https://doi.org/10.1021/acsbiomaterials.9b01185.

[23] Placone JK, Engler AJ. Recent advances in extrusion-based 3D printing for biomedical applications. Adv Healthc Mater 2018;7:1–11. https://doi.org/10.1002/adhm.201701161.

[24] Jose RR, Rodriguez MJ, Dixon TA, Omenetto F, Kaplan DL. Evolution of bioinks and additive manufacturing technologies for 3D bioprinting. ACS Biomater Sci Eng 2016;2:1662–1678. https://doi.org/10.1021/acsbiomaterials.6b00088.

[25] Khaled SA, Burley JC, Alexander MR, Yang J, Roberts CJ. 3D printing of tablets containing multiple drugs with defined release profiles. Int J Pharm 2015;494:643–650. https://doi.org/10.1016/j.ijpharm.2015.07.067.

[26] Kolesky DB, Homan KA, Skylar-Scott MA, Lewis JA. Three-dimensional bioprinting of thick vascularized tissues. Proc Natl Acad Sci U S A 2016;113:3179–3184. https://doi.org/10.1073/pnas.1521342113.

[27] Hölzl K, Lin S, Tytgat L, Van Vlierberghe S, Gu L, Ovsianikov A. Bioink properties before, during and after 3D bioprinting. Biofabrication 2016;8:1–19. https://doi.org/10.1088/1758-5090/8/3/032002.

[28] Li L, Lin Q, Tang M, Duncan AJE, Ke C. Advanced polymer designs for direct-ink-write 3D printing. Chem A Eur J 2019;25:10768–10781. https://doi.org/10.1002/chem.201900975.

[29] Ouyang L, Yao R, Zhao Y, Sun W. Effect of bioink properties on printability and cell viability for 3D bioplotting of embryonic stem cells. Biofabrication 2016;8:3-7. https://doi.org/10.1088/1758-5090/8/3/035020.

[30] Groll J, Burdick JA, Cho DW, Derby B, Gelinsky M, Heilshorn SC, Jüngst T, Malda J, Mironov VA, Nakayama K, Ovsianikov A, Sun W, Takeuchi S, Yoo JJ, Woodfield TBF. A definition of bioinks and their distinction from biomaterial inks. Biofabrication 2019;11:013001-013010. https://doi.org/10.1088/1758-5090/aaec52.

[31] Ramiah P, du Toit LC, Choonara YE, Kondiah PPD, Pillay V. Hydrogel-Based Bioinks for 3D Bioprinting in Tissue Regeneration. Front Mater 2020;7:1–13. https://doi.org/10.3389/fmats.2020.00076.

[32] Varanko A, Saha S, Chilkoti A. Recent trends in protein and peptide-based biomaterials for advanced drug delivery. Adv Drug Deliv Rev 2020;156:133–187. https://doi.org/10.1016/j.addr.2020.08.008.

[33] Lerman MJ, Lembong J, Gillen G, Fisher JP. 3D printing in cell culture systems and medical applications. Appl Phys Rev 2018;5:041109-041118. https://doi.org/10.1063/1.5046087.

[34] Foulkes R, Man E, Thind J, Yeung S, Joy A, Hoskins C. The regulation of nanomaterials and nanomedicines for clinical application: Current and future perspectives. Biomater Sci 2020;8:4653–4664. https://doi.org/10.1039/d0bm00558d.

[35] Kyle S, Jessop ZM, Al-Sabah A, Whitaker IS. 'Printability'' of candidate biomaterials for extrusion based 3D printing: State-of-the-art.' Adv Healthc Mater 2017;6:1–16. https://doi.org/10.1002/adhm.201700264.

[36] Markstedt K, Mantas A, Tournier I, Martínez Ávila H, Hägg D, Gatenholm P. 3D bioprinting human chondrocytes with nanocellulose-alginate bioink for cartilage tissue engineering applications. Biomacromolecules 2015;16:1489–1496. https://doi.org/10.1021/acs.biomac.5b00188.

[37] Liu F, Wang X. Synthetic polymers for organ 3D printing. Polymers 2020;12:1765-1771. https://doi.org/10.3390/polym12081765.

[38] Murphy SV., Skardal A, Atala A. Evaluation of hydrogels for bio-printing applications. J Biomed Mater Res - Part A 2013;101 A:272–284. https://doi.org/10.1002/jbm.a.34326.

[39] Rutz AL, Hyland KE, Jakus AE, Burghardt WR, Shah RN. A multimaterial bioink method for 3D printing tunable, cell-compatible hydrogels. Adv Mater 2015;27:1607–1614. https://doi.org/10.1002/adma.201405076.

[40] Nikam VK, Kotade KB, Gaware VM, Dolas RT, Dhamak KB, Somwanshi BS, Khdse AN, Kashid VA. Eudragit a versatile polymer: a review. Pharmacologyonline 2011;1:152–164.

[41] Freedman BR, Mooney DJ. Biomaterials to mimic and heal connective tissues. Adv Mater 2019;31:1–27. https://doi.org/10.1002/adma.201806695.

[42] Gad SC, Schuh JACL. Toxicologic pathology forum opinion paper: considerations for toxicologic pathologists evaluating the safety of biomaterials and finished medical devices. Toxicol Pathol 2018;46:366–371. https://doi.org/10.1177/0192623318768719.

[43] Park K, Skidmore S, Hadar J, Garner J, Park H, Otte A, Soh BK, Yoon G, Yu D, Yun Y, Lee BK. Injectable, long-acting PLGA formulations: Analyzing PLGA and understanding microparticle formation. J Control Release 2019;304:125–134. https://doi.org/10.1016/j.jconrel.2019.05.003.

[44] Liu Z, Bhandari B, Prakash S, Mantihal S, Zhang M. Linking rheology and printability of a multicomponent gel system of carrageenan-xanthan-starch in extrusion based additive manufacturing. Food Hydrocoll 2019;87:413–424. https://doi.org/10.1016/j.foodhyd.2018.08.026.

[45] Paxton N, Smolan W, Böck T, Melchels F, Groll J, Jungst T. Proposal to assess printability of bioinks for extrusion-based bioprinting and evaluation of rheological properties governing bioprintability. Biofabrication 2017;9:044107-044120. https://doi.org/10.1088/1758-5090/aa8dd8.

[46] Liu Z, Zhang M, Bhandari B, Yang C. Impact of rheological properties of mashed potatoes on 3D printing. J Food Eng 2018;220:76–82. https://doi.org/10.1016/j.jfoodeng.2017.04.017.

[47] Gao T, Gillispie GJ, Copus JS, Kumar APR, Seol YJ, Atala A, Yoo JJ, Lee SJ. Optimization of gelatin-alginate composite bioink printability using rheological parameters: A systematic approach. Biofabrication 2018;10:34106-34118. https://doi.org/10.1088/1758-5090/aacdc7.

[48] Liu Y, Yu Y, Liu C, Regenstein JM, Liu X, Zhou P. Rheological and mechanical behavior of milk protein composite gel for extrusion-based 3D food printing. Lwt-Food Sci Technol 2019;102:338–346. https://doi.org/10.1016/j.lwt.2018.12.053.

[49] Abouzeid RE, Khiari R, Beneventi D, Dufresne A. Biomimetic mineralization of three-dimensional printed alginate/TEMPO-oxidized cellulose nanofibril scaffolds for bone tissue engineering. Biomacromolecules 2018;19:4442–4452. https://doi.org/10.1021/acs.biomac.8b01325.

[50] He Y, Yang F, Zhao H, Gao Q, Xia B, Fu J. Research on the printability of hydrogels in 3D bioprinting. Sci Rep 2016;6:1–13. https://doi.org/10.1038/srep29977.

[51] Schramm G. A practical approach to rheology and rheometry 2nd edition. Karlsruhe: Haake 1994. Germany

[52] Blaeser A, Duarte Campos DF, Puster U, Richtering W, Stevens MM, Fischer H. Controlling shear stress in 3D bioprinting is a key factor to balance printing resolution and stem cell integrity. Adv Healthc Mater 2016;5:326–333. https://doi.org/10.1002/adhm.201500677.

[53] Zhao Y, Li Y, Mao S, Sun W, Yao R. The influence of printing parameters on cell survival rate and printability in microextrusion-based 3D cell printing technology. Biofabrication 2015;7:045002-045015 https://doi.org/10.1088/1758-5090/7/4/045002.

[54] Chan RW, Titze IR. Viscosities of implantable biomaterials in vocal fold augmentation surgery. Laryngoscope 1998;108:725–731. https://doi.org/10.1097/00005537-199805000-00019.

[55] Hong S, Sanchez C, Du H, Kim N. Fabrication of 3D printed metal structures by use of high-viscosity Cu paste and a screw extruder. J Electron Mater 2015;44:836–841. https://doi.org/10.1007/s11664-014-3601-8.

[56] Krieger I, Elrod H. Direct determination of the flow curves of non-Newtonian fluids. II. Shearing rate in the concentric cylinder viscometer. J Appl Phyisics 1953;24:134–136. https://doi.org/https://doi.org/10.1063/1.1721226.

[57] Barman PC, Kairi RR, Das A, Islam MR. An overview of non-Newtonian fluid. Int J Appl Sci Eng 2016;4:97–101. https://doi.org/10.5958/2322-0465.2016.00011.3.

[58] Mahmood R, Bilal S, Majeed AH, Khan I, Nisar KS. Assessment of pseudo-plastic and dilatant materials flow in channel driven cavity: Application of metallurgical processes. J Mater Res Technol 2020;9:3829–3837. https://doi.org/10.1016/j.jmrt.2020.02.009.

[59] Highley CB, Rodell CB, Burdick JA. Direct 3D printing of shear-thinning hydrogels into self-healing hydrogels. Adv Mater 2015;27:5075–5079. https://doi.org/10.1002/adma.201501234.

[60] Barnes HA. Shear-thickening ("dilatancy") in suspensions of nonaggregating solid particles dispersed in newtonian liquids. J Rheol 1989;33:329–366. https://doi.org/10.1122/1.550017.

[61] Pipe CJ, Majmudar TS, McKinley GH. High shear rate viscometry. Rheol Acta 2008;47:621–642. https://doi.org/10.1007/s00397-008-0268-1.

[62] Roberts GP, Barnes HA, Carew P. Modelling the flow behaviour of very shear-thinning liquids. Chem Eng Sci 2001;56:5617–5623. https://doi.org/10.1016/S0009-2509(01)00291-3.

[63] Amanullah A, Hjorth SA, Nienow AW. A new mathematical model to predict cavern diameters in highly shear-thinning, power law liquids using axial flow impellers. Chem Eng Sci 1998;53:455–469. https://doi.org/10.1016/S0009-2509(97)00200-5.

[64] Hanks RW, Larsen KM. The flow of power-law non-Newtonian fluids in concentric annuli. Ind Eng Chem Fundam 1979;18:33–35. https://doi.org/10.1021/i160069a008.

[65] Esmaeilpour M, Korzani MG. Analyzing impacts of interfacial instabilities on the sweeping power of newtonian fluids to immiscibly displace power-law materials. Processes 2021;9:742-763. https://doi.org/10.3390/pr9050742.

[66] Hadigol M, Nosrati R, Nourbakhsh A, Raisee M. Numerical study of electroosmotic micromixing of non-Newtonian fluids. J Nonnewton Fluid Mech 2011;166:965–971. https://doi.org/10.1016/j.jnnfm.2011.05.001.

[67] Rahman J, Quodbach J. Versatility on demand – The case for semi-solid micro-extrusion in pharmaceutics. Adv Drug Deliv Rev 2021;172:104–126. https://doi.org/10.1016/j.addr.2021.02.013.

[68] Panda B, Ruan S, Unluer C, Tan MJ. Investigation of the properties of alkali-activated slag mixes involving the use of nanoclay and nucleation seeds for 3D printing. Compos Part B Eng 2020;186:107826-107842. https://doi.org/10.1016/j.compositesb.2020.107826.

[69] Amorim PA, D'Ávila MA, Anand R, Moldenaers P, Van Puyvelde P, Bloemen V.

Insights on shear rheology of inks for extrusion-based 3D bioprinting. Bioprinting 2021;22:129-145. https://doi.org/10.1016/j.bprint.2021.e00129.

[70] Vadillo J, Larraza I, Calvo-correas T, Gabilondo N, Derail C, Eceiza A. Design of a waterborne polyurethane–urea ink for direct ink writing 3d printing. Materials (Basel) 2021;14:1–13. https://doi.org/10.3390/ma14123287.

[71] Leppiniemi J, Lahtinen P, Paajanen A, Mahlberg R, Metsä-Kortelainen S, Pinomaa T, Pajari H, Vikholm-Lundin I, Pursula P, Hytonen VP. 3D-printable bioactivated nanocellulose-alginate hydrogels. ACS Appl Mater Interfaces 2017;9:21959–21970. https://doi.org/10.1021/acsami.7b02756.

[72] Li H, Liu S, Li L. Rheological study on 3D printability of alginate hydrogel and effect of graphene oxide. Int J Bioprinting 2016;2:54–66. https://doi.org/10.18063/IJB.2016.02.007.

[73] Ribeiro A, Blokzijl MM, Levato R, Visser CW, Castilho M, Hennink WE, Vermonden T, Malda J. Assessing bioink shape fidelity to aid material development in 3D bioprinting. Biofabrication 2018;10:014102-01411. https://doi.org/10.1088/1758-5090/aa90e2.

[74] Rehage H, Hoffmann H. Rheological properties of viscoelastic surfactant systems. J Phys Chem 1988;92:4712–4719. https://doi.org/10.1021/j100327a031.

[75] Klapper I, Rupp CJ, Cargo R, Purvedorj B, Stoodley P. Viscoelastic fluid description of bacterial biofilm material properties. Biotechnol Bioeng 2002;80:289–296. https://doi.org/10.1002/bit.10376.

[76] Han CD, Jhon MS. Correlations of the first normal stress difference with shear stress and of the storage modulus with loss modulus for homopolymers. J Appl Polym Sci 1986;32:3809–3840. https://doi.org/10.1002/app.1986.070320302.

[77] Fu K, Yao Y, Dai J, Hu L. Progress in 3D printing of carbon materials for energy-related applications. Adv Mater 2017;29:1603486-1603498. https://doi.org/10.1002/adma.201603486.

[78] Pérez B, Nykvist H, Brøgger AF, Larsen MB, Falkeborg MF. Impact of macronutrients printability and 3D-printer parameters on 3D-food printing: A review. Food Chem 2019;287:249–257. https://doi.org/10.1016/j.foodchem.2019.02.090.

[79] Lee SC, Gillispie G, Prim P, Lee SJ. Physical and chemical factors influencing the printability of hydrogel-based extrusion bioinks. Chem Rev 2020;120:10834–10886. https://doi.org/10.1021/acs.chemrev.0c00015.

[80] Sun A, Gunasekaran S. Yield stress in foods: Measurements and applications. Int J of Food Prop 2009;12:70-101. https://doi.org/10.1080/10942910802308502.

[81] Chen H, Xie F, Chen L, Zheng B. Effect of rheological properties of potato, rice and corn starches on their hot-extrusion 3D printing behaviors. J Food Eng 2019;244:150–158. https://doi.org/10.1016/j.jfoodeng.2018.09.011.

[82] Liu Z, Zhang M, Bhandari B. Effect of gums on the rheological, microstructural and extrusion printing characteristics of mashed potatoes. Int J Biol Macromol

2018;117:1179–1187. https://doi.org/10.1016/j.ijbiomac.2018.06.048.

[83] Sultan S, Mathew AP. 3D printed porous cellulose nanocomposite hydrogel scaffolds. J Vis Exp 2019;2019:3–8. https://doi.org/10.3791/59401.

[84] Jongprasitkul H, Turunen S, Parihar VS, Kellomäki M. Two-step crosslinking to enhance the printability of methacrylated gellan gum biomaterial ink for extrusion-based 3D bioprinting. Bioprinting 2022;25:185-198. https://doi.org/10.1016/j.bprint.2021.e00185.

[85] Ouyang L, Yao R, Zhao Y, Sun W. Effect of bioink properties on printability and cell viability for 3D bioplotting of embryonic stem cells. Biofabrication 2016;8:3–7. https://doi.org/10.1088/1758-5090/8/3/035020.

[86] Mouser VHM, Melchels FPW, Visser J, Dhert WJA, Gawlitta D, Malda J. Yield stress determines bioprintability of hydrogels based on gelatin-methacryloyl and gellan gum for cartilage bioprinting. Biofabrication 2016;8:035003-035013. https://doi.org/10.1088/1758-5090/8/3/035003.

[87] Tidball JG. Energy stored and dissipated in skeletal muscle basement membranes during sinusoidal oscillations. Biophys J 1986;50:1127–1138. https://doi.org/10.1016/S0006-3495(86)83557-3.

[88] Mazzocchi A, Devarasetty M, Huntwork R, Soker S, Skardal A. Optimization of collagen type I-hyaluronan hybrid bioink for 3D bioprinted liver microenvironments. Biofabrication 2019;11:015003-015014. https://doi.org/10.1088/1758-5090/aae543.

[89] Hsieh FY, Lin HH, Hsu SH. 3D bioprinting of neural stem cell-laden thermoresponsive biodegradable polyurethane hydrogel and potential in central nervous system repair. Biomaterials 2015;71:48–57. https://doi.org/10.1016/j.biomaterials.2015.08.028.

[90] Markstedt K, Mantas A, Tournier I, Martínez Ávila H, Hägg D, Gatenholm P. 3D bioprinting human chondrocytes with nanocellulose-alginate bioink for cartilage tissue engineering applications. Biomacromolecules 2015;16:1489–1496. https://doi.org/10.1021/acs.biomac.5b00188.

[91] Vadillo J, Larraza I, Calvo-Correas T, Gabilondo N, Derail C, Eceiza A. Role of in situ added cellulose nanocrystals as rheological modulator of novel waterborne polyurethane urea for 3D-printing technology. Cellulose 2021;28:4729–4744. https://doi.org/10.1007/s10570-021-03826-6.

[92] Hölzl K, Lin S, Tytgat L, Van Vlierberghe S, Gu L, Ovsianikov A. Bioink properties before, during and after 3D bioprinting. Biofabrication 2016;8:032002-032015. https://doi.org/10.1088/1758-5090/8/3/032002.

[93] Moroni L, Boland T, Burdick JA, De Maria C, Derby B, Forgacs G, Groll J, Li Q Malda J, Mironov VA, Mota C, Nakamura M, Shu W, Takeuchi S, Woodfield T, Xu T, Yoo JJ, Vozzi, G. Biofabrication: A guide to technology and terminology. Trends Biotechnol 2018;36:384–402. https://doi.org/10.1016/j.tibtech.2017.10.015.

[94] Malda J, Visser J, Melchels FP, Jüngst T, Hennink WE, Dhert WJA, Groll J,

Hutmacher DW. 25th anniversary article: Engineering hydrogels for biofabrication. Adv Mater 2013;25:5011–5028. https://doi.org/10.1002/adma.201302042.

[95] Ahmed EM. Hydrogel: Preparation, characterization, and applications: A review. J Adv Res 2015;6:105–121. https://doi.org/10.1016/j.jare.2013.07.006.

[96] Ji S, Guvendiren M. Recent advances in bioink design for 3D bioprinting of tissues and organs. Front Bioeng Biotechnol 2017;5:1–8. https://doi.org/10.3389/fbioe.2017.00023.

[97] GhavamiNejad A, Ashammakhi N, Wu XY, Khademhosseini A. Crosslinking strategies for 3D bioprinting of polymeric hydrogels. Small 2020;16:1–30. https://doi.org/10.1002/smll.202002931.

[98] Lepowsky E, Muradoglu M, Tasoglu S. Towards preserving post-printing cell viability and improving the resolution: Past, present, and future of 3D bioprinting theory. Bioprinting 2018;11:1–17. https://doi.org/10.1016/j.bprint.2018.e00034.

[99] Karakurt I, Lin L. 3D printing technologies: Techniques, materials, and post-processing. Curr Opin Chem Eng 2020;28:134–143. https://doi.org/10.1016/j.coche.2020.04.001.

[100] Siow CRS, Wan Sia Heng P, Chan LW. Application of freeze-drying in the development of oral drug delivery systems. Expert Opin Drug Deliv 2016;13:1595–608. https://doi.org/10.1080/17425247.2016.1198767.

[101] Abdelwahed W, Degobert G, Stainmesse S, Fessi H. Freeze-drying of nanoparticles: Formulation, process and storage considerations. Adv Drug Deliv Rev 2006;58:1688–1713. https://doi.org/10.1016/j.addr.2006.09.017.

[102] Jia J, Richards DJ, Pollard S, Tan Y, Rodriguez J, Visconti RP, Trusk TC, Yost MJ, Yao H, Markwald RR, Mei Y. Engineering alginate as bioink for bioprinting. Acta Biomater 2014;10:4323–4331. https://doi.org/10.1016/j.actbio.2014.06.034.

[103] Irvine SA, Agrawal A, Lee BH, Chua HY, Low KY, Lau BC, Machluf M, Venkatraman S. Printing cell-laden gelatin constructs by free-form fabrication and enzymatic protein crosslinking. Biomed Microdevices 2015;17:1–8. https://doi.org/10.1007/s10544-014-9915-8.

[104] Bakarich SE, Panhuis M In Het, Beirne S, Wallace GG, Spinks GM. Extrusion printing of ionic-covalent entanglement hydrogels with high toughness. J Mater Chem B 2013;1:4939–4946. https://doi.org/10.1039/c3tb21159b.

[105] Pereira RF, Sousa A, Barrias CC, Bártolo PJ, Granja PL. A single-component hydrogel bioink for bioprinting of bioengineered 3D constructs for dermal tissue engineering. Mater Horizons 2018;5:1100–1111. https://doi.org/10.1039/c8mh00525g.

[106] Mawad D, Stewart E, Officer DL, Romeo T, Wagner P, Wagner K, Wallace GG. A single component conducting polymer hydrogel as a scaffold for tissue engineering. Adv Funct Mater 2012;22:2692–2699. https://doi.org/10.1002/adfm.201102373.

[107] Erkoc P, Uvak I, Nazeer MA, Batool SR, Odeh YN, Akdogan O, Kizilel S. 3D

printing of cytocompatible gelatin-cellulose-alginate blend hydrogels. Macromol Biosci 2020;20:1–15. https://doi.org/10.1002/mabi.202000106.

[108] Chung JHY, Naficy S, Yue Z, Kapsa R, Quigley A, Moulton SE, Wallace GG. Bio-ink properties and printability for extrusion printing living cells. Biomater Sci 2013;1:763–773. https://doi.org/10.1039/c3bm00012e.

[109] Axpe E, Oyen ML. Applications of alginate-based bioinks in 3D bioprinting. Int J Mol Sci 2016;17:1976-1987. https://doi.org/10.3390/ijms17121976.

[110] Mallakpour S, Azadi E, Hussain CM. State-of-the-art of 3D printing technology of alginate-based hydrogels—An emerging technique for industrial applications. Adv Colloid Interface Sci 2021;293:102436-102448. https://doi.org/10.1016/j.cis.2021.102436.

[111] Kuo CC, Qin H, Cheng Y, Jiang X, Shi X. An integrated manufacturing strategy to fabricate delivery system using gelatin/alginate hybrid hydrogels: 3D printing and freeze-drying. Food Hydrocoll 2021;111:106262-106276. https://doi.org/10.1016/j.foodhyd.2020.106262.

[112] Reig-Vano B, Tylkowski B, Montané X, Giamberini M. Alginate-based hydrogels for cancer therapy and research. Int J Biol Macromol 2021;170:424–436. https://doi.org/10.1016/j.ijbiomac.2020.12.161.

[113] Rastogi P, Kandasubramanian B. Review of alginate-based hydrogel bioprinting for application in tissue engineering. Biofabrication 2019;11: 042002-042014. https://doi.org/10.1088/1758-5090/ab331e.

[114] Gomez CG, Pérez Lambrecht M V., Lozano JE, Rinaudo M, Villar MA. Influence of the extraction-purification conditions on final properties of alginates obtained from brown algae (Macrocystis pyrifera). Int J Biol Macromol 2009;44:365–371. https://doi.org/10.1016/j.ijbiomac.2009.02.005.

[115] Maleki S, Mærk M, Hrudikova R, Valla S, Ertesvåg H. New insights into Pseudomonas fluorescens alginate biosynthesis relevant for the establishment of an efficient production process for microbial alginates. N Biotechnol 2017;37:2–8. https://doi.org/10.1016/j.nbt.2016.08.005.

[116] Gombotz WR, Wee SF. Protein release from alginate matrices. Adv Drug Deliv Rev 2012;64:194–205. https://doi.org/10.1016/j.addr.2012.09.007.

[117] Daemi H, Barikani M. Synthesis and characterization of calcium alginate nanoparticles, sodium homopolymannuronate salt and its calcium nanoparticles. Sci Iran 2012;19:2023–2028. https://doi.org/10.1016/j.scient.2012.10.005.

[118] Draget KI, Taylor C. Chemical, physical and biological properties of alginates and their biomedical implications. Food Hydrocoll 2011;25:251–256. https://doi.org/10.1016/j.foodhyd.2009.10.007.

[119] Bidarra SJ, Barrias CC, Granja PL. Injectable alginate hydrogels for cell delivery in tissue engineering. Acta Biomater 2014;10:1646–1662. https://doi.org/10.1016/j.actbio.2013.12.006.

[120] Hoffman AS. Hydrogels for biomedical applications. Adv Drug Deliv Rev

2012;64:18–23. https://doi.org/10.1016/j.addr.2012.09.010.

[121] Desai RM, Koshy ST, Hilderbrand SA, Mooney DJ, Joshi NS. Versatile click alginate hydrogels crosslinked via tetrazine-norbornene chemistry. Biomaterials 2015;50:30–7. https://doi.org/10.1016/j.biomaterials.2015.01.048.

[122] Yang JS, Xie YJ, He W. Research progress on chemical modification of alginate: A review. Carbohydr Polym 2011;84:33–39. https://doi.org/10.1016/j.carbpol.2010.11.048.

[123] Paques JP, Van Der Linden E, Van Rijn CJM, Sagis LMC. Preparation methods of alginate nanoparticles. Adv Colloid Interface Sci 2014;209:163–171. https://doi.org/10.1016/j.cis.2014.03.009.

[124] Heggset EB, Strand BL, Sundby KW, Simon S, Chinga-Carrasco G, Syverud K. Viscoelastic properties of nanocellulose based inks for 3D printing and mechanical properties of CNF/alginate biocomposite gels. Cellulose 2019;26:581–595. https://doi.org/10.1007/s10570-018-2142-3.

[125] Hung KC, Tseng CS, Dai LG, Hsu SH. Water-based polyurethane 3D printed scaffolds with controlled release function for customized cartilage tissue engineering. Biomaterials 2016;83:156–168. https://doi.org/10.1016/j.biomaterials.2016.01.019.

[126] Wen YT, Dai NT, Hsu SH. Biodegradable water-based polyurethane scaffolds with a sequential release function for cell-free cartilage tissue engineering. Acta Biomater 2019;88:301–313. https://doi.org/10.1016/j.actbio.2019.02.044.

[127] Davis FJ, Mitchell GR. Polyurethane based materials with applications in medical devices. Bio-Materials Prototyp. Appl. Med., 2008, p. 27–48. https://doi.org/10.1007/978-0-387-47683-4_3.

[128] Hung KC, Tseng CS, Hsu SH. Synthesis and 3D printing of biodegradable polyurethane elastomer by a water-based process for cartilage tissue engineering applications. Adv Healthc Mater 2014;3:1578–1587. https://doi.org/10.1002/adhm.201400018.

[129] Santamaria-Echart A, Arbelaiz A, Saralegi A, Fernández-d'Arlas B, Eceiza A, Corcuera MA. Relationship between reagents molar ratio and dispersion stability and film properties of waterborne polyurethanes. Colloids Surfaces A Physicochem Eng Asp 2015;482:554–561. https://doi.org/10.1016/j.colsurfa.2015.07.012.

[130] Honarkar H. Waterborne polyurethanes: A review. J Dispers Sci Technol 2018;39:507–516. https://doi.org/10.1080/01932691.2017.1327818.

[131] Hormaiztegui ME V., Daga B, Aranguren MI, Mucci V. Bio-based waterborne polyurethanes reinforced with cellulose nanocrystals as coating films. Prog Org Coatings 2020;144:105649-105661. https://doi.org/10.1016/j.porgcoat.2020.105649.

[132] Kang SY, Ji Z, Tseng LF, Turner SA, Villanueva DA, Johnson R, Albano A, Langer R. Design and synthesis of waterborne polyurethanes. Adv Mater 2018;30:1–7.

https://doi.org/10.1002/adma.201706237.

[133] Bao LH, Lan YJ, Zhang SF. Synthesis and properties of waterborne polyurethane dispersions with ions in the soft segments. J Polym Res 2006;13:507–514. https://doi.org/10.1007/s10965-006-9073-7.

[134] Hsieh CT, Hsu SH. Double-network polyurethane-gelatin hydrogel with tunable modulus for high-resolution 3D bioprinting. ACS Appl Mater Interfaces 2019;11:32746–32757. https://doi.org/10.1021/acsami.9b10784.

[135] Griffin M, Castro N, Bas O, Saifzadeh S, Butler P, Hutmacher DW. The current versatility of polyurethane three-dimensional printing for biomedical applications. Tissue Eng - Part B Rev 2020;26:272–283. https://doi.org/10.1089/ten.teb.2019.0224.

[136] Siró I, Plackett D. Microfibrillated cellulose and new nanocomposite materials: A review. Cellulose 2010;17:459–494. https://doi.org/10.1007/s10570-010-9405-y.

[137] Seddiqi H, Oliaei E, Honarkar H, Jin J, Geonzon LC, Bacabac RG, Klein-Nulend J. Cellulose and its derivatives: Towards biomedical applications. Cellulose 2021;28:1893–1931. https://doi.org/10.1007/s10570-020-03674-w.

[138] de Amorim JDP, de Souza KC, Duarte CR, da Silva Duarte I, de Assis Sales Ribeiro F, Silva GS, Albuquerque PM, Stingl A, Santana AF, Vinhas GM, Sarubbo LA. Plant and bacterial nanocellulose: production, properties and applications in medicine, food, cosmetics, electronics and engineering. A review. Environ Chem Lett 2020;18:851–869. https://doi.org/10.1007/s10311-020-00989-9.

[139] Poletto M, Ornaghi Júnior HL, Zattera AJ. Native cellulose: Structure, characterization and thermal properties. Materials 2014;7:6105–6119. https://doi.org/10.3390/ma7096105.

[140] Gomes TCF, Skaf MS. Cellulose-builder: A toolkit for building crystalline structures of cellulose. J Comput Chem 2012;33:1338–1346. https://doi.org/10.1002/jcc.22959.

[141] Ng HM, Sin LT, Tee TT, Bee ST, Hui D, Low CY, Rahmat. Extraction of cellulose nanocrystals from plant sources for application as reinforcing agent in polymers. Compos Part B Eng 2015;75:176–200. https://doi.org/10.1016/j.compositesb.2015.01.008.

[142] Mokhena TC, Sadiku ER, Mochane MJ, Ray SS, John MJ, Mtibe A. Mechanical properties of cellulose nanofibril papers and their bionanocomposites: A review. Carbohydr Polym 2021;273:118507-118521. https://doi.org/10.1016/j.carbpol.2021.118507.

[143] Moon RJ, Martini A, Nairn J, Simonsen J, Youngblood J. Cellulose nanomaterials review: Structure, properties and nanocomposites. Chem Soc Rev 2011;40:3941–3994. https://doi.org/10.1039/c0cs00108b.

[144] Reid MS, Villalobos M, Cranston ED. Benchmarking Cellulose Nanocrystals: From the Laboratory to Industrial Production. Langmuir 2017;33:1583–1598. https://doi.org/10.1021/acs.langmuir.6b03765.

[145] Wang R, Chen L, Zhu JY, Yang R. Tailored and integrated production of carboxylated cellulose nanocrystals (CNC) with nanofibrils (CNF) through maleic acid hydrolysis. ChemNanoMat 2017;3:328–335. https://doi.org/10.1002/cnma.201700015.

[146] Tang Y, Shen X, Zhang J, Guo D, Kong F, Zhang N. Extraction of cellulose nano-crystals from old corrugated container fiber using phosphoric acid and enzymatic hydrolysis followed by sonication. Carbohydr Polym 2015;125:360–366. https://doi.org/10.1016/j.carbpol.2015.02.063.

[147] Soeiro VS, Tundisi LL, Novaes LCL, Mazzola PG, Aranha N, Grotto D, Junior JMO, Komatsu D, Gama FMP, Chaud MV, Jozala AF. Production of bacterial cellulose nanocrystals via enzymatic hydrolysis and evaluation of their coating on alginate particles formed by ionotropic gelation. Carbohydr Polym Technol Appl 2021;2:100155-100168. https://doi.org/10.1016/j.carpta.2021.100155.

[148] Alonso-Lerma B, Barandiaran L, Ugarte L, Larraza I, Reifs A, Olmos-Juste R, Barruetabeña N, Amenabar I, Hillenbrand R, Eceiza A, Perez-Jimenez R. High performance crystalline nanocellulose using an ancestral endoglucanase. Commun Mater 2020;1:1-10. https://doi.org/10.1038/s43246-020-00055-5.

[149] de Campos A, Correa AC, Cannella D, de M Teixeira E, Marconcini JM, Dufresne A, Mattoso LHC, Cassland P, Sanadi AR. Obtaining nanofibers from curauá and sugarcane bagasse fibers using enzymatic hydrolysis followed by sonication. Cellulose 2013;20:1491–1500. https://doi.org/10.1007/s10570-013-9909-3.

[150] Siqueira G, Kokkinis D, Libanori R, Hausmann MK, Gladman AS, Neels A, Tingaut P, Zimmermann T, Lewis JA, Studart AR. Cellulose nanocrystal inks for 3D printing of textured cellular architectures. Adv Funct Mater 2017;27:1604619-1604629. https://doi.org/10.1002/adfm.201604619.

[151] Piras CC, Fernández-Prieto S, De Borggraeve WM. Nanocellulosic materials as bioinks for 3D bioprinting. Biomater Sci 2017;5:1988–1992. https://doi.org/10.1039/c7bm00510e.

[152] Alonso-Lerma B, Larraza I, Barandiaran L, Ugarte L, Saralegi A, Corcuera MA, Perez-Jimenez R, Eceiza A. Enzymatically produced cellulose nanocrystals as reinforcement for waterborne polyurethane and its applications. Carbohydr Polym 2021;254:117478-117489. https://doi.org/10.1016/j.carbpol.2020.117478.

[153] Zema L, Melocchi A, Maroni A, Gazzaniga A. Three-Dimensional Printing of Medicinal Products and the Challenge of Personalized Therapy. J Pharm Sci 2017;106:1697–1705. https://doi.org/10.1016/j.xphs.2017.03.021.

[154] Vaz VM, Kumar L. 3D Printing as a promising tool in personalized medicine. AAPS PharmSciTech 2021;22:49-69. https://doi.org/10.1208/s12249-020-01905-8.

[155] Lee Ventola C. Medical applications for 3D printing: Current and projected uses. Pharm Ther 2014;39:704–711.

[156] Jamróz W, Szafraniec J, Kurek M, Jachowicz R. 3D printing in pharmaceutical and medical applications. Recent achievements and changes. Pharm Res 2018;35:176-196. https://doi.org/10.1007/s11095-018-2454-x

[157] Memon AR, Wang E, Hu J, Egger J, Chen X. A review on computer-aided design and manufacturing of patient-specific maxillofacial implants. Expert Rev Med Devices 2020;17:345–356. https://doi.org/10.1080/17434440.2020.1736040.

[158] Haleem A, Javaid M. 3D scanning applications in medical field: A literature-based review. Clin Epidemiol Glob Heal 2019;7:199–210. https://doi.org/10.1016/j.cegh.2018.05.006.

[159] Wong KC. 3D-printed patient-specific applications in orthopedics. Orthop Res Rev 2016;Volume 8:57–66. https://doi.org/10.2147/ORR.S99614.

[160] Domínguez-Robles J, Mancinelli C, Mancuso E, García-Romero I, Gilmore BF, Casettari L, Larrañeta E, Lamprou DA. 3D printing of drug-loaded thermoplastic polyurethane meshes: A potential material for soft tissue reinforcement in vaginal surgery. Pharmaceutics 2020;12:63-79. https://doi.org/10.3390/pharmaceutics12010063.

[161] Kneebone R. Simulation in surgical training: Educational issues and practical implications. Med Educ 2003;37:267–277. https://doi.org/10.1046/j.1365-2923.2003.01440.x.

[162] Smith ML, Jones JFX. Dual-extrusion 3D printing of anatomical models for education. Anat Sci Educ 2018;11:65–72. https://doi.org/10.1002/ase.1730.

[163] Manmadhachary A, Aditya Mohan A, Haranadha Reddy M. Manufacturing of customized implants for orbital fractures using 3D printing. Bioprinting 2021;21:118-129. https://doi.org/10.1016/j.bprint.2020.e00118.

[164] Johannesson J, Khan J, Hubert M, Teleki A, Bergström CAS. 3D-printing of solid lipid tablets from emulsion gels. Int J Pharm 2021;597:120304-120315. https://doi.org/10.1016/j.ijpharm.2021.120304.

[165] Chen G, Xu Y, Kwok PCL, Kang L. Pharmaceutical applications of 3D printing. Addit Manuf 2020;34:101209-101222. https://doi.org/10.1016/j.addma.2020.101209.

[166] Dodziuk H. Applications of 3D printing in healthcare. Kardiochirurgia i Torakochirurgia Pol 2016;13:283–293. https://doi.org/10.5114/kitp.2016.62625.

[167] Khaled SA, Burley JC, Alexander MR, Roberts CJ. Desktop 3D printing of controlled release pharmaceutical bilayer tablets. Int J Pharm 2014;461:105–111. https://doi.org/10.1016/j.ijpharm.2013.11.021.

[168] Yi HG, Choi YJ, Kang KS, Hong JM, Pati RG, Park MN, Shim IK, Lee CM, Kim SC, Cho DW. A 3D-printed local drug delivery patch for pancreatic cancer growth suppression. J Control Release 2016;238:231–241. https://doi.org/10.1016/j.jconrel.2016.06.015.

[169] Holländer J, Genina N, Jukarainen H, Khajeheian M, Rosling A, Mäkilä E, Sandler N. Three-dimensional printed PCL-based implantable prototypes of medical devices for controlled drug delivery. J Pharm Sci 2016;105:2665–2676. https://doi.org/10.1016/j.xphs.2015.12.012.

[170] Vithani K, Goyanes A, Jannin V, Basit AW, Gaisford S, Boyd BJ. A proof of

concept for 3D printing of solid lipid-based formulations of poorly water-soluble drugs to control formulation dispersion kinetics. Pharm Res 2019;36:102-122. https://doi.org/10.1007/s11095-019-2639-y.

[171] Altunbas A, Lee SJ, Rajasekaran SA, Schneider JP, Pochan DJ. Encapsulation of curcumin in self-assembling peptide hydrogels as injectable drug delivery vehicles. Biomaterials 2011;32:5906–5914. https://doi.org/10.1016/j.biomaterials.2011.04.069.

[172] Bhutani U, Laha A, Mitra K, Majumdar S. Sodium alginate and gelatin hydrogels: Viscosity effect on hydrophobic drug release. Mater Lett 2016;164:76–79. https://doi.org/10.1016/j.matlet.2015.10.114.

[173] Vijayavenkataraman S, Yan WC, Lu WF, Wang CH, Fuh JYH. 3D bioprinting of tissues and organs for regenerative medicine. Adv Drug Deliv Rev 2018;132:296–332. https://doi.org/10.1016/j.addr.2018.07.004.

[174] Faramarzi N, Yazdi IK, Nabavinia M, Gemma A, Fanelli A, Caizzone A, Ptaszek LM, Sinha I, Khademhosseini A, Ruskin JN, Tamayol A. Patient-specific bioinks for 3D bioprinting of tissue engineering scaffolds. Adv Healthc Mater 2018;7:1–9. https://doi.org/10.1002/adhm.201701347.

[175] Chan BP, Leong KW. Scaffolding in tissue engineering: General approaches and tissue-specific considerations. Eur Spine J 2008;17:1-12. https://doi.org/10.1007/s00586-008-0745-3.

[176] Moreno Madrid AP, Vrech SM, Sanchez MA, Rodriguez AP. Advances in additive manufacturing for bone tissue engineering scaffolds. Mater Sci Eng C 2019;100:631–644. https://doi.org/10.1016/j.msec.2019.03.037.

[177] Nguyen D, Hgg DA, Forsman A, Ekholm J, Nimkingratana P, Brantsing C, Enejder A, Simonsson S. Cartilage tissue engineering by the 3D bioprinting of iPS cells in a nanocellulose/alginate bioink. Sci Rep 2017;7:1–10. https://doi.org/10.1038/s41598-017-00690-y.

[178] Bittner SM, Guo JL, Melchiorri A, Mikos AG. Three-dimensional printing of multilayered tissue engineering scaffolds. Mater Today 2018;21:861–874. https://doi.org/10.1016/j.mattod.2018.02.006.

[179] Gleadall A, Visscher D, Yang J, Thomas D, Segal J. Review of additive manufactured tissue engineering scaffolds: relationship between geometry and performance. Burn Trauma 2018;6:1–16. https://doi.org/10.1186/s41038-018-0121-4.

[180] Iturriaga L, Van Gordon KD, Larrañaga-Jaurrieta G, Camarero-Espinosa S. Strategies to introduce topographical and structural cues in 3D-printed scaffolds and implications in tissue regeneration. Adv NanoBiomed Res 2021;1:2100068-2100081. https://doi.org/10.1002/anbr.202100068.

[181] Sun W, Lee J, Zhang S, Benyshek C, Dokmeci MR, Khademhosseini A. Engineering precision medicine. Adv Sci 2019;6:1801039-1801049. https://doi.org/10.1002/advs.201801039.

Chapter 2

Materials and methods

CHAPTER 2 - Materials and methods

2. Materials and methods

2.1. Aim of the chapter

In this chapter, the materials employed for the development of the bioinks and biomaterial inks as well as the material needed for the isolation of enzymatic cellulose nanocrystals (EnCNC) are described. All methodology and equipment used for the characterization of the materials, 3D printing process and the characterization of the printed scaffolds, as well as the techniques employed to test the applications of these samples are well explained.

2.2. Materials

Medium viscosity alginate from brown algae (A2033) was purchased from Sigma-Aldrich. Commercial anionic aliphatic polyester-polyurethane waterborne dispersion (WBPU, Impraperm® DL 3746 XP) with a solid content of 40 % was kindly provided from Covestro. Cellulose nanofibers (CNF, Lot. 9004-34-6) were bought from Maine University (USA). Di-hydrated calcium chloride ($CaCl_2 \cdot 2H_2O$, >99%) was purchased from Sigma-Aldrich. Commercial PBS tablets (Phosphate Buffer Saline) at pH = 7.4, were purchased from PanReac. For EnCNC isolation, Whatman® filter paper was employed as a substrate. For drug delivery applications, curcumin from *Curcuma longa* (Turmeric, purity >65%) was acquired from Sigma-Aldrich. Chloramphenicol powder ($C_{11}H_{12}Cl_2N_2O_5$ purity ≥ 98%) was purchased from Sigma Aldrich. A commercial polypropylene hernia mesh was kindly donated for research.

The described materials were blended or processed alone to be employed as biomaterial inks or bioinks. All developed formulations are described and summarized in **Table 2.1**.

Table 2.1. *Summary of the principal components of the developed bioinks/biomaterial inks.*

Bioink/Biomaterial ink formulation	**Components**
A-Ca	Alginate, calcium chloride
EnCNC	Enzymatic cellulose nanocrystals
A-CNF	Alginate, cellulose nanofibers
A-CNF-cur	Alginate, cellulose nanofibers, curcumin
A-CNF-clph	Alginate, cellulose nanofibers, chloramphenicol
A-CNF-cur-clph	Alginate, cellulose nanofibers, curcumin, chloramphenicol
A-WBPU	Alginate, waterborne polyurethane
A-WBPU+Ca	Alginate, waterborne polyurethane, calcium chloride coating

2.3. Methods

2.3.1. Materials characterization

2.3.1.1. Dispersion characterization

- *Solid content*

Solid content of WBPU dispersion and EnCNC obtained slurry was determined by a general gravimetric method according to UNE-EN ISO 638 normative. In brief, 2mL of material dispersion were added in a glass recipient previously weighted. Then, the material + recipient were weighted and introduced in an oven at 100 ºC overnight in order to guarantee all water elimination from the samples. After the drying process and subsequent room temperature equilibration, the glass recipients with the dried samples were weighted again and the solid content was calculated subtracting the recipient weight. These measurements were carried out at least in triplicate.

- *Particle size*

Particle size from WBPU dispersion and polydispersity were measured by dynamic light scattering (DLS), using a BI-200SM goniometer from Brookhaven. The intensity of dispersed light was measured with the aid of a luminous source of He-Ne laser (Mini L-30, wavelength 637 nm, 400 mW) and the detector (BI–APD) located on a rotary arm that allows the measurement of the light intensity at 90º. Samples were prepared by diluting a drop of WBPU dispersion into distilled water. All measurements were performed at room temperature in triplicate.

- *Dispersion stability*

The stability of the WBPU dispersion was evaluated by zeta potential measurements. The Zetasizer Ultra equipment (Malvern Panalytical) was employed for this measurement. The zeta potential of the dispersion was measured by applying an electric field across the sample. Particles with zeta potential will be displaced toward the electrode of the opposite charge with a proportional speed of the zeta potential magnitude and thus, determining the stability of the dispersion.

- *pH*

The pH of the WBPU dispersion was measured in triplicate with a pH meter COND50 VIOLAB, calibrated with pH 4.00 and 7.00 buffer solution standards.

2.3.1.2. Morphological characterization

- *Atomic force microscopy (AFM)*

AFM in tapping mode was used to characterize the morphology of the CNF and EnCNC, using a Nanoscope III scanning probe microscope (Multimode TM Digital instruments) with an integrated force generated by cantilever/silicon probes, applying a resonance frequency of about 180 kHz. The cantilever had a tip radius of 5–10 nm and was 125 nm long. Samples were prepared by spin-coating technique using P6700 Spin-coater at 2000 rpm for 120 s. A droplet from a CNF and EnCNC suspension of 0.01 wt. % was deposited on mica substrates.

2.3.1.3. Physicochemical characterization

- *Molecular weight*

The molecular weight of alginate was obtained from intrinsic viscosity measurements. Different alginate concentrations (from $5 \cdot 10^{-3}$ g·mL^{-1} to $6.25 \cdot 10^{-4}$ g·mL^{-1}) in NaCl 0.1 M were prepared in order to calculate relative viscosity of alginate at 25 ºC, using a capillary viscometer in a water bath. The relative and the reduced viscosity values were obtained and from them intrinsic viscosity was calculated [1]. Then, the molecular weight of the alginate was calculated using viscometric equation described as follows [2,3]:

$$[\eta] = Kv \cdot M^{Av} \quad \text{(Eq. 1)}$$

Where [η] is the intrinsic viscosity and M is the molecular weight of the biopolymer. For alginate derived from brown algae dissolved in NaCl 0.1 M viscosimetric constants of Kv and Av of $7.3 \cdot 10^{-3}$ cm^3/g and 0.92, respectively, were used [3].

- *Fourier transform infrared spectroscopy (FTIR)*

The characteristic functional groups of alginate, WBPU, CNF, and EnCNC were analyzed by FTIR using a Nicolet Nexus spectrophotometer in attenuated total reflection (ATR) mode with a Specac MKII Golden Gate accessory with a diamond crystal at a nominal incidence angle of 45º and ZnSe lens. Spectra were recorded between 4000 and 500 cm^{-1} and 32 scans, with a resolution of 4 cm^{-1}.

- *Carbon nuclear magnetic resonance (^{13}C NMR)*

^{13}C NMR spectrum of CNF was recorded with an Advance Bruker equipped with BBO z-gradient probe. Experimental conditions were 125.5 MHz, number of scans 14000,

spectral window 25000 Hz with a recovery delay of 2 sec. The solvent employed for all experiments was deuterated H_2O.

- *X-Ray diffraction (XRD)*

Crystallinity of CNF was determined by XRD using a Philips X'pert PRO automatic diffractometer performing at 40 kV and 40 mA, in theta-theta configuration, a secondary monochromator with Cu-Kα radiation (λ = 1.5418 Å) and a PIXcel solid state detector (active length in 2θ 3.347º). Data were obtained from 2θ = 5 to 75º (step size 0.026 and time per step 80 s) at room temperature. A fixed divergence and antiscattering slit were used to provide a constant volume of sample illumination. In order to calculate crystallinity index, Segal equation [4] was used:

$$\text{Crystallinity index (\%)} = \frac{(I_{200} - I_{am})}{I_{200}} \cdot 100 \qquad \text{(Eq. 2)}$$

where I_{200} corresponds to the intensity of crystalline peak and I_{am} is referred to the intensity of the amorphous peak.

2.3.1.4. Thermal characterization

- *Thermogravimetric analysis (TGA)*

Thermal stability of alginate, WBPU, CNF and EnCNC was performed by TGA using a Mettler Toledo TGA/DSC 3+ instrument. Samples of 2-3 mg were heated from 25 to 800 °C at a heating rate of 10 °C·min^{-1} in nitrogen atmosphere to prevent thermoxidative degradation. The initial degradation temperature (T_0) was calculated as temperature at which the weight loss was 5 %. The maximum degradation temperature (Td) was calculated as the minimum of the degradation peak in the derivative curve.

- *Differential scanning calorimetry (DSC)*

Thermal properties of WBPU, curcumin, chloramphenicol, A-CNF matrix and A-Ca based inks were studied by DSC, using a Mettler Toledo DSC 3+ equipment, provided with a robotic arm and an electric intracooler. Aluminum pan containing sample with a weight of 5–10 mg was heated from -75 to 250 °C for WBPU at a scanning rate of 10 °C·min^{-1} in nitrogen atmosphere. The glass transition temperature was determined as the inflection point of the heat capacity change, whereas the short range order-disorder transition and enthalpy were established as the temperature of the maximum and the

area of the endothermic peak. Curcumin, chloramphenicol and A-CNF loaded and unloaded samples were heated from 0 to 200 ºC at 10 ºC·min^{-1}, whereas A-Ca based inks were heated from 25 to 300 ºC at 10 ºC·min^{-1}.

2.3.1.5. Mechanical characterization

Tensile tests of alginate and WBPU films was performed using an INSTRON 5967 testing machine provided with a 500 N load cell and pneumatic clamps to grip the samples. Young's Modulus, stress at yield, stress at break and strain at break were calculated from stress-strain curves. Five tests were carried out for each material and average values were calculated and collected. All samples were cut with a pneumatic die in 2.75 mm in width, 0.5 mm in thickness and 10 mm in length and then were tested at a speed of 20 mm·min^{-1} at room temperature.

2.3.1.6. Rheological characterization

Rheological measurements of employed materials and bioinks/biomaterial inks were performed using a Haake Viscotester iQ Rheometer (Thermo Scientific) at 25 ºC in a 35 mm parallel plate-plate geometry with a gap of 1 mm using 1 mL of sample for viscosity under steady shear rate in rotary mode, viscosity recovery and oscillatory stress sweep assays. Coaxial cylinders geometry with a piston radius of 12.54 mm and a ring gap of 1 mm at 25 ºC was used for WBPU viscosity measurements, while oscillatory stress assays for this material were carried out using a 60 mm cone-plate geometry of 2º with a gap of 0.1 mm at 25 ºC. Ares G2 Rheometer (TA Instruments) was employed for oscillatory strain sweep and frequency sweep tests, using 25 mm parallel plate-plate geometry with a gap of 1.5 mm among them and 0.5 mL of sample. All measurements were performed in triplicate.

All viscosity flow analyses were previously equilibrated during 40 seconds at a constant shear rate of 0.2 s^{-1}, and then viscosity data from 0.2 s^{-1} to 100 s^{-1} were collected. Experimental results of viscosity test were compared to power-law model described as follows:

$$\eta = K \cdot (\dot{\gamma})^{n-1} \qquad \text{(Eq. 3)}$$

where η is the viscosity of the ink (Pa·s), K is the consistency coefficient (Pa·s^n), $\dot{\gamma}$ is the shear rate (s^{-1}) and n is the power-law index (dimensionless).

Viscosity recovery measurements of the A-CNF based inks, drug-loaded A-CNF based inks and A-WBPU based inks, samples were carried out by submitting the sample to different consecutive shear rates. The first at 0.2 s^{-1} during 100 seconds, then a shear rate ranging from 10 to 100 s^{-1} (agreeing with printing conditions in each case) for 100 seconds, and finally, a step of 0.2 s^{-1} for the last 100 seconds and the recovery percentages at the end of the experiment were calculated using the software RheoWin Data Manager. In the case of A-Ca based inks, EnCNC inks and A-WBPU bioinks, samples were subjected to a shear rate sequence of 0.2 s^{-1} during 40 seconds, then a shear rate ranging from 10 to 50 s^{-1} (agreeing with printing conditions in each study) for 20 seconds, and a final step at 0.2 s^{-1} for the last 60 seconds. Recovery percentages after 20 seconds and 60 seconds were calculated using RheoWin Data Manager.

Oscillatory stress sweep tests from all the developed inks were performed during an increase of shear stress from 10 to 2000 Pa at a constant frequency of 1 Hz. Storage modulus (G') and loss modulus (G'') variations were measured.

Linear Viscoelastic Range (LVR) was determined from strain sweep tests working at 1 Hz between 0.01 and 100 % of strain for each ink. Oscillatory frequency sweep measurements were performed in the LVR, at 1 % of strain from 0.1 to 100 Hz for A-CNF based inks and drug-loaded A-CNF based inks, and at 1% of strain from 0.1 to 10 Hz for A-Ca based inks and EnCNC inks.

2.3.2. Extrusion 3D printing and bioprinting

Samples of A-CNF based inks, drug-loaded A-CNF inks and A-WBPU inks with different shapes and sizes were printed with a Voladora 3D printer (Tumaker, S.L. Spain) which has been modified for layer-by-layer syringe extrusion printing. The modification of the printer consists in the replacement of the FDM head for a mechanical piston able to move the embolus of a syringe, allowing the extrusion of the material through a needle in X and Y directions. All inks were 3D printed at room temperature, with a speed of 4 mm s^{-1} through a 5 mL plastic syringe of 12.4 mm in diameter with a needle of 0.8 mm in diameter at a constant pressure controlled by the printer software.

A-CNF samples were printed in a dog bone shape of 45 mm in length and 3 mm in height and in cylinders of 15 mm in diameter and 10 or 5 mm in height. A-CNF-cur samples were printed in a prism shape of 25x25x4 mm^3, whereas A-CNF-clph samples were printed in cylinders of 20 mm in diameter and 8 mm in height. Cylinders of 12 mm in diameter and 8 mm in height and prism shape of 15x15x4 mm^3 were chosen for A-CNF-

cur-clph ink formulation. CAD mesh model of 50x58x0.65 mm with holds in hexagonal shape of 2.8 mm in diameter was chosen for A-WBPU inks.

Samples of A-Ca based inks, EnCNC inks and A-WBPU bioinks were 3D printed using a REGEMAT 3D printer, with a constant pressure controlled by the software according to printing speed. A-Ca and EnCNC inks were 3D printed using the same printing conditions than for previous samples while A-WBPU bioinks were 3D printed at room temperature at a velocity of 2 $mm \cdot s^{-1}$ through a 5 mL plastic syringe of 12.4 mm in diameter with a nozzle of 0.4 mm.

A-Ca inks were 3D printed in cylinder shape of 10 mm in diameter and 5 mm in height, while EnCNC were 3D printed in dog bone shape of 45 mm in length and 3 mm in height and cylinders of 10 mm in diameter and 5 mm in height. A-WBPU bioinks were 3D printed in mesh-cylinder shape of 10 mm in diameter and 1.5 mm in height with a square hole shape of 1.5x1.5 mm.

2.3.2.1. Printability test

Printability (Pr) assays were performed to evaluate gelation conditions of A-Ca based inks and proper solid content of EnCNC formulations. A square shape mesh of 20x20x0.65 mm with square holes of 3x3 mm was 3D printed at a speed of 3 $mm \cdot s^{-1}$. ImageJ software was used in order to measure the perimeter and area of each square hole, and Pr was calculated using the following equation [5]:

$$Pr = \frac{L^2}{16 \cdot A} \qquad \text{(Eq. 4)}$$

where L is the perimeter of the square shape holes while A represents the area of the holes. Pr values lower than 1 means under-gelation and poor accuracy on shape reproduction, Pr= 1 means proper-gelation and suitable accuracy and finally Pr values higher than 1 means over-gelation and unsuitable accuracy due to poor interconnection between layers.

2.3.2.2. Post-printing processes

- *Freeze-drying*

The freeze-drying process of scaffolds after 3D printing was carried out using a Telstar LyoQuest equipment. The samples were previously frozen at -20 ºC for at least 2 hours and then were placed into the lyophilizer cabinet with conditions of 0.1 mbar of vacuum pressure and -80 ºC during 24-48 h to achieve an optimal freeze-drying process.

- *Ca^{2+} crosslinking*

Ca^{2+} crosslinking process from 3D printed samples was carried out immersing the scaffolds in a $CaCl_2$ solution. Drug loaded A-CNF scaffolds were soaked into a 0.5 M solution of $CaCl_2$ during 4 h and then dried at room temperature for one week. A-WBPU meshes were coated with a Ca^{2+} ion crosslinking layer by soaking the air-dried A-WBPU meshes into a $CaCl_2$ 0.2 M solution during 24 hours. Then, the meshes were oven-dried (80 ºC) during 2 hours to ensure the complete water elimination. A-WBPU cell-laden scaffolds were immersed in 0.1 M $CaCl_2$ sterile solution during 5 min immediately after 3D printing to preserve the architecture of the samples during culture process.

2.3.3. Characterization of the scaffolds

2.3.3.1. Morphological characterization

- *Dimensions characterization of the samples*

Dimensions of the post-printed scaffolds and meshes were measured using a caliper and a micrometer. Thickness and pore size of the A-WBPU 3D printed air-dried meshes and commercial PP mesh were also measured, as well as the specific weight of the meshes that was calculated as the weight (g) divided by the area of the sample (m^2), neglecting the thickness [6,7].

- *Scanning electron microscopy (SEM)*

Morphology (surface and cross section) of the scaffolds was analyzed by SEM. Freeze-dried A-CNF scaffolds were analyzed using a FEI ESEM Quanta 200 microscope operating at 5-20 kV. Freeze-dried and Ca^{2+} crosslinked/air-dried A-CNF-cur-clph were analyzed using a Hitachi S-4800 microscope with a cold field emission electron source for high resolution, operating from 0.5 to 30 kV accelerating voltage with a resolution of 1 nm at 15 kV and 1.4 nm at 1 kV. A-WBPU chondrocyte-laden scaffolds were analyzed using a TM3030Plus (Hitachi High-Technologies) equipment, operating at 15 kV. These scaffolds were firstly processed for this technique through incubation with a solution of 4 % of paraformaldehyde in PBS during 20 min for cell fixation and then they were immersed in a sequentially ethanol solutions (from 50 to 100 %) during 15-20 min in each in order to dehydrate the cells. Finally, the samples were incubated for 15-20 min in hexametyldisilazane (HMDS) to dry completely the scaffolds. Dried samples were coated with gold using a SC7620 Mini Sputter Coater before morphological analysis.

- *Confocal microscopy*

Human embryonic kidney cell line (HEK239) cells from A-CNF, A-Ca and EnCNC scaffolds were observed using a Zeiss 710 confocal laser scanning microscope. The presence of cells were evaluated in fluorescence using 4′,6-diamidino-2-phenylindole (DAPI) staining for the viewing of cell nucleus at the range of blue and green light spectra (λ=400 - 550 nm) using an UV lamp, performing multilayer analysis from the base to the surface of the seeded scaffolds.

LIVE/DEAD experiments from A-WBPU+Ca meshes were evaluated using the confocal microscope Olympus LV500 and fluorescence images were taken at a magnitude of 10x. Living cells were identified in the green fluorescence spectrum (calcein: λ = 495-515 nm) and dead cells were observed in red fluorescence spectrum (propidium iodide: λ = 535-617 nm).

2.3.3.2. Mechanical characterization

- *Tensile tests*

Uniaxial tensile tests of the 3D printed A-WBPU meshes and the commercial PP meshes were carried out using an INSTRON 5967 with a load cell of 30 kN. Samples of air-dried meshes from all compositions, as well as the commercial PP meshes were cut in rectangular pieces of 30 mm in length and 10 mm in width. Samples were vertically clamped between the two grips with a distance of 10 mm and force-displacement assays were performed at a speed of 20 $mm \cdot min^{-1}$. Tensile stiffness was calculated from the linear part of elastic region in load-displacement curves [7,8]. Breaking force was determined as the maximum load (N) per width (cm) of tested sample [6,9]. Elastic limit was calculated from force-elongation curves using the 0.2 % offset method [10] and elastic elongation was measured from the force-elongation curves as the percentage change in length at the end of the elastic region (elastic limit) divided by its initial length [7].

- *Compression tests*

Mechanical properties of A-CNF based (n=5), A-Ca (n=3) based and EnCNC (n=3) freeze-dried cylindrical scaffolds were evaluated by compression tests using an INSTRON 5967 with a load cell of 30 kN at a speed of 5 $mm \cdot min^{-1}$. Tests of A-CNF based scaffolds were performed up to 80 % of strain while A-Ca based and EnCNC were performed up to 90 %. Compressive modulus, calculated from the slope of the stress-strain curve in the elastic region, compressive strength, calculated as the maximum

stress value at the maximum compressive strain, and densification strain, calculated as the strain value at the intersection point between the lines of stress plateau and densification were determined from stress-stain curves.

2.3.3.3. Water absorption and *in vitro* scaffolds disintegration

Water absorption, also called swelling degree, was studied by a general gravimetric method. The samples were introduced in PBS solution (pH 7.4) at 37 ºC and the swelling behavior was evaluated by weighting swollen samples at different time intervals of 30 min, 1, 2, 4, 6, and 24 hours. Three samples from each time point were tested to check the repeatability of the analysis. Swelling degree (SD) was calculated as follows:

$$SD\ (\%) = \left(\frac{Ws\text{-}Wi}{Wi}\right) \cdot 100 \qquad \text{(Eq. 5)}$$

where Ws represents the weight of swollen samples and Wi represents the weight of initial freeze-dried scaffold. Equilibrium was considered at 24 hours.

The swollen samples were then freeze-dried and weighted again in order to calculate the disintegration degree of the scaffolds along the experiment, following the next equation:

$$\text{Disintegration degree } (\%) = 100 - \left(\frac{Wd}{Wi} \cdot 100\right) \qquad \text{(Eq. 6)}$$

where Wd is the weight of the freeze-dried samples at different times and Wi is the initial weight.

To quantify the *in vitro* degradation of the A-WBPU meshes and $CaCl_2$ coated A-WBPU meshes over time, small pieces of the original meshes were weighted, and introduced into a PBS solution and stored at 37 ºC during 21 days. At predetermined times, the samples were collected, washed twice with distilled water to remove the impurities and then they were weighted again after an oven-drying process to ensure all water removal.

2.3.4. Biomedical applications

2.3.4.1. Drug delivery

- *Drug solubility determination*

Solubility determination assays of curcumin and chloramphenicol were performed in water, PBS (pH 7.4) and ethanol. Standard calibration curves were prepared from dissolutions with known concentrations of the drugs in different solvents using the UV-

VIS-NIR Shimadzu 3600 spectrophotometer. Absorbance of curcumin solutions from 0.025 to 2.5 $mg \cdot mL^{-1}$ were determined in water and in PBS with a maximum absorbance wavelength of 430 nm, while absorbance of curcumin in ethanol (from 0 to 0.025 $mg \cdot mL^{-1}$) was determined at a maximum wavelength of 426 nm. Chloramphenicol absorbance was calculated in water from solutions of 0.025 to 2.5 $mg \cdot mL^{-1}$ and in PBS from solutions of 0 to 0.125 $mg \cdot mL^{-1}$ at an absorption wavelength maximum of 278 nm, while the absorbance in ethanol solutions of 0.001 to 0.125 $mg \cdot mL^{-1}$ was determined at a maximum wavelength of 273 nm. To determine the solubility of drugs in water, PBS and ethanol, saturated solutions were prepared by adding an excessive content of drug to each solvent, and then the mixtures were sonicated for 2 h. The saturated solutions were incubated at 37 ºC for 48 h with constant stirring of 150 rpm until reaching the equilibrium. The equilibrated solutions were centrifuged at 2500 rpm during 5 min to remove the excess of drug and then measured using UV-VIS-NIR equipment at predetermined absorption wavelengths maximum for each solvent.

- *In vitro drug delivery tests*

Drug release experiments were carried out *in vitro* conditions (PBS pH= 7.4, 37 ºC with constant stirring). To quantify the amount of released curcumin from A-CNF-cur scaffolds, freeze-dried (n=3) and Ca^{2+} crosslinked/air-dried (n=3) samples were weighted and then soaked in 40 mL of PBS solution. Due to the low solubility of curcumin in aqueous media, the drug amount released was evaluated based on protocol proposed by Sanoj Rejinol et al. [11]. In brief, at predetermined time points, 40 mL of PBS medium containing the released drug were removed and centrifuged for 30 min at 14000 rpm, and 40 mL of fresh PBS at 37 ºC were added to the glass containing the sample to continue the release experiment. After the centrifugation step, the PBS (liquid phase) was discarded while the solid phase containing the A-CNF matrix and the non-dissolved curcumin was resuspended in 15 mL of ethanol (96 %). The amount of released curcumin at each time point was determined at room temperature using UV-VIS-NIR spectrophotometer by comparing the absorbance at λ= 426 nm with the standard curve with known concentrations of curcumin dissolved in ethanol, as follows [12]:

$$\text{Drug release (\%)} = \frac{[Mr]}{[Mt]} \cdot 100 \qquad \text{(Eq. 7)}$$

where [Mr] is the concentration of drug released at each time interval and [Mt] is the total amount of drug present in the scaffold.

The quantification of chloramphenicol release was also performed *in vitro* conditions. Freeze-dried (n=2) and Ca^{2+} crosslinked/air-dried scaffolds (n=2) of A-CNF-clph were weighted and introduced in 40 mL of PBS solution at 37°C with constant stirring. At each time point, 10 µL of PBS medium were collected from the release experiment and then diluted in 990 µL of fresh PBS. The resulted dilution was measured at room temperature using UV-VIS-NIR spectrophotometer to determine the amount of released chloramphenicol by comparing the absorbance at λ= 278 nm with the prepared standard curve of known chloramphenicol concentrations diluted in PBS applying Eq. 7.

To evaluate the release of curcumin and chloramphenicol simultaneously from A-CNF-cur-clph freeze-dried (n=2) and Ca^{2+} crosslinked/air-dried (n=2) scaffolds, samples were first weighted and introduced in 30 mL of PBS. At each time interval, PBS was discarded and replaced by fresh one, as previously. Removed PBS was centrifuged for 30 min at 14000 rpm, the supernatant was collected and diluted 1:100 in fresh PBS to measure the dissolved chloramphenicol concentration by UV-VIS-NIR, following the method described above. The solid pellet containing A-CNF matrix and curcumin was diluted in 12 mL of ethanol (96 %) enabling the measurement of curcumin by UV-VIS-NIR equipment at room temperature, as previously. The sink conditions were maintained along the whole experiment [13].

Chloramphenicol release from antibiotic-loaded A-WBPU+Ca meshes (n=3), A-Ca (n=3) and EnCNC (n=3) samples was also evaluated *in vitro* (PBS, 37 ºC, constant stirring), following the same method described above for chloramphenicol release experiments. The measurements were carried out using UV-VIS-NIR (Shimadzu 3600) equipment and the quantification of the delivered chloramphenicol was calculated using Eq. 7.

2.3.4.2. Tissue engineering

- *In vitro cell cultures*

HEK293 cell line was a kind gift of Dra. María Muñoz Caffarel. The cells were defrosted at passage 4 and expanded *in vitro* at 37 ºC, 5 % of CO_2, replacing the culture medium every 72 h. Dulbecco's Modified Eagle Medium (DMEM) supplemented with 10 % of fetal bovine serum (FBS) and 1 % (100 $U \cdot mL^{-1}$) of penicillin-streptomycin (Pen/Strep) composed the culture media for this cell line. The freeze-dried A-CNF (n= 3), A-Ca (n=9) and EnCNC (n=9) scaffolds were transferred into a 24 well plate after sterilization process, carried out by UV light inside the laminar flow hood for 3 h, with no evidence of scaffold damage. After sterilization process HEK cells at passage 15 were trypsinized, counted and seeded on the scaffolds at a density of $2 \cdot 10^5$ cells per sample. Besides,

$2 \cdot 10^5$ cells were seeded in an empty well in monolayer as a control. The culture medium was replaced every 72 h and the scaffolds were harvested at time points of 0 (6 h), 7, 14 and 21 days, except of A-CNF scaffolds that were harvested after 7 days of culture. The presence and proliferation rate of the cells into the scaffolds and controls were monitored by staining the nucleus with DAPI solution (5 $mg \cdot mL^{-1}$) diluted in PBS (1:2000), after washing twice the scaffolds with PBS. DAPI-stained cells were observed after 10 min of incubation using a confocal laser-scanning microscope.

Murine teratocarcinoma derived chondrogenic cell line (ATDC5) were defrosted at a passage 15 and cultured under *in vitro* conditions of 37 ºC and 5 % of CO_2 at a density of 10,000 $cell \cdot cm^2$ in maintenance media formed by Dulbecco's Modified Eagle Medium: Nutrient Mixture F-12 (DMEM:F-12) supplemented with 5 % FBS and 1 % of Pen/Strep. The cells were expanded changing the culture medium every 48 h until reaching over than 80 % of confluence. Afterwards, the cells were thrypsinized and counted before added to the A-WBPU bioinks at a density of $2 \cdot 10^6$ cells per milliliter of material. After 3D printing and $CaCl_2$ crosslinking process, A-WBPU (n=60) scaffolds were placed in 6 well plates and then were cultured in maintenance media. Moreover, other 24 scaffolds from each formulation were also cultured in differentiation media composed by DMEM:F-12 supplemented with 5 % of FBS, 1 % Pen/Strep, 100 $\mu g \cdot mL^{-1}$ insulin transferrin selenium (ITS) and 0.2 mM L-Ascorbic acid-2-phosphate. The scaffolds were harvested after 24 hours, 14 and 28 days of *in vitro* culture for further analysis.

- *Cytotoxicity tests*

  - *Short-term cytotoxicity test*

The extractive method for film materials (ISO 10993−11:2009) was employed to measure the cytotoxicity of the WBPU film. For this assay, murine fibroblasts (L929 cells) were seeded into 96-well plate at a density of 4×10^3 cells per well with 100 µL of complete culture medium composed by DMEM supplemented with 10 % FBS and 1 % Pen/Strep. After 24 h of culture, the medium was replaced with 100 µL of negative control (complete medium), positive control containing 10 % of dimethyl sulfoxide (DMSO) in complete medium and extractive medium previously cultured with the biomaterial during 24 h. A 10 % of PrestoBlue®, which is a resazurin-based solution that indicates cell viability, was added to each well and the optical density was measured at 570 and 600 nm with a spectrophotometer at time points of 0, 24, 48 and 72 h. The viability of the cells was calculated following the Eq. 8.

$$\text{Viability (\%)} = \frac{[A]\text{sample}}{[A]\text{control}} \cdot 100 \qquad \text{(Eq. 8)}$$

where [A]sample is the absorbance of the sample cells and [A]control is the absorbance of the negative control. All assays were performed in triplicate.

- *Lactate dehydrogenase (LDH) release cytotoxicity test*

LDH release quantification was performed to evaluate the effect of cell encapsulation into the A-WBPU bioinks. The measurement of LDH content into the culture media is a well indicator of cell damage and cytotoxicity of the employed materials. The LDH release analysis was performed using the culture media of encapsulated cells on the A-WBPU bioinks by means of CyQUANT™ LDH Cytotoxicity Assay Kit. The amount of LDH released in the culture media can be quantified by a series of coupled enzymatic reactions, giving rise to a red formazan product that can be spectroscopically measured. The amount of formazan product is directly proportional to the amount of LDH released into the medium, indicating the levels of cytotoxicity. To perform these experiments, all culture media of cell-laden A-WBPU droplets were harvested after 24h, 72h and 7 days of culturing. The culture media were centrifuged at 8000 rpm during 5 minutes to remove all residual material and ECM. A negative control was also prepared by harvesting the medium of confluent monolayer chondrocytes cultured during 24 h. The cells for the negative control were lysed using 200 µL of 10X lysis buffer and incubated during 45 min before culture harvesting to ensure that all LDH from the cells was released to the medium. Then, the LDH content was measured in triplicate from 50 µL of each culture sample and standard solutions, following the manufacturer instructions. The amount of red formazan from each sample was calculated by measuring the absorbance at 490 nm and 680 nm, subtracting the 680 nm value from the 490 nm. Finally, the LDH concentration was calculated from the standard curve and thereafter, the LDH measurement of each sample was normalized using the negative control.

- *Cell proliferation and protein quantification*

- *Preliminary LIVE-DEAD assays*

Preliminary LIVE/DEAD assay was performed to evaluate the cell viability on the developed A2.5-WBPU+Ca meshes. A mesh sample was cut in 5x5 mm pieces, sterilized during 30 min under UV light and then introduced in 500 µL of culture medium (DMEM + 10 % FBS + 1 % Pen/Strep) to achieve material moistening. Murine fibroblast L929 cell line were cultured under *in vitro* conditions of 37 ºC and 5 % of CO_2 until

reaching a cell density of $2.5x10^6$ cell·mL^{-1}. Cultured cells were collected through trypsinization and $5x10^4$ cells were seeded on the surface of the moist mesh samples in a 24 well plate. Furthermore, $5x10^4$ cells were also seeded in empty wells as a control. Then, seeded samples were incubated during 24 h at 37 ºC to allow cell adhesion, and then 500 µL of culture medium were added afterwards. Culture maintenance was carried out by replacing the medium every four days. After 3 and 7 days of seeding, samples were harvested for LIVE/DEAD assay. Firstly, culture medium was removed from the wells, samples were washed three times with PBS and then moved to a clean well plate. Afterwards, 250 µL of a solution containing 4 µM of calcein and 5 µM of propidium iodide were added into the wells with the seeded samples and PBS, and then they were incubated at room temperature for 20 min. The cells were observed by confocal microscopy and the viability was calculated counting the total number of green-fluorescent cells (live) and red-fluorescent cells (dead) from the images using ImageJ (Fiji) software. The number of living cells were divided by the total amount of counted cells to obtain the viability percentages.

- *Cell number quantification*

Cell number quantification into the A-WBPU bioprinted scaffolds after culture was carried out by deoxyribonucleic acid (DNA) analysis. Firstly, for the measurement of cell number into laden A-WBPU droplets, samples were harvested after 24 h, 72 h and 7 days from culture and frozen at -80 ºC. Moreover, A-WBPU printed scaffolds were harvested after 24 hours, 14 and 28 days, and frozen at −80 °C afterwards. To enable the digestion of the extracellular matrix and cell lysis, the scaffolds were freeze-thawed 3 times with liquid N_2 and then Proteinase K treatment was applied to digest the extracellular matrix. Samples placed in Eppendorf tubes were incubated at 56 °C for 16 h with 300 µL of 50 mM Tris/1 mM EDTA/1 mM iodoacetamide (TRIS/EDTA) solution that contained Proteinase K in a concentration of 1 mg·mL^{-1}. After the digestion, the samples were again freeze-thawed 3 times with liquid N_2 to facilitate DNA extraction. DNA was quantified using a CyQuant cell proliferation assay kit. In brief, cellular ribonucleic acid (RNA) was degraded by incubating the samples with 200 µL of a lysis buffer that contained RNase A during 1 h at room temperature. Moreover, a standard curve was prepared with known DNA concentrations from 0 to 2 µg·mL^{-1}. Then, 100 µL of each sample and standards were placed in a 96 well black plate in triplicate and 100 µL of 2x GR-dye solution were added in each sample and incubate for 15 min at room temperature before measuring. Fluorescence intensity was measured at an emission wavelength of 520 nm and excitation wavelength of 480 nm using a Multi-Mode Plate Reader.

- *Glycosaminoglycan (GAG) quantification*

Samples from Proteinase K digestion were used to measure GAG content from time points of 14 days and 28 days. 100 µL from the digested samples were extracted after freeze-thawed step. The GAG content was determined by adding 25 µL of each sample and standards into a 96 well plate in triplicate. Then, 5 µL of 2.3 M NaCl and 150 µL of 1,9-dimethylmethylene blue (DMMB) solution, composed by 16 mg DMMB in 5 mL of ethanol were added per each well. A standard curve with known concentrations of chondroitin sulfate from shark cartilage was previously prepared from 0 to 10 $\mu g \cdot mL^{-1}$ in TRIS/EDTA buffer solution. The absorbance at 525 and 595 nm was measured using a Multi-Mode Plate Reader. The values from 595 nm were subtracted from 525 nm ones and the concentrations were obtained from the standard curve.

- *Histology*

Histological analysis from A-WBPU (n=8) chondrocyte-laden scaffolds harvested after 28 days of culture in both maintenance and differentiation media were carried out. Samples were immersed in an optimal cutting temperature (OCT) compound creating blocks that were sectioned using a cryostat LEICA CM1950. Hematoxylin & Eosin, Masson's Trichrome and Safranin-O (with fast green and Weigert's Iron Hematoxylin solutions as counter stains) staining were performed in scaffolds slides to observe both cells and ECM deposition. Samples were observed using an optical microscope (Nikon eclipse Ts2) equipped with a camera to record the images.

- *Gene expression analysis*

After 28 days of culturing in maintenance and differentiation conditions, A-WBPU (n=12) chondrocyte-laden scaffolds were harvested, placed in Eppendorf tubes containing 750 µL of Trizol solution and stored at -80 ºC for further analysis. Afterwards, the samples were freeze-thaw three times to enable RNA extraction from the encapsulated cells. RNA extraction from scaffolds was carried out using PureLink RNA Mini Kit (Thermo Scientific), following manufacturer instructions. First, samples were centrifuged 5 min at 12000 G to remove scaffold and ECM. Then 0.2 mL of chloroform were added per mL of Trizol and after 3 min of incubation at room temperature, the samples were centrifuged at 12000 G for 15 min. The aqueous phase containing the RNA was collected and the organic was removed. For small samples, 0.5 mL of isopropanol were added and incubated for 10 min at room temperature. Then, the samples were centrifuged for 10 min at 12000 G to form a white gel-like pellet where the total RNA were placed. The

pellet containing RNA was mixed in a ratio 1:1 with ethanol 70 % and then 700 µL of the mix were introduced to the Pink mini column kit, removing the rest of the cell components and isolating the messenger ribonucleic acid (mRNA). The final amount of mRNA was eluded from the column using 30 µL of RNase-free water and then the mRNA concentration was measured in each sample using a NanoDrop.

Copy deoxyribonucleic acid (cDNA) was synthesized from isolated mRNA using 100-200 ng per sample by means of reverse transcriptase (RT) enzymatic reaction. In brief, samples were incubated with RT enzyme for 5 min at 25 ºC, then 20 min at 46 ºC and finally at 95 ºC during 1 min. Real-time quantitative polymerase chain reactions (RT-qPCR) were prepared on a total volume of 20 µL per sample using a primer stock solution that contains 10 µL of iQ SYBR green (Thermo Fisher), 2 µL of cDNA, 1 µL of reverse primer and 1 µL of forward primer (**Table 2.2**.).

Table 2.2. *List of primers used for RT-qPCR experiments.*

Gene	Forward primer 5'-3'	Reverse primer 5'-3'
GAPDH	TGGCAAAGTGGAGATTGTTGCC	AAGATGGTGATGGGCTTCCCG
SOX9	AGTACCCGCATCTGCACAAC	ACGAAGGGTCTCTTCTCGCT
Col1a1	GCTCCTCTTAGGGGCCACT	CCACGTCTCACCATTGGGG
Col2a1	AGTACCTTGAGACAGCACGAC	GCTCTCAATCTGGTTGTTCAG
ACAN	AGAACCTTCGCTCCAATGACTC	AGAACCTTCGCTCCAATGACTC

Polymerase chain reactions (PCR) for transcription factor SOX9, collagen I (Col1a1), collagen II (Col2a1) and aggrecan (ACAN) genes were carried out using a thermocycler (QuantStudio™ 5 Real-Time PCR System). Firstly, two thermal cycles of 50 °C for 2 min and 95 °C for 2 min were performed and then, cycles of 95 °C for 15 s and 60 °C for 30 s repeated 40 times were carried out. Obtained cycle threshold (Ct) values of RT-qPCR samples were normalized against glyceraldehyde-3-phosphate dehydrogenase (GAPDH) gene employed as housekeeping, and finally the gene expression of each sample was analyzed using the ΔΔCt model [14].

2.3.5. Statistical analysis

Statistical analysis was performed using SPSS statistics software version 26. Data were expressed as mean ± standard deviation ($n \geq 3$), and one-way analysis of variance (ANOVA) tests were performed considering $^*p < 0.05$ as statistically significant.

2.4. References

[1] Harding SE. The intrinsic viscosity of biological macromolecules. Progress in measurement, interpretation and application to structure in dilute solution. Prog Biophys Mol Biol 1997;68:207–262. https://doi.org/10.1016/S0079-6107(97)00027-8.

[2] Pamies R, Schmidt RR, Martínez M del CL, Torre JG. The influence of mono and divalent cations on dilute and non-dilute aqueous solutions of sodium alginates. Carbohydr Polym 2010;80:248–253. https://doi.org/10.1016/j.carbpol.2009.11.020.

[3] Martinsen A, Skjåk-Bræk G, Smidsrød O, Zanetti F, Paoletti S. Comparison of different methods for determination of molecular weight and molecular weight distribution of alginates. Carbohydr Polym 1991;15:171–193. https://doi.org/10.1016/0144-8617(91)90031-7.

[4] Segal L, Creely JJ, Martin AE, Conrad CM. An empirical method for estimating the degree of crystallinity of native cellulose using the X-ray diffractometer. Text Res J 1959;29:786–794. https://doi.org/10.1177/004051755902901003.

[5] Ouyang L, Yao R, Zhao Y, Sun W. Effect of bioink properties on printability and cell viability for 3D bioplotting of embryonic stem cells. Biofabrication 2016;8:3-7. https://doi.org/10.1088/1758-5090/8/3/035020.

[6] Deeken CR, Abdo MS, Frisella MM, Matthews BD. Physicomechanical evaluation of polypropylene, polyester, and polytetrafluoroethylene meshes for inguinal hernia repair. J Am Coll Surg 2011;212:68–79. https://doi.org/10.1016/j.jamcollsurg.2010.09.012.

[7] Cobb WS, Peindl RM, Zerey M, Carbonell AM, Heniford BT. Mesh terminology 101. Hernia 2009;13:1–6. https://doi.org/10.1007/s10029-008-0428-3.

[8] Afonso JS, Martins PALS, Girao MJBC, Natal Jorge RM, Ferreira AJM, Mascarenhas T, Fernandes AA, Bernardes J, Baracat EC, Rodrigues G, Patricio B. Mechanical properties of polypropylene mesh used in pelvic floor repair. Int Urogynecol J 2008;19:375–380. https://doi.org/10.1007/s00192-007-0446-1.

[9] Zhu L-M. Mesh implants: An overview of crucial mesh parameters. World J Gastrointest Surg 2015;7:226-236. https://doi.org/10.4240/wjgs.v7.i10.226.

[10] Hou X, Zheng W, Kodur V, Sun H. Effect of temperature on mechanical properties of prestressing bars. Constr Build Mater 2014;61:24–32. https://doi.org/10.1016/j.conbuildmat.2014.03.001.

[11] Sanoj Rejinold N, Muthunarayanan M, Divyarani V V., Sreerekha PR, Chennazhi KP, Nair SV, Tamura H, Jayakumar R. Curcumin-loaded biocompatible thermoresponsive polymeric nanoparticles for cancer drug delivery. J Colloid Interface Sci 2011;360:39–51. https://doi.org/10.1016/j.jcis.2011.04.006.

[12] Guaresti O, García–Astrain C, Palomares T, Alonso–Varona A, Eceiza A, Gabilondo N. Synthesis and characterization of a biocompatible chitosan–based hydrogel cross–linked via ‘click’ chemistry for controlled drug release. Int J Biol

Macromol 2017;102:1–9. https://doi.org/10.1016/j.ijbiomac.2017.04.003.

[13] Saarinen-Savolainen P, Järvinen T, Taipale H, Urtti A. Method for evaluating drug release from liposomes in sink conditions. Int J Pharm 1997;159:27–33. https://doi.org/10.1016/S0378-5173(97)00264-0.

[14] Schmittgen TD, Livak KJ. Analyzing real-time PCR data by the comparative CT method. Nat Protoc 2008;3:1101–1108. https://doi.org/10.1038/nprot.2008.73.

Chapter 3

Characterization of alginate, WBPU and cellulose nanoentities

CHAPTER 3 - Characterization of alginate, WBPU and cellulose nanoentities

3. Characterization of alginate, WBPU and cellulose nanoentities

3.1. Aim of the chapter

This chapter is focused on the characterization of commercial alginate and WBPU, as well as in the preparation and characterization of different types of cellulose nanostructures, which show potential in the field of 3D printing technology. Two types of cellulose nanoentities were characterized: commercial CNF and EnCNC. Besides, the obtaining process of CNCs via enzymatic hydrolysis is well described in this chapter.

First, the molecular weight of the alginate was calculated by intrinsic viscosity. Subsequently, it was dissolved in water at 4 wt.% and a film was prepared by solvent casting and subsequently characterized. The commercial WBPU dispersion was characterized regarding its solid content, pH, stability and particle size. Then, a film was also prepared by solvent casting and characterized. Morphological, physicochemical, thermal and mechanical properties and biocompatibility were analyzed. The morphology, physicochemical and thermal properties of freeze-dried CNF and EnCNC were analyzed.

These materials will be the basis for the development of new biomaterial-based inks for 3D printing technology. After the determination of their characteristics, the inks will be prepared through blending these materials, acting as rheological modifiers to each other or even as single-component inks.

3.2. Characterization of alginate

The molecular weight of the employed commercial alginate was calculated from the intrinsic viscosity using Eq. 1, resulting in 2.4×10^5 $g \cdot mol^{-1}$. The ratio among M and G subunits that composed this biopolymer is 1.56 [1]. It has been reported that the M/G ratio influences the alginate properties when it is crosslinked with Ca^{2+} ions. In this case, the high content of M subunits would lead to crosslinked alginate matrices with higher flexibility due to the lower affinity to Ca^{2+} ions in comparison with those with high G subunits content [2].

An 8x8 cm^2 film was prepared by casting an aqueous alginate solution in a Teflon mold, which was left to dry at room temperature for 7 days, obtaining a brown film that shows certain transparency and rigidity (**Figure 3.1 A**). Thereafter, the obtained film was characterized in order to study the properties of this biopolymer before use it as a 3D printing ink component.

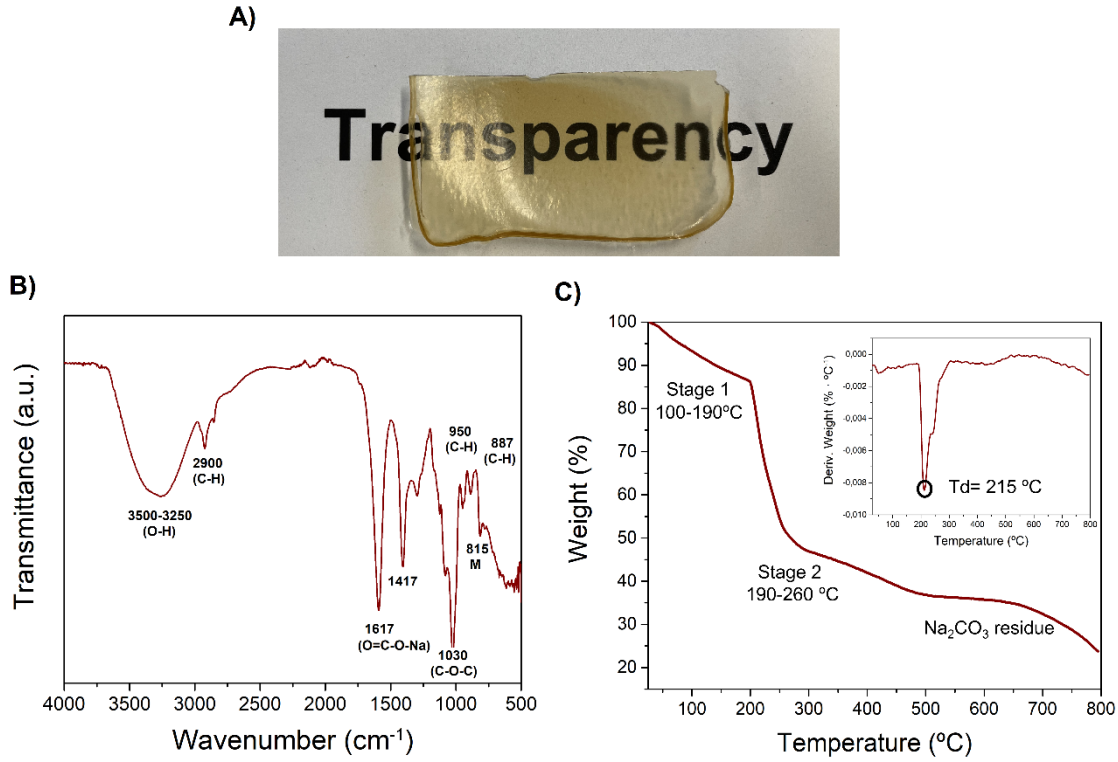

Figure 3.1 *A) Digital image of an alginate film, B) FTIR spectrum, and C) TGA results of the alginate.*

The chemical structure of the alginate was analyzed by FTIR (**Figure 3.1 B**). The spectrum showed the stretching vibration of the O–H groups in the 3500-3250 cm^{-1} interval, and the stretching vibration of C–H at 2924 cm^{-1}. The peaks located at 1617 and 1417 cm^{-1} corresponded to the symmetric and asymmetric stretching vibrations of O=C-O-Na^+ ion salt, and the band at 1030 cm^{-1} to the C–O stretching vibration. Finally, the bands at 950 cm^{-1} and 887 cm^{-1} corresponded to C–H stretching vibrations from M and G units, respectively [3,4]. The band at 815 cm^{-1} was related to the predominance of M groups in this biopolymer [2].

The thermal stability of alginate was studied through TGA analysis. The weight loss and its derivative curves shown in **Figure 3.1 C** revealed that alginate undergoes a two-stage thermal degradation. The first one occurred between 100 and 190 ºC, which was attributed to the dehydration of the polymer, while the second one occurred in the range of 190 to 260 ºC. This second weight loss was attributed to the progressive deconstruction of the polymer entanglement and the formation of a carbonaceous residue that finally yields to Na_2CO_3 char compound [5]. The pronounced peak at 215 ºC observed in derivative curve represented the degradation temperature of this polymer.

Mechanical characterization of the alginate film was also performed by means of tensile test. The obtained Young modulus, tensile strength and elongation at break values are summarized in **Table 3.1**. The alginate film showed high Young's modulus and stress at break values, with low elongation at break (5.33 %). These values are in accordance with those reported in the literature for sodium alginate films [6], concluding that this material showed rigidity and high resistance at break.

Table 3.1. *Mechanical properties of the alginate film.*

	Young's modulus (GPa)	**Stress at break (MPa)**	**Strain at break (%)**
Alginate film (n=5)	2.28 ± 0.66	45.10 ± 15.22	5.33 ± 2.29

3.3. Characterization of WBPU

Solid content of the WBPU dispersion was determined by weight difference. The measurements were done by duplicate and an average solid content of 40.25 ± 0.18 % was measured, which is in accordance with the data provided by the manufacturer.

The particle size and distribution of the WBPU dispersion were analyzed by DLS. Particle size is an essential parameter to measure the stability of the WBPU dispersion [7]. Dispersions with small particle sizes tend to be highly stable, while dispersions with larger particle sizes have less stability, causing the precipitation of these particles [7,8]. The results of this experiment showed a particle size of 87.1 ± 0.3 nm, with a polydispersity of 0.083. The stability of the dispersion was studied through Z potential measurements, and the obtained value was -70.64 mV. For stable dispersion, Z potential values above +30 mV and below -30 mV indicate stable dispersions [9], so the selected WBPU dispersion is stable and was maintained over and extended duration.

pH was also measured in triplicate and the obtained average value was 7.38 ± 0.12, similar to those reported in the literature for WBPU dispersions [8,9]. This value matches the human physiological range of 7.35-7.45 of the interstitial fluids [10] and thus, this is an indication that the WBPU dispersion could present biocompatible character [11].

After the analysis of the WBPU dispersion, 10 mL of this material were placed in a Teflon mold of 8x8 cm^2 and allowed to dry at room temperature for 7 days to obtain a film that will be characterized. The obtained film showed transparency and flexibility (**Figure 3.2 A**).

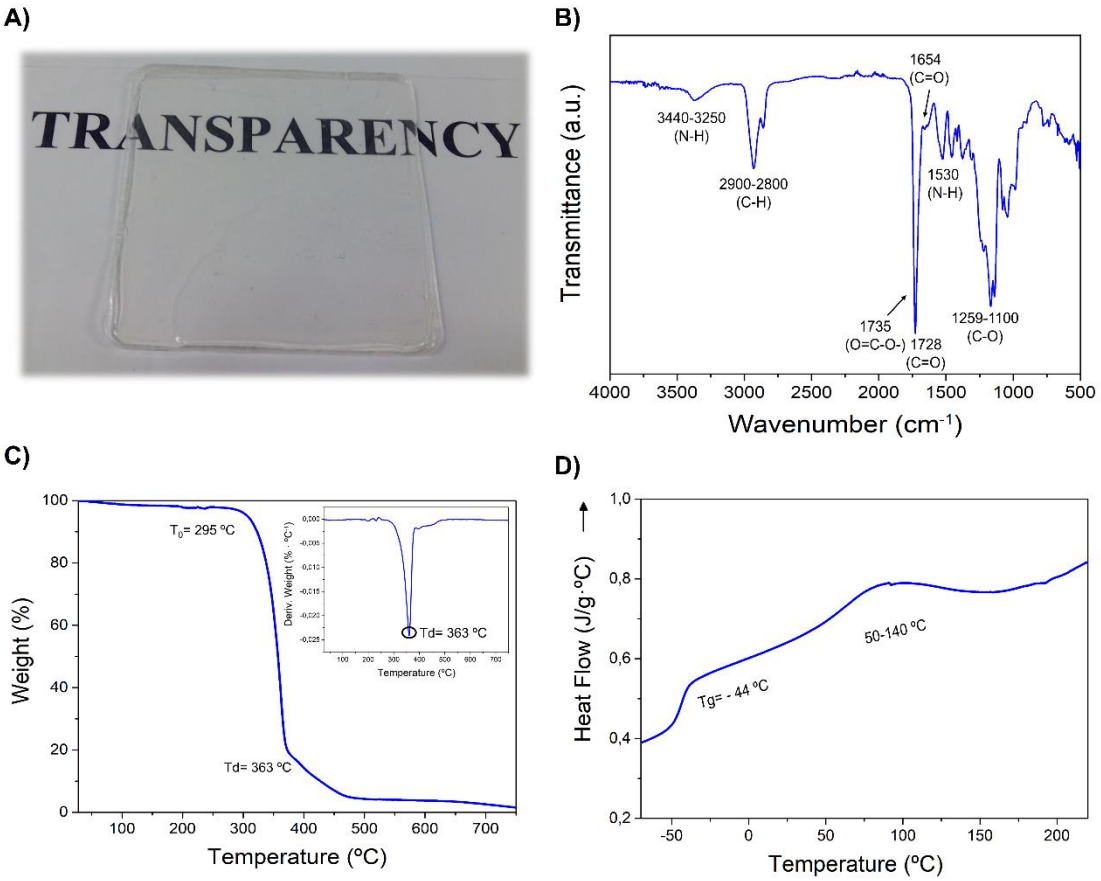

Figure 3.2. *A) Digital image, B) FTIR spectrum, C) TGA results and D) DSC thermogram of the WBPU film.*

The chemical structure analysis of the WBPU film was performed by FTIR (**Figure 3.2 B**). The spectrum showed an absorption band corresponding to the N-H stretching vibration at 3440-3250 cm^{-1} and a band attributed to the in-plane bending vibration of N-H at 1530 cm^{-1}. The aliphatic C-H stretching vibration band appeared from 2900 to 2800 cm^{-1}. The band of the stretching absorption of the C=O group of the ester and urethane appeared at 1728 cm^{-1} and 1654 cm^{-1}, respectively. In this interval the typical absorption band of carboxylate group at 1735 cm^{-1} should also appear, overlapped with urethane and ester band. The band observed between 1259 and 1100 cm^{-1} corresponds to stretching vibration of C–O bonds of the ester and urethane groups. [12,13]. This analysis revealed that this WBPU presented the typical bands corresponding to the structure of the anionic aliphatic polyester-polyurethane waterborne dispersion.

The thermal stability and degradation properties of this WBPU film were studied by TGA and the results are shown in **Figure 3.2 C.** The weight evolution curve did not show any loss up to 295 ºC, starting to degrade at this temperature (T_0). This behavior indicated that the WBPU film barely contained water molecules. The firstderivative curve analysis

showed a single pick corresponding to the degradation temperature (T_d) of this WBPU at 363 ºC, where the most of the weight loss occurred.

DSC analysis of WBPU film (**Figure 3.2 D**) showed two transitions. The first transition was observed at low temperatures (from -50 to -38 °C) and it was related to the glass transition temperature (Tg) stablished at -44 ºC. The second transition was observed in the broad range of 50–140 °C, showing an endothermic peak with a maximum at 91 ºC and an enthalpy of 11.60 $J \cdot g^{-1}$ associated to order-disorder transition related to the short range ordering of the hard segment of the WBPU [15]. In this interval, the enthalpy value could be influenced by water molecules traces remained in the film after drying process. However, TGA curve showed that weight loss in the range of 50 to 140 ºC hardly occurs and thus, the observed enthalpy would correspond mainly to the order-disorder transition of WBPU.

Mechanical characterization of the WBPU films was carried out by means of tensile test and the results are collected in **Table 3.2**. This WBPU showed low Young's modulus, stress at break and stress at yield values and high strain at break, characteristic of materials of high flexibility. The low value of stress at yield suggests that most of the deformation of the sample occurs on the plastic zone, where the sample is not able to recover the original shape [14]. These mechanical characteristics are typical from WBPU, and these results matched with those observed in the literature for WBPU films [15].

Table 3.2. *Mechanical properties of the WBPU film.*

	Young's modulus (MPa)	**Stress at break (MPa)**	**Strain at break (%)**	**Stress at yield (MPa)**
WBPU film (n=5)	6.89 ± 2.06	4.37 ± 2.21	779.47 ± 164.27	1.89 ± 0.49

Cytotoxicity tests of WBPU were carried out in order to guarantee its suitability for biomedical applications and the results are shown in **Figure 3.3**. WBPU film was incubated with culture media and then the medium was extracted to culture with L929 murine fibroblast.

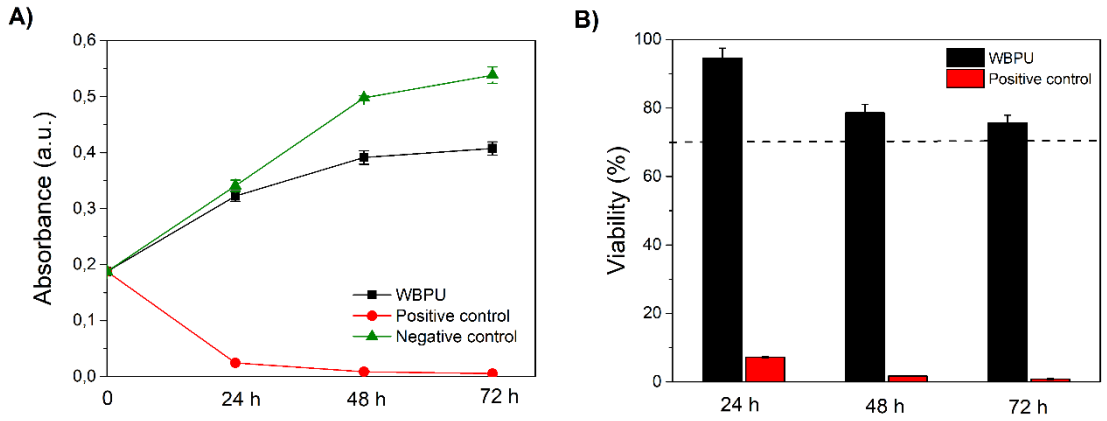

Figure 3.3. *Short-term cytotoxicity assays of the WBPU film. A) Absorbance versus incubation time of a positive control (DMSO), negative control (culture medium) and WBPU film. B) Viability (percentage in respect of the negative control) of live fibroblast cells on WBPU.*

In **Figure 3.3 A**, the absorbance versus incubation time for the positive (culture medium + 10 % of DMSO) and negative (culture medium) controls, as well as for the WBPU film is shown. As can be observed, the WBPU film did not affect to cell growth, showing similar absorbance values to the negative control at 24 h of incubation. At 48 and 72 h the absorbance and consequently, the cell growth levels were maintained. The cell viability in respect to the negative control as a function of the incubation time is represented in **Figure 3.3 B**. It was observed that the viability values of the cells cultured with the extracted media of the WBPU film were higher than the established acceptance limit by the ISO 10993-5 of 70% in respect to the negative control. After these analyses, it can be concluded that WBPU is non-cytotoxic and suitable for biomedical purposes.

3.4. Characterization of CNFs

Freeze-dried commercial CNFs (**Figure 3.4 A**) were analyzed in order to determine their morphology, physicochemical and thermal characteristics. Morphological characteristics and dimensions of CNFs were studied by AFM. As can be observed in **Figure 3.4 B**, height and phase images showed cellulose nanofibers with several micrometers in length and with diameters between 50-200 nm.

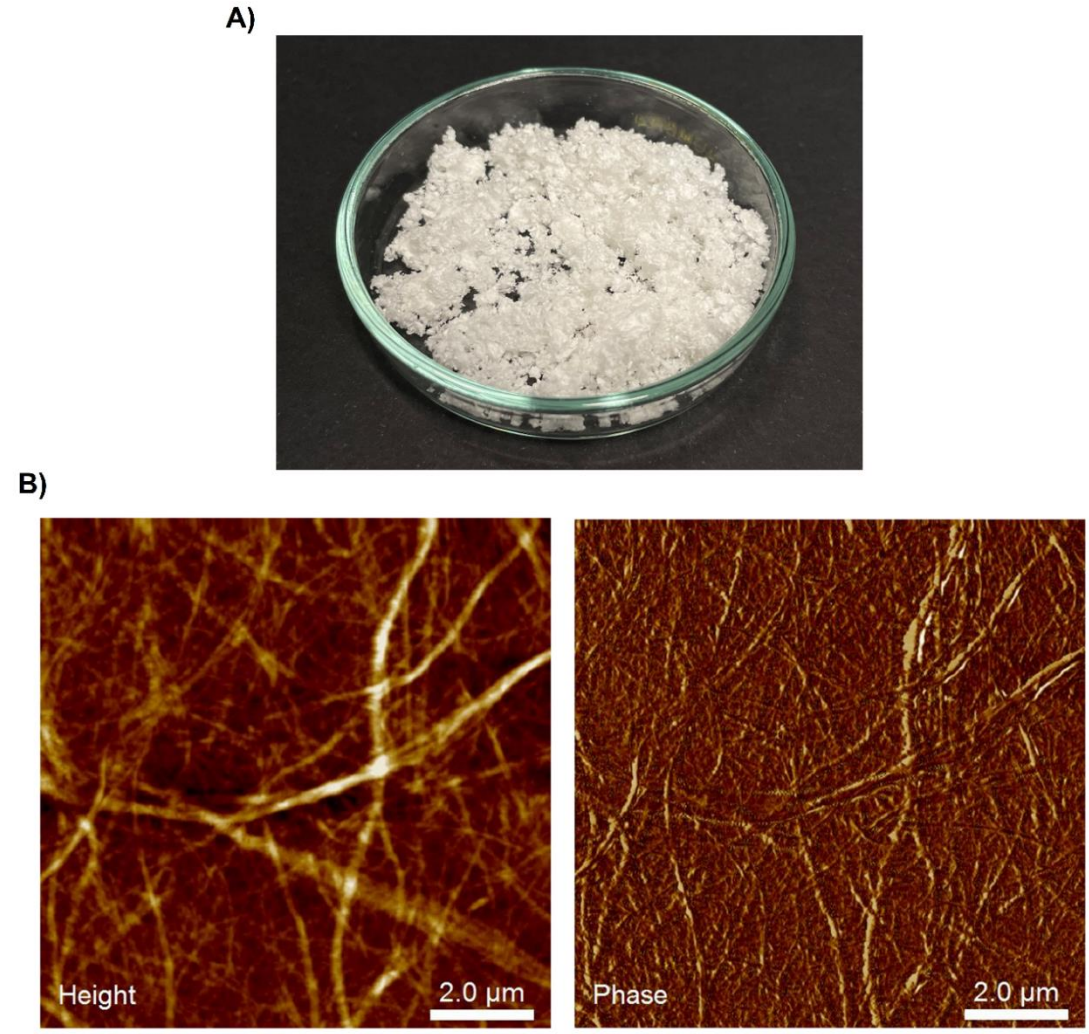

Figure 3.4. *A) Image of freeze-dried CNF and B) AFM height and phase images of CNF (10x10 µm).*

The ^{13}C NMR spectrum of CNF is shown in **Figure 3.5 A**, where the different peaks corresponding to each carbon of the cellulose molecule can be observed. C_1 was located between 100 and 110 ppm, whereas C_4 peak was observed between 85 and 90 ppm. The broad peak between 70 and 80 ppm was attributed to the C_2, C_3 and C_5 of the D-glucose molecule. Finally, the peak observed among 70 and 60 ppm corresponded to C_6 bonded to the primary –OH group. The spectrum is characteristic of cellulose I structure [15].

The XRD pattern of CNF (**Figure 3.5 B**) showed strong diffraction peaks at 2θ = 14.5º, 16.5º and 23º, and a small peak at 34º corresponded to $(1\bar{1}0)$, (110), (200) and (004) crystallographic planes, respectively, associated to cellulose I crystalline structure [18]. A crystallinity index of 71 % was estimated according to Eq. 2.

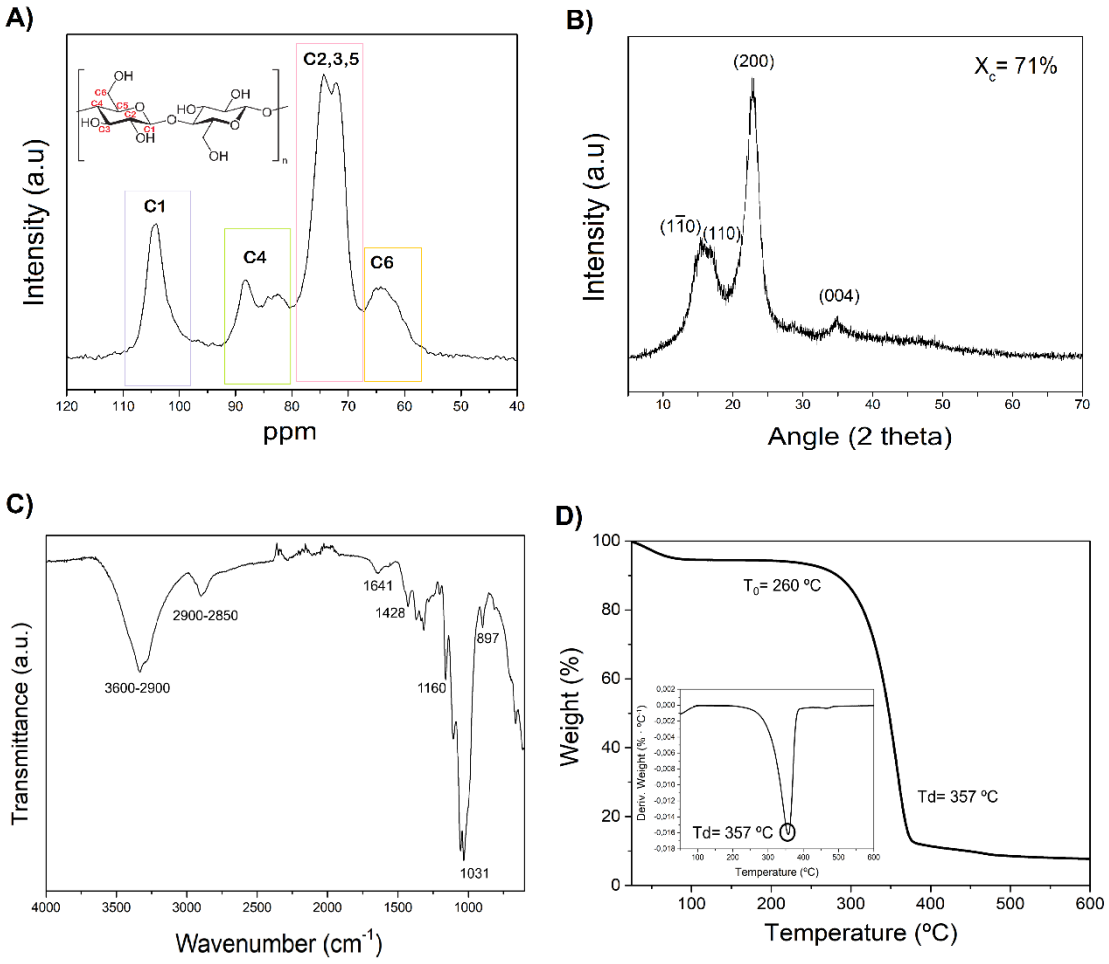

Figure 3.5. *A) ^{13}C NMR spectrum, B) XRD pattern, C) FTIR spectrum and D) TGA results of CNF.*

FTIR analysis spectrum (**Figure 3.5 C**) showed a broad band from 3600 to 2900 cm^{-1} corresponding to the stretching vibration of the hydrogen-bonded –OH groups. The band between 2900-2850 cm^{-1} was assigned to the C–H stretching vibration and the band at 1428 cm^{-1} corresponded to the CH_2 bending vibration. The band at 1641 cm^{-1} was associated to water absorption, whereas the bands located at 1160 and 1031 cm^{-1} corresponded to the stretching vibrations of C–O–C and C–O β-glycosidic bonds, respectively. Finally, the band at 897 cm^{-1} was assigned to the β-glycosidic linkage of cellulose structure [16,17].

TGA analysis was performed and the results are shown in **Figure 3.5 D.** A 5% of weight loss was observed from 25 to 100 ºC resulted from the residual water evaporation. Thermal stability was observed until 260 ºC (T_0), where the weight of the sample is starting to drop. Derivative curve showed a marked peak corresponding to the degradation temperature at 357 ºC (T_d) of this biopolymer.

3.5. Enzymatically-obtained cellulose nanocrystals (EnCNC)

3.5.1. Enzyme isolation and CNC obtaining process

EnCNCs were obtained from the hydrolysis of 100 % cellulose filter paper carried out by a reconstructed ancestral endoglucanase. In previous works, ancestral sequence reconstruction techniques were used to rebuild ancient proteins that had more specific activity than existing enzymes [19,20]. In this case, the reconstructed ancestral endoglucanase had the specificity to break β-1,4-glycosidic bonds from cellulose polymer randomly, attaching to the amorphous regions and thus, isolating crystalline cellulose parts from cellulose fibers [21,22] (**Figure 3.6**).

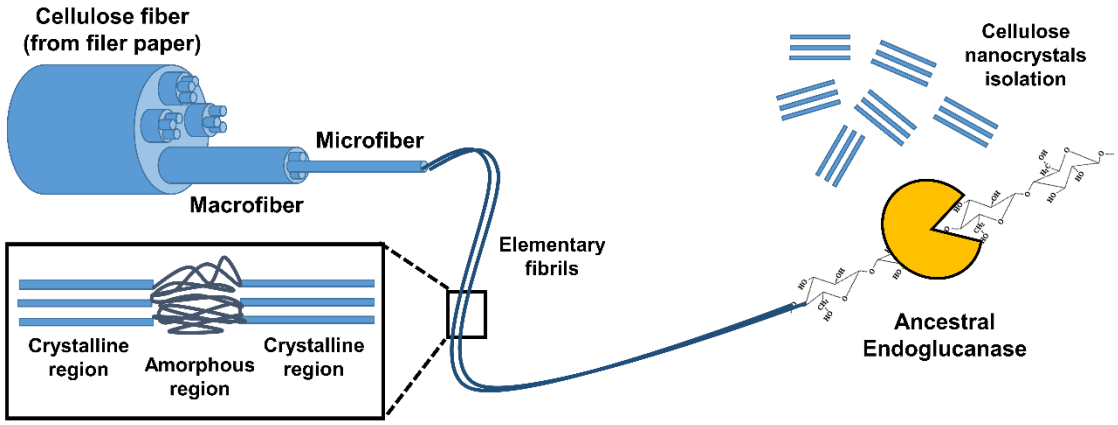

Figure 3.6. *Schematic representation of ancestral endoglucanase performance: CNCs isolation from cellulosic filter paper by means of β-1,4-glycosidic bonds breakdown.*

To perform the enzymatic hydrolysis of the cellulose from the filter paper, the endoglucanase protein had to be expressed and purified following a protocol developed in previous work [21]. In brief, the reconstructed sequence of the ancient endoglucanase contained in a plasmid expression vector (pQE-80L) was expressed using *E.coli* BL21 as a bacterial host. The BL21 bacteria were transformed with the pQE-80L plasmid and then plated in a Luria-Bertani (LB) plate with carbenicillin. After overnight incubation of the plate at 37 ºC, 3-4 colonies were collected to make an inoculum in LB medium with carbenicillin and chloramphenicol. The transformed BL21 bacterial culture was incubated overnight at 37 ºC with gently agitation and isopropyl β-D-1-thiogalactopyranoside (IPTG) compound was added for induction of plasmid overexpression into the bacteria.

The enzyme purification process is summarized in **Figure 3.7 A**. The culture of transformed BL21 bacteria was centrifuged and the bacterial pellet was washed with extraction buffer. Then, the bacteria were lysed by lysozyme incubation and ultrasonication during 15-20 min. The residual parts of the bacteria were eliminated by

ultracentrifugation and the supernatant was incubated at 50 ºC in order to precipitate the no thermostable proteins that were then removed by centrifugation. The protein solution containing the endoglucanase was incubated with a HisTrap cobalt affinity resin that was able to join specifically with a histidine chain residue present in the endoglucanase sequence to facilitate the purification of this protein specifically. The unspecific proteins that were not joined to the cobalt column resin were removed by washing and centrifugation. Finally, the endoglucanase was extracted from the HisTrap cobalt column with the aid of a specific elution buffer containing imidazole. The final concentration of the enzyme was measured using a NanoDrop 2000 spectrophotometer and then stored at 4 ºC.

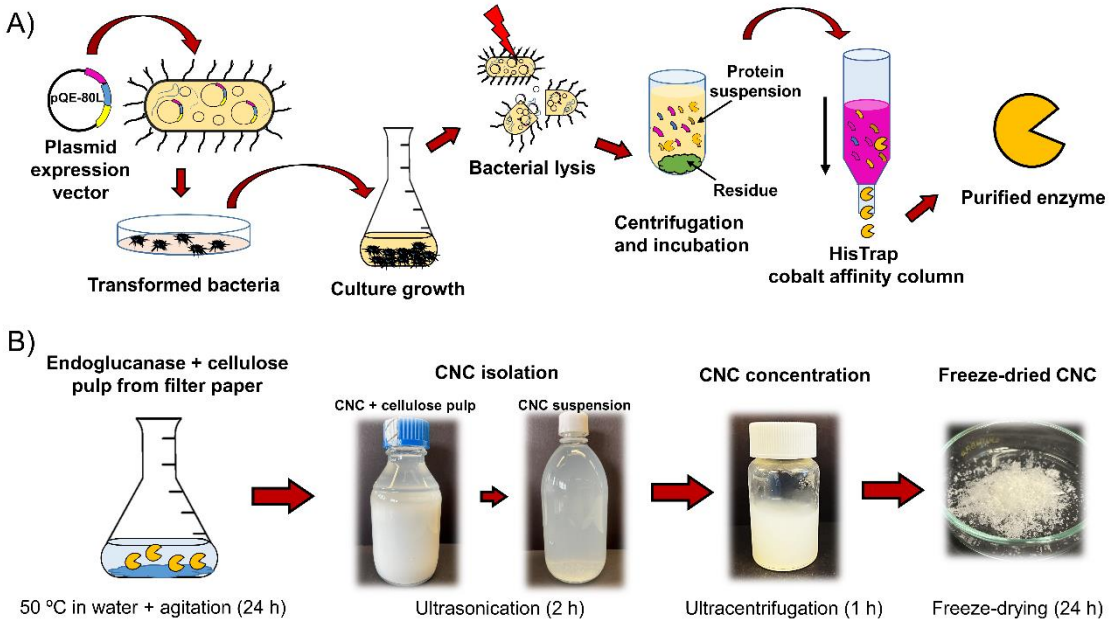

***Figure 3.7**. Schematic representation of A) bacterial transformation with pQE-80L expression plasmid and endoglucanase purification process and B) enzymatic hydrolysis of filter paper and CNCs extraction process.*

Once the endoglucanase enzyme was isolated, the hydrolysis process of the cellulose was carried out (**Figure 3.7 B**). Filter paper composed by 100 % cellulose fibers was cut and smashed in water in a proportion of 4 wt. %, until a cellulose paste was obtained. Then, the purified endoglucanase was added to the cellulose pulp in a proportion of 5 mg of enzyme per gram of substrate and it was incubated at 50 ºC during 24 h with gently stirring. After the hydrolysis process of the cellulose, the reaction was stopped by ultrasonicating the CNCs and cellulose pulp mixture during 2 hours at 30 % of amplitude. The obtained CNCs in water after the sonication process were ultracentrifuged at 33000 G during 1 h to obtain a CNCs slurry that were freeze-dried or directly stored after solid

content quantification. The measured solid content of the slurry was estimated at 9.60 ± 0.05 wt. %.

3.5.2. CNCs characterization

The obtained EnCNC obtained through the above mentioned method were widely characterized in previous work [21]. In this study, a brief morphological, physicochemical and thermal characterization was performed.

Morphological characteristics and dimensions of EnCNC were determined by AFM. In **Figure 3.8 A,** height and phase images of EnCNC can be observed, showing 540 ± 450 nm length and diameters around 21 ± 10 nm, in accordance with CNCs sizes observed in previous morphological characterizations [21].

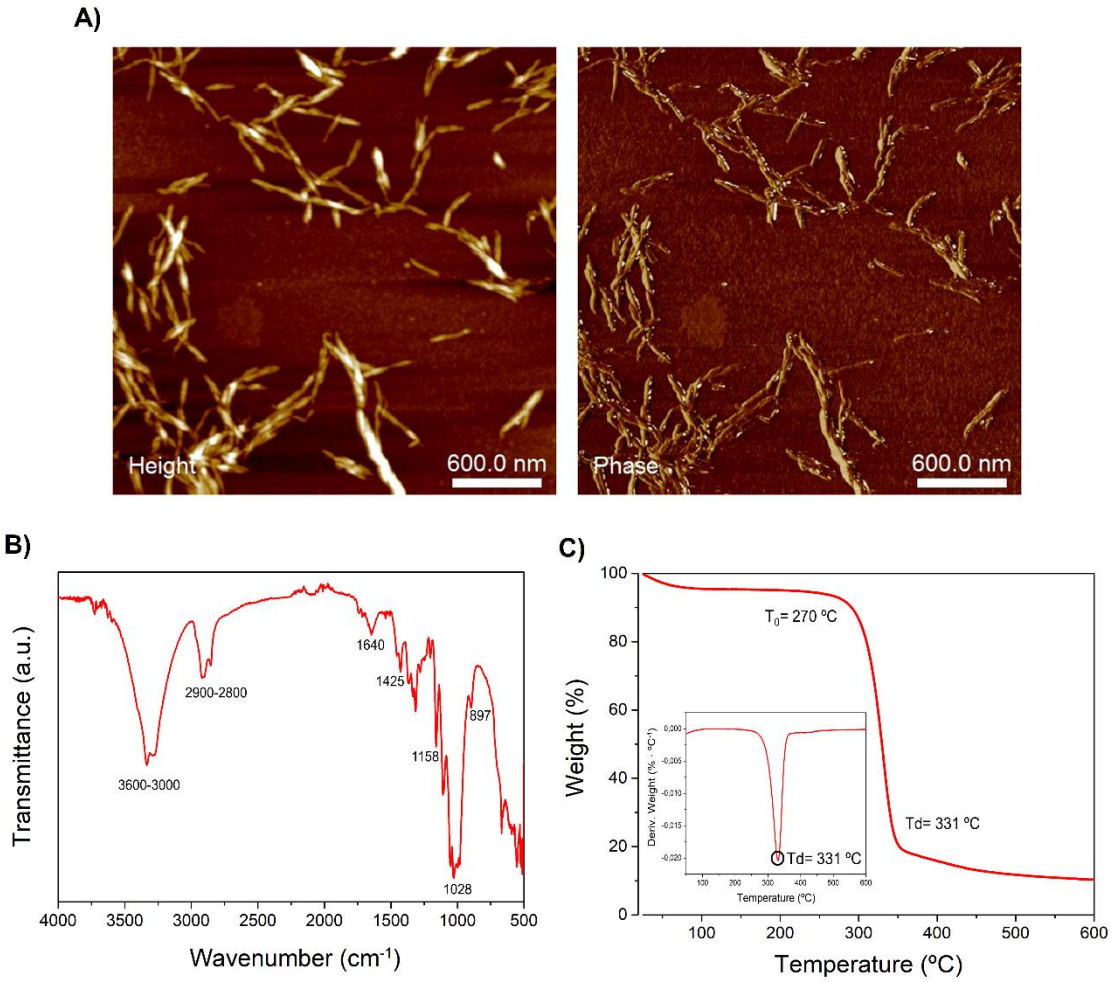

Figure 3.8. *A) AFM height and phase images (3x3 µm) B) FTIR spectrum and C) TGA results of EnCNCs.*

As can be observed in **Figure 3.8 B**, the FTIR analysis revealed that EnCNC presented a typical cellulose pattern, similar to that previously observed for CNF. A broad band from 3600 cm^{-1} to 3000 cm^{-1} is shown and corresponded to –OH vibration. Another broad band from 2900 to 2800 cm^{-1} was observed and attributed to C-H stretching vibration. At 1640 cm^{-1} a band related to the absorbed water was observed, and at 1425 cm^{-1} a band corresponding to C-H bending. The bands located at 1158 and 1028 cm^{-1} corresponded to C–O–C and C–O stretching vibrations, respectively. The band at 897 cm^{-1} was attributed to the β-glycosidic bond [17,23]. The spectrum is similar to those observed in previous studies [21].

Thermal characteristics of EnCNC were determined. TGA analysis curves shown in **Figure 3.8 C** also presented similar characteristics observed in TGA analysis of CNF. In this case, the T_0 is located at 270 ºC due to the higher crystallinity [21] if it is compared to CNF [24]. The degradation temperature (Td) observed in the first derivative curve is stablished at 331 ºC.

3.6. Conclusions

In this chapter, commercial alginate, WBPU dispersion and CNFs have been characterized. These materials will be used afterwards in this thesis work for the development of the bioinks and biomaterial inks.

An alginate film was prepared by solvent casting, and physicochemical characterization showed the typical structure of alginate biopolymers with a majority of M units, whereas mechanical tensile tests indicated high stiffness and strength at break of this material.

WBPU dispersion presented high particle stability maintained over time as well as pH values in the range of physiological human body. A solvent casted film was prepared, obtaining a transparent and flexible material. Physicochemical analysis revealed that the structure of this WBPU corresponded to an anionic aliphatic polyester-polyurethane dispersion, while mechanical tensile tests showed low stiffness and strength and high values of strain at break characteristics of a material with high flexibility. Cytotoxicity tests showed cell viability rates above 70 % after 3 days of incubation and thus, suitability for biomedical applications.

Regarding the freeze-dried CNFs, morphological characterization revealed fiber sizes of several micrometers in length and diameters in nanometer scale. Physicochemical analysis performed by FTIR, ^{13}C NMR and XRD confirmed the typical structure of cellulose biopolymer.

The obtaining process of EnCNCs was carried out firstly by means of the purification of an ancestral endoglucanase. Thereafter, second step consisted in the hydrolysis of cellulose filter paper by the enzyme, followed by the CNCs isolation and finally CNCs concentration. Morphological analysis revealed that the obtained CNCs were located in nanometer scale and physicochemical and thermal analyses confirmed the characteristics of cellulose structure

3.7. References

[1] Pamies R, Schmidt RR, Lopez-Martínez MC, Torre JG. The influence of mono and divalent cations on dilute and non-dilute aqueous solutions of sodium alginates. Carbohydr Polym 2010;80:248–253. https://doi.org/10.1016/j.carbpol.2009.11.020.

[2] Ramos PE, Silva P, Alario MM, Pastrana LM, Teixeira JA, Cerqueira MA, Vicente AA. Effect of alginate molecular weight and M/G ratio in beads properties foreseeing the protection of probiotics. Food Hydrocoll 2018;77:8–16. https://doi.org/10.1016/j.foodhyd.2017.08.031.

[3] Daemi H, Barikani M. Synthesis and characterization of calcium alginate nanoparticles, sodium homopolymannuronate salt and its calcium nanoparticles. Sci Iran 2012;19:2023–2028. https://doi.org/10.1016/j.scient.2012.10.005.

[4] Sarmento B, Ferreira D, Veiga F, Ribeiro A. Characterization of insulin-loaded alginate nanoparticles produced by ionotropic pre-gelation through DSC and FTIR studies. Carbohydr Polym 2006;66:1–7. https://doi.org/10.1016/j.carbpol.2006.02.008.

[5] Siddaramaiah, T. M. Mruthyunjaya Swamy, B. Ramaraj J, Lee JH. Sodium alginate and its blends with starch: Thermal and morphological properties. J Appl Polym Sci 2008;109:4075-4081. https://doi.org/10.1002/app.28625.

[6] Rhim JW. Physical and mechanical properties of water resistant sodium alginate films. Food Sci Technol 2004;37:323–330. https://doi.org/10.1016/j.lwt.2003.09.008.

[7] Santamaria-Echart A, Arbelaiz A, Saralegi A, Fernández-d'Arlas B, Eceiza A, Corcuera MA. Relationship between reagents molar ratio and dispersion stability and film properties of waterborne polyurethanes. Colloids Surfaces A Physicochem Eng Asp 2015;482:554–561. https://doi.org/10.1016/j.colsurfa.2015.07.012.

[8] Santamaria-Echart A, Fernandes I, Ugarte L, Barreiro F, Arbelaiz A, Corcuera MA, Eceiza A. Waterborne polyurethane-urea dispersion with chain extension step in homogeneous medium reinforced with cellulose nanocrystals. Compos Part B Eng 2018;137:31–38. https://doi.org/10.1016/j.compositesb.2017.11.004.

[9] Rahman MM. Stability and properties of waterborne polyurethane/clay nanocomposite dispersions. J Coatings Technol Res 2017;14:1357–1368.

https://doi.org/10.1007/s11998-017-9944-3.

[10] Proksch E. pH in nature, humans and skin. J Dermatol 2018;45:1044–1052. https://doi.org/10.1111/1346-8138.14489.

[11] Feng Z, Wang D, Zheng Y, Zhao L, Xu T, Guo Z, Hussain MI, Zeng J, Lou L, Sun Y, Jiang H. A novel waterborne polyurethane with biodegradability and high flexibility for 3D printing. Biofabrication 2020;12:1-33. https://doi.org/10.1088/1758-5090/ab7de0.

[12] Najafi F, Manouchehri F, Shaabanzadeh M. Synthesis and characterization of anionic polyester-polyurethane dispersion as environmentally-friendly water based resins. J Chem Heal Risks 2011;1:23–26.

[13] Urbina L, Alonso-Varona A, Saralegi A, Palomares T, Eceiza A, Corcuera MÁ, Retegi A. Hybrid and biocompatible cellulose/polyurethane nanocomposites with water-activated shape memory properties. Carbohydr Polym 2019;216:86–96. https://doi.org/10.1016/j.carbpol.2019.04.010.

[14] Hormaiztegui ME V., Daga B, Aranguren MI, Mucci V. Bio-based waterborne polyurethanes reinforced with cellulose nanocrystals as coating films. Prog Org Coatings 2020;144:105649-105671. https://doi.org/10.1016/j.porgcoat.2020.105649.

[15] Larraza I, Vadillo J, Santamaria-Echart A, Tejado A, Azpeitia M, Vesga E, Orue A, Saralegi A, Arbelaiz A, Eceiza A. The effect of the carboxylation degree on cellulose nanofibers and waterborne polyurethane/cellulose nanofiber nanocomposites properties. Polym Degrad Stab 2020;173:109084-109098. https://doi.org/10.1016/j.polymdegradstab.2020.109084.

[16] Li VCF, Dunn CK, Zhang Z, Deng Y, Qi HJ. Direct ink write (DIW) 3D printed cellulose nanocrystal aerogel structures. Sci Rep 2017;7:1–8. https://doi.org/10.1038/s41598-017-07771-y.

[17] Thiripura Sundari M, Ramesh A. Isolation and characterization of cellulose nanofibers from the aquatic weed water hyacinth - Eichhornia crassipes. Carbohydr Polym 2012;87:1701–1705. https://doi.org/10.1016/j.carbpol.2011.09.076.

[18] Gong J, Li J, Xu J, Xiang Z, Mo L. Research on cellulose nanocrystals produced from cellulose sources with various polymorphs. RSC Adv 2017;7:33486–33493. https://doi.org/10.1039/c7ra06222b.

[19] Perez-Jimenez R, Inglés-Prieto A, Zhao ZM, Sanchez-Romero I, Alegre-Cebollada J, Kosuri P, Garcia-Manyes S, Kappock TJ, Tanokura M, Holmgren A, Sanchez-Ruiz JM, Gaucher EA, Fernandez JM. Single-molecule paleoenzymology probes the chemistry of resurrected enzymes. Nat Struct Mol Biol 2011;18:592–596. https://doi.org/10.1038/nsmb.2020.

[20] Manteca A, Schönfelder J, Alonso-Caballero A, Fertin MJ, Barruetabeña N, Faria BF, Herrero-Galan E, Alegre-Cebollada J, Sancho D, Perez-Jimenez R. Mechanochemical evolution of the giant muscle protein titin as inferred from resurrected proteins. Nat Struct Mol Biol 2017;24:652–657.

https://doi.org/10.1038/nsmb.3426.

[21] Alonso-Lerma B, Barandiaran L, Ugarte L, Larraza I, Reifs A, Olmos-Juste R, Barruetabeña N, Amenabar I, Hillenbrand R, Eceiza A, Perez-Jimenez R. High performance crystalline nanocellulose using an ancestral endoglucanase. Commun Mater 2020;1:1-10. https://doi.org/10.1038/s43246-020-00055-5.

[22] Risso VA, Gavira JA, Mejia-Carmona DF, Gaucher EA, Sanchez-Ruiz JM. Hyperstability and substrate promiscuity in laboratory resurrections of precambrian β-lactamases. J Am Chem Soc 2013;135:2899–2902. https://doi.org/10.1021/ja311630a.

[23] Li M, Wang LJ, Li D, Cheng YL, Adhikari B. Preparation and characterization of cellulose nanofibers from de-pectinated sugar beet pulp. Carbohydr Polym 2014;102:136–143. https://doi.org/10.1016/j.carbpol.2013.11.021.

[24] Ghetti P, Ricca L, Angelini L. Thermal analysis of biomass and corresponding pyrolysis products. Fuel 1996;75:565–573. https://doi.org/10.1016/0016-2361(95)

Chapter 4

Single-component inks for 3D printing and its biomedical applications

CHAPTER 4 - Single-component inks for 3D printing and its biomedical applications

4. Single-component inks for 3D printing and its biomedical applications

4.1. Aim of the chapter

The aim of this chapter is the development of monocomponent inks with suitable characteristics for 3D printing technology, without the necessity of rheological modifiers such as nanoentities or biomaterials blending. Alginate is a biopolymer widely employed for extrusion 3D printing, despite neat alginate aqueous suspensions are not able to retain a desired 3D shape. As it was explained in chapter 1, this biopolymer can form ionic crosslinking between their carboxylic groups and divalent cations such as Ca^{2+} or Mg^{2+}, obtaining hydrogels that present a strong and moldable gel-like structure. In this study, alginate at 4 wt. % in water was selected to prepare different hydrogel based inks with different gelation degrees by means of Ca^{2+} crosslinking. Besides, the obtained inks were fully characterized for their use in extrusion 3D printing.

Moreover, biomaterial ink formulations based on the EnCNC obtained as described in the previous chapter were also developed. Nanocellulose is a biopolymer commonly used in 3D printing as rheological modifier with the purpose of optimizing the viscoelasticity and shear-thinning properties. CNC-based inks are usually blended with other polymeric matrices or crosslinked with different agents, but sometimes those crosslinking molecules are cytotoxic, compromising the biocompatibility of the cellulosic material. However, CNC inks can present suitable conditions for 3D printing at high solid contents as it has been demonstrated in the literature [1]. Therefore, the objective of this section was to optimize the proper solid content of EnCNC suspended in water needed to be correctly 3D printed showing shape fidelity, without the need for other polymeric blends. The preparation and characterization of all biomaterial inks are well described in this chapter. Rheological characterization and printability evaluation were carried out.

On the other hand, the obtained single-component printed samples were processed by freeze-drying technique. The scaffolds were morphological and mechanical characterized, and finally, their capacity for drug release was assessed and preliminary cell proliferation experiments were performed.

4.2. Alginate-Ca^{2+} (A-Ca) and EnCNC inks preparation

In order to prepare the A-Ca biomaterial inks, the alginate powder fully characterized in Chapter 3 was dissolved at 4 wt. % in water mixing with a mechanical stirrer until a homogeneous suspension was achieved. As explained in the introduction section, sodium alginate can crosslink with Ca^{2+} ions to form a gel-like network, and therefore,

for the development of A-Ca biomaterial inks, the theoretical maximum amount of this crosslinking was calculated. The molecular weight of the alginate was analyzed in chapter 3, and from this result ($2.4x10^5$ g·mol^{-1}) and the molar weight of the COO^- molecules (175 g·mol^{-1}), the total weight of carboxylic groups present in the alginate was calculated. Then, the total amount of $CaCl_2$ molecules needed to fully crosslink a specific amount of alginate was determined, considering a molar relation of 1:2 among the Ca^{2+} ions and COO^- groups for each alginate subunit.

The total crosslinking of alginate resulted in a stiff material with solid-like characteristics that was not possible to be extruded through a nozzle. Therefore, less crosslinking degree was established in order to obtain gel-like biomaterial inks with desirable characteristics for 3D printing. The crosslinking degree chosen for these ink formulations were 5, 10 and 20 % in respect of the total amount of $CaCl_2$ needed (**Table 4.1**). The specific amount of $CaCl_2$ required in each formulation was prepared in 0.2 mL of water and then added to the 4 wt. % alginate solution. The A-Ca blends were mixed by mechanical stirring until homogenization.

Table 4.1. *Solid contents and crosslinking percentage of A-Ca and EnCNC biomaterial ink formulations.*

Biomaterial ink formulation	**Alginate (wt. %)**	**Ca^{2+} crosslinking (%)**	**EnCNC (wt. %)**
A4	4	0	-
A4-Ca5	4	5	-
A4-Ca10	4	10	-
A4-Ca20	4	20	-
EnCNC6	-	-	6
EnCNC10	-	-	10

The crosslinking degree of the developed Alginate/Ca^{2+} inks was assessed by DSC analysis, which highlighting the impact of Ca^{2+} as a crosslinking agent (**Figure 4.1**). The alginate curve showed a large endothermic band from 75 to 125 ºC, which is related to the presence of bonded water, followed by an exothermic peak at 244 ºC corresponding to the degradation of this polymer [2]. The alginate-Ca^{2+} crosslinked network led to a slight shift of the degradation exothermic peak from 244 ºC (neat alginate) to 257 ºC for A4-Ca20 ink, indicating an increased resistance to thermal degradation of A-Ca based formulations as the gelation degree increased. These thermograms showed that the heat

needed for the breakage of calcium–carboxylate bonds in the formed hydrogel structure was dependent on the gelation degree, indicating that larger amount of physical unions are formed as the Ca^{2+} content increased in the ink formulations [3].

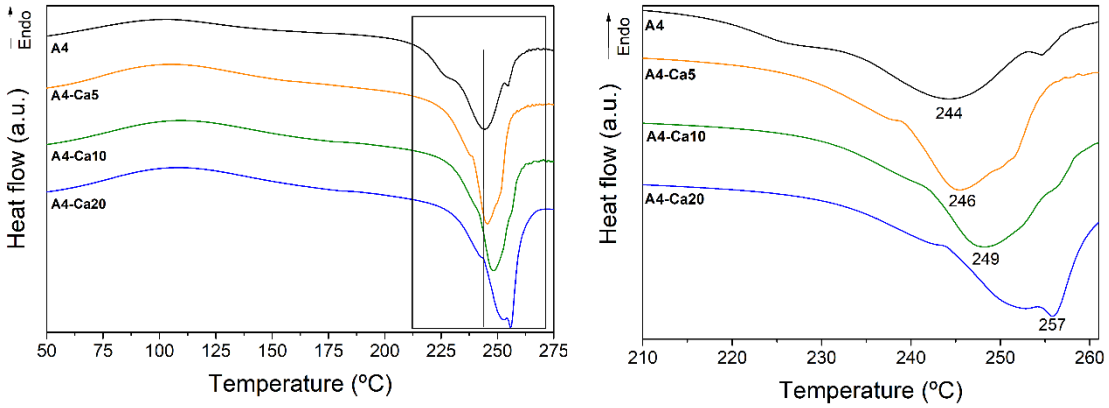

Figure 4.1. *DSC curves of neat alginate (A4) and A-Ca based biomaterial inks.*

Besides, the obtaining process and the characterization of EnCNC were described in Chapter 3. From the freeze-dried EnCNC pellets, 6 and 10 wt. % water-based EnCNC formulations were mixed and homogenized by sonication in a bath during 2 hours. These data are collected in **Table 4.1**.

4.3. Rheological characterization of A-Ca and EnCNC inks

Neat alginate 4 wt. % solution (A4) and the developed A-Ca and EnCNC biomaterial ink formulations were rheologically characterized in order to overview their potential for 3D printing.

Flow viscosity assays were performed and the results are shown in **Figure 4.2**. For A-Ca based formulations (**Figure 4.2 A**), shear-thinning behavior as well as high viscosity values at low shear rates were observed, demonstrating strong dependence of viscosity on shear rate changes, which are typical from non-Newtonian fluids [4,5]. Nevertheless, low viscosity values of 100 Pa·s at low shear rate were observed for A4, indicating that neat alginate solution presented more fluid-like characteristics than the crosslinked ones. On the contrary, the viscosity values of A-Ca biomaterial inks at low shear rates increased as the crosslinking degree increased in the formulations (**Table 4.2**). The non-Newtonian behavior of the A-Ca based formulations could be demonstrated by adjusting the experimental results to a power-law model (Eq. 3). Obtained data are collected in **Table 4.2.** Power-law index (n) values of 0.11 and 0.21 were calculated for A4-Ca20 and A4-Ca10, respectively. These values indicated non-Newtonian shear-thinning behavior

since these values are closer to 0, while the n values for A4 and A4-Ca5 formulation were 0.58 and 0.40 demonstrating that these formulations presented closer behavior of Newtonian fluids with less viscosity changes with the increase of shear rate. Consistency coefficient (K) raised as the Ca^{2+} crosslinking percentage increased (from 73.47 $Pa{\cdot}s^n$ for A4 solution to 683.97 $Pa{\cdot}s^n$ for A4-Ca20), and Pearson correlation coefficient (R^2) showed strong relationship among the experimental results and the theoretical power-law model ($R^2 > 0.96$ for all cases).

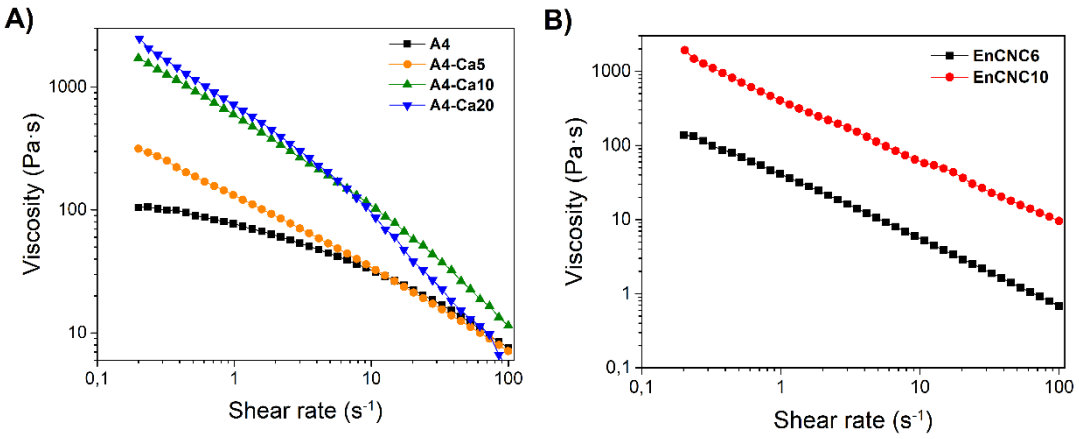

Figure 4.2. *Flow viscosity versus shear rate curves. A) Viscosity curves of A4-Ca based formulations and B) Viscosity curves of EnCNC6 and EnCNC10 biomaterial ink formulations.*

Table 4.2. *Viscosity measured at 0.2 s^{-1}, power-law index (n), consistency coefficient (K), Pearson correlation coefficient (R^2), recovery percentage after 20 seconds and after 60 seconds.*

Biomaterial ink	Viscosity (Pa·s)	n	K ($Pa{\cdot}s^n$)	R^2	Recovery after 20 sec. (%)	Recovery after 60 sec. (%)
A4	112 ± 8	0.58	73.47	0.96	89 ± 4	95 ± 2
A4-Ca5	299 ± 22	0.40	121.07	0.99	76 ± 3	83 ± 2
A4-Ca10	1745 ± 60	0.21	581.48	0.99	87 ± 2	87 ± 2
A4-Ca20	2068 ± 359	0.11	683.97	0.98	84 ± 3	85 ± 3
EnCNC6	129 ± 25	0.17	39.59	0.99	70 ± 3	73 ± 2
EnCNC10	2372 ± 417	0.15	618.94	0.99	74 ± 2	77 ± 4

The evolution of viscosity with increasing shear rate of EnCNC6 and EnCNC10 ink formulations are shown in **Figure 4.2 B**. Both formulations showed shear-thinning and non-Newtonian behavior, as it could be demonstrated by the comparison with the

theoretical power-law model (**Table 4.2**). For these nanocellulose-based formulations, power-law index showed low values (0.17 and 0.15) indicating strong shear-thinning behavior. However, K coefficient and viscosity at low shear rate (0.2 s^{-1}) of EnCNC6 showed values of 39.59 $Pa \cdot s^n$ and 129 ± 25 Pa·s, respectively, which are much lower if compared to the 360 $Pa \cdot s^n$ and $4 \cdot 10^3$ Pa·s values reported in the literature for printable materials [5,6]. Nevertheless, EnCNC10 presented viscosity values of 2372 ± 417 Pa·s at low shear rate of 0.2 s^{-1} and K value of 618.94 $Pa \cdot s^n$, stablished within a suitable printability window [6].

Shape recovery tests were carried out in order to simulate printing conditions, and the calculated recovery results are collected in **Table 4.2**, while the graphical representations are shown in **Figure 4.3**. The percentages of viscosity recovery for A4-Ca formulations after 20 seconds of applying a high shear rate stage were between 76 and 89 % for all biomaterial inks, while after 60 seconds the percentage increased as the crosslinking degree decreased.

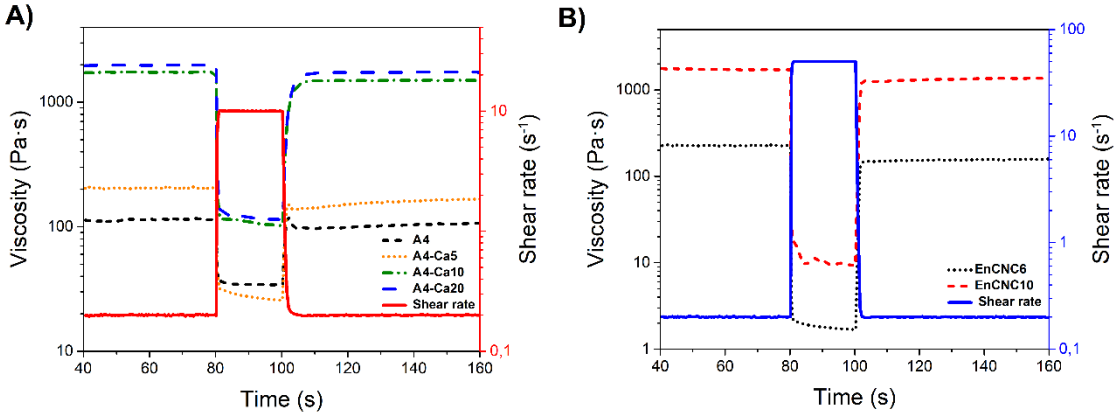

Figure 4.3. *Shape recovery experiments. A) Viscosity values at different shear rate applications of A4-Ca based biomaterial ink formulations. B) Viscosity values at different shear rate application of EnCNC based inks.*

This behavior suggest that the higher crosslinking degree the faster viscosity recovery after removal of the high shear rate. Regarding EnCNC based inks, it can be observed a viscosity recovery increase of 2 % for both formulations among 20 and 60 seconds after stopping the high shear rate application.

Oscillatory tests were also performed to study the viscoelastic characteristics of the developed A4-Ca and EnCNC based inks. The evolution of G' and G'' with an increase of shear stress is represented in **Figure 4.4**. A4 biomaterial ink always showed G'' above G', indicating liquid-like behavior and predominance of viscous characteristics (**Figure 4.4 A**). Nevertheless, in A4-Ca crosslinked formulations, G' was always above G'' in the

LVR, predominating the elastic behavior and gel-like structure. As it is well known, G' values in LVR represents the resistance of a material to be elastically deformed and thus, the presence of elastic behavior and the mechanical strength [4,7]. In **Figure 4.4 B**, EnCNC6 and EnCNC10 ink formulations showed G' over G'' indicating gel-like behavior and elasticity. The G' values of the different formulations in LVR could be correlated to shape fidelity of the printing materials [8].

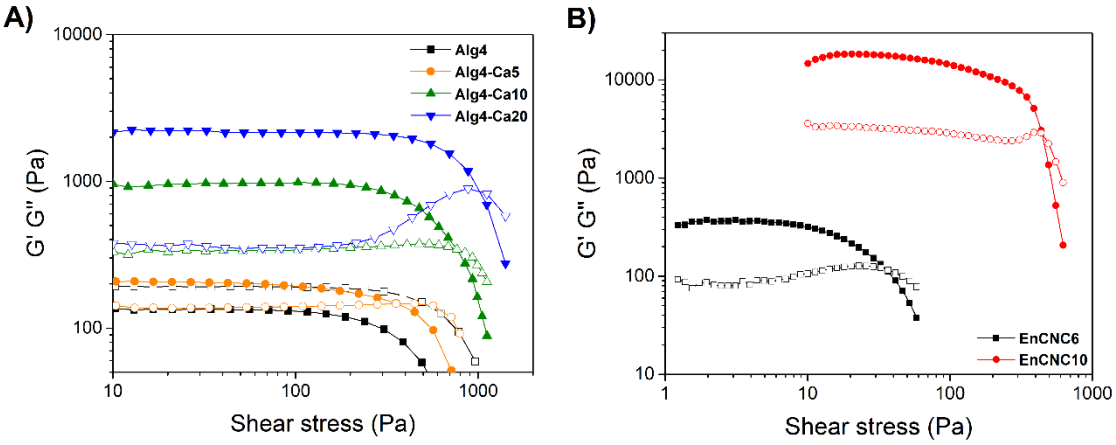

Figure 4.4. *Storage modulus (solid symbols) and loss modulus (open symbols) versus shear stress of A) A4-Ca based biomaterial inks and B) EnCNC based biomaterial inks.*

In **Table 4.3**, the G' values for all developed formulations in LVR (plateau zone) are collected. In the literature, G' values from 600 to 4000 Pa are related to shape fidelity of the printed materials [8,9], therefore the observed G' values of A4-Ca10 (1521 Pa) and A4-Ca20 (2209 Pa) suggested that the 3D printed samples will retain the designed shape. On the other hand, A4-Ca5 and A4 formulations presented G' values below 600 Pa, suggesting that the printed shape of these biomaterial inks would not be maintained. As the shear stress increased, the G' values drop below G'', reaching a viscous and liquid-like behavior at high shear stress rates [11].

As explained in Chapter 1, the stress value at which G' value drops leaving the LVR is known as yield stress and it is related to the required minimum pressure to start the extrusion of the inks [12]. From this value, the interactions between molecules start to break. Furthermore, the crossover between G' and G'', is known as yield point and it is commonly related to the necessary shear stress value to extrude the material through a nozzle during 3D printing process [4]. Therefore, the storage modulus value in LVR, yield stress and yield point values enable the establishment of printing pressure ranges for a specific material [12,13]. In this case, the values increased as the Ca^{2+} crosslinking degree raised in the A4-Ca biomaterial inks and thus, the required printing pressure range to extrude the developed formulations.

Table 4.3. *G' in the LVR, yield stress, yield point and tan δ values at 1 Hz of the A4-Ca based formulations and EnCNC based inks.*

Biomaterial ink	G' in LVR (Pa)	Yield stress (Pa)	Yield point (Pa)	Tan δ (1 Hz)
A4	140 ± 8	-	-	1.32 ± 0.04
A4-Ca5	201 ± 4	146 ± 11	312 ± 73	0.53 ± 0.01
A4-Ca10	1522 ± 585	270 ± 145	795 ± 107	0.37 ± 0.01
A4-Ca20	2209 ± 127	333 ± 36	983 ± 53	0.23 ± 0.01
EnCNC6	293 ± 70	9 ± 3	42 ± 8	0.35 ± 0.02
EnCNC10	21180 ± 3363	71 ± 3	495 ± 51	0.070 ± 0.001

Regarding the EnCNC based ink formulations, G' of EnCNC6 in LVR showed a value of 293 Pa, which is lower than the mentioned value of 600 Pa reported in the literature [1,8] and therefore, EnCNC6 would not present shape fidelity. However, the EnCNC10 ink showed a higher G' value of 21180 ± 3363 Pa, suitable to maintain the desired shape after printing, and in the range of 10^4 Pa reported for 20 wt. % CNC inks [1]. This behavior could be explained by the shape and size of these enzymatic CNCs discussed in the previous chapter, which allowed enough flexibility under shear stress and stiffness in relaxing condition. Moreover, with an increment of 4 % in the solid content of enzymatic CNCs, the solid-like behavior and viscoelasticity increased significantly under low-pressure conditions. The yield stress and yield point values denoted that the hydrogen bond interactions among CNCs and water molecules are more labile than ionic ones and thus, the alignment of CNCs would occur at 3D printing process [1,14]. The biomaterial ink based on 10 wt. % of enzymatic nanocellulose presented similar rheological characteristics than other CNC biomaterial inks with double solid content reported in the literature [1].

In **Figure 4.5 A**, frequency sweep tests for A4-Ca and EnCNC based inks are presented. In general, G' and G'' presented frequency dependency and the two moduli increased as the oscillation frequency raised. Furthermore, it is known that the larger difference between G' and G'' values indicates highly organized gel-like structure, as it was the case for A4-Ca based biomaterial inks as the gelation degree increased [15,16]. In the case of EnCNC10 biomaterial ink, high G' and G'' values were observed indicating solid-like behavior and stiffness. Similar values of G' and G'' or G'' above G' indicate poor

elastic behavior and weakly organized network structure of the material [10,17] as it was observed for A4 solution.

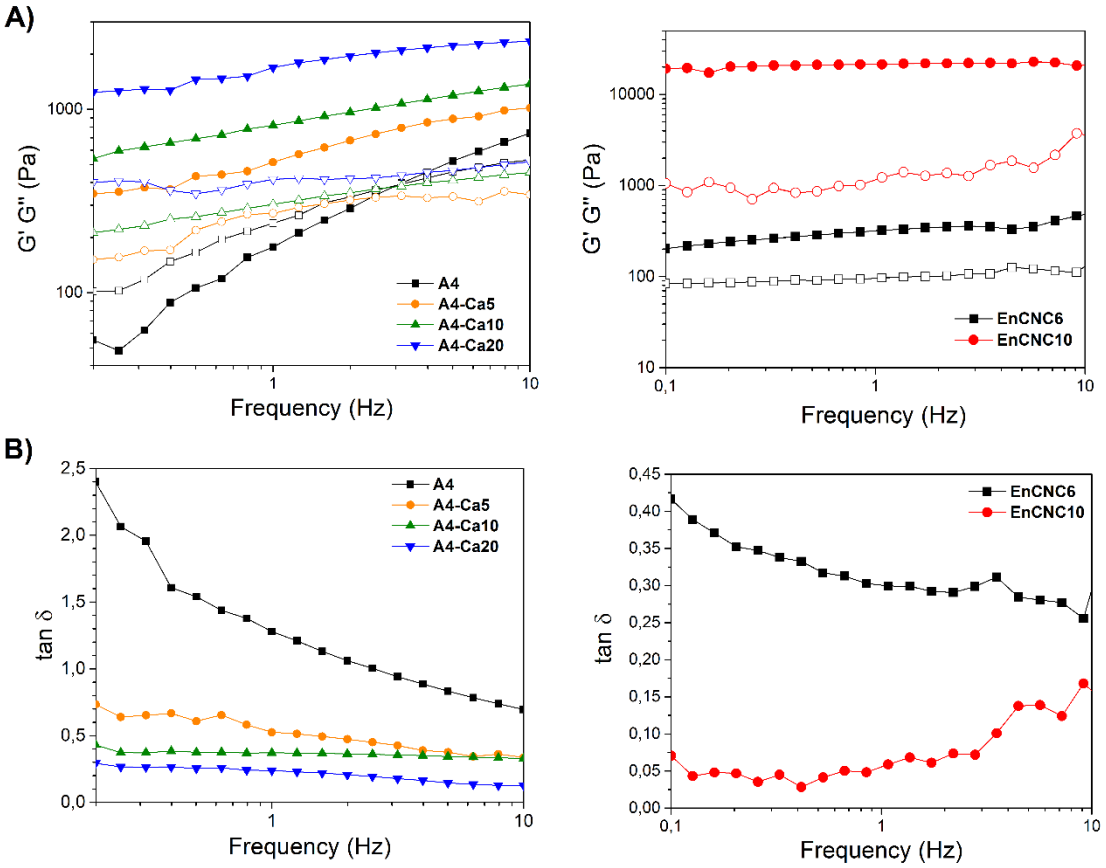

Figure 4.5. *A) Frequency sweep test of A4-Ca based inks (left) and EnCNC based inks (right). B) Tan δ values as a function of frequency sweep test of A4-Ca based inks (left) and EnCNC based inks (right).*

For an ideal 3D printing performance, inks also need a good solid-liquid balance to retain the desired structure, with proper interconnection between layers and correct shape fidelity. The ratio between G'' and G' (G''/G') is known as tan δ, and can be correlated with shape strength and the highly organized internal network structure [18,19]. Tan δ versus frequency is represented in **Figure 4.5 B** and values at 1 Hz are collected in **Table 4.3**. It had been reported that tan δ values close to 0 indicated strong solid-like behavior, and values close to 1 represent liquid-like behavior [10,18]. Values of A4 and A4-Ca5 were higher than 0.5 representing liquid-like behavior while A4-Ca10 and A4-Ca20 showed values between 0 and 0.5, indicating solid and elastic behavior. Moreover, tan δ values of the developed biomaterial inks can also be related to the different gelation degrees of alginate-Ca^{2+}. Tan δ values between 0.25 and 0.45 are correlated with regular filament extrusion, structural integrity and shape fidelity after printing of alginate-based formulations, as it has been reported by Gao et al. [18]. Therefore, following this

tendency, A4-Ca10 ink would present smooth filament extrusion and shape fidelity, while A4 and A4-Ca5 would show structural collapse. A4-Ca20 biomaterial ink formulation will present irregular filament extrusion and, thus poor layer interconnection and low accuracy on shape reproduction. Regarding EnCNC6 and EnCNC10 inks, they presented tan δ values of 0.37 and 0.07, respectively, representing solid-like characteristics.

4.4. 3D printing of A-Ca and EnCNC biomaterial inks and scaffolds characterization

4.4.1. Printability test and 3D printing of A-Ca and EnCNC biomaterial inks

After rheological characterization, the printability of the developed inks was tested by means of the 3D printing of a mesh with a regular square shape. When biomaterial inks have ideal gelation conditions or ideal printing characteristics, the extruded filament will present a clear morphology with smooth surface and constant width in three dimensions, resulting in this case in a regular mesh with perfect square shape holes in the printed scaffolds [15].

Figure 4.6 A shows the results of the printability tests of A4-Ca based inks. It can be observed that A4 solution presented a total loss of the regular square shape after printing with the subsequent layers fusing each other, demonstrating liquid-like and under-gelation characteristics as it was previously observed in the rheological characterization. For A4-Ca5 biomaterial ink formulation, it was observed that the Pr value was 0.81 ± 0.02, expressing under-gelation conditions and liquid-like characteristics, as predicted in the rheological tests. As can be appreciated, the square shape of the printed mesh structure was not regular, indicating that this biomaterial ink formulation would not be able to retain the desired shape. In the case of A4-Ca10 biomaterial ink, Pr value was 0.95 ± 0.06 and, as it was observed in the literature, the Pr values in the range of 0.9 and 1.1 for alginate-based inks resulted in suitable gelation conditions [15], and thus A4-Ca10 biomaterial ink presented ideal printing conditions. For A4-Ca20 ink, the calculated Pr value was 1.40 ± 0.39, which indicated over-gelation conditions, irregular filament extrusion and poor interconnection between layers. According to this printability tests, the A4-Ca10 ink formulation presented ideal gelation conditions, correct printing performance and accuracy on shape reproduction, as previously predicted in the rheological characterization.

After the evaluation of printability, A4 showed an immediate structural collapse of the printed sample whereas A4-Ca5, A4-Ca10 and A4-Ca20 inks printed into cylinder shape

showed different shape retention degrees, following the tendency observed in rheological evaluation. However, only proper-gelled A4-Ca10 scaffolds demonstrated correct shape fidelity and accuracy on cylinder shape reproduction (**Figure 4.6 B**).

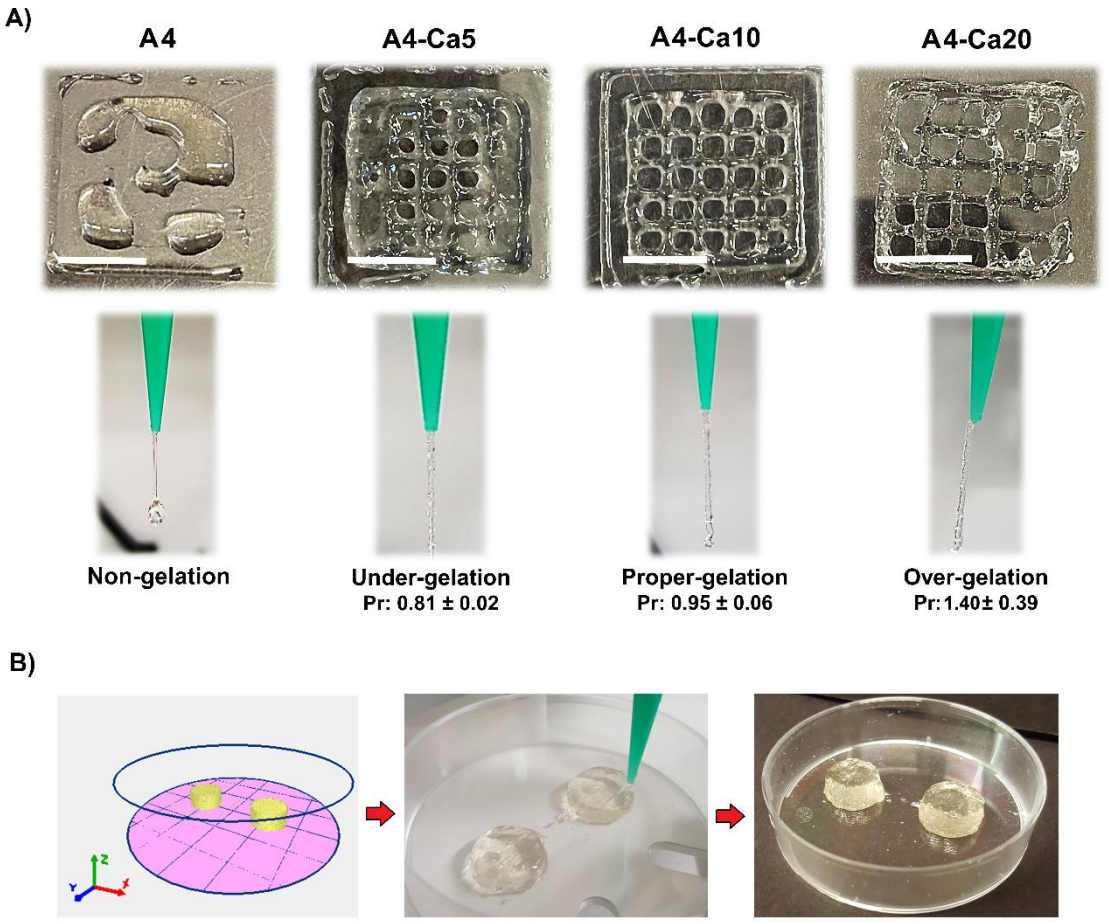

Figure 4.6. *A) Evaluation of the printability of the A4-Ca based biomaterial inks. White scale bar represents 20 mm. B) Cylinder CAD model and subsequent 3D printing of A4-Ca10 ink in a shape of 10 mm in diameter and 5 mm in height.*

The printability of EnCNC based inks was also assessed. As can be seen in **Figure 4.7 A** (upper), the EnCNC6 ink with a Pr value of 0.81 ± 0.04 showed poor accuracy in square shape reproduction and subsequently a tendency to fluid. The Pr value for the EnCNC10 ink was 0.93 ± 0.05, which translates to a suitable biomaterial ink that would retain the desired shape and a correct mesh reproduction in the case of EnCNC10 formulation. Dog bone pieces were 3D printed to evaluate shape fidelity of both ink formulations (**Figure 4.7 A**, down). As could be observed, EnCNC6 did not show proper shape fidelity and suitable printing conditions, thus confirming the results obtained in the rheological tests. In contrast, EnCNC10 dog bone pieces showed good printability and shape fidelity.

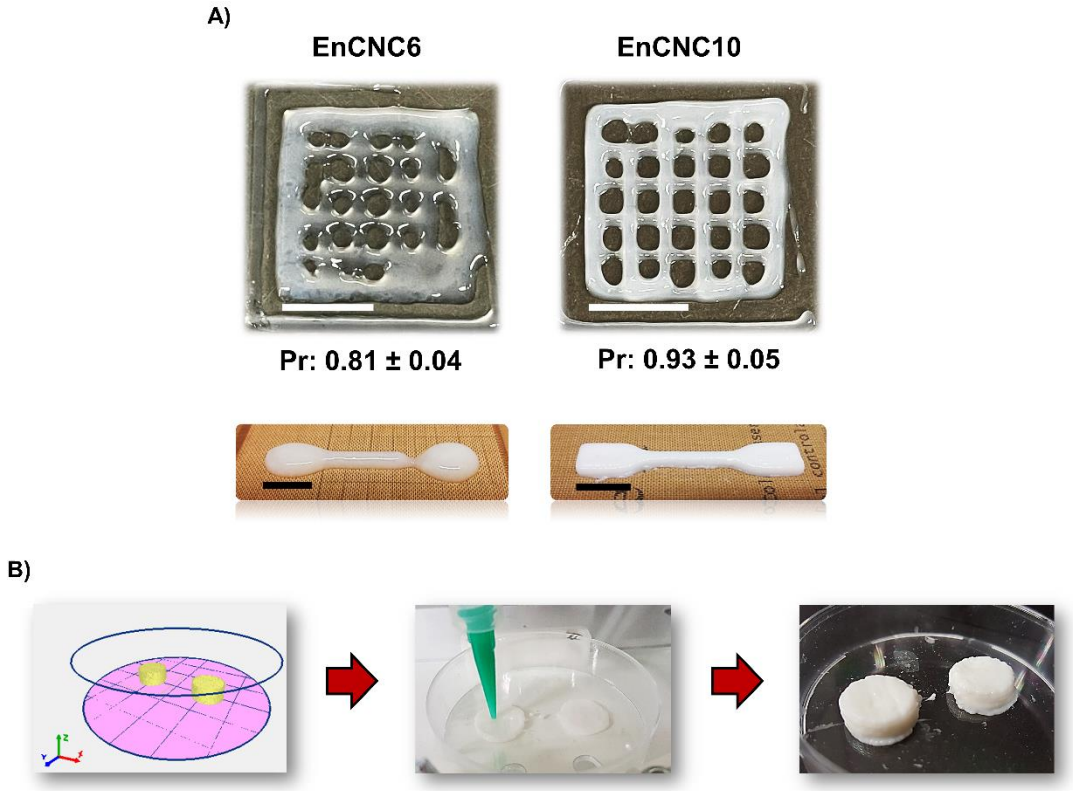

Figure 4.7. *A) Printability test of the EnCNC based inks (upper images) and 3D printed dog bone samples (bottom images). White scale bar represents 20 mm and black scale bar represents 10 mm. B) Cylinder CAD model and subsequent 3D printing of EnCNC10 ink in a cylinder shape of 10 mm in diameter and 5 mm in height.*

After the printability evaluation, it could be concluded that 10 wt.% of EnCNCs, was the minimum content required to obtain a biomaterial ink with suitable conditions for 3D printing technology. Siqueira et al. reported a minimum of 20 wt. % of acidic CNCs for a proper 3D printing performance [1,20]. The difference could be related to their different dimensions, namely, 540 ± 450 nm in length and 21 ± 10 nm in diameter the EnCNC,, and 120 nm in length and 6.5 nm in diameter acidic CNCs. Cylindrical scaffolds of EnCNC10 were 3D printed showing shape retention and accuracy on CAD model reproduction (**Figure 4.7 B**), without the aid of any matrix or any crosslinker.

4.4.2. Morphological characterization of A4-Ca based and EnCNC scaffolds

All cylindrical printed pieces from A4-Ca based inks and EnCNC10 ink were freeze-dried in order to eliminate water and retain the given shape. Freeze-drying consists on the elimination of water from the printed samples directly by sublimation, achieving scaffolds with a porous structure. The dimension and the amount of pores in the resulted structures are dependent on the water crystal size and thus, the larger water amount in the

formulation, the larger pore size on the scaffolds [21]. Consequently, the solid content and the water amount of the ink formulation will control the final porosity, increasing as the solid content decreases [22].

After freeze-drying, the obtained scaffolds were morphologically characterized. A4-Ca5, A4-Ca10 and A4-Ca20 scaffolds are shown in **Figure 4.8.** As can be appreciated, the appearance of the printed pieces corroborated the printability assessment in the three cases. A4-Ca5 showed structural collapse due to its under-gelation characteristics, whereas the over-gelation condition of the A4-Ca20 ink led to irregular final shaped forms. Finally, A4-Ca10 scaffolds showed proper shape fidelity and accuracy on the shape reproduction, as it was predicted.

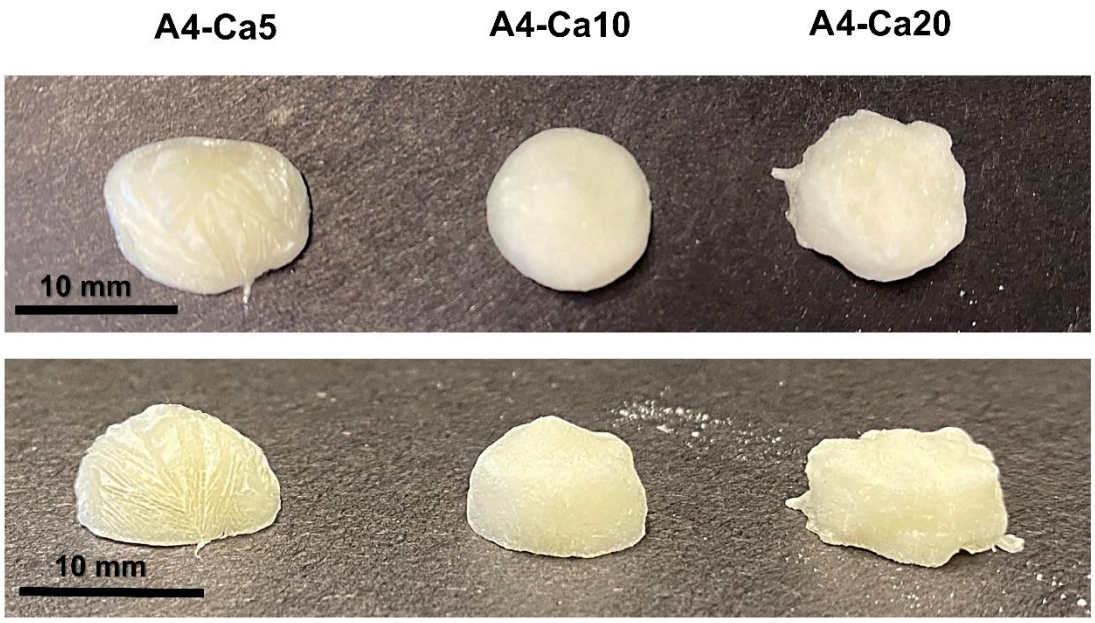

Figure 4.8. *Freeze-dried A4-Ca based scaffolds.*

The internal morphology of the scaffolds was evaluated by SEM, and the obtained images are shown in **Figure 4.9**. As can be observed, the pores are larger as the gelation degree decreased in the scaffold. A4-Ca5 scaffold shows larger pore amount and size than A4-Ca10 and A4-Ca20 scaffolds, which present similar porosities between them. Higher gelation degree implies higher compactness and contraction of the internal structure. Polymeric chains of the crosslinked alginate presented more interactions one another reducing the space among them and thus, the ice crystal size during freeze-drying process. Therefore, due to the low printing accuracy and the irregular morphology, the A4-Ca5 scaffolds were discarded for further characterization and application.

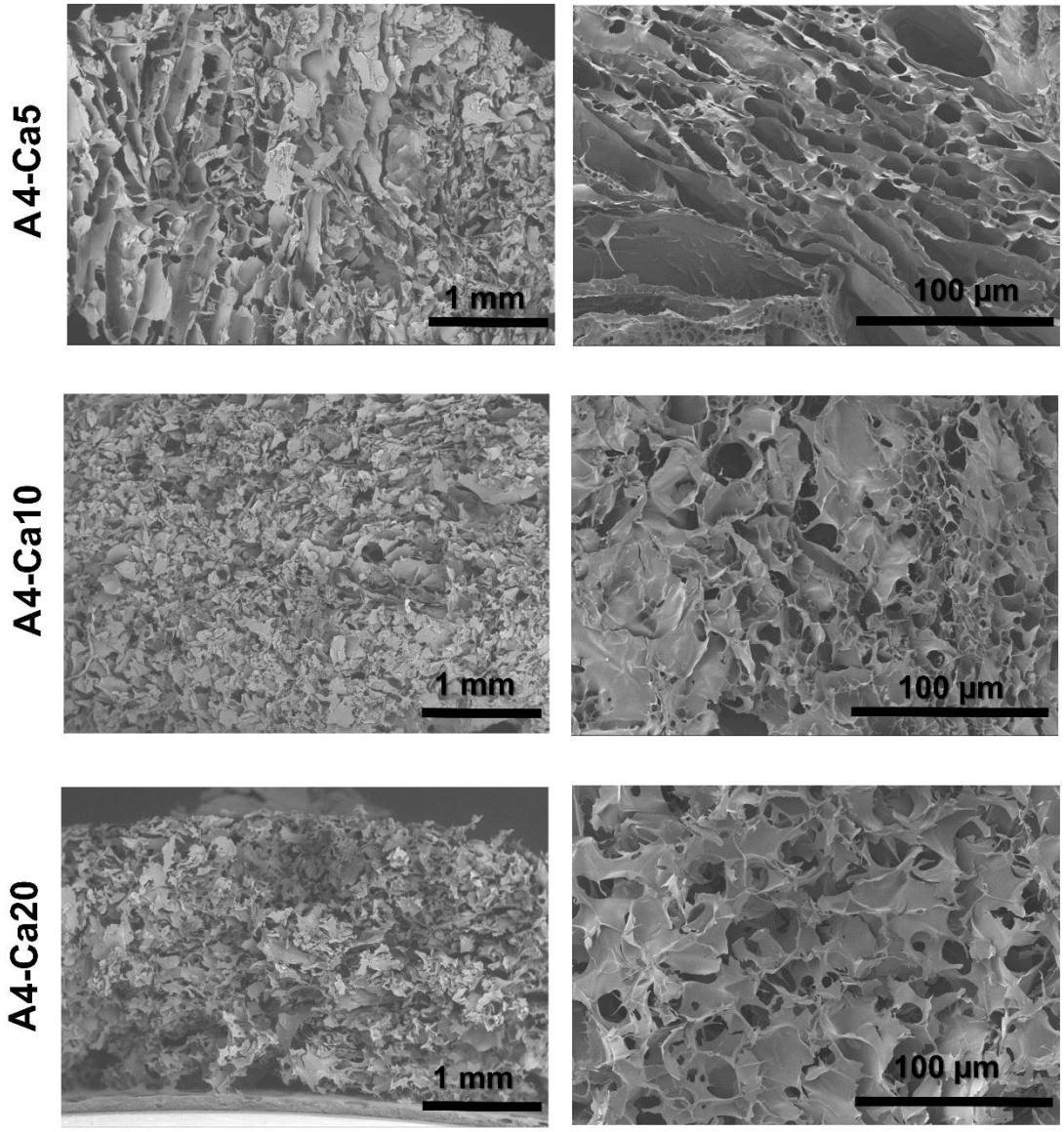

Figure 4.9. *SEM images of the cross-section at different magnifications of A-Ca based scaffolds.*

EnCNC10 cylindrical scaffolds were also morphologically characterized (**Figure 4.10**). As can be seen, these scaffolds show shape fidelity and proper cylinder shape after freeze-drying process. The internal structure was also analyzed by SEM and porous distribution is observed, presenting small and irregular pores where CNCs aggregates can be distinguished at higher magnifications. As it was previously explained, pore size depends on the ice crystal size and thus, on the water content, being these pores larger as the CNCs are forced to aggregate [20].

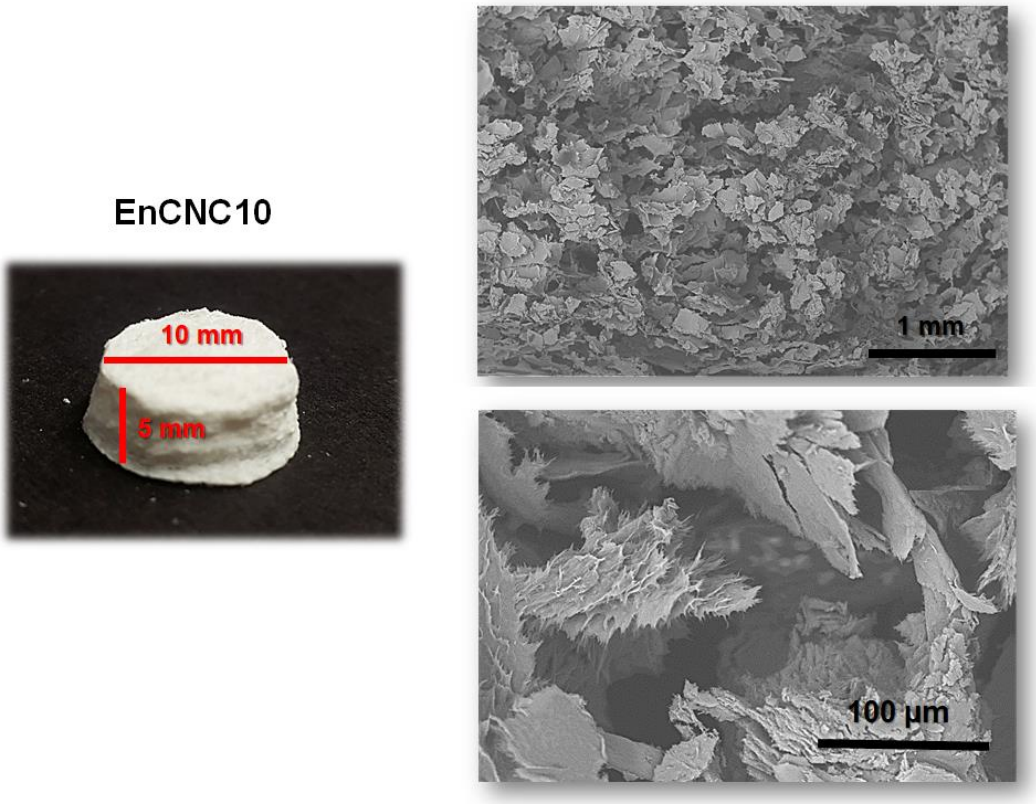

Figure 4.10. *EnCNC10 freeze-dried scaffold (left) and SEM images (right) at different magnifications of the cross-section.*

4.4.3. Mechanical characterization of A-Ca based and EnCNC10 scaffolds

Compressive mechanical stress-strain curves of A4-Ca10, A4-Ca20 and EnCNC10 scaffolds are shown in **Figure 4.11**.

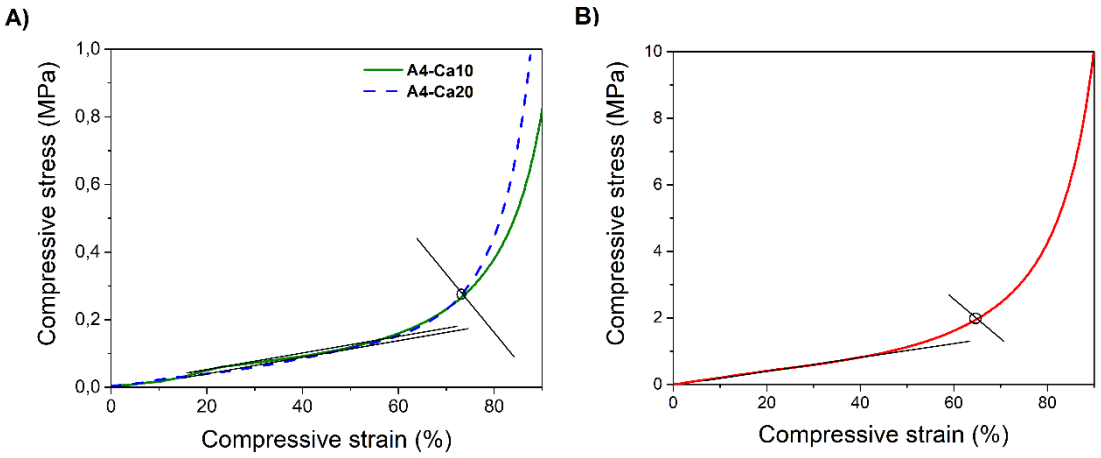

Figure 4.11. *Compressive stress-strain curves of A) A4-Ca10 and A4-Ca20 scaffolds and B) EnCNC10 scaffold.*

Young's modulus, compressive strength at 90 % of strain and densification strain values obtained from the curves are summarized in **Table 4.4**. All samples followed the typical compression behavior of porous materials, with a linear elastic region at low stress values, followed by an extended plateau ending in a densification region, where the stress dramatically increased. A4-Ca10 scaffolds showed similar mechanical strength and Young's modulus than A4-Ca20 (**Table 4.4**).

Table 4.4. *Young's modulus, compressive strength and densification strain of A4-Ca10, A4-Ca20 and EnCNC10 scaffolds.*

Scaffold (n=3)	Young's modulus (MPa)	Compressive strength (MPa)	Densification strain (%)
A4-Ca10	12.37 ± 2.56	1.19 ± 0.24	75.11 ± 1.57
A4-Ca20	7.68 ± 3.30	0.81 ± 0.15	74.33 ± 0.65
EnCNC10	105.99 ± 14.11	8.84 ± 1.00	64.34 ± 1.84

Besides, the densification strain for both A-Ca cylindrical scaffolds remained similar, which was in accordance to the similar porosity observed in SEM images. However, the irregular structure achieved after printing of over-gelled A4-Ca20 might interfere the correct mechanical behavior, and thus it is important to remark that it is needed to achieve an accurate and regular shape after 3D printing in order to obtain proper mechanical properties. After the assessment of the mechanical properties, A4-Ca10 scaffolds were selected as the most suitable to be tested for possible biomedical use.

Mechanical analysis of EnCNC10 scaffolds showed high Young's modulus value of 106 ± 14.11 MPa (**Table 4.4**), and a compressive strength of 8.84 ± 1.00 MPa at 90 % of strain. These scaffolds also showed a densification strain of 64.34 ± 1.84 % due to the high stiffness and subsequent low deformability of the structure. Cellulose nanoentities present great mechanical properties itself, as it was reflected in this compression analysis [23]. The hydrogen bond formation among CNCs gave rise to scaffolds with high mechanical properties and thus, promising applicability on bone tissue engineering [24]. Young's modulus values from 0.2 to 2 GPa have been reported for natural bone tissue and therefore these porous scaffolds could imitate the original trabecular bone structures [24,25].

4.4.4. Water absorption

The porous structure of these scaffolds would allow water entry into the structure, which is crucial for drug release applications as well as for tissue engineering, as it ensures the presence of nutrients and growth factors throughout the scaffold, allowing cell growth inside. The swelling capacity by water absorption of A4-Ca10 and EnCNC10 scaffolds was thus assessed. A4-Ca10 swelling ratio was evaluated during 24 hours (**Figure 4.12 A**), where a rapid swelling occurred in the first 2 hours, followed by slower increase period. Moreover, the scaffolds did not lost their structural integrity along the experiment. This high water absorption capacity observed in the hydrogel could be explained due to the high M content of this alginate [26]. As it was explained in Chapter 1, the egg-box structure formed among the carboxylate groups of alginate and the Ca^{2+} ions present higher affinity for G subunits, creating a weaker gel-like network with high swelling capacity due to the presence of higher M subunits in this case.

The swelling degree of EnCNC10 scaffolds is represented in **Figure 4.12 B** where a similar pattern observed in A4-Ca10 scaffolds is observed, with a rapid water absorption in the first hours and then a slow increase sustained over time.

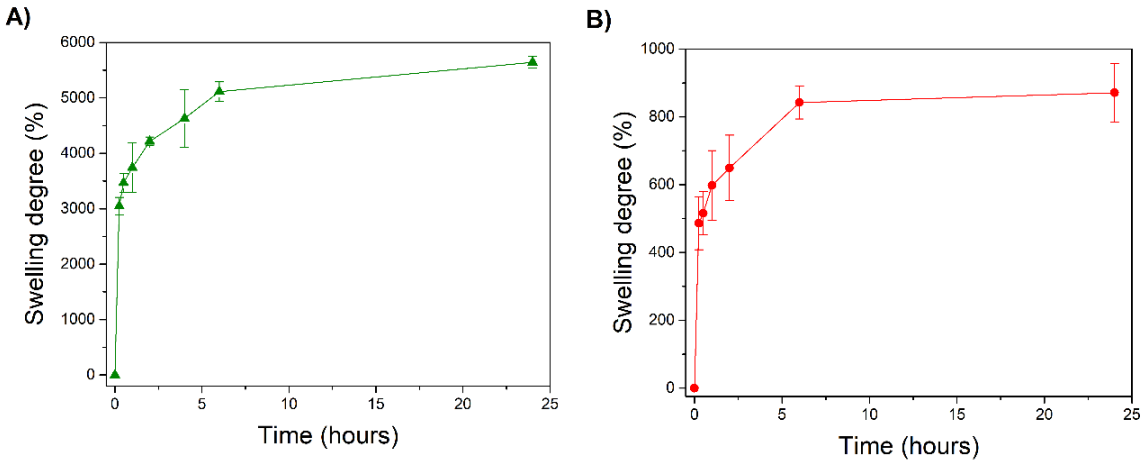

Figure 4.12. *Swelling degree of A) A4-Ca10 scaffolds and B) EnCNC10 scaffolds.*

4.5. Biomedical applications of A-Ca and EnCNC biomaterial inks

4.5.1. Preliminary *in vitro* cell proliferation test

With the aim of assess the biocompatible character and the suitability of these scaffolds for tissue engineering applications, preliminary qualitative analyses of cell proliferation were performed. For that purpose, HEK293 was chosen as a cell line model for these experiments. $2 \cdot 10^5$ cells were seeded in each A4-Ca10 and EnCNC10 scaffold and they

were then incubated *in vitro* (at 37 ºC with 5 % of CO_2) during 21 days. After that time o soaking culture medium, it was observed that none of the scaffolds lost their structural integrity. The nucleus of the cells were dyed with DAPI before the qualitative analysis at different time points and then, the presence of cells was evaluated by confocal laser scanning microscopy. The images of the seeded scaffolds and controls at time points 0 (6 hours after seeding), 7, 14 and 21 days are shown in **Figure 4.13.**

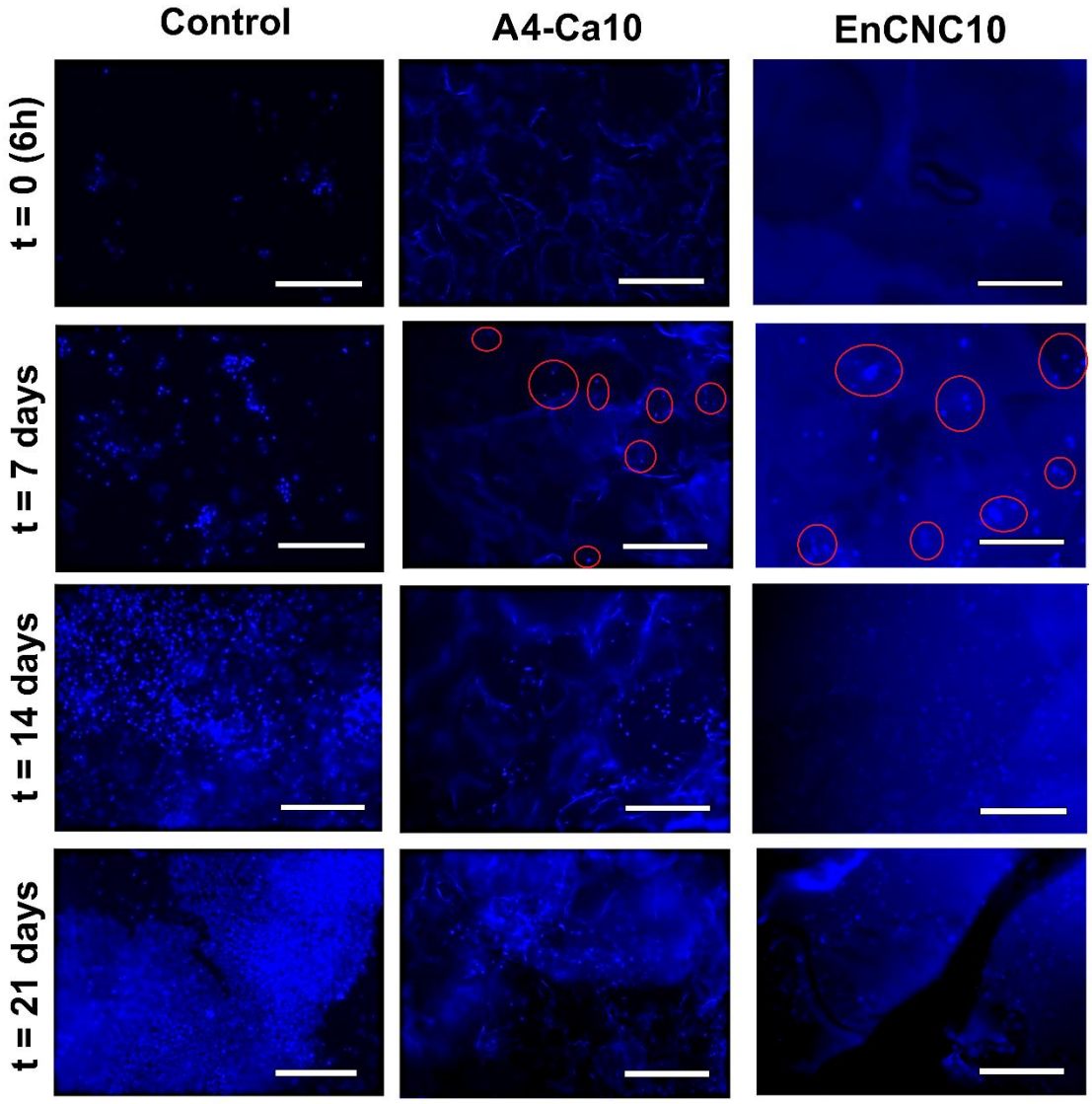

Figure 4.13. *Confocal microscopy images (10x) of controls and seeded A4-Ca10 and EnCNC10 scaffolds at different time points. Blue stained circles represent the nucleus of the HEK293 cells. Scale bar represent 250 µm.*

As could be clearly observed, HEK293 cells appeared as blue fluorescent stained circles whereas both the cells and the materials could be detected in the images from the seeded scaffolds. Comparing the images taken from the two scaffolds to that obtained for the monolayer control at 6 hours after cells seeding, it could be appreciated that no

cell growing was detected in the scaffolding structures. However, after 7 days of seeding some groups of cells were already observed into the scaffolds (denoted by red circles). At time points of 14 and 21 days, big cell groups could be detected into the scaffolding matrices, increasing the number over time. The observed cell proliferation in the 3D cultures was lower compared to monolayer controls, especially for the first two weeks. Nevertheless, the 3D cultures of HEK293 cells presented a visible increase in their number from 14 day after seeding that would be extended over time if were compared to monolayer controls, which presented high proliferation only up to 14 days [27]. This fact demonstrated that these 3D scaffolds could host cells and enable their proliferation for a longer period, and therefore, they would present promising characteristics for use as supporting materials for tissue engineering. HEK293 cells proliferate on the porous matrices and further demonstrating the biocompatibility of these materials.

4.5.2. *In vitro* drug delivery test

The drug release capacity from A4-Ca10 and EnCNC10 scaffolds was tested in order to demonstrate the possible application of these 3D printed scaffolds as drug delivery systems. In this case, 5.5 wt % of chloramphenicol was loaded into A4-Ca10 and EnCNC 10 biomaterial inks, which is a broad-spectrum water soluble antibiotic classified as class III drug in the biopharmaceutical system [28]. The antibiotic-loaded scaffolds from both formulations were successfully 3D printed in cylinder form, showing proper shape fidelity, and concluding that neither printability nor morphology were changed respect to the unloaded inks. *In vitro* chloramphenicol release experiments from these scaffolds were performed, and the results are shown in **Figure 4.14**.

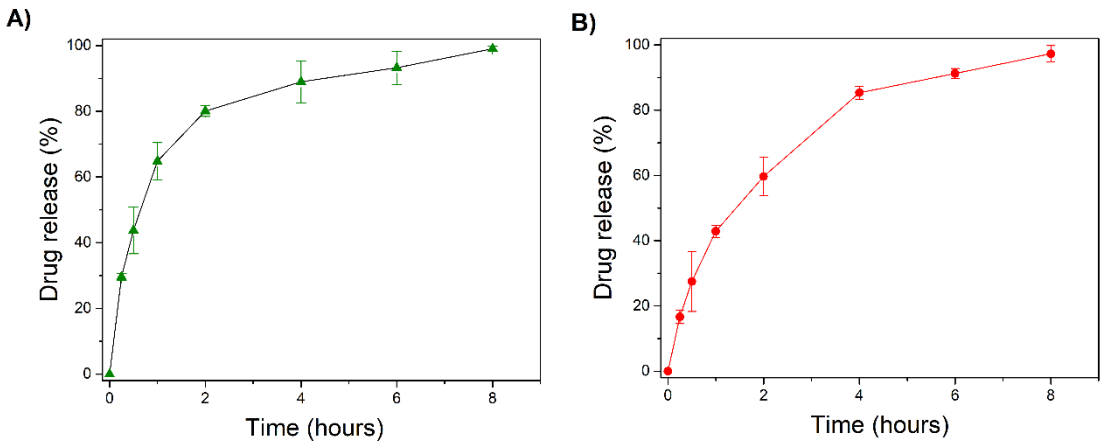

Figure 4.14. *Chloramphenicol release patterns from A) A4-Ca10 and B) EnCNC10 scaffolds.*

A4-Ca10 loaded scaffolds were able to release almost the 100 % of the antibiotic to the physiological medium in 8 hours (**Figure 4.14 A**). Similar release behavior was observed for EnCNC10 loaded scaffolds, where chloramphenicol was released almost totally in 8 hours (**Figure 4.14 B**). These chloramphenicol release profiles agree with those reported by Zao et al. [30], where 90 % of loaded chloramphenicol was released from alginate-CNC hydrogels in 8 h.

The *in vitro* drug release results of chloramphenicol-loaded A4-Ca10 and EnCNC10 scaffolds demonstrated that 3D printing technology and freeze-drying process enabled the manufacturing of drug-loaded scaffolds with porous structure, which allowed controlled release to the physiological medium of drugs with high solubility in aqueous media. Therefore, A4-Ca10 and EnCNC10 3D printed scaffolds could be employed as tablets for drug delivery applications.

4.6. Conclusions

In this chapter, single-component ink formulations for extrusion 3D printing technology have been successfully developed.

On one hand, Alginate/Ca^{2+} based inks were rheologically characterized, presenting an enhanced shear-thinning behavior as well as increased viscosity and yield points as the gelation degree increased. Printability tests showed that alginate gelation degree below 10 % resulted in structural collapse, while above 10 % resulted in over-extrusion, leading to irregular filament and inaccuracy in the printed samples. Consequently, alginate inks with a gelation degree of 10 % exhibited adequate filament formation and shape fidelity, with a homogeneous porosity after freeze-drying process.

On the other hand, a 10 wt. % concentration of EnCNC was enough to obtain an ink with suitable conditions for 3D printing, thanks to the particular shape and size of such CNCs. This ink presented high shear-thinning behavior and viscosity at low shear rates, as well as high G' and yield point values that translated into regular extrusion properties and shape fidelity in the printability tests. Thereafter, although morphological analysis of the freeze-died scaffolds showed an irregular porosity, mechanical analysis showed a high Young's modulus value attributed to the intrinsic properties of nanocellulose itself.

Regarding the possible biomedical applications of the single-component scaffolds, preliminary drug delivery and cell proliferation tests were performed. Both scaffolds showed a high swelling capacity that would ensure cell proliferation and an efficient mechanism for drug release. Qualitative cell proliferation tests were carried out showing

progressive cell growth over time after seeding, demonstrating a potential application as supporting materials for tissue engineering. The drug release capacity was *in vitro* tested, showing a fast delivery of chloramphenicol to the physiological medium from both single-component scaffolds.

4.7. References

[1] Siqueira G, Kokkinis D, Libanori R, Hausmann MK, Gladman AS, Neels A, Tingaut P, Zimmermann T, Lewis JA, Studart AR. Cellulose nanocrystal inks for 3D printing of textured cellular architectures. Adv Funct Mater 2017;27:1604619-1604629. https://doi.org/10.1002/adfm.201604619.

[2] Sarmento B, Ferreira D, Veiga F, Ribeiro A. Characterization of insulin-loaded alginate nanoparticles produced by ionotropic pre-gelation through DSC and FTIR studies. Carbohydr Polym 2006;66:1–7. https://doi.org/10.1016/j.carbpol.2006.02.008.

[3] Falcone G, Mazzei P, Piccolo A, Esposito T, Mencherini T, Aquino RP. Advanced printable hydrogels from pre-crosslinked alginate as a new tool in semi solid extrusion 3D printing process. Carbohydr Polym 2022;276:118746-118758. https://doi.org/10.1016/j.carbpol.2021.118746.

[4] Chen H, Xie F, Chen L, Zheng B. Effect of rheological properties of potato, rice and corn starches on their hot-extrusion 3D printing behaviors. J Food Eng 2019;244:150–158. https://doi.org/10.1016/j.jfoodeng.2018.09.011.

[5] Li H, Liu S, Li L. Rheological study on 3D printability of alginate hydrogel and effect of graphene oxide. Int J Bioprinting 2016;2:54–66. https://doi.org/10.18063/IJB.2016.02.007.

[6] Vadillo J, Larraza I, Calvo-correas T, Gabilondo N, Derail C, Eceiza A. Design of a waterborne polyurethane–urea ink for direct ink writing 3d printing. Materials 2021;14:1–13. https://doi.org/10.3390/ma14123287.

[7] Liu Z, Zhang M, Bhandari B, Yang C. Impact of rheological properties of mashed potatoes on 3D printing. J Food Eng 2018;220:76–82. https://doi.org/10.1016/j.jfoodeng.2017.04.017.

[8] Bendtsen ST, Quinnell SP, Wei M. Development of a novel alginate-polyvinyl alcohol-hydroxyapatite hydrogel for 3D bioprinting bone tissue engineered scaffolds. J Biomed Mater Res - Part A 2017;105:1457–1468. https://doi.org/10.1002/jbm.a.36036.

[9] Hsieh FY, Lin HH, Hsu SH. 3D bioprinting of neural stem cell-laden thermoresponsive biodegradable polyurethane hydrogel and potential in central nervous system repair. Biomaterials 2015;71:48–57. https://doi.org/10.1016/j.biomaterials.2015.08.028.

[10] Abouzeid RE, Khiari R, Beneventi D, Dufresne A. Biomimetic mineralization of three-dimensional printed alginate/TEMPO-oxidized cellulose nanofibril scaffolds

for bone tissue engineering. Biomacromolecules 2018;19:4442–4452. https://doi.org/10.1021/acs.biomac.8b01325.

[11] Liu Z, Bhandari B, Prakash S, Mantihal S, Zhang M. Linking rheology and printability of a multicomponent gel system of carrageenan-xanthan-starch in extrusion based additive manufacturing. Food Hydrocoll 2019;87:413–424. https://doi.org/10.1016/j.foodhyd.2018.08.026.

[12] Rocha VG, Saiz E, Tirichenko IS, García-Tuñón E. Direct ink writing advances in multi-material structures for a sustainable future. J Mater Chem A 2020;8:15646–15657. https://doi.org/10.1039/d0ta04181e.

[13] Schwab A, Levato R, D'este M, Piluso S, Eglin D, Malda J. Printability and shape fidelity of bioinks in 3D bioprinting. Chem Rev 2020;120:11028–1155. https://doi.org/10.1021/acs.chemrev.0c00084.

[14] Hausmann MK, Rühs PA, Siqueira G, Läuger J, Libanori R, Zimmermann T, Studart AR. Dynamics of cellulose nanocrystal alignment during 3D printing. ACS Nano 2018;12:6926–6937. https://doi.org/10.1021/acsnano.8b02366.

[15] Ouyang L, Yao R, Zhao Y, Sun W. Effect of bioink properties on printability and cell viability for 3D bioplotting of embryonic stem cells. Biofabrication 2016;8:3-7. https://doi.org/10.1088/1758-5090/8/3/035020.

[16] Chung JHY, Naficy S, Yue Z, Kapsa R, Quigley A, Moulton SE, Wallace GG. Bio-ink properties and printability for extrusion printing living cells. Biomater Sci 2013;1:763–773. https://doi.org/10.1039/c3bm00012e.

[17] Liu Y, Yu Y, Liu C, Regenstein JM, Liu X, Zhou P. Rheological and mechanical behavior of milk protein composite gel for extrusion-based 3D food printing. Lwt-Food Sci Technol 2019;102:338–46. https://doi.org/10.1016/j.lwt.2018.12.053.

[18] Gao T, Gillispie GJ, Copus JS, Kumar APR, Seol YJ, Atala A, Yoo JJ, Lee SJ. Optimization of gelatin-alginate composite bioink printability using rheological parameters: A systematic approach. Biofabrication 2018;10:34106-34118. https://doi.org/10.1088/1758-5090/aacdc7.

[19] Liu Z, Zhang M, Bhandari B. Effect of gums on the rheological, microstructural and extrusion printing characteristics of mashed potatoes. Int J Biol Macromol 2018;117:1179–1187. https://doi.org/10.1016/j.ijbiomac.2018.06.048.

[20] Li VCF, Dunn CK, Zhang Z, Deng Y, Qi HJ. Direct ink write (DIW) 3D printed cellulose nanocrystal aerogel structures. Sci Rep 2017;7:1–8. https://doi.org/10.1038/s41598-017-07771-y.

[21] Siow CRS, Wan Sia Heng P, Chan LW. Application of freeze-drying in the development of oral drug delivery systems. Expert Opin Drug Deliv 2016;13:1595–1608. https://doi.org/10.1080/17425247.2016.1198767.

[22] Wu X, Liu Y, Li X, Wen P, Zhang Y, Long Y, Wang X, Guo Y, Xing F, Gao J. Preparation of aligned porous gelatin scaffolds by unidirectional freeze-drying method. Acta Biomater 2010;6:1167–1177. https://doi.org/10.1016/j.actbio.2009.08.041.

[23] Gomes TCF, Skaf MS. Cellulose-builder: A toolkit for building crystalline structures of cellulose. J Comput Chem 2012;33:1338–1346. https://doi.org/10.1002/jcc.22959.

[24] Zhang XY, Fang G, Zhou J. Additively manufactured scaffolds for bone tissue engineering and the prediction of their mechanical behavior: A review. Materials 2017;10:1-27. https://doi.org/10.3390/ma10010050.

[25] Gibson LJ. The mechanical behaviour of cancellous bone. J Biomech 1985;18:317–328. https://doi.org/10.1016/0021-9290(85)90287-8.

[26] Ramos PE, Silva P, Alario MM, Pastrana LM, Teixeira JA, Cerqueira MA, Vicente AA. Effect of alginate molecular weight and M/G ratio in beads properties foreseeing the protection of probiotics. Food Hydrocoll 2018;77:8–16. https://doi.org/10.1016/j.foodhyd.2017.08.031.

[27] Ouyang L, Yao R, Chen X, Na J, Sun W. 3D printing of HEK 293FT cell-laden hydrogel into macroporous constructs with high cell viability and normal biological functions. Biofabrication 2015;7:3-7. https://doi.org/10.1088/1758-5090/7/1/015010.

[28] Khalid F, Hassan SMF, Mushtaque M, Noor R, Ghayas S, Muhammad IN, Hassan F. Comparative analysis of biopharmaceutic classification system (BCS) based biowaiver protocols to validate equivalence of a multisource product. African J Pharm Pharmacol 2020;14:212–220. https://doi.org/10.5897/ajpp2020.5130.

Chapter 5

A-CNF inks for 3D printing and drug-loaded scaffolds for controlled release

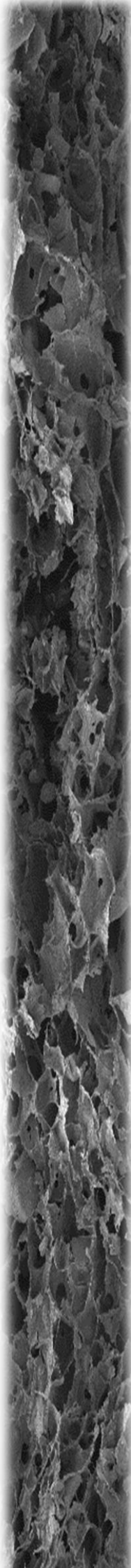

CHAPTER 5 – A-CNF inks for 3D printing and drug-loaded scaffolds for controlled release

5. Alginate-CNF inks for 3D printing and drug-loaded scaffolds for controlled release

5.1. Aim of the chapter

The main objective of the work described in this chapter was the development of multicomponent biomaterial ink formulations, more specifically based on alginate and cellulose nanofibers, with suitable characteristics for 3D printing technology. As demonstrated in the previous chapter, alginate-water solutions do not present proper rheological characteristics such as high viscosity and viscoelasticity, to be extruded through a nozzle and hold the printed shape. However, it is well known that the addition of nanoentities to a polymeric water dispersion can modulate its rheological properties. CNFs are one of the most used rheological modifiers in 3D printing technology due to their versatility and biocompatibility, as explained in Chapter 1. Therefore, in this chapter, five biomaterial inks of alginate and different CNF contents were developed and rheologically characterized.

The natural origin and the biocompatible character of these materials allowed their use for biomedical applications and thus, A-CNF inks that presented suitable characteristics for 3D printing were tested for their use as scaffolds for drug delivery. After 3D printing, post-printing processes are commonly used to dry the printed samples, to preserve the desired shape and create solid structures that can be employed, for instance, as drug delivery systems. Hence, A-CNF printed samples were subjected to post-printing processes and the obtained constructs were well characterized in this chapter.

With the purpose to test the drug release from A-CNF based scaffolds, a hydrophobic and a hydrophilic model drugs were chosen. Hydrophobic drug molecules usually present bioavailability issues due to its low solubility in physiological conditions, and therefore, its encapsulation and localized release from biopolymeric platforms could enhance its availability in target site. Hydrophilic drug molecules require high doses due to its high solubility in physiological medium and consequently, its rapid elimination from the body. The manufacturing of advanced drug delivery devices can focus and control the release of a wide range of drug molecules.

Therefore, the second objective was the development of drug-loaded A-CNF based inks suitable for 3D printing technology and the manufacture of devices for controlled drug delivery. The release of hydrophobic and hydrophilic drugs, as well as the simultaneous release of both drugs from A-CNF based scaffolds were tested *in vitro.*

5.2. A-CNF biomaterial inks preparation and characterization

Five biomaterial ink formulations were prepared from alginate (A) and cellulose nanofibers (CNF). CNF dispersions with different contents were prepared by mixing the CNF at concentrations of 1, 2, 3, 4 and 5 wt. % with 60 mL of distilled water, and dispersed using an Ultraturrax for 15 minutes at 12000 rpm and finally ultrasonicated for 2 hours until well homogenization. Alginate powder was added to the CNF dispersions at 4 wt. % with respect to the total content of the formulation, and blended with an Ultraturrax until complete homogenization. Samples were maintained refrigerated during the whole procedure in order to prevent water evaporation. The obtained ink formulations (**Table 5.1**) were named as A-CNFX, representing X the CNF wt. % on the biomaterial ink.

Table 5.1. *Summary of developed A-CNF biomaterial ink formulations. Material contents are expressed with respect to the total mass of the formulation.*

Biomaterial ink formulation	Alginate (wt. %)	CNF (wt. %)
A-CNF1	4	1
A-CNF2	4	2
A-CNF3	4	3
A-CNF4	4	4
A-CNF5	4	5

5.3. Rheological characterization of A-CNF biomaterial inks

Rheological characterization of the developed A-CNF biomaterial inks was performed with the aim of predicting both the printability and shape fidelity, following the same experiments preformed in the previous chapter. As it could be observed in the flow viscosity curves (**Figure 5.1 A**), these biomaterial inks presented high viscosity at zero shear rate, being higher with the increase of CNF content, and shear-thinning behavior in all cases. Power-law equation (Eq. 3) was employed to calculate the power-law index (n), consistency coefficient (K) and Pearson correlation coefficient (R^2) and obtained values are collected in **Table 5.2**. It was found that n values are approaching to zero while K values increased from 150 to 698 $Pa{\cdot}s^n$ as the CNF content raised in the formulations, indicating non-Newtonian fluid and shear-thinning behavior [1,2]. R^2 values close to unity showed a strong correlation between experimental data with the power-

law model. All these data demonstrates that an increase in CNF content in the ink formulations produced an increment of shear-thinning behavior and non-Newtonian fluid characteristics.

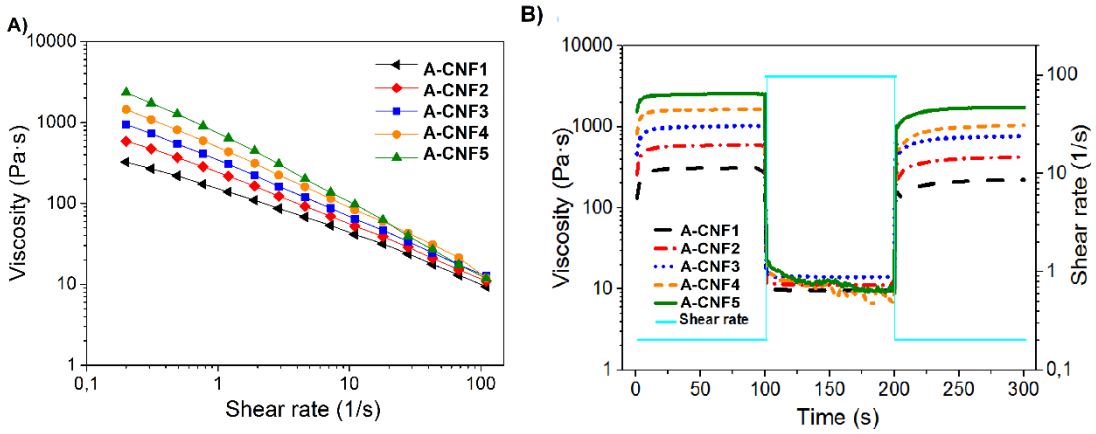

Figure 5.1. *Rheological characterization of the five A-CNF formulations: A) Viscosity as a function of shear rate increase. B) Viscosity recovery tests.*

Viscosity recovery test were performed in order to determine the recovery degree of the A-CNF based inks and thus, simulate printing conditions (**Figure 5.1 B**). Recovery percentage was calculated from recovery assays and summarized in **Table 5.2**. The obtained results indicated that, in general, recovery percentage increased as the CNF content increased. In the case of A-CNF4 and A-CNF5, the unexpected slightly lower recovery value could be caused by the partial loss of material during the experiment at the maximum shear rate values. However, the viscosity achieved when the shear rate stopped would be enough to hold the shape of printed scaffolds.

Table 5.2. *Viscosity measured at 0.2 s^{-1}, power-law coefficients viscosity recovery percentages, yield point values and G' at strain of 0.1 % of the five A-CNF based biomaterial inks.*

Biomaterial ink	Viscosity (Pa·s)	n	K (Pa·s^n)	R^2	Recovery (%)	Yield point (Pa)	G' in LVR (Pa)
A-CNF1	290 ± 32	0.44	149.15	0.99	72 ± 2	-	277 ± 51
A-CNF2	518 ± 59	0.36	234.08	0.99	72 ± 1	90 ± 12	463 ± 55
A-CNF3	850 ± 93	0.31	333.44	0.99	75 ± 3	284 ± 46	1233 ± 76
A-CNF4	1418 ± 71	0.26	481.37	0.99	65 ± 6	365 ± 16	2177 ± 68
A-CNF5	2266 ± 99	0.15	697.53	0.99	66 ± 3	600 ± 21	5583 ± 76

In **Figure 5.2 A** the storage modulus (G') and the loss modulus (G'') as a function of stress are shown. As it could be observed, G'' was always above G' for A-CNF1

indicating liquid-like behavior. For the rest of the A-CNF based formulations G' was higher than G'' indicating solid-like behavior. Yield point values (black circles) were determined, and the values are collected in **Table 5.1**. As it could be observed, these values were higher as CNF content increased, indicating that the higher CNF content in the formulation the higher force will be needed to extrude the material during 3D printing.

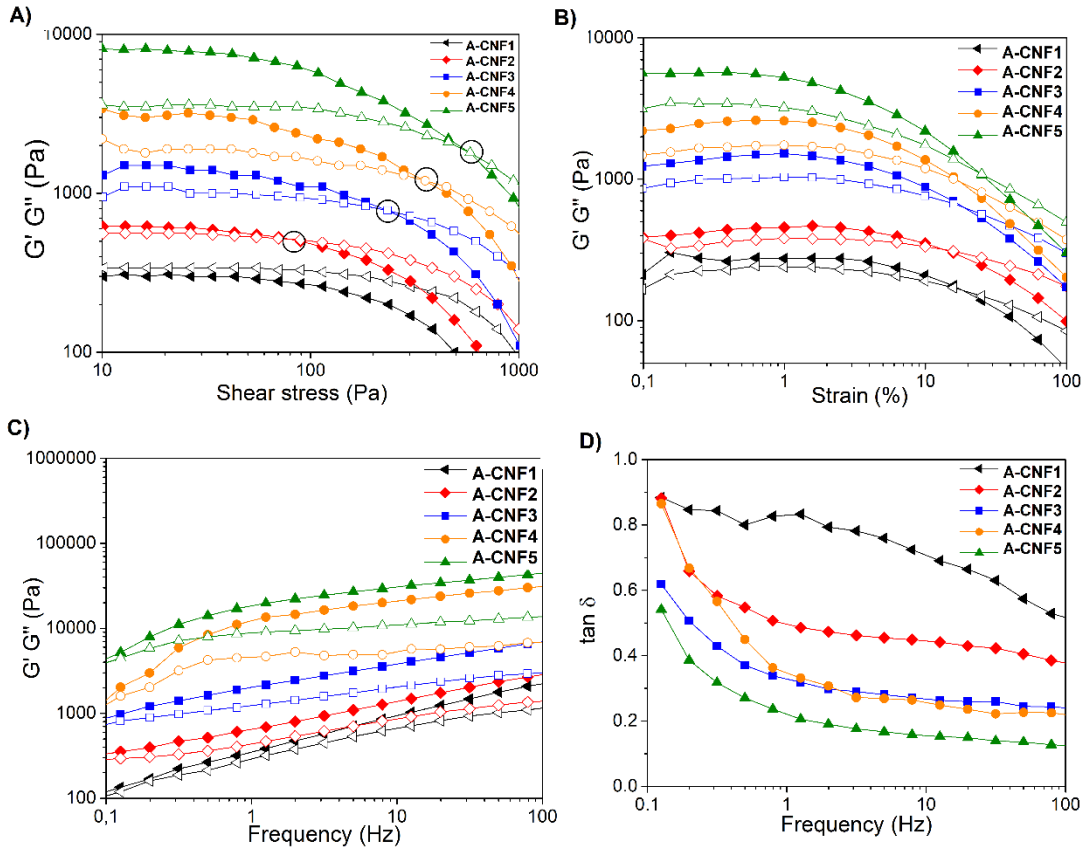

Figure 5.2. *Oscillatory sweep tests of the A-CNF based biomaterial inks. A) G' (solid symbols) and G'' (open symbols) as a function of shear stress. B) G' (solid symbols) and G'' (open symbols) versus strain. C) G' (solid symbols) and G'' (open symbols) as a function of frequency. D) Tan δ values from frequency sweep test.*

The LVR of these A-CNF based biomaterial inks was determined by strain sweep test (**Figure 5.2 B**). At values between 0.1 and 1 %, the G' and G'' were independent of the strain, and G' was higher than G'' demonstrating highly structured gel-like network in the LVR at lowest strain conditions. At strain values above 1 %, G' and G'' began to decrease, indicating the deformation of the material and loss of the gel-like network, resulting G'' higher than G'. The G' values at 0.1 % of strain are summarized in **Table 5.2.** The results denoted, a significant stiffness enhancement as the CNF amount increased in the formulation, and consequently, an increase of elasticity and strength characteristics of these A-CNF based inks. Indeed, the G' values of A-CNF3, A-CNF4 and A-CNF5 formulations at LVR were higher than 1200 Pa.

Frequency sweep tests of A-CNF based formulations are shown in **Figure 5.2 C**. All results presented frequency dependence of G' and G'' showing the increase of the two moduli as increasing the oscillation frequency. As it could also be observed, inks with the highest modulus values corresponded to those with higher CNF content, as well as higher difference between G' and G'' with the increment of applied frequency, achieving its maximum value at the highest frequency, where the solid-like behavior of the viscoelastic ink predominated. On the contrary, A-CNF1 presented similar values of G' and G'' indicating fluidity and weakly network structure of the material.

Tan δ values from frequency sweep test were also measured, and the results are shown in **Figure 5.2 D.** Tan δ values of A-CNF3, A-CNF4 and A-CNF5 denoted shape fidelity whereas values higher than 0.5 observed for A-CNF1 and A-CNF2 indicated liquid-like behavior and thus, poor shape retention properties.

After the rheological characterization, it can be concluded that CNFs added to an alginate solution acted as rheological modifiers, increasing the viscosity, shear-thinning behavior and viscoelastic properties of the developed biomaterial inks. A-CNF3, A-CNF4 and A-CNF5 presented suitable characteristics to be extruded through the nozzle and hold the printed shape, whereas A-CNF1 and A-CNF2 presented liquid-like characteristics and poor conditions for 3D printing technology.

5.4. 3D printing, post-printing and scaffolds characterization

5.4.1. 3D printing of A-CNF inks

A-CNF based biomaterial inks were 3D printed in several forms (**Figure 5.3**) in order to correlate with rheological parameters 3D printing visualization. All developed inks were able to be extruded through the nozzle, showing proper filament formation and correct layer deposition, but, as it could be noticed, printed samples from A-CNF1 and A-CNF2 biomaterial inks did no present accuracy on dog-bone shape reproduction and collapsed. A-CNF3, A-CNF4 and A-CNF5 showed shape fidelity and structural integrity as well as smooth uniformity and good connection between layers after printing.

The structural collapse and poor shape fidelity of A-CNF1 and A-CNF2 biomaterial inks were in accordance to the measured low viscosity values at low shear rate, as well as to the fluidity and liquid-like behavior above discussed.

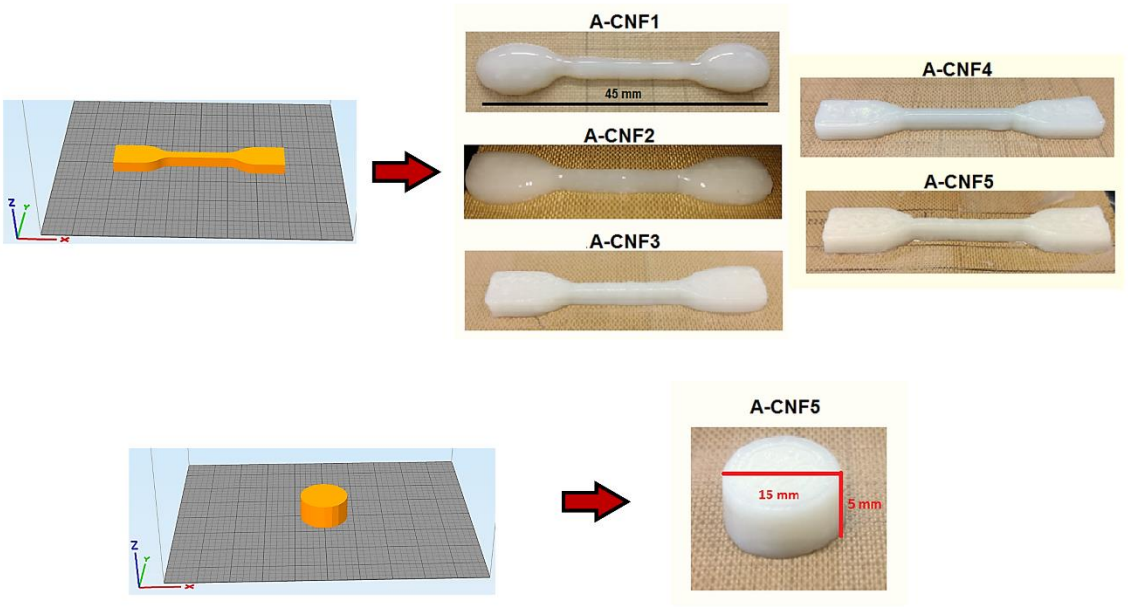

Figure 5.3. *Computer-aided design (CAD) models of dog-bone and cylinder, and digital images of 3D printed samples from the developed A-CNF based biomaterial inks.*

In conclusion, formulations with CNF content of at least 3 wt. % presented suitable characteristics to be successfully 3D printed. The printed samples showed a more accurate representation of the CAD model as the CNF content in the A-CNF based formulations increased. The CNFs acted as rheological modifier increasing shape fidelity and structural integrity, as well as avoiding collapse of printed samples. Therefore, A-CNF1 and A-CNF2 formulations were discarded due to their poor suitability for 3D printing technology, whereas A-CNF3, A-CNF4 and A-CNF5 biomaterial ink formulations were selected as suitable for 3D printing technology. Cylindrical samples of these A-CNF ink formulations were 3D printed and subjected to freeze-drying as a post-printing modification.

5.4.2. Morphological characterization of the scaffolds

A-CNF scaffolds were characterized by SEM after freeze-drying process. Both the surface and cross-section perpendicular to the deposition of the layers of freeze-dried scaffolds are shown in **Figure 5.4**. It can be observed that the surface of A-CNF3 scaffold presented larger porosity than A-CNF4 and A-CNF5, where non-homogeneous porosity surfaces were noticed, with compact and porous regions appearing together. As it can be observed in cross-section images, the porosity decreased and higher compactness was observed as the CNF content increased in the ink formulation. The different layers were correctly merged during the 3D printing process and thus, no separated threads

were observed. Moreover, the scaffolds appeared as a single piece, demonstrating extrusion uniformity of the inks and proper material deposition.

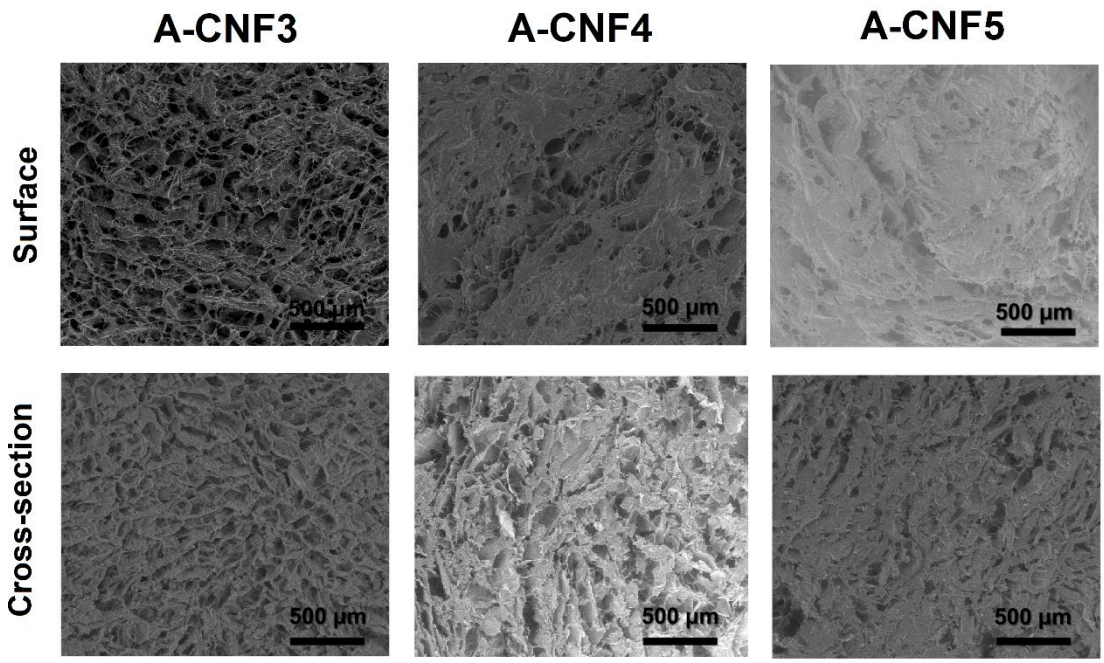

Figure 5.4. *SEM images of A-CNF based freeze-dried scaffolds.*

In summary, higher CNF content in the biomaterial ink formulations led to a reduced porosity both in the surface and in the internal structure of the scaffolds. It is worthy to note that varying the amount of CNF only in 1 wt. % was enough to observe morphology, porosity and compactness changes between A-CNF3, A-CNF4 and A-CNF5 printed scaffolds.

5.4.3. Mechanical characterization of the scaffolds

Compressive mechanical tests of the freeze-dried scaffolds from A-CNF3, A-CNF4 and A-CNF5 were performed and the curves are shown in **Figure 5.5**. Compressive modulus, compressive stress and densification strain values obtained from the curves are collected in **Table 5.3**.

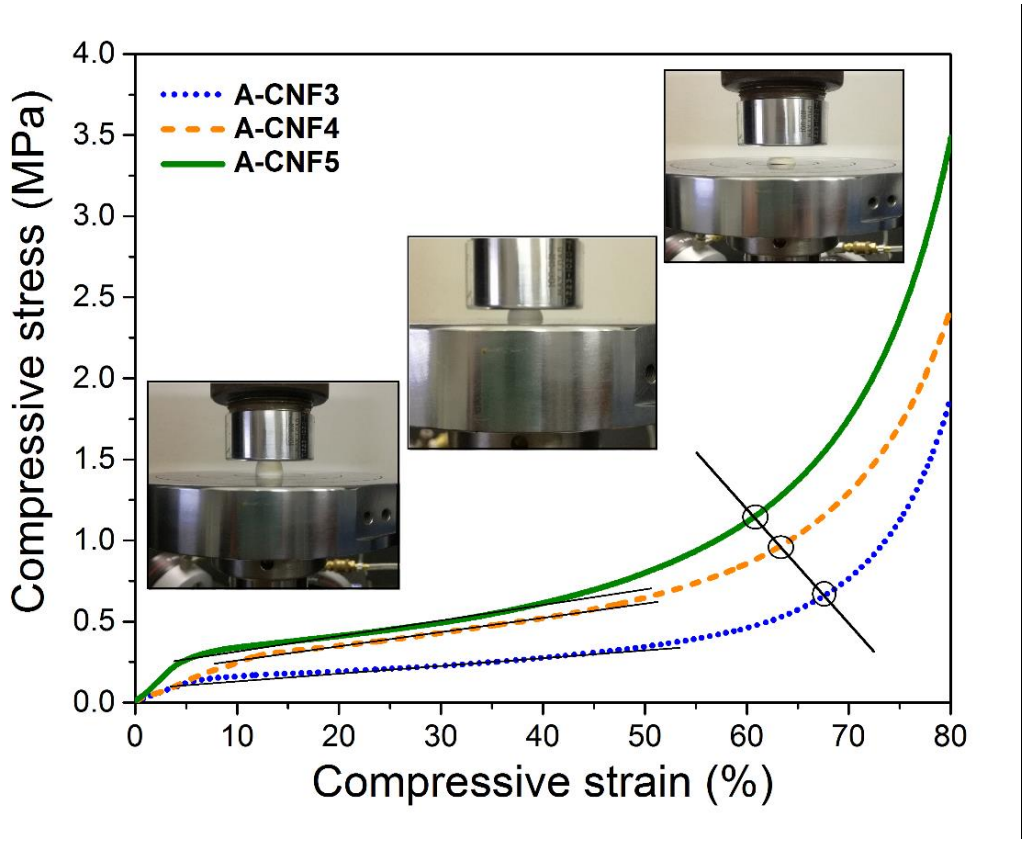

Figure 5.5. *Compressive stress-strain curves of A-CNF3, A-CNF4 and A-CNF5 freeze-dried scaffolds as well as images of mechanical performance associated to each phase of the experiment.*

Table 5.3. *Compressive properties of freeze-dried A-CNF based scaffolds.*

Scaffold (n= 5)	Young's modulus (MPa)	Compressive stress (MPa)	Densification strain (%)
A-CNF3	12.0 ± 5.7	1.5 ± 0.4	66.6 ± 2.1
A-CNF4	22.8 ± 12.3	2.7 ± 0.8	65.6 ± 1.3
A-CNF5	28.1 ± 13.4	3.2 ± 0.8	63.0 ± 1.2

A-CNF5 scaffolds showed higher mechanical strength and stiffness due to the reinforcing effect of CNF, in agreement with the rheological results. Indeed, mechanical results showed an increase of Young's modulus and compressive stress values as CNF content increased, whereas the densification strain values decreased due to the porosity reduction. Lower modulus for A-CNF3 scaffolds and lower compressive stress than A-CNF4 and A-CNF5 was measured, while A-CNF5 reached non-porous behavior zone faster than A-CNF3 and A-CNF4.

5.4.4. Water absorption and scaffold disintegration

Water absorption capacity and disintegration degree of A-CNF based scaffolds were assessed for 24 hours and the obtained results are shown in **Figure 5.6**. Swelling degree was calculated using Eq. 5, and the results showed that it was higher in A-CNF3 scaffolds than A-CNF4 and A-CNF5 (**Figure 5.6 A**). This could be caused by the larger porosity observed in A-CNF3 scaffolds that enabled faster water penetration, compared to those scaffolds with higher CNF content that showed higher compactness.

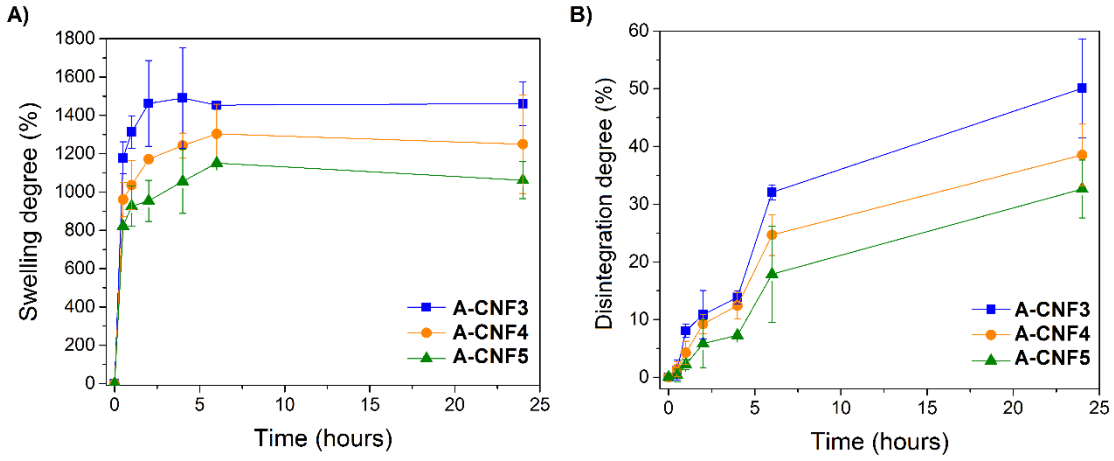

Figure 5.6. *A) Water absorption capacity and B) disintegration degree of A-CNF based scaffolds.*

It should be taken into account the progressive disintegration of the scaffolds in PBS, and thus the mass gain due to the water uptake and the mass loss were competing particularly from the 4th hour of the experiment. The faster swelling degree and the higher porosity resulted in higher disintegration over time, as it can be observed in **Figure 5.6 B**. The disintegration degree was assessed using Eq. 6 described in Chapter 2. A-CNF3 scaffold showed the highest water absorption and fastest disintegration due to its larger porosity observed by SEM.

5.4.5. Preliminary cell biocompatibility test

Preliminary qualitative assessment of cell growth was performed and hence, the biocompatibility of the developed A-CNF based scaffolds was also tested. HEK293 cells were seeded in A-CNF3 and then they were incubated for one week under *in vitro* conditions (37 ºC and 5 % CO_2). It was observed that the scaffolds did not totally lose their structure after culturing. In this case, the seeded scaffolds were evaluated through a Z-axis multilayer analysis by confocal laser scanning microscopy, observing the

nucleus of the cells stained with DAPI and taking images of the scaffolds layer-by-layer at different heights, from the base to the surface, as it is shown in **Figure 5.7.**

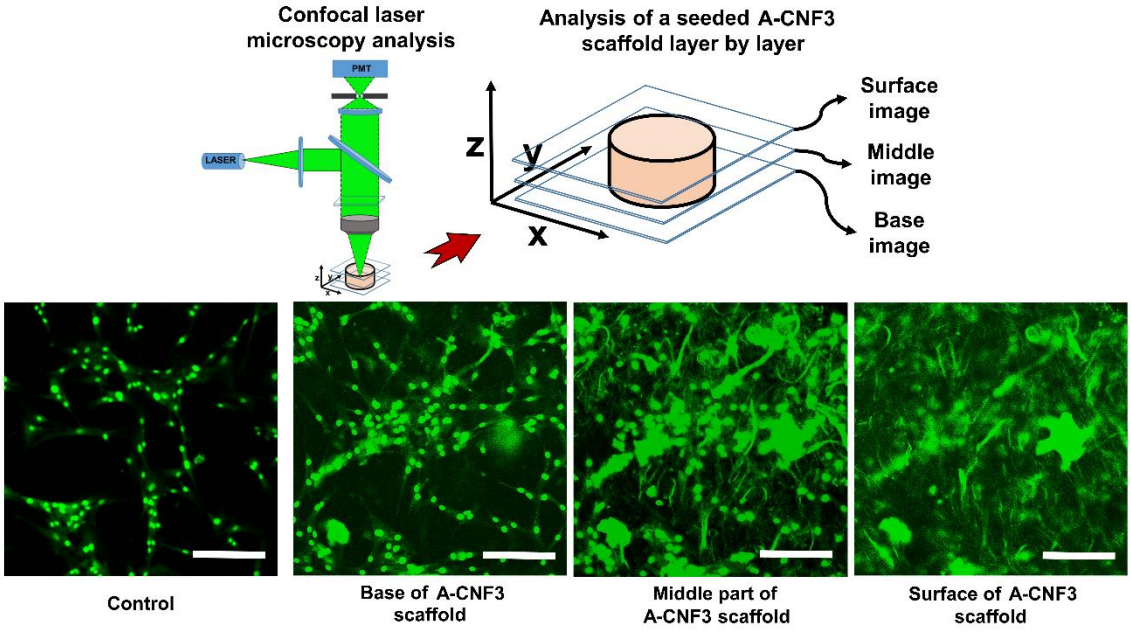

Figure 5.7. *Preliminary qualitative biocompatibility test in the A-CNF3 scaffold. The images of the upper part summarized the Z-multilayer analysis of a cylindrical scaffold performed by confocal laser microscopy. Down part of the figure shows the control (seeded cells without scaffold) and the images of a seeded A-CNF3 scaffold taken layer by layer from the base to the surface by confocal laser microscopy. Scale bars represent 100 µm.*

As can be observed in the control, the nuclei of the HEK293 cells were observed as green fluorescent stained circles, while other structures such as the extended cytoplasm could also be detected. In the images taken from the seeded A-CNF3 scaffold, both the cells and the scaffold were observed. It has been reported in the literature that cellulose nanofibers can be observed by confocal laser microscope between blue and green fluorescence emission spectra [3], and consequently they could be detected in the images, particularly in the middle and the surface of the scaffold. After 7 days of culturing, the analysis revealed that cells appeared throughout the scaffold and they were able to integrate and growth in the porous A-CNF based scaffolds, demonstrating the biocompatible character of these biomaterial inks.

The morphological and mechanical analyses, as well as the water absorption capacity, the biocompatibility and cell growth into these A-CNF based scaffolds revealed their suitability to be used for biomedical purposes. In the following study, the application of these A-CNF based inks for controlled drug delivery was assessed.

5.5. Drug-loaded A-CNF scaffolds for controlled release

5.5.1. Drugs characterization and integration into the A-CNF inks

Once the biomaterial inks were characterized, the manufacturing of A-CNF printed devices for controlled drug release was carried out. For that purpose, curcumin was chosen as a hydrophobic drug model whereas chloramphenicol was again selected for this study as a hydrophilic drug model due to its well integration into the polymeric matrices shown in the previous chapter. Both drugs were deeply characterized before and after their incorporation into the A-CNF based inks.

5.5.1.1. Drug solubility determination

The solubility of both drugs in the different solvents employed in the release and extraction processes, as well as their crystallinity were analyzed. Curcumin is extracted from natural sources (from turmeric) and classified as class II drug in the Biopharmaceutics Classification System (BCS), showing low solubility in aqueous solutions but high permeability in targeted site [4]. The solubility of curcumin was evaluated at 37 ºC, and the results were 7.4 $mg \cdot mL^{-1}$ in water, 6.7 $mg \cdot mL^{-1}$ in PBS and 26.4 $mg \cdot mL^{-1}$ in ethanol, being higher in ethanol than in aqueous media.

Chloramphenicol is a synthetic drug employed as broad-spectrum antibiotic and classified as class III according to BCS, presenting high solubility in aqueous solutions but low permeability in target zone [5]. The solubility of chloramphenicol was also measured at 37 ºC, being the values 29.3 $mg \cdot mL^{-1}$ in water, 28.8 $mg \cdot mL^{-1}$ in PBS and 380.4 $mg \cdot mL^{-1}$ in ethanol. Both drugs presented higher solubility in ethanol than in aqueous media, although chloramphenicol showed higher values in water and PBS than curcumin.

5.5.1.2. Drug crystallinity and integration into A-CNF based inks

Six different drug-loaded formulations were prepared from the previous developed A-CNF based biomaterial inks. A-CNF3, A-CNF4 and A-CNF5 were chosen for these experiments due to their suitability for 3D printing technology and the previous characterization that showed their adequacy of these scaffolds for biomedical purposes.

Curcumin in 15 wt. % or chloramphenicol in 50 wt. % were incorporated to A-CNF3, A-CNF4 and A-CNF5 in respect of the total solid content in the formulation, and the developed drug-loaded formulations are summarized in **Table 5.4**.

Table 5.4. *Summary of developed drug-loaded A-CNF biomaterial ink formulations.*

Biomaterial ink formulation	Alginate (wt. %)	CNF (wt. %)	Curcumin (wt. %)	Chloramphenicol (wt. %)
A-CNF3-cur	4	3	15	-
A-CNF4-cur	4	4	15	-
A-CNF5-cur	4	5	15	-
A-CNF3-clph	4	3	-	50
A-CNF4-clph	4	4	-	50
A-CNF5-clph	4	5	-	50
A-CNF3-cur-clph	4	3	15	50

The amount of chloramphenicol was added according to recommended daily dosage of 50 $mg \cdot kg^{-1}$ in adults [6], while the amount of curcumin was selected following similar procedures in the literature [7] due to the non-officially determined daily dosage, but without surpassing the toxicity levels reported [8].

Despite the low solubility observed for curcumin in water or in PBS, it is reported that this drug can be stabilized in alginate aqueous solutions [9]. When curcumin is mixed with alginate in solution, the hydrophobic drug particles are trapped and stabilized by the polymeric chains of alginate and thus, they stay homogeneously distributed throughout the aqueous alginate matrix [9,10]. Moreover, CNF could even improve this stabilization through Pickering effect [11,12] and consequently curcumin was successfully integrated and stabilized in A-CNF based inks. Prepared formulations were denoted as A-CNFX-cur and A-CNFX-clph, being X the CNF content (in wt. %) in the formulation. Moreover, a biomaterial ink containing both drugs was also prepared from A-CNF3 ink formulation, preserving the same drug contents determined for the previous formulations, and denoted as A-CNF3-cur-clph.

The crystallinity and integration degree of the drugs into the A-CNF based inks were studied by DSC and showed in **Figure 5.8**.

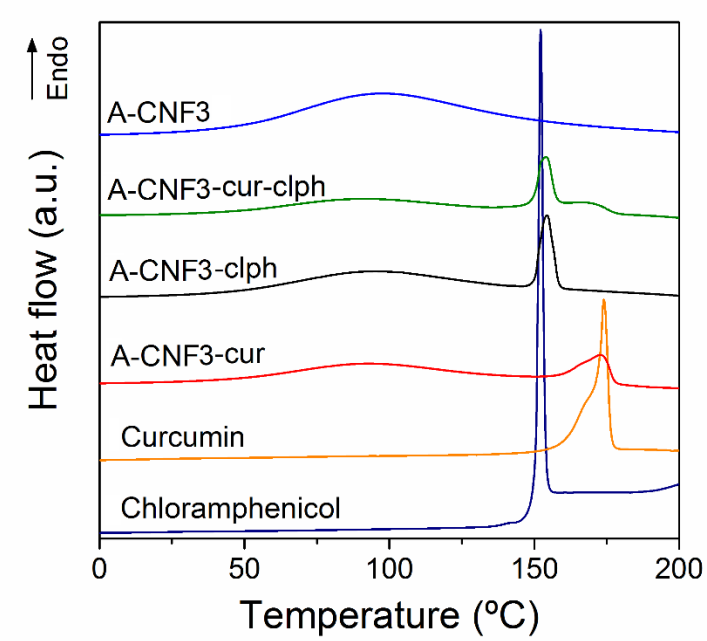

Figure 5.8. *DSC curves of curcumin, chloramphenicol, A-CNF3 matrix, A-CNF3-cur, A-CNF3-clph and A-CNF3-cur-clph.*

DSC patterns of neat curcumin and chloramphenicol showed their melting temperatures at 173 ºC and 150 ºC, respectively, in accordance to the crystalline structure of both drugs. DSC curve of A-CNF3 matrix showed a broad endothermic peak corresponding to water evaporation that was bonded to the hydroxyl groups of alginate and CNF [13]. As it could be noted in the thermograms of A-CNF3-cur and A-CNF3-clph inks the melting peaks associated to curcumin and chloramphenicol appeared at almost the same temperatures as those observed individually, demonstrating that both drugs preserved their crystalline structure once integrated into the A-CNF3 biomaterial ink. DSC curve of A-CNF3-cur-clph biomaterial ink also showed the mentioned endothermic peaks associated with crystalline domains of curcumin and chloramphenicol.

These results revealed that both drugs were present in crystalline form in the ink, and this characteristic was preserved in all developed formulations due to non-thermal modification during the ink manufacturing process.

5.5.1.3. Rheological characterization of drug-loaded A-CNF inks

The suitability of drug-loaded A-CNF biomaterial inks for extrusion 3D printing technology was tested carrying out similar rheological measurements than those performed previously for A-CNF based ink formulations. Moreover, this rheological characterization would assess whether the addition of curcumin or chloramphenicol to the formulations

interfered in the printability properties and shape fidelity of those drug-loaded inks.Flow viscosity tests of the different loaded biomaterial inks were carried out and the results are shown in **Figure 5.9 A**.

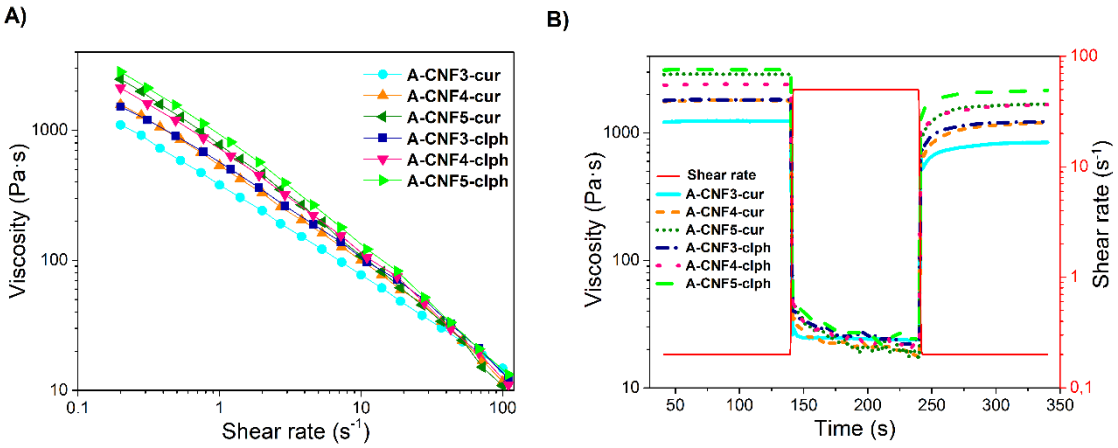

Figure 5.9. *Rheological characterization of A-CNF-cur and A-CNF-clph based ink formulations. A) Flow viscosity versus shear rate increase and B) Viscosity recovery tests.*

As it can be observed, all A-CNF-cur and A-CNF-clph based formulations showed shear-thinning behavior and high viscosity values at zero shear rate. In this case, the shear-thinning behavior was affected by the different CNF content as well as by the characteristics of the loaded drug in the inks such as structure and content. These changes in the properties of the inks could be quantified by comparing the experimental flow viscosity values to a power-law model using Eq. 3, as in previous characterizations. The consistency coefficient and power-law index values, as well as Pearson correlation coefficient for all drug-loaded biomaterial ink formulations are summarized in **Table 5.5**.

Table 5.5. *Viscosity measured at 0.2 s^{-1}, power-law coefficients, recovery percentage, yield point values and storage modulus measured at 0.1 % of strain (LVR).*

Biomaterial ink	Viscosity (Pa·s)	n	K (Pa·s^n)	R^2	Recovery (%)	Yield point (Pa)	G' in LVR (Pa)
A-CNF3-cur	1269 ± 23	0.30	380.68	0.99	68 ± 3	337 ± 52	2773 ± 540
A-CNF4-cur	1826 ± 52	0.23	534.91	0.99	70 ± 5	476 ± 29	3002 ± 659
A-CNF5-cur	2528 ± 237	0.19	660.79	0.99	60 ± 2	568 ± 20	6234 ± 290
A-CNF3-clph	1510 ± 107	0.24	568.63	0.99	65 ± 4	589 ± 39	3030 ± 364
A-CNF4-clph	2193 ± 167	0.18	659.54	0.99	66 ± 3	862 ± 35	5747 ± 719
A-CNF5-clph	2833 ± 121	0.14	880.85	0.99	67 ± 3	1419 ± 179	9017 ± 448

As the CNF content of the inks increased, K values increased from 380.68 to 660.79 $Pa{\cdot}s^n$ for A-CNF-cur inks and from 568.63 to 880.85 $Pa{\cdot}s^n$ for A-CNF-clph based formulations. Power-law index values decreased from 0.30 to 0.19 for curcumin-loaded inks and from 0.24 to 0.14 for chloramphenicol-loaded inks, indicating strong non-Newtonian behavior and enhanced shear-thinning behavior as the CNF content increased in the formulation [1,2,14]. This shear thinning is higher in chloramphenicol-loaded inks, demonstrating that drug characteristics and content also influenced the shear-thinning behavior. R^2 coefficients of 0.99 in all cases demonstrated the strong relationship between the experimental data and the theoretical power-law model. All these results confirmed that curcumin and chloramphenicol, as well as the CNF content, performed as rheological modifiers increasing viscosity and shear-thinning behavior of the developed biomaterial inks.

The structure recovery of the developed drug-loaded A-CNF based inks was assessed (**Figure 5.9 B**) and the recovery percentages are collected in **Table 5.5.** Viscosity recovery percentages from 60 to 70 % were obtained for the developed formulations and those values should be enough to support the 3D structure of the printed samples after printing.

Oscillatory stress sweep tests (**Figure 5.10 A**) were carried out to assess the viscoelastic properties of the developed A-CNF-cur and A-CNF-clph ink formulations. All formulations showed G'' below G' indicating solid-like structure and elastic behavior of the material, as it was previously observed for A-CNF based formulations.

Yield point (G'=G'') values are collected in **Table 5.5** and, as it could be noticed, the addition of drugs contributed to increase the yield point values (denoted by circles), from 337 ± 52 to 1419 ± 179 Pa and from 589 ± 39 to 1419 ± 179 Pa for curcumin and chloramphenicol loaded A-CNF inks, respectively. If these results are compared to those of the A-CNF based inks, whose values oscillated from 284 to 600 Pa, it should be remarked that both drugs and the CNF content of the biomaterial inks caused the increase of the necessary force to extrude the inks through a nozzle [14].

G' and G'' versus strain are represented in **Figure 5.10 B**. It can be observed that in the LVR, G' values were always above G'' ones indicating dominance of elastic behavior in this zone in all formulations. However, at high strains G' values dropped while G'' raised, indicating the disruption of the structure network and predominance of viscous behavior.

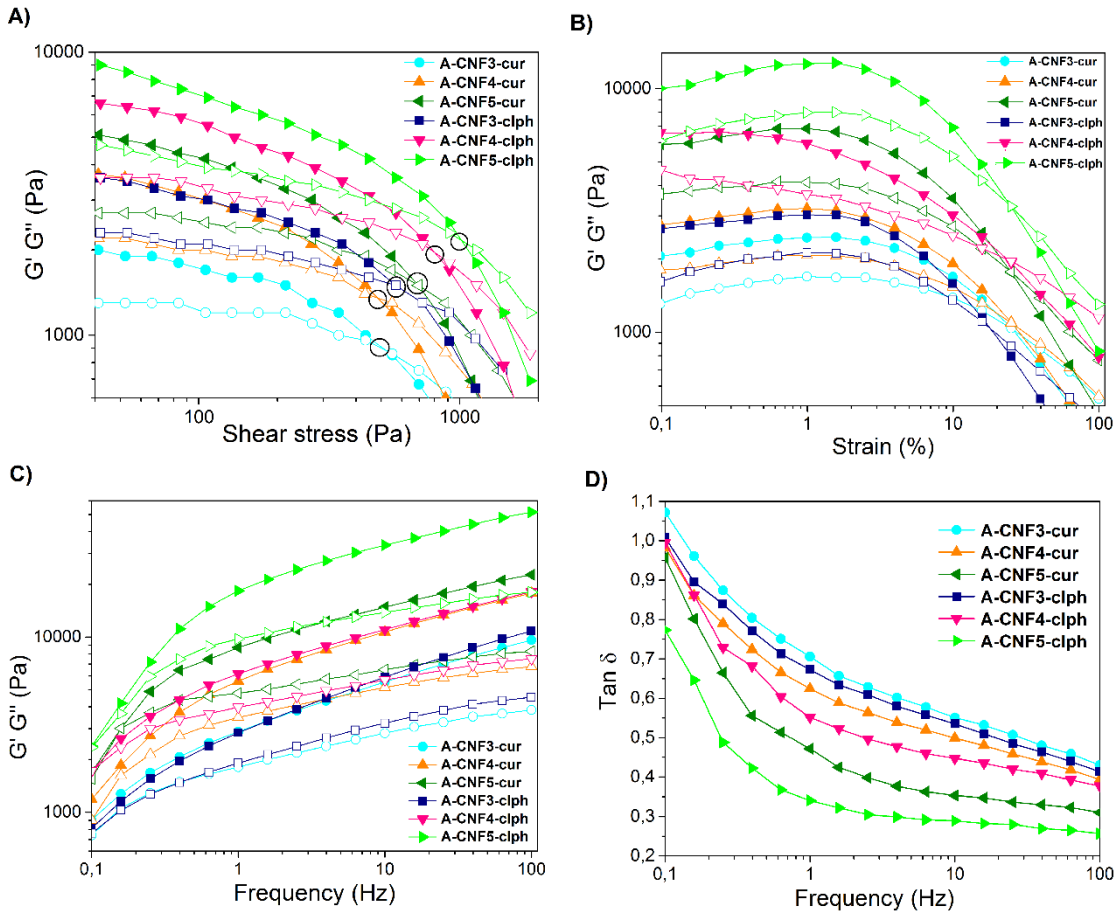

Figure 5.10. *Oscillatory rheological measurements for A-CNF-cur and A-CNF-clph based biomaterial inks. A) G' (solid symbols) and G'' (open symbols) versus shear stress. Yield point values are denoted by black circles. B) G' (solid symbols) and G'' (open symbols) versus strain. C) G' (solid symbols) and G'' (open symbols) as a function of frequency. D) Tan δ as a function of frequency sweep test.*

As it could be observed, G' values (**Table 5.5**) increased as CNF and drugs content did, contributing to the increase of solid-like behavior and viscoelasticity of the inks, especially in the case of chloramphenicol. The obtained G' values in LVR from 2773 ± 540 to 6234 ± 290 for curcumin loaded inks and from 3030 ± 364 to 9017 ± 448 Pa for chloramphenicol loaded inks were significantly higher compared to those of the unloaded inks (from 1233 to 5583 Pa). Consequently, observed G' values for A-CNF-cur and A-CNF-clph biomaterial inks suggested that the 3D printed samples will be able to hold the shape with a successful reproduction of the CAD design.

Frequency sweep tests are shown in **Figure 5.10 C**. As the frequency increased, G' was above G'' indicating solid-like behavior, following the same tendency observed in the previous oscillatory assays for A-CNF based biomaterial inks. Tan δ values from frequency sweep tests are also represented in **Figure 5.10 D**, showing decreased values as the CNF content increased in the formulation and indicating elastic and gel-like

behavior for all formulations. Moreover, for the formulations with equal CNF content, chloramphenicol-loaded inks showed lower tan δ values than curcumin loaded ones, probably due to the higher drug amount present in A-CNF-clph ink formulations.

In conclusion, the addition of either curcumin or chloramphenicol to the developed A-CNF based inks increased the viscosity and shear-thinning behavior of the unloaded A-CNF inks. Moreover, these drug-loaded biomaterial inks guaranteed shape retention of the 3D printed samples due to the gel-like behavior and viscoelasticity higher than the observed for unloaded A-CNF ink formulations.

5.5.2. 3D printing of drug-loaded A-CNF inks and scaffolds characterization

A-CNF-cur and A-CNF-clph biomaterial ink formulations were 3D printed, showing in general suitable printing performance, filament uniformity, shape retention and accuracy on CAD model reproduction (**Figure 5.11 A**).

Prism and cylinder shapes with similar volume but different surface area were 3D printed for A-CNF-cur and A-CNF-clph, respectively, demonstrating that these biomaterial inks reproduced successfully the predetermined CAD model. All A-CNF-cur inks, A-CNF3-clph and A-CNF4-clph formulations presented suitable printability, correct layer deposition and shape fidelity. However, the 3D printer used was not able to supply the necessary force to extrude A-CNF5-clph ink through the nozzle and thus, this biomaterial ink was not used for further experiments.

In order to evaluate the capacity of A-CNF based scaffolds to release hydrophobic and hydrophilic drugs simultaneously, both curcumin and chloramphenicol were added to A-CNF3 ink formulation in the same contents, as it was previously used for A-CNF-cur and A-CNF-clph inks (**Figure 5.11 B**). A-CNF based formulation with 3 wt. % of CNF was chosen to ensure its extrusion through the nozzle during 3D printing after the addition of the drugs, supported by previous rheological measurements.

5.5.2.1. Post-printing processes

After the 3D printing process of A-CNF-cur based inks, A-CNF3-clph, A-CNF4-clph and A-CNF3-cur-clph ink formulations, the obtained samples were subjected to post-printing processes in order to retain the 3D structure (**Figure 5.11**). These post-printing processes consisted in freeze-drying and ionic crosslinking of the structure through Ca^{2+}. The printed samples were crosslinked in a $CaCl_2$ 0.5 M solution for 4 h and then air-dried to obtain pharmaceutical forms. As it could be observed in the images, the Ca^{2+}

crosslinked samples lose their accuracy on shape reproduction due to the contraction of the sample as a consequence of the ionic bond formation during the crosslinking process, while the freeze-dried scaffolds preserved the original shape.

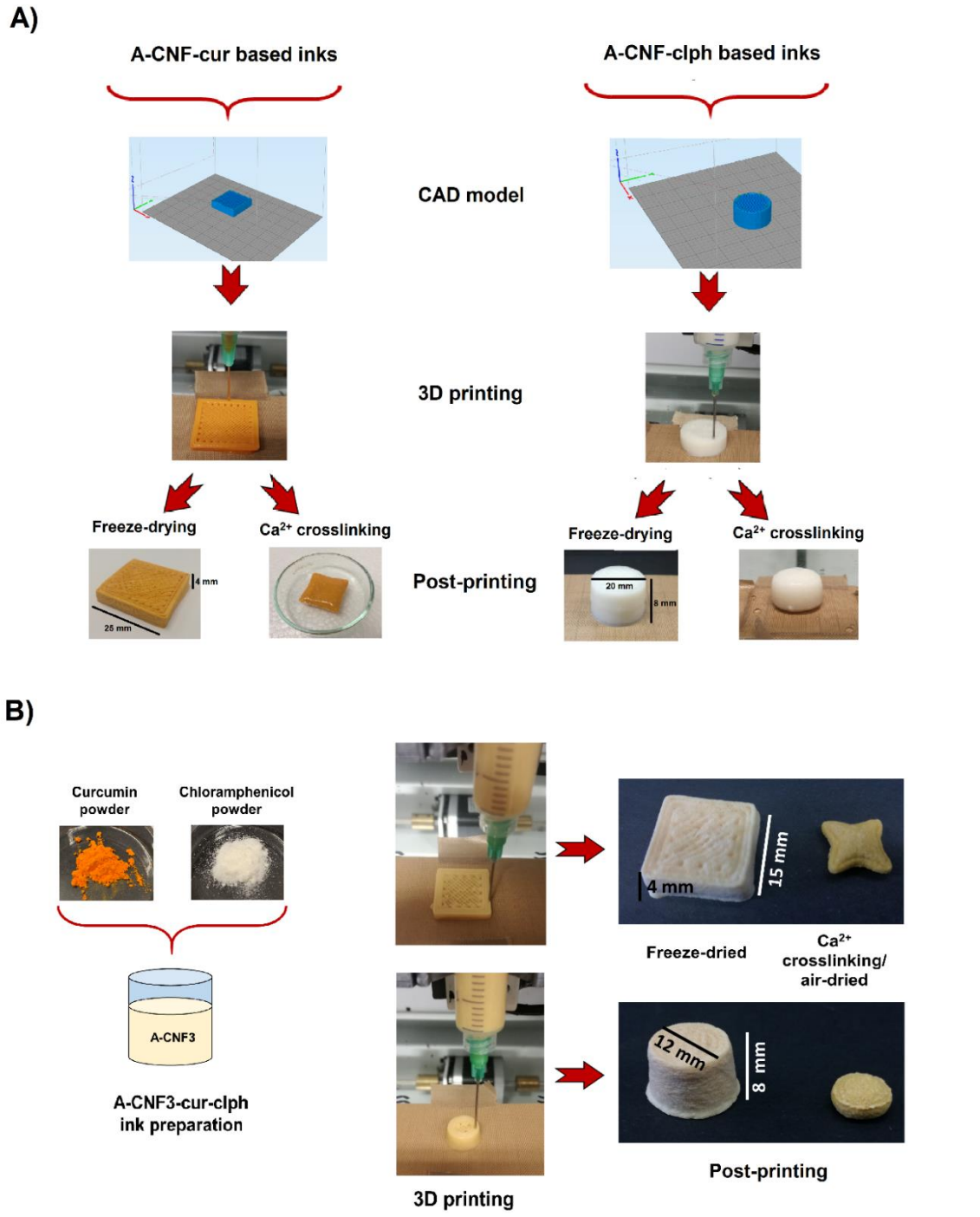

Figure 5.11. *Schematic representation of 3D printing process of drug-loaded A-CNF based biomaterial ink formulations: from CAD models, 3D printing and finally post-printing processes that consisted in freeze-drying or Ca^{2+} crosslinking. A) Left images corresponded to A-CNF3-cur ink printed in a prism shape and right images represented A-CNF3-clph ink 3D printed as cylindrical samples. B) Schematic representation of A-CNF3-cur-clph ink preparation, 3D printing in different shapes and the result after post-printing processes.*

Developed A-CNF3-cur-clph biomaterial ink was successfully 3D printed in cylindrical and patch shapes, and the obtained samples were also freeze-dried or Ca^{2+} crosslinked and air-dried afterwards to manufacture pharmaceutical tablets with different characteristics, morphologies and sizes as it can be seen in **Figure 5.11 B**.

5.5.2.2. Morphological characterization of the scaffolds

The morphology of freeze-dried and Ca^{2+} crosslinked/air-dried drug-loaded A-CNF scaffolds was analyzed by SEM to check the morphological differences between the two post-printing processes. The images of surface, cross-section and inner part of freeze-dried and Ca^{2+} crosslinked/air-dried scaffolds are shown in **Figure 5.12**.

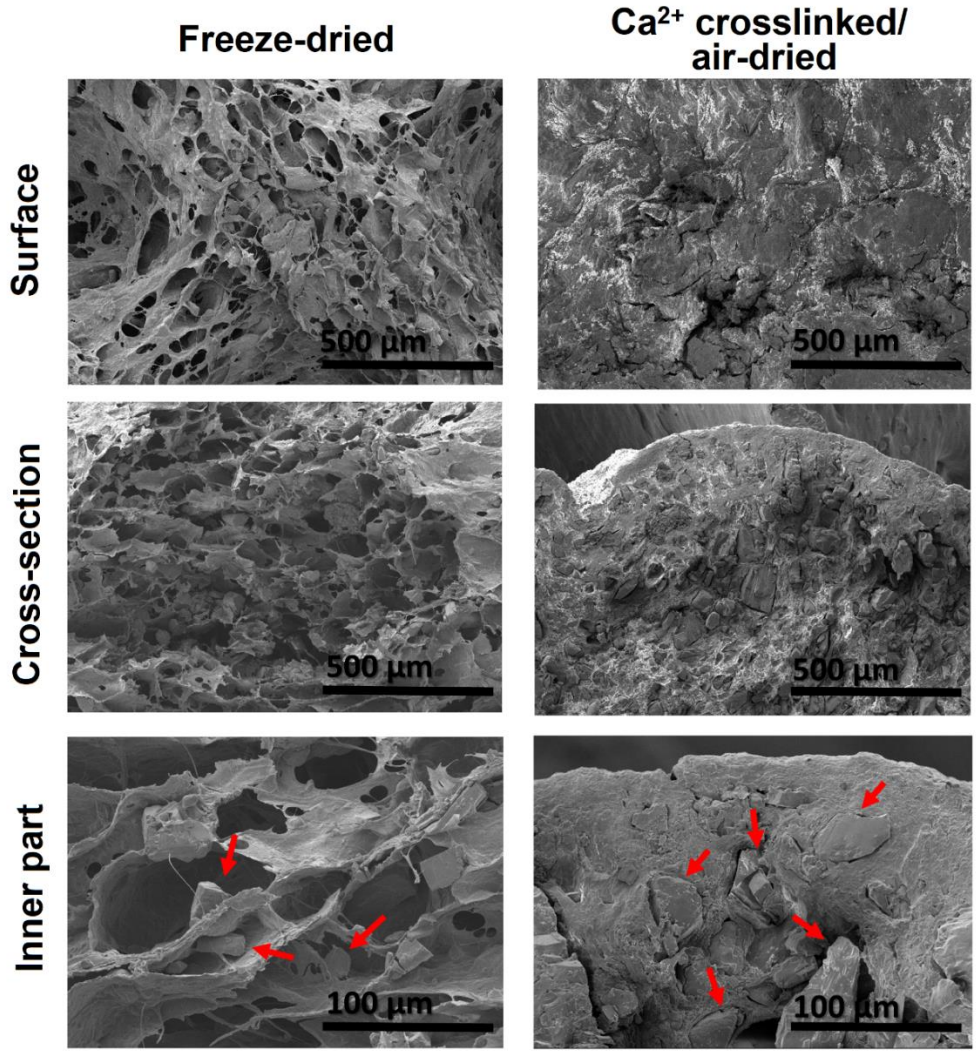

Figure 5.12. *SEM images of freeze-dried and Ca^{2+} crosslinked/air-dried A-CNF3-cur-clph scaffolds. Upper images corresponded to the surface, middle images to the cross-section and down images corresponded to inner part of the scaffolds. Red arrows indicate the drug crystals.*

As it could be appreciated, freeze-dried scaffold showed a porous matrix throughout the tablet, in the surface as well as in the cross-section, as it was previously observed for A-CNF based freeze-dried samples. In the inner-part image, drug crystals (red arrows) were observed into the porous structure, distributed throughout the scaffold. The morphology of Ca^{2+} crosslinked/air-dried scaffolds was also studied. The SEM images revealed that in this case, an enveloped compact form was obtained due to the higher ionic crosslinking achieved in the external part compared to the inner part of the sample. In these compact forms, drug crystals were also observed into the A-CNF matrix (red arrows).

In conclusion, the SEM images revealed that the drugs were uniformly distributed throughout the loaded A-CNF samples. The porous and compact morphologies achieved after freeze-drying or Ca^{2+} crosslinking/air-drying, respectively, suggested possible differences in drug release patterns.

5.5.3. *In vitro* drug delivery tests

The capacity of drug release from 3D printed A-CNF-cur, A-CNF-clph and A-CNF3-cur-clph samples, both freeze-dried and Ca^{2+} crosslinked/air-dried forms, was evaluated *in vitro*. The released amount of drugs was measured by UV-VIS-NIR spectroscopy at different time points.

5.5.3.1. Curcumin release

Curcumin release from A-CNF-cur based scaffolds was tested and the delivery patterns are shown in **Figure 5.13**. As it can be observed, curcumin release was faster in freeze-dried forms than in Ca^{2+} crosslinked/air-dried ones for all formulations. It was also observed, that curcumin delivery was carried out through progressive scaffold disintegration and subsequent release of the drug to the physiological medium for both freeze-dried and crosslinked tablets. The porous structure and the high water absorption capacity of the freeze-dried scaffolds allowed faster water entry causing scaffold disintegration, which triggered in shorter time of curcumin release than in case of Ca^{2+} crosslinked ones. *In vitro* curcumin release values less than 60 % in the first 8 h from chitosan-based hydrogels were reported by Nakawaga et al. [15], being slower than in the freeze-dried samples. The envelope observed in the Ca^{2+} crosslinked forms could retard the water absorption into the scaffold until the progressive loss of formed coat, and consequently, cause a slower scaffold disintegration and slower curcumin release. In addition, the internal compact microstructure could also contribute to delay drug

release. Curcumin release values of 42.5 % in the first 4 h from crosslinked cress seed gum hydrogels were reported by Shahbazizadeh et al. [16], being higher than the values measured for A-CNF-cur Ca^{2+} crosslinked/air-dried scaffolds.

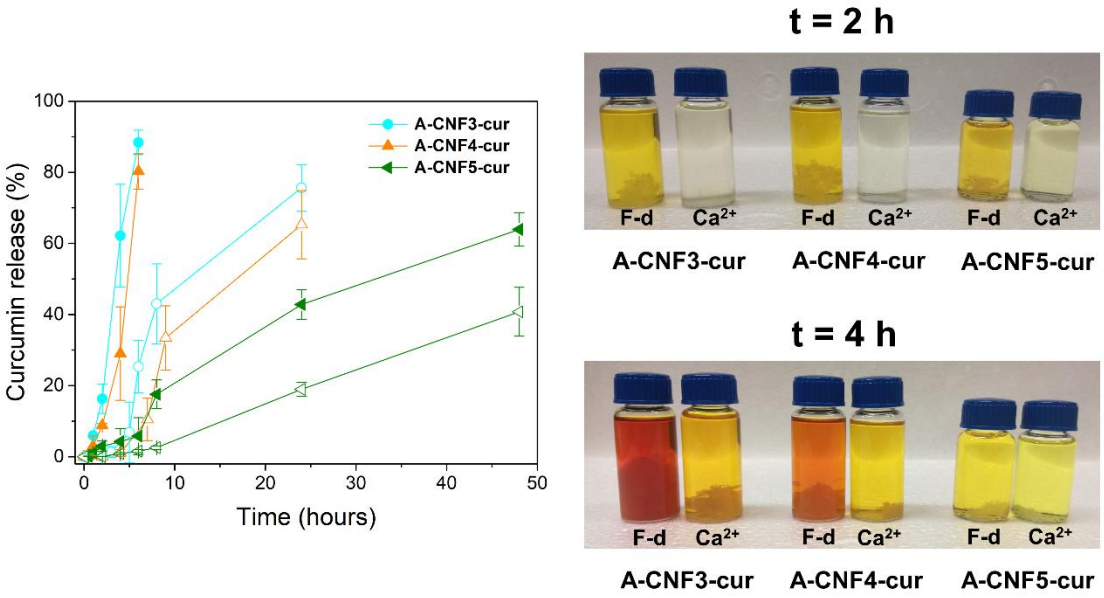

Figure 5.13. *Release patterns from A-CNF-cur based tablets. Curcumin release from A-CNF-cur freeze-dried (solid symbols) and Ca^{2+} crosslinked/air-dried (open symbols) scaffolds. Images of curcumin release taken at 2 and 4 hours from the A-CNF-cur based freeze-dried (F-d) and Ca^{2+} crosslinked/air-dried (Ca^{2+}) scaffolds.*

Regarding the effect of the CNF content in curcumin release patterns, A-CNF3-cur and A-CNF4-cur showed similar release patterns and shorter delivery time than A-CNF5-cur, in both freeze-dried and Ca^{2+} crosslinked/air-dried scaffolds. Higher content of CNF into the scaffolds leaded to lower porosity and greater stiffness, which triggered a slower water uptake and consequently, lower disintegration and slower curcumin release. As it can be observed in **Figure 5.13** (right images), large differences in curcumin release between freeze-dried and Ca^{2+} crosslinked/air-dried samples, as well as the CNF content were noticed. After 2 h, curcumin was hardly delivered from Ca^{2+} crosslinked/air-dried scaffolds compared to the freeze-dried ones. After 4 h, the differences in the release patterns remained significant and more evident among the three formulations depending on their CNF content.

In conclusion, curcumin release kinetics was found to be dependent on the CNF content and the morphology of the sample (porous or compact) that conditioned the disintegration degree of the scaffolds. The freeze-dried forms would improve the bioavailability of this hydrophobic drug in respect of the Ca^{2+} crosslinked/air-dried tables

and thus, it can represent an advantageous method to enable the delivery of hydrophobic drugs that present low solubility in physiological conditions.

5.5.3.2. Chloramphenicol release

Chloramphenicol release patterns from A-CNF3-clph and A-CNF4-clph are shown in **Figure 5.14**.

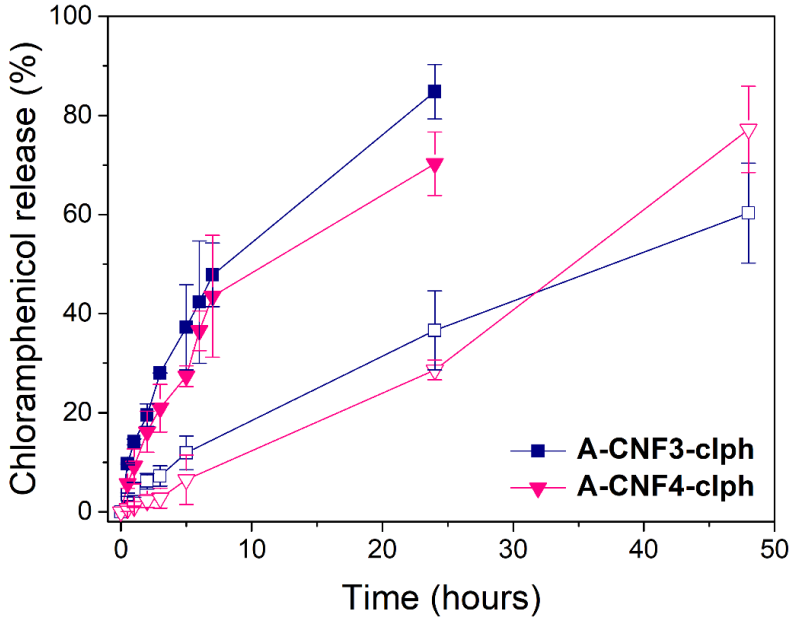

Figure 5.14. *Chloramphenicol release patterns from A-CNF3-clph and A-CNF4-clph scaffolds. Solid symbols represent freeze-dried scaffolds and open symbols represent Ca^{2+} crosslinked/air-dried scaffolds.*

As it could be observed, chloramphenicol release performed faster in freeze-dried scaffolds than Ca^{2+} crosslinked/air-dried ones, as it was previously observed in curcumin release patterns. A-CNF porous matrix from freeze-dried scaffolds again enabled a faster drug release to the physiological medium, while Ca^{2+} crosslinking/air-drying method provided a compact structure that increased the delivery time of chloramphenicol. Among 60-80 % of drug was measured in 24 h for freeze-dried forms whereas around 50-70 % of chloramphenicol were released in 48 h from Ca^{2+} crosslinked tablets. In this case, chloramphenicol release was not triggered by the disintegration of the scaffold since the A-CNF matrices remained almost complete after the experiments, suggesting that the release occured due to its hydrophilic character and its rapid dissolution into the physiological medium. There were no remarkable differences in the release patterns between the two formulations regarding the CNF content, suggesting that the amount of CNF present in the scaffolds did not interfere in the chloramphenicol release. Release

values of almost 100 % of chloramphenicol in 24 h from porous cellulose-based hydrogels were reported by Laçin et al. [17], while release values of 80 % in 6 h from polyvinyl alcohol-sodium alginate crosslinked hydrogels were reported by Xie et al. [18], representing a fast release than those observed in A-CNF-clph forms. Therefore, the Ca^{2+} crosslinking/air-drying post-printing method represents an option to retard the delivery of hydrophilic drugs in physiological conditions during larger periods and thus, avoid their rapid elimination from the body.

5.5.3.3. Curcumin-chloramphenicol release

Curcumin and chloramphenicol simultaneous release from A-CNF3-cur-clph scaffolds was *in vitro* evaluated. 3D printed A-CNF3-cur-clph scaffolds in prism and cylindrical shapes, both freeze-dried and Ca^{2+} crosslinked/air-dried were tested and their release patterns are shown in **Figure 5.15.**

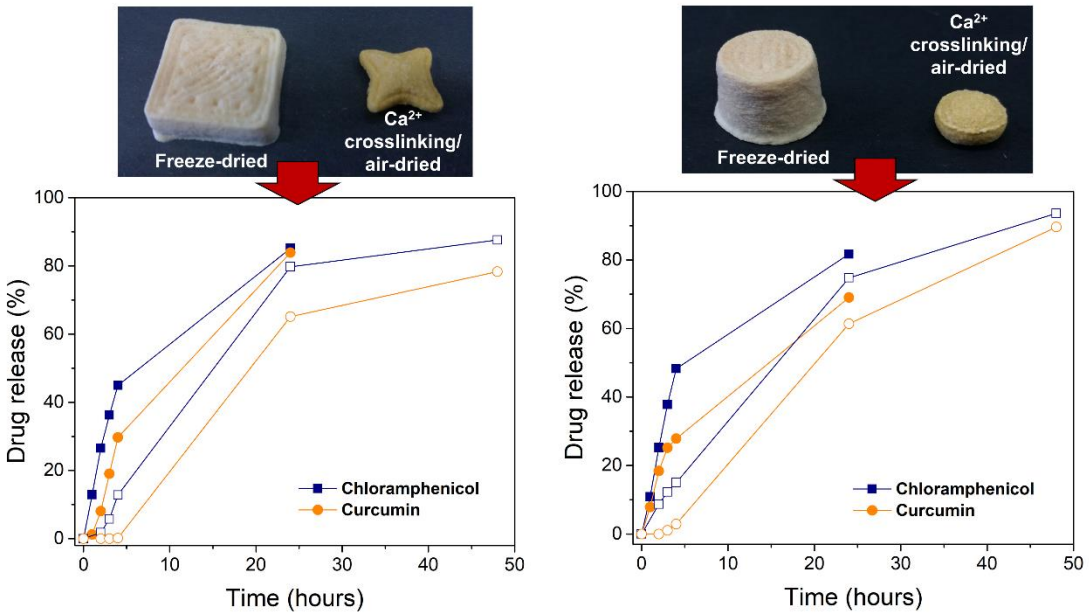

Figure 5.15. *Curcumin and chloramphenicol simultaneous release curves from the A-CNF3-cur-clph freeze-dried (solid symbols) and Ca^{2+} crosslinked/air-dried (open symbols) scaffolds. Left graph represent drug release from prism shape samples and right graph represent drug release from cylindrical ones.*

It was observed that the release of both drugs was performed faster in freeze-dried scaffolds than in Ca^{2+} crosslinked/air-dried forms, following the same tendency described before for A-CNF-cur and A-CNF-clph scaffolds. No remarkable differences in release patterns between the prism shape and cylindrical ones were observed for chloramphenicol, whereas small differences were observed in curcumin delivery, since

it was delayed in respect to the previous release curves when this drug was delivered alone, in both freeze-dried and Ca^{2+} crosslinked/air-dried scaffolds. A-CNF3-cur-clph samples, both prism shape and cylinders, showed lower surface area than A-CNF3-cur prism samples, so these differences in the surface area could directly retard the disintegration degree of these pharmaceutical forms and thus, curcumin release. However, chloramphenicol release patterns were similar than when it was delivered alone, in either freeze-dried or Ca^{2+} crosslinked/air-dried samples, demonstrating that the release of this drug did not depend on the scaffold disintegration or the surface area.

These release curves demonstrated that the surface area and scaffold disintegration did not affect to the chloramphenicol release from A-CNF based scaffolds, whereas curcumin delivery was directly caused by the disintegration of the sample, as it was previously observed when it was delivered alone, and this disintegration degree depends on the surface area of the 3D printed sample. The design of a porous drug delivery scaffold with specific surface area could be a method to control the release of hydrophobic drugs in physiological conditions.

5.6. Conclusions

In this chapter, A-CNF based ink formulations were developed and rheologically characterized in order to check their properties for 3D printing. Biomaterial inks with CNF contents above 3 wt. % showed high viscosity, shear thinning behavior and viscoelastic properties suitable for 3D printing technology, which were corroborated after 3D printing performance. A-CNF3, A-CNF4 and A-CNF5 showed accuracy on CAD model reproduction and shape fidelity of the printed samples. The A-CNF based scaffolds were freeze-dried and porous matrices were achieved, showing less porosity but higher mechanical properties as the CNF content increased, while the swelling capacity and disintegration degree of the scaffolds decreased with the reduction of the porosity.

Regarding the potential application of the A-CNF 3D printed scaffolds for drug delivery, curcumin (hydrophobic) and chloramphenicol (hydrophilic) were added to suitable biomaterial inks. Rheological test showed that all formulations presented an increase of the viscosity and shear-thinning behavior in comparison to A-CNF biomaterial inks without drugs. Drug-loaded 3D printed samples with different shapes and sizes were freeze-dried to achieve low-density porous structures or Ca^{2+} crosslinked and air-dried, to create compact and stiff tablets.

In vitro drug release tests from A-CNF-cur and A-CNF-clph scaffolds, both freeze-dried and Ca^{2+} crosslinked/air-dried, revealed that the release was faster in all freeze-dried

scaffolds compared to Ca^{2+} crosslinked/air-dried ones in all cases. Hence, 3D printed and freeze-dried scaffolds with a porous structure could enable the release of hydrophobic drugs that present low solubility in physiological conditions, while Ca^{2+} crosslinking/air-dried tablets would delay the administration of hydrophilic drugs during longer periods, and thus, avoiding their rapid elimination from the body.

Release experiments carried out *in vitro* from A-CNF3-cur-clph pharmaceutical forms of both drugs simultaneously suggested that an increase of the surface area of the 3D printed samples could be a method to accelerate the release of hydrophobic drugs to the physiological medium, while the shape and size of the scaffold did not affect the delivery of hydrophilic drugs.

The developed A-CNF inks are suitable for manufacturing functional pharmaceutical forms through 3D printing technology for the controlled release of hydrophobic and hydrophilic drugs.

5.7. References

[1] Li H, Liu S, Li L. Rheological study on 3D printability of alginate hydrogel and effect of graphene oxide. Int J Bioprinting 2016;2:54–66. https://doi.org/10.18063/IJB.2016.02.007.

[2] Liu Z, Zhang M, Bhandari B, Yang C. Impact of rheological properties of mashed potatoes on 3D printing. J Food Eng 2018;220:76–82. https://doi.org/10.1016/j.jfoodeng.2017.04.017.

[3] Khalid A, Zhang L, Tetienne JP, Abraham AN, Poddar A, Shukla R, Tmljenovic-Hanic S. Intrinsic fluorescence from cellulose nanofibers and nanoparticles at cell friendly wavelengths. APL Photonics 2019;4:020803-020816. https://doi.org/10.1063/1.5079883.

[4] Hu L, Shi Y, Li JH, Gao N, Ji J, Niu F, Chen Q, Yang X, Wang S. Enhancement of oral bioavailability of curcumin by a novel solid dispersion system. AAPS PharmSciTech 2015;16:1327–1334. https://doi.org/10.1208/s12249-014-0254-0.

[5] Khalid F, Hassan SMF, Mushtaque M, Noor R, Ghayas S, Muhammad IN, Hassan F. Comparative analysis of biopharmaceutic classification system (BCS) based biowaiver protocols to validate equivalence of a multisource product. African J Pharm Pharmacol 2020;14:212–220. https://doi.org/10.5897/ajpp2020.5130.

[6] Kasten MJ. Clindamycin, metronidazole, and chloramphenicol. Mayo Clin Proc 1999;74:825–833.

[7] Yakub G, Toncheva A, Manolova N, Rashkov I, Danchev D, Kussovski V. Electrospun polylactide-based materials for curcumin release: Photostability, antimicrobial activity, and anticoagulant effect. J Appl Polym Sci 2016;133:1–11. https://doi.org/10.1002/app.42940.

[8] Sharma RA, McLelland HR, Hill KA, Euden SA, Steward WP, Gescher AJ, Steward WP. Pharmacodynamic and pharmacokinetic study of oral Curcuma extract in patients with colorectal cancer. Clin Cancer Res 2001;7:1894–1900.

[9] Dey S, Sreenivasan K. Conjugation of curcumin onto alginate enhances aqueous solubility and stability of curcumin. Carbohydr Polym 2014;99:499–507. https://doi.org/10.1016/j.carbpol.2013.08.067.

[10] Sookkasem A, Chatpun S, Yuenyongsawad S, Wiwattanapatapee R. Alginate beads for colon specific delivery of self-emulsifying curcumin. J Drug Deliv Sci Technol 2015;29:159–166. https://doi.org/10.1016/j.jddst.2015.07.005.

[11] Li B, Konecke S, Wegiel LA, Taylor LS, Edgar KJ. Both solubility and chemical stability of curcumin are enhanced by solid dispersion in cellulose derivative matrices. Carbohydr Polym 2013;98:1108–1116. https://doi.org/10.1016/j.carbpol.2013.07.017.

[12] Buffiere J, Balogh-Michels Z, Borrega M, Geiger T, Zimmermann T, Sixta H. The chemical-free production of nanocelluloses from microcrystalline cellulose and their use as Pickering emulsion stabilizer. Carbohydr Polym 2017;178:48–56. https://doi.org/10.1016/j.carbpol.2017.09.028.

[13] Sarmento B, Ferreira D, Veiga F, Ribeiro A. Characterization of insulin-loaded alginate nanoparticles produced by ionotropic pre-gelation through DSC and FTIR studies. Carbohydr Polym 2006;66:1–7. https://doi.org/10.1016/j.carbpol.2006.02.008.

[14] Chen H, Xie F, Chen L, Zheng B. Effect of rheological properties of potato, rice and corn starches on their hot-extrusion 3D printing behaviors. J Food Eng 2019;244:150–158. https://doi.org/10.1016/j.jfoodeng.2018.09.011.

[15] Nakagawa K, Sowasod N, Tanthapanichakoon W, Charinpanitkul T. Hydrogel based oil encapsulation for controlled release of curcumin byusing a ternary system of chitosan, kappa-carrageenan, and carboxymethylcellulose sodium salt. LWT - Food Sci Technol 2013;54:600–605. https://doi.org/10.1016/j.lwt.2013.06.011.

[16] Shahbazizadeh S, Naji-Tabasi S, Shahidi-Noghabi M, Pourfarzad A. Development of cress seed gum hydrogel and investigation of its potential application in the delivery of curcumin. J Sci Food Agric 2021;101:6505–6513. https://doi.org/10.1002/jsfa.11322.

[17] Laçin NT. Development of biodegradable antibacterial cellulose based hydrogel membranes for wound healing. Int J Biol Macromol 2014;67:22–27. https://doi.org/10.1016/j.ijbiomac.2014.03.003.

[18] Xie L, Wei H, Kou L, Ren L, Zhou J. Antibiotic drug release behavior of poly (vinyl alcohol)/sodium alginate hydrogels. Materwiss Werksttech 2020;51:850–855. https://doi.org/10.1002/mawe.201900163.

Chapter 6

A-WBPU inks for 3D printing of tailor-made mesh implants for hernia repair

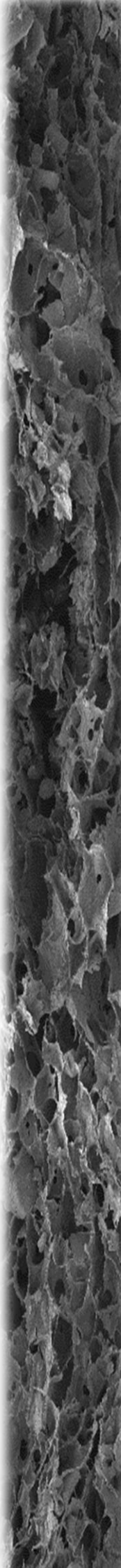

CHAPTER 6 – A-WBPU inks for 3D printing of tailor-made mesh implants for hernia repair

6. Alginate-WBPU inks for 3D printing of tailor-made mesh implants for hernia repair

6.1. Aim of the chapter

The objective of this chapter is the development of tailor-made mesh implants from safer materials adaptable to specific needs of the patients through 3D printing technology, which would suppose an alternative for conventional ones. Hernia injuries are the main conditions where mesh implants are needed to provide a suitable reinforcement of the damaged tissue. Commercial implants made of polypropylene (PP) knitted fibers are commonly used for this application, but complications related to the lack of flexibility, elasticity or mesh infection have been reported. These commercial meshes usually present high tensile strength values, as well as poor elasticity that could restrict physiological movements. The materials commonly used in commercial mesh fabrication are non-absorbable synthetic polymers that can induce high inflammatory responses and form adhesion with the viscera. Therefore, it is important to use safer materials with proper characteristics to enable tissue ingrowth of the damaged area and minimize immunological host response caused by either foreign materials or possible post-surgical infections.

Alginate and WBPU films characterized in previous chapters presented high values of tensile strength and high elasticity and flexibility, respectively, in the performed mechanical analysis. Due to the versatility of these materials, their biocompatible character and their suitable mechanical and rheological properties, alginate and WBPU were chosen for the manufacture of these alternative implants. Both materials were blended in different proportions, and the prepared inks were properly characterized through rheological measurements to evaluate their suitability for 3D printing technology. The mesh implants were designed according to morphological characteristics observed in the commercial meshes since those properties such as pore size, mesh weight and thickness are important parameters to ensure proper reinforcement of the damaged area.

The developed 3D printed meshes were widely characterized in this chapter. Morphology, mechanical properties and tissue ingrowth were measured and compared with reported physiological values to evaluate the adequacy of these meshes for hernia repair application. Moreover, the addition of an antibiotic to the ink formulations was studied in order to manufacture meshes able to release this antibiotic in wound area and thus, avoiding possible infection complications.

6.2. A-WBPU inks preparation

Five different biomaterial ink formulations were prepared from alginate (A) and waterborne polyurethane (WBPU) dispersion. Alginate powder was added in 0.5, 1, 1.5, 2 and 2.5 wt. % in respect of the total amount of WBPU dispersion. Both materials were mixed gently with a mechanical stirrer until complete homogenization. The obtained biomaterial ink formulations were denoted as AX-WBPU, being X the A content in respect to the total amount of WBPU, and are summarized in **Table 6.1**. The antibiotic-loaded ink with chloramphenicol (clph) content of 5.5 wt. % in respect of the total solid content was prepared by adding it to A2.5-WBPU ink formulation.

Table 6.1. *Summary of developed A-WBPU biomaterial inks. Proportions of alginate and WBPU weights in the different formulations and total solid contents present in each formulation*.

Biomaterial ink formulation	Alginate/WBPU (w/w)	Total solid content (wt. %)
WBPU	0/100	40
A0.5-WBPU	0.5/100	41.2
A1-WBPU	1/100	42.5
A1.5-WBPU	1.5/100	43.7
A2-WBPU	2/100	44.8
A2.5-WBPU	2.5/100	46
A2.5-WBPU-clph	2.5/100	51.5

6.3. Rheological characterization of A-WBPU inks

In order to evaluate the suitability of the developed inks for 3D printing technology, rheological tests were performed as in previous chapters. First, flow viscosity curves versus shear rate increase were represented for the neat WBPU dispersion and the A-WBPU inks (**Figure 6.1 A**). WBPU dispersion showed low viscosity values at low and high shear rates, demonstrating that the neat WBPU presented Newtonian fluid characteristics. However, the five A-WBPU based inks presented shear-thinning behavior and high viscosities at low shear rates and thus, strong dependence of viscosity on shear rate changes and non-Newtonian fluids characteristics [1,2]. As the alginate content increased in the formulations, viscosity values at zero shear rate also increased, as it can be observed in **Table 6.2**.

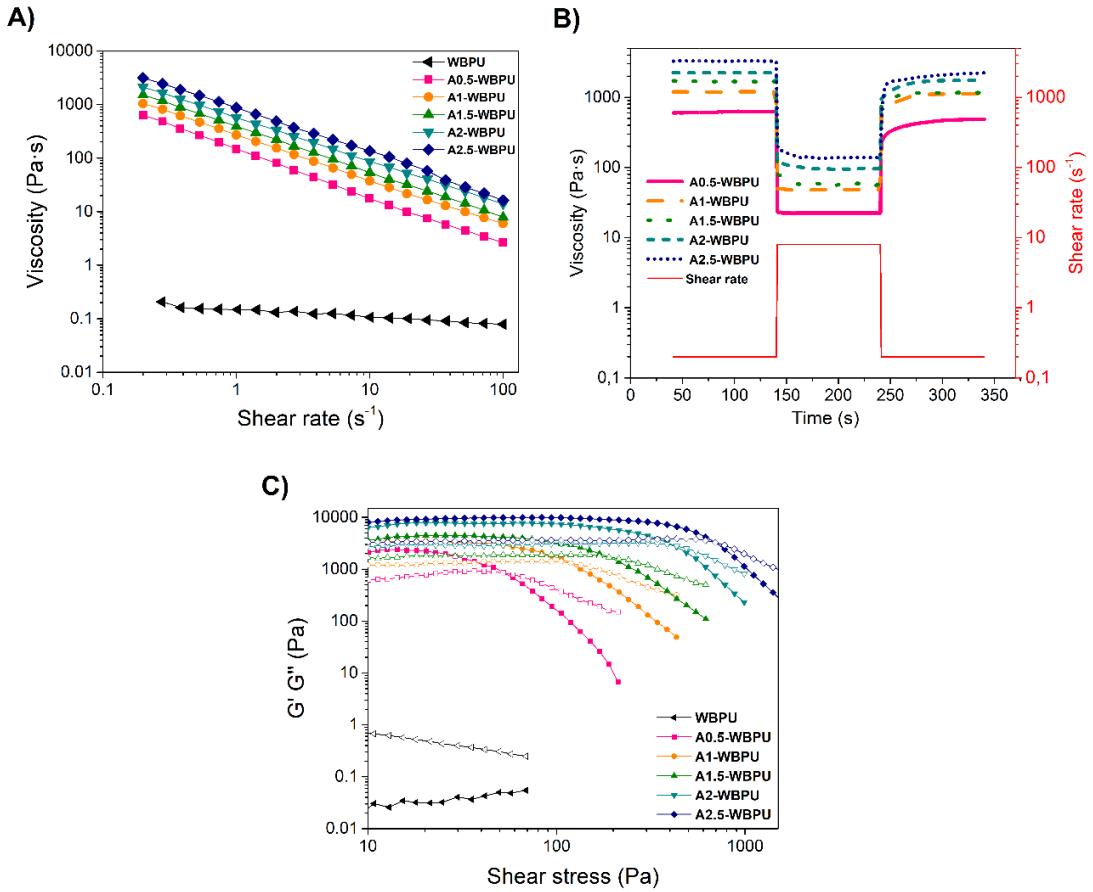

Figure 6.1. *Rheological characterization of WBPU and A-WBPU inks. A) Viscosity versus a shear rate increase. B) Viscosity recovery tests. C) Shear stress sweep tests where the storage modulus is represented by solid symbols and the loss modulus is represented by open symbols.*

Table 6.2. *Viscosity measured at 0.2 s^{-1}, power-law index, consistency coefficient, Pearson correlation coefficient, recovery percentage after 100 sec, G' in LVR and yield point values.*

Biomaterial ink	Viscosity (Pa·s)	n	K ($Pa \cdot s^n$)	R^2	Recovery (%)	G' in LVR (Pa)	Yield point (Pa)
WBPU	0.30 ± 0.09	0.87	0.14	0.95	-	-	-
A0.5-WBPU	615 ± 19	0.10	148.57	0.99	83 ± 5	2113 ± 280	54 ± 1
A1-WBPU	1018 ± 47	0.16	272.71	0.99	86 ± 7	3193 ± 665	117 ± 23
A1.5-WBPU	1450 ± 120	0.16	401.93	0.99	73 ± 6	4821 ± 654	192 ± 24
A2-WBPU	2093 ± 17	0.17	569.76	0.99	79 ± 6	7885 ± 362	429 ± 10
A2.5-WBPU	3024 ± 161	0.17	796.87	0.99	68 ± 1	9912 ± 122	712 ± 62

The Newtonian and non-Newtonian behavior of the WBPU dispersion and the A-WBPU ink formulations, respectively, were explained by comparing the experimental data with the power-law model (Eq. 3), as it has been done in previous rheological characterizations. Values of power-law index from 0.10 to 0.17 were observed for A-

WBPU formulations (**Table 6.2**) indicating strong shear-thinning and non-Newtonian behavior, while the n value for neat WBPU was 0.87, close to 1, denoting thus the Newtonian-like behavior of this dispersion [3]. Consistency coefficient increased as the alginate content did (from 148 to 797 $Pa \cdot s^n$), and Pearson correlation coefficient showed strong relationship among the experimental results and the theoretical model.

Viscosity recovery tests were also carried out and the results are shown in **Figure 6.1 B**. The recovery percentages were calculated and the obtained results were collected in **Table 6.2,** showing values from 68 to 90 % for all inks that suggested shape fidelity after 3D printing.

Oscillatory sweep tests were also performed to study the viscoelastic characteristics of the developed A-WBPU inks. Storage modulus and loss modulus versus shear stress are shown in **Figure 6.1 C**. WBPU dispersion presented G'' always above G', which indicated liquid-like and viscous characteristics. However, the five A-WBPU ink formulations showed always G' above G'' in the LVR, indicating solid-like behavior. The G' values of the different formulations in LVR could be related to shape fidelity characteristics and are collected in **Table 6.2**. The observed increase in G' values of A-WBPU inks (from 2113 ± 280 to 9912 ± 122 Pa) as the alginate content raised in the formulation suggested that the 3D printed samples could retain the shape if they are compared to the values of 647, 1154, 2400 and 4000 Pa reported in the literature [4,5].

As the shear stress was increased during the experiment, the values of G' drop below G'', reaching a viscous and liquid-like behavior at highest shear stress rates [6]. The measured yield point values (G'=G'') increased as the alginate content raised in the A-WBPU based formulations from 54 ± 1 to 712 ± 62 Pa and thus, the required force to print it [1].

The rheological characterization results showed that the neat WBPU dispersion behaved as a Newtonian fluid with poor characteristics for 3D printing. However, after the addition of different contents of alginate to the dispersion, the obtained blends achieved desirable characteristics for 3D printing, acting this alginate as rheological modifier of the biomaterial inks. The developed A-WBPU formulations reached high viscosity, shear-thinning behavior and the viscoelasticity required for a suitable 3D printing performance.

6.4. 3D printing and characterization of the meshes

After the rheological characterization, the five developed A-WBPU inks were 3D printed according to a CAD model of a mesh featuring hexagonal shape holes. The results are

shown in **Figure 6.2**. All developed ink formulations presented good printability, proper layer deposition, accuracy on reproduction of mesh model and shape fidelity, demonstrating that the five A-WBPU ink formulations were suitable for 3D printing technology, as it was previously demonstrated by rheological characterization. After 3D printing A-WBPU printed meshes were dried at room temperature showing uniformity and maintaining the original shape and size after air-drying.

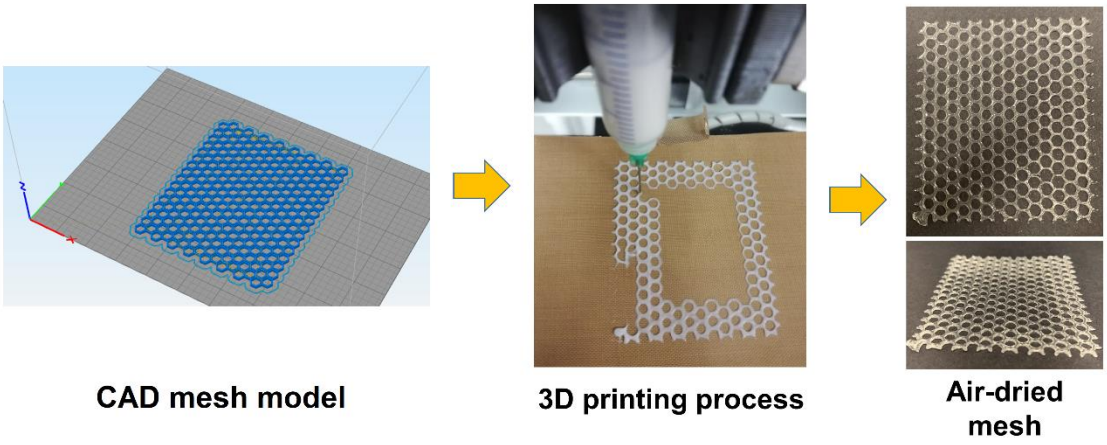

Figure 6.2. *3D printing process of A-WBPU inks: from CAD model to air-drying process.*

6.4.1. Morphological characterization of A-WBPU meshes

After 3D printing and air-drying process, the meshes were morphologically characterized. Morphological characteristics such a mesh weight, the diameter and shape of the pores, the thickness or the material degradation and subsequent absorption into the body are important parameters to ensure a proper implantation and behavior of the mesh during patient hernia recovery. Pore diameter in the range of 0.1-0.6 mm is considered small, while medium pore size is established between 0.6-1 mm, and pores with diameters larger than 2 mm are denominated as very large. Mesh weight is another important parameter related to the amount of foreign material present in the host body. According to some authors, meshes can be classified as lightweight (35-70 $g \cdot m^{-2}$), standard weight (70 -140 $g \cdot m^{-2}$) and heavyweight meshes (≥ 140 $g \cdot m^{-2}$) [7-9].

In **Figure 6.3** the uniformity and transparency of dried meshes from the five A-WBPU inks can be appreciated, what would enable their successful implantation during surgery process [7]. The mentioned morphological parameters are listed in **Table 6.3.** A-WBPU meshes presented weight values higher than 140 $g \cdot m^{-2}$ and were then classified as heavyweight meshes [8].

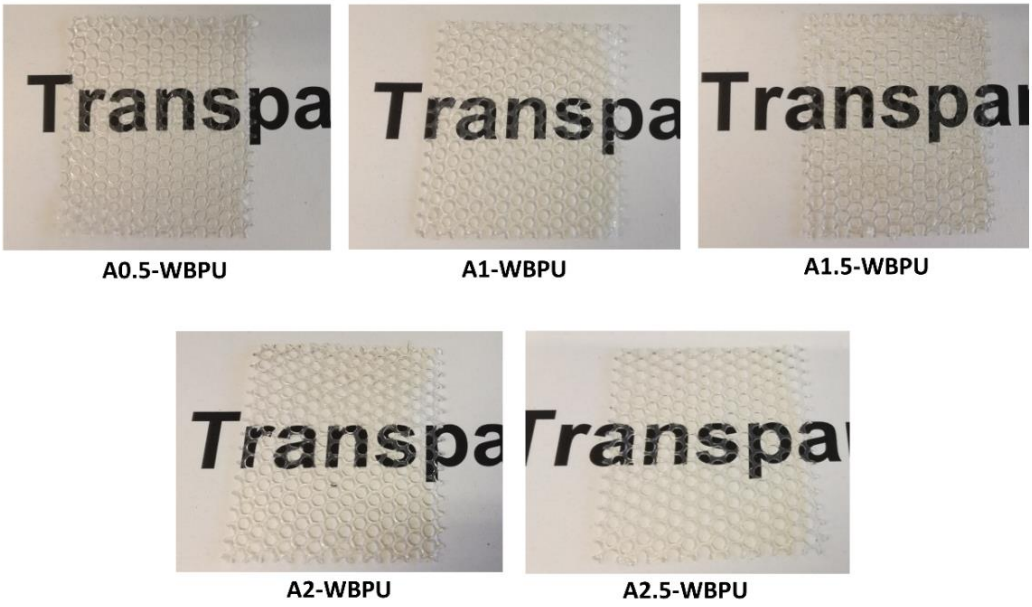

Figure 6.3. *Images of the five A-WBPU meshes after air-drying process.*

Table 6.3. *Morphological parameters of A-WBPU meshes.*

Mesh formulation	Weight ($g \cdot m^{-2}$)	Pore diameter (mm)	Thickness (mm)
A0.5-WBPU n=4	307.47 ± 49.95 (heavy weight)	2.75 ± 0.22 (very large)	0.48 ± 0.03
A1-WBPU n=4	315.40 ± 60.44 (heavy weight)	2.95 ± 0.05 (very large)	0.67 ± 0.02
A1.5-WBPU n=4	293.72 ± 63.50 (heavy weight)	2.69 ± 0.24 (very large)	0.52 ± 0.08
A2-WBPU n=4	334.49 ± 58.96 (heavy weight)	2.76 ± 0.23 (very large)	0.59 ± 0.08
A2.5-WBPU n=4	313.02 ± 45.54 (heavy weight)	3.05 ± 0.06 (very large)	0.50 ± 0.03

Regarding the pore shape and size, the hexagonal pores of the printed A-WBPU meshes measured around 2.8 mm (**Figure 6.4 A**) and were therefore classified as very large pore size meshes due to their pore diameter larger than 2 mm [8,9]. As it has been reported in the literature, that hexagonal pore shape allow better tissue regeneration than the diamond or square pore shapes usually present in commercial meshes, as well as

very large pores facilitate the tissue ingrowth and avoid granuloma infection [9,10]. Thickness of the meshes is another important parameter of hernia mesh and A-WBPU based meshes presented values around 0.55 mm, which is the standard value for hernia meshes compared to commercial ones [11,12]. These studied morphological parameters were compared among the different mesh formulations and no significant differences in weight, thickness, and pore diameter were observed ($p>0.05$ for all characteristics).

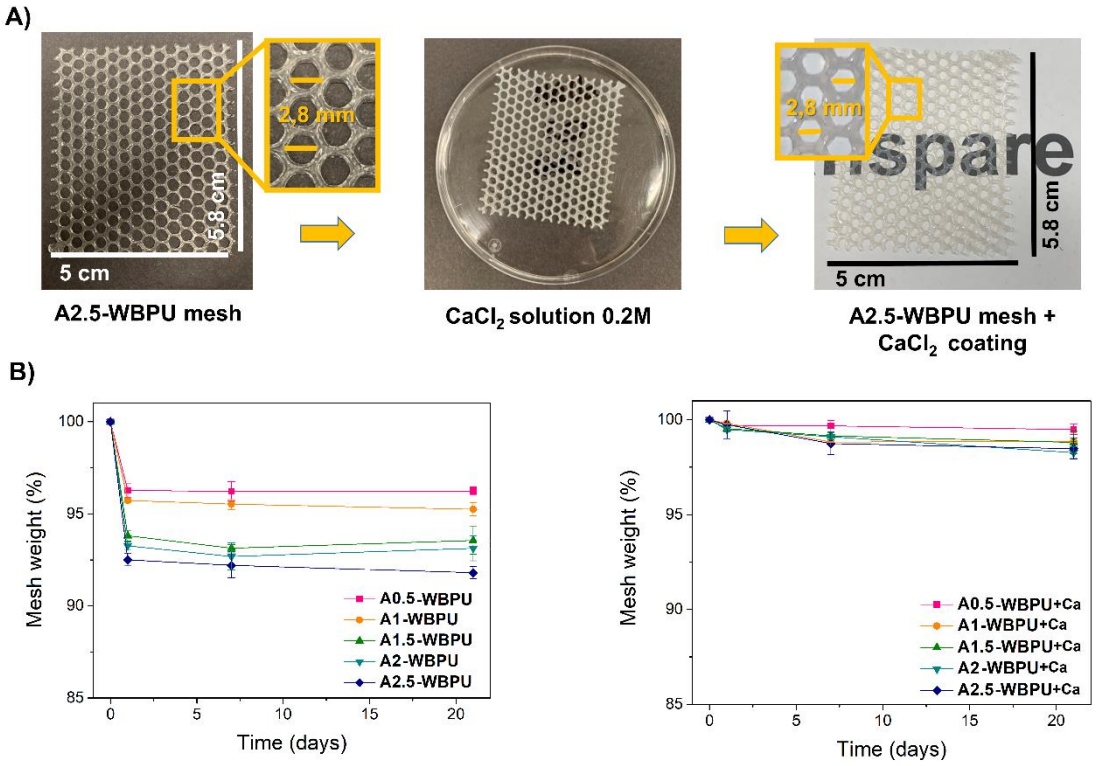

Figure 6.4. *A) Morphological properties of A2.5-WBPU mesh after air-drying, $CaCl_2$ coating process and subsequent morphological characterization of the A2.5-WBPU+Ca mesh. B) In vitro degradation studies of A-WBPU meshes (left graph) and A-WBPU+Ca meshes (right graph).*

In conclusion, the morphological characteristics of these meshes did not depend on the alginate content in the ink formulation, but on the CAD mesh model before 3D printing and the total solid content. The desired morphological characteristics of the meshes could be achieved through the modification of the CAD mesh model dimensions during the manufacturing process, and thus, the size of the mesh could be adjust to the specific patient injury.

In vitro degradation studies of the meshes were performed and the results are presented in **Figure 6.4 B** (left image). It was observed that the mesh weight decreased in the first 24 h as the alginate content did in the formulations, and then the weight was maintained during 21 days, which is generally the minimum time to recover from hernia surgery [13],

and consequently, considering these meshes as partially absorbable. Dried WBPU cannot be degraded or dissolved in aqueous media [14], while alginate could be dissolved by extracellular fluids and eliminated from the host body [15]. After the observation of these degradation results, it was concluded that in the first 24 hours, alginate from the meshes was fast dissolved in physiological conditions, and thus, the mesh structure and its properties might be affected. In order to avoid alginate loss, a $CaCl_2$ coating was applied to the A-WBPU meshes by introducing the air-dried meshes in a $CaCl_2$ 0.2 M solution for 24 hours (**Figure 6.4 A**). The Ca^{2+} cations from the solution stablished ionic interactions among carboxylic groups from both alginate and WBPU in the surface of the meshes, reinforcing their structure and avoiding the rapid loss of alginate in the PBS, as it was demonstrated in the *in vitro* degradation studies performed from the coated meshes (**Figure 6.4 B**, right graph). The mesh weight of all $CaCl_2$ coated A-WBPU meshes showed a slight change after 21 days of degradation experiment, but these meshes should still be considered as partially-absorbable meshes. Morphological parameters of these new A-WBPU+Ca meshes were also evaluated and summarized in **Table 6.4**.

Table 6.4. *Morphological characteristics of A-WBPU+Ca based meshes and commercial polypropylene mesh.*

Mesh formulation	Weight ($g \cdot m^{-2}$)	Pore diameter (mm)	Thickness (mm)
A0.5-WBPU+Ca n=4	294.68 ± 72.26 (heavy weight)	2.79 ± 0.22 (very large)	0.53 ± 0.05
A1-WBPU+Ca n=4	295.12 ± 53.87 (heavy weight)	3.03 ± 0.10 (very large)	0.56 ± 0.12
A1.5-WBPU+Ca n=4	284.49 ± 51.21 (heavy weight)	2.87 ± 0.13 (very large)	0.58 ± 0.05
A2-WBPU+Ca n=4	294.86 ± 53.62 (heavy weight)	2.90 ± 0.12 (very large)	0.57 ± 0.06
A2.5-WBPU+Ca n=4	285.80 ± 33.47 (heavy weight)	2.88 ± 0.12 (very large)	0.49 ± 0.02
Commercial PP n=1	37.90 (light weight)	3 (very large)	0.40

There were no significant differences in these characteristics between the coated and uncoated meshes ($p>0.05$ for all categories). The weight, pore size and thickness remained almost unchanged, as well as the dimensions and transparency, thus concluding that the $CaCl_2$ coating process did not affected to the morphological properties of the printed A-WBPU meshes.

A commercial mesh implant commonly used for hernia repair was also characterized. This implant is composed by a PP knitted fibers that remains into human body for a longer period and thus, considered as non-absorbable material [7]. The studied mesh is shown in **Figure 6.5** and its morphological characteristics are listed in **Table 6.4.**

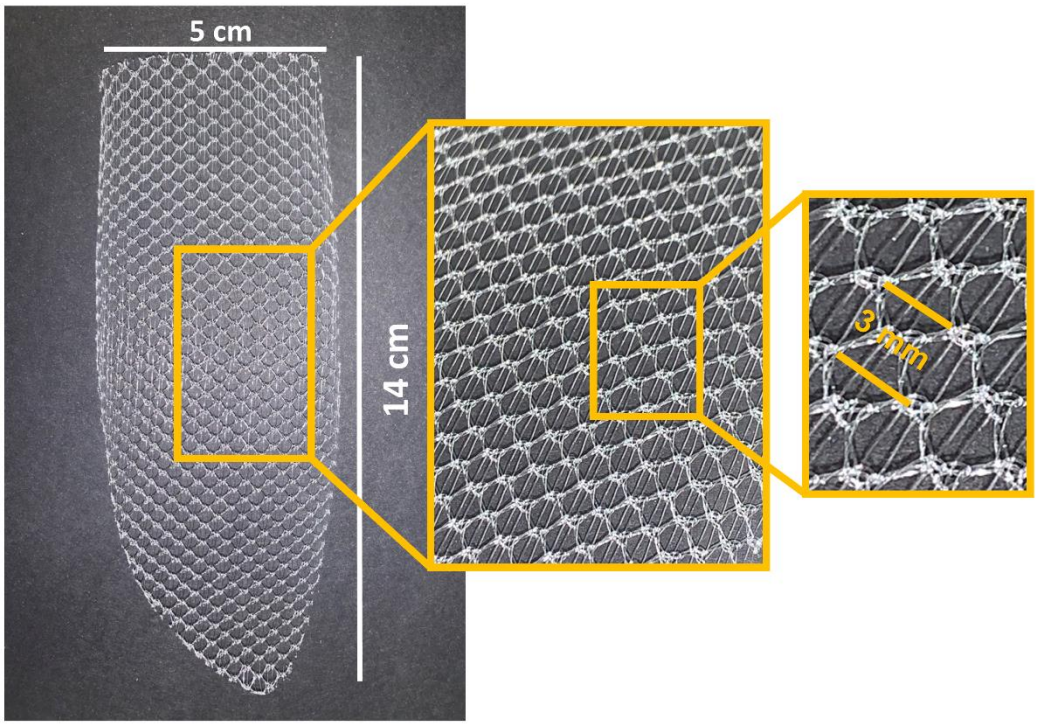

Figure 6.5. *Image of a commercial PP mesh usually employed in abdominal hernia injuries repair.*

The commercial mesh was classified as light weight mesh, presenting diamond shaped pores of 3 mm in diameter, thickness of 0.40 mm and a fiber diameter of 0.105 mm, which are common morphological characteristics from the most used meshes in hernia repair [16,17].

In conclusion, A-WBPU and A-WBPU+Ca meshes presented suitable morphological characteristics to perform as hernia repair implants that would contribute to tissue regeneration due to their very large hexagonal pores, which, as it has been reported in

the literature [9,10], avoids inflammatory reaction. Very large pores and transparency properties would enable their implantation, allowing better visibility of the structures and proper fixation. Moreover, the developed A-WBPU and A-WBPU+Ca meshes could be adapted to the specific patient injury, changing the dimensions of the CAD mesh model and thus, suitable and customized hernia mesh implants composed of alginate and WBPU can be manufactured by 3D printing technology.

6.4.2. Mechanical characterization of A-WBPU and A-WBPU+Ca

The developed A-WBPU and A-WBPU+Ca meshes were mechanically characterized to evaluate the suitability of the meshes to the biomechanical requirements of the human body [18,19]. Mechanical performance evaluation of the developed A-WBPU, A-WBPU+Ca and commercial PP meshes was performed by comparing them with strain data of human groin area. The meshes were gripped to pneumatic clamps and tensile tests were carried out as it can be observed in **Figure 6.6**.

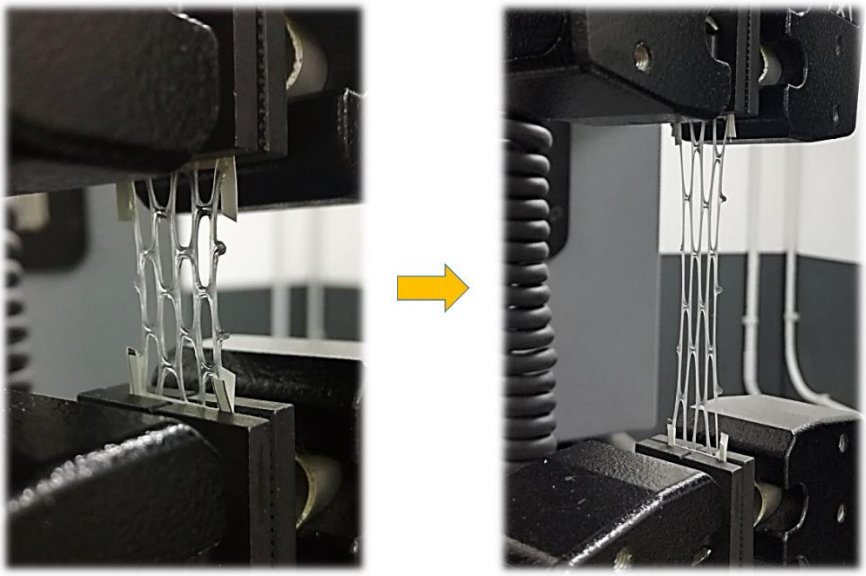

Figure 6.6. *Images of mechanical tensile test of a A-WBPU based mesh.*

Mechanical parameters such as tensile stiffness, breaking force, elastic limit and elastic elongation of the meshes were evaluated and shown in **Table 6.5**. All 3D printed meshes presented isotropic behavior since they responded equally when they were tensioned in both longitudinal and transversal directions, and consequently their fixation in the injury zone would be easier than commercial anisotropic ones, without paying attention to a specific orientation, and enabling optimal adaptation to the anatomical structures as well [20]. On the contrary, commercial PP mesh showed anisotropic behavior, meaning that it must be inserted in the appropriate orientation to match the physiological stress [12].

Table 6.5. *Tensile stiffness, breaking force, elastic limit and elastic elongation of the studied A-WBPU, A-WBPU+Ca and commercial PP meshes (in longitudinal and transversal directions).*

Mesh formulation	Tensile stiffness ($N \cdot mm^{-1}$)	Breaking force ($N \cdot cm^{-1}$)	Elastic limit ($N \cdot cm^{-1}$)	Elastic elongation (%)
A0.5-WBPU n=10	0.99 ± 0.23	14.89 ± 3.09	5.22 ± 0.67	76.97 ± 8.02
A1-WBPU n=10	1.83 ± 0.24	16.12 ± 1.51	7.34 ± 0.8	64.75 ± 3.25
A1.5-WBPU n=10	2.43 ± 0.48	17.40 ± 2.07	8 ± 0.81	57.15 ± 3.76
A2-WBPU n=10	3.80 ± 0.50	17.98 ± 0.62	9.24 ± 0.58	47.80 ± 5.42
A2.5-WBPU n=10	4.70 ± 0.60	19.17 ± 2.70	11.27 ± 0.95	42.63 ± 1.88
A0.5-WBPU+Ca n=8	1.03 ± 0.12	16.13 ± 3.24	5.24 ± 0.17	61.20 ± 5.15
A1-WBPU+Ca n=8	1.75 ± 0.41	20.10 ± 4.11	6.47 ± 2.81	54,82 ± 3.06
A1.5-WBPU+Ca n=8	3.02 ± 0.36	24.47 ± 1.21	11.14 ± 1.70	49.40 ± 3.00
A2-WBPU+Ca n=8	4.80 ± 0.50	26.29 ± 1.31	14.32 ± 0.91	40.52 ± 6.34
A2.5-WBPU+Ca n=8	4.51 ± 0.79	26.38 ± 1.08	15.83 ± 1.04	42.57 ± 6.60
Comm. PP long. n=6	3.03 ± 1.69	33.14 ± 11.66	3.8 ± 1.5	19.20 ± 3.06
Comm. PP transv. n=6	9.52 ± 0.84	57.17 ± 4.08	36.83 ± 3.20	39.23 ± 5.81

Tensile stiffness is referred to the ratio between the force that acts on an elastic material, and the displacement resulted in an uniaxial plane [20,21]. Results of the A-WBPU and A-WBPU+Ca meshes showed an increase in tensile stiffness values as the alginate content increased in the formulation, suggesting that the alginate contributed to the reinforcement of the mesh structure. Comparing the tensile stiffness of the developed meshes with the commercial PP, longitudinal value for the PP mesh was similar to the formulations with higher content of alginate, whereas the result of transversal value for PP was significantly higher than the measured for A-WBPU and A-WBPU+Ca meshes. Tensile stiffness values of 0.44 ± 0.12 $N \cdot mm^{-1}$ for 3D printed thermoplastic polyurethane meshes were reported in the literature [22], which are significantly lower than the obtained for all A-WBPU and A-WBPU+Ca meshes.

Breaking force is a mesh parameter equivalent to the tensile strength, referred as the maximum force measured in Newton that the mesh will withstand before breaking, in respect to the width of the tested specimen measured in centimeter [20,21]. Breaking force values of 16 $N \cdot cm^{-1}$ have been reported in the literature for small and groin hernias [7], [20]. The breaking force values of the developed A-WBPU meshes increased as the

alginate content raised in the formulations and, if the values are compared to the physiological ones reported, all of them would be able to support the required tensile strength of 16 N·cm^{-1} without breaking. However, it is crucial that the physiological tensile value of 16 N·cm^{-1} is close to the range of the elastic limit to enable the recovery of the implant after corporal movements.

The elastic limit of the developed meshes was calculated from the force-elongation curves as the force required to cause a plastic deformation of 0.2 % [23], and the graphical representation of A-WBPU and A-WBPU+Ca values is shown in **Figure 6.7 A.** The elastic limit values of the developed meshes were smaller than the required physiological tensile strength of 16 N·cm^{-1}. However, after the $CaCl_2$ coating, an increase of the elastic limit of the meshes was observed, reaching values of 15.83 ± 1.04 N·cm^{-1} for A2.5-WBPU+Ca formulation, and thus, achieving required physiological value of 16 N·cm^{-1} in the elastic zone. It was observed that the differences on elastic limit values among the formulations with and without $CaCl_2$ coating were higher as the alginate content increased, suggesting that the created crosslinking network also acted as mesh reinforcement, increasing its mechanical strength.

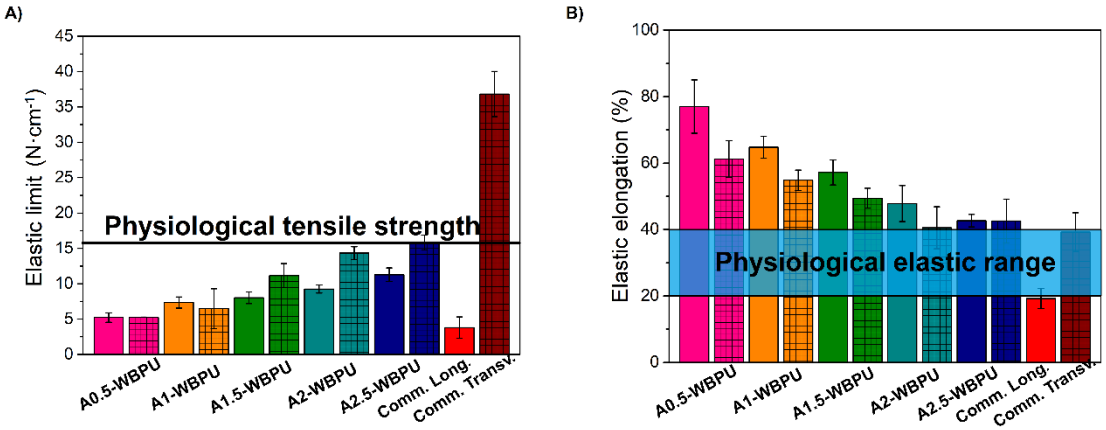

Figure 6.7. *Graphical representation of mechanical parameters of the A-WBPU, A-WBPU+Ca and commercial PP meshes: A) Elastic limit values and comparison to the physiological tensile strength value of 16 N·cm^{-1}. B) Measured elastic elongation values of the developed meshes and comparison to the physiological elastic range from 20 to 40 %. Bars without pattern represents A-WBPU meshes and square pattern represents A-WBPU+Ca meshes.*

Elasticity or elastic elongation is also an important mechanical parameter of hernia mesh implants, related to the deformation percentage of the material under the action of opposing tensile forces. However, when the forces stop, the material should be able to recover its original shape [20,21]. The elasticity of the human abdominal wall has also been studied in literature and, physiological elastic elongation values of 23 ± 7 % for men and 32 ± 17 % for women were measured in the longitudinal direction under 16 N·cm^{-1},

whereas 15 ± 5 % for men and 17 ± 5 % for women were measured [19]. Consequently, the physiological elastic elongation range has been considered in between 20-40 % [20]. The elastic elongation values of the studied meshes were also measured from force-elongation curves and the obtained values are shown in **Figure 6.7 B**. As can be observed, all developed formulations showed suitable elastic elongation values to support physiological elasticity requirements of 20-40 %, being much higher the values measured in the formulations with lower alginate content. This also demonstrated that the alginate content contributed to the stiffness while WBPU provided the elasticity to the A-WBPU and A-WBPU+Ca mesh formulations. Commercial PP mesh showed elastic elongation values under the physiological range for longitudinal direction but high values in the transversal direction. Therefore, these commercial meshes should improve their elastic elongation range in longitudinal plane to match specifically the physiological movements to avoid tension in the scar area and problems of mesh shrinkage [10].

Force-elongation experiments of A-WBPU and A-WBPU+Ca meshes before and after 21 days introduced in PBS were performed and the results are represented in **Figure 6.8**.

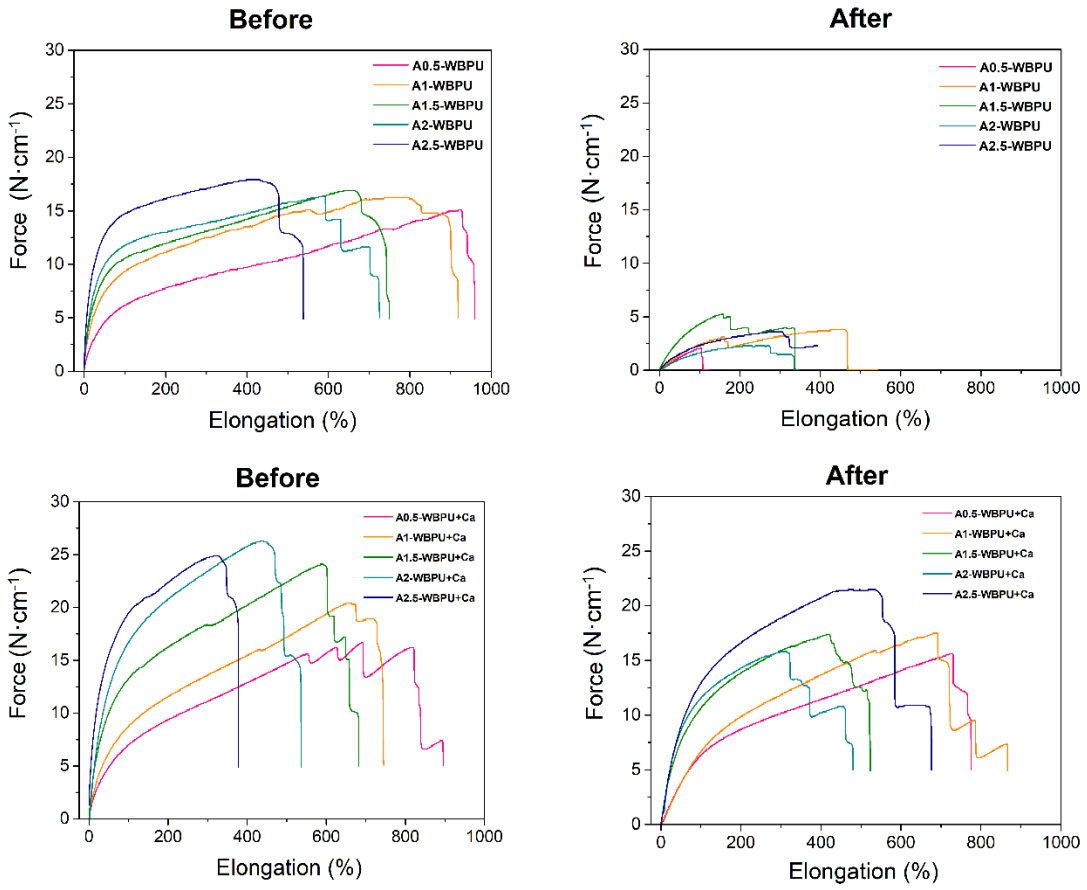

Figure 6.8. *Force-elongation curves of the A-WBPU (upper images) and A-WBPU+Ca (down images) meshes before and after the immersion in PBS during 21 days.*

This experiment reproduced the mesh state after patient recovery time from a groin hernia surgery that requires a minimum of three weeks, according to the specialists [13]. The force-elongation curves performed after 21 days introduced in PBS showed poor mechanical properties of A-WBPU meshes due to the dissolution of alginate in the medium, while mechanical properties of A-WBPU+Ca formulations remained almost similar after three weeks of immersion. This analysis also corroborated that the $CaCl_2$ coating reinforced mesh structure, increasing tensile strength and elastic limit values of the A-WBPU implants and thus, demonstrating functionality at least along critical recovery time of three weeks after surgery. Consequently, the ionic bonds remained in the meshes for a longer period without compromising their mechanical properties.

In conclusion, after mechanical analysis of the developed meshes, it was concluded that A2.5-WBPU+Ca formulation was the most suitable to manufacture hernia mesh implants through 3D printing technology, since it presented elastic limit values of 15.83 ± 1.04 $N \cdot cm^{-1}$ and maximum elastic elongation values of 42.57 ± 6.60 %, both under physiological ranges. A2.5-WBPU+Ca isotropic meshes would be fixed easier without paying attention to a specific orientation in groin area or small hernias, supporting the required tensile forces in their elastic range and thus recovering their original shape after the physiological movements during patient recovery time.

6.5. Cell viability test from A2.5-WBPU+Ca mesh

Preliminary LIVE/DEAD analysis was performed to evaluate the cell growth and proliferation on the A2.5-WBPU+Ca meshes. L929 murine fibroblasts were seeded on the surface of the selected mesh, and their viability were evaluated at 3 and 7 days after seeding through LIVE/DEAD staining. The obtained images are shown in **Figure 6.9**, revealing that there were a large number of viable cells (green) and a shortage of dead cells (red). The culture on the A2.5-WBPU+Ca meshes after 3 days reached the monolayer in some parts, with a shorter cell density compared to the control. This could be due to slow cell adhesion and proliferation during the first days. However, confocal images of both the mesh and the control were crowded of live cells after 7 days of seeding. Cell viability was quantified by measuring the ratio between green-fluorescent cells (live) and red-fluorescent cells (dead), obtaining viability values above 90 % in all cases.

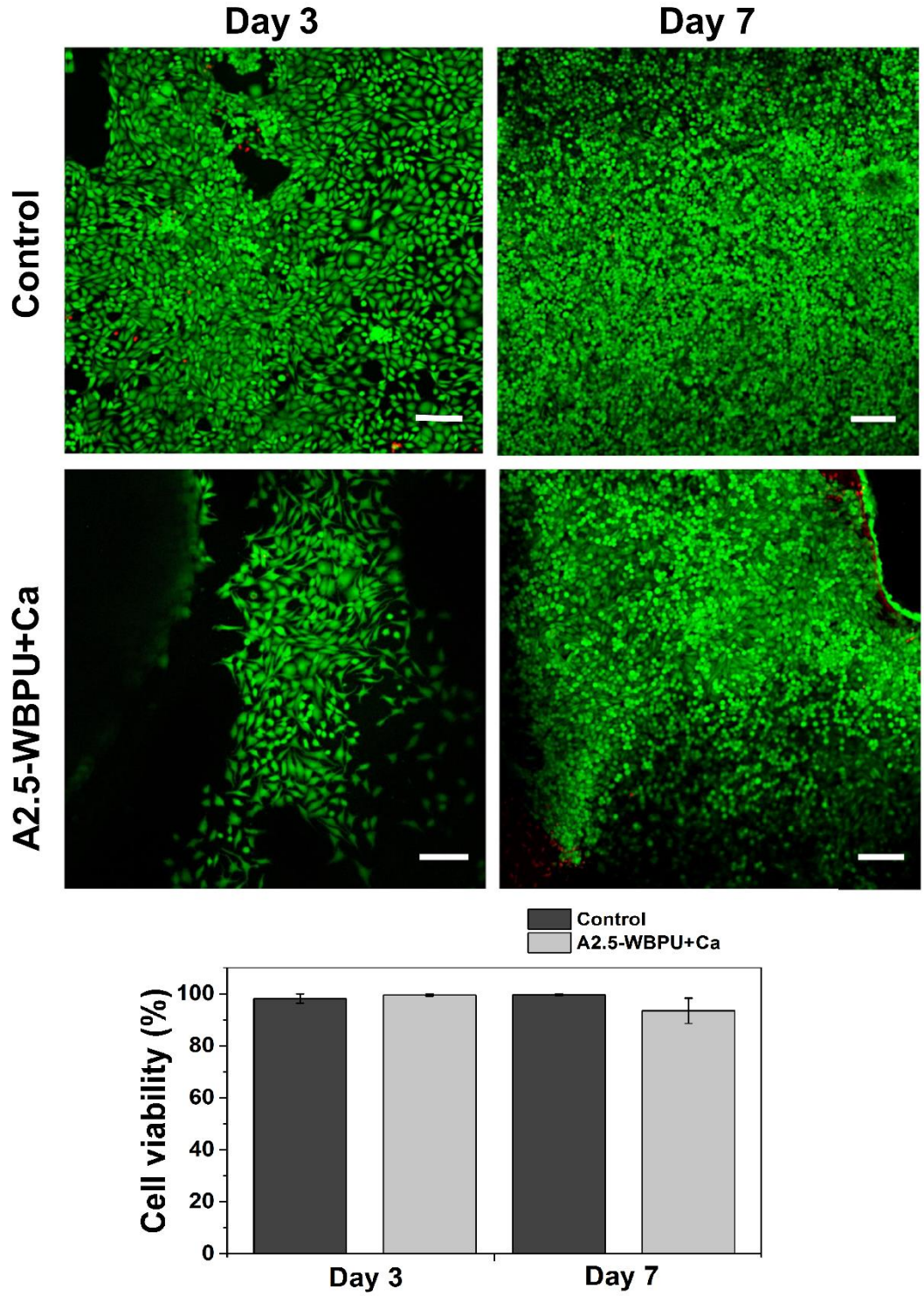

Figure 6.9. *LIVE/DEAD images at 3 and 7 days after seeding for cell viability examination from A2.5-WBPU+Ca mesh. Calcein represent cell viability (green stained circles) and propidium iodide represent non-viable cells (red stained circles). Images were obtained by confocal microscopy at 20x magnification. Scale bar represented 100 μm. Graphical representation of cell viability percentages in the A2.5-WBPU+Ca mesh and the control after 3 and 7 days of seeding.*

In conclusion, LIVE/DEAD experiments demonstrated that during the first week after mesh implantation fibroblast cells would grow throughout the surface of the mesh, what would enable tissue repair of the damaged area. This experiment also corroborated the biocompatible character of the alginate and WBPU.

6.6. *In vitro* antibiotic delivery from A2.5-WBPU-clph+Ca mesh

The addition of antibiotics to the developed 3D printed meshes would allow their focalized release in the damaged area after implantation, avoiding future mesh replacement caused by infection complications [22,24]. As demonstrated in the previous chapters, 3D printing technology enables the manufacture of drug-loaded devices by adding the necessary drug dosage in the ink formulation.

In this case, 5.5 wt. % of chloramphenicol, which as a broad-spectrum antibiotic is often used for surgical prophylaxis in the wound area [25], was added in the A2.5-WBPU biomaterial ink formulation after selection of A2.5-WBPU+Ca mesh as the most suitable for hernia repair, according to the previous experiments. The antibiotic-loaded A2.5-WBPU-clph biomaterial ink was successfully 3D printed and then coated with $CaCl_2$ after the air-drying process, as before, obtaining a chloramphenicol loaded mesh designated as A2.5-WBPU-clph+Ca. Swelling degree and *in vitro* chloramphenicol release from A2.5-WBPU-clph+Ca meshes were analyzed for 24 h and the results are shown in **Figure 6.10**.

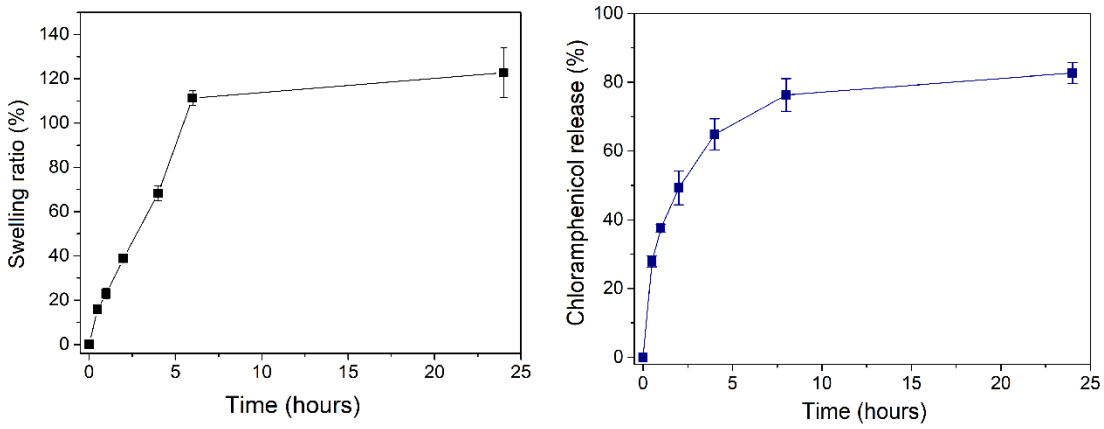

Figure 6.10. *Swelling ratio and in vitro chloramphenicol release experiments from the antibiotic-loaded A2.5-WBPU-clph+Ca meshes during 24 hours.*

The meshes showed a swelling capacity of 120 % in 24 h and the 80 % of the loaded chloramphenicol was released to the physiological medium in the first 24 h.

In summary, antibiotic-loaded meshes from A-WBPU inks can be developed by 3D printing technology. Swelling and release experiments demonstrated that the antibiotic could be delivered into the wound site during the first 24 h after implantation, and thus infection and a future mesh replacement could be avoided.

6.6. Conclusions

In this chapter, five A-WBPU biomaterial ink formulations with different alginate contents were developed in order to manufacture 3D printed mesh implants that could be potentially employed for hernia repair.

The obtained A-WBPU inks were rheologically characterized showing shear-thinning behavior, high viscosities and viscoelasticity, characteristics that increased as the alginate content increased in the ink formulations.

A-WBPU 3D printed meshes showed suitable printing performance, shape fidelity and accuracy in model reproduction, being adaptable to a specific patient injury by modifying the CAD mesh model. Besides, a $CaCl_2$ coating was applied to the air-dried meshes as physical reinforcement, obtaining implants that present the following characteristics: partially-absorbable, heavyweight, very large pores, transparency and isotropic behavior, which could facilitate their implantation.

Mechanical tests of the developed meshes revealed that the alginate, as well as the $CaCl_2$ coating, reinforced the mesh structure increasing the tensile strength and elastic limit, while WBPU provided the elasticity. The obtained mechanical results were compared with the reported physiological values and it was concluded that A2.5-WBPU+Ca mesh formulation was the most suitable for hernia repair, being able to support the physiological tensions of small and inguinal hernias.

Finally, antibiotic-loaded A-WBPU mesh implants were developed for their local administration. *In vitro* antibiotic delivery experiments revealed that the drug was released in the first 24 h, and thus, post-surgical infection complications and future mesh replacement would be avoided.

6.7 References

[1] Chen H, Xie F, Chen L, Zheng B. Effect of rheological properties of potato, rice and corn starches on their hot-extrusion 3D printing behaviors. J Food Eng 2019;244:150–158. https://doi.org/10.1016/j.jfoodeng.2018.09.011.

[2] Li H, Liu S, Li L. Rheological study on 3D printability of alginate hydrogel and effect

of graphene oxide. Int J Bioprinting 2016;2:54–66. https://doi.org/10.18063/IJB.2016.02.007.

[3] Liu Z, Bhandari B, Prakash S, Mantihal S, Zhang M. Linking rheology and printability of a multicomponent gel system of carrageenan-xanthan-starch in extrusion based additive manufacturing. Food Hydrocoll 2019;87:413–424. https://doi.org/10.1016/j.foodhyd.2018.08.026.

[4] Bendtsen ST, Quinnell SP, Wei M. Development of a novel alginate-polyvinyl alcohol-hydroxyapatite hydrogel for 3D bioprinting bone tissue engineered scaffolds. J Biomed Mater Res - Part A 2017;105:1457–1468. https://doi.org/10.1002/jbm.a.36036.

[5] Hsieh FY, Lin HH, Hsu SH. 3D bioprinting of neural stem cell-laden thermoresponsive biodegradable polyurethane hydrogel and potential in central nervous system repair. Biomaterials 2015;71:48–57. https://doi.org/10.1016/j.biomaterials.2015.08.028.

[6] Abouzeid RE, Khiari R, Beneventi D, Dufresne A. Biomimetic mineralization of three-dimensional printed alginate/TEMPO-oxidized cellulose nanofibril scaffolds for bone tissue engineering. Biomacromolecules 2018;19:4442–4452. https://doi.org/10.1021/acs.biomac.8b01325.

[7] Klinge U, Klosterhalfen B, Conze J, Limberg W, Obolenski B, Öttinger AP, Schumpelick V. Modified mesh for hernia repair that is adapted to the physiology of the abdominal wall. Eur J Surg 1998;164:951–960. https://doi.org/10.1080/110241598750005138.

[8] Klosterhalfen B, Junge K, Klinge U. The lightweight and large porous mesh concept for hernia repair. Expert Rev Med Devices 2005;2:103–117. https://doi.org/10.1586/17434440.2.1.103.

[9] Lake SP, Ray S, Zihni AM, Thompson DM, Gluckstein J, Deeken CR. Pore size and pore shape - but not mesh density - alter the mechanical strength of tissue ingrowth and host tissue response to synthetic mesh materials in a porcine model of ventral hernia repair. J Mech Behav Biomed Mater 2015;42:186–197. https://doi.org/10.1016/j.jmbbm.2014.11.011.

[10] Sanbhal N, Miao L, Xu R, Khatri A, Wang L. Physical structure and mechanical properties of knitted hernia mesh materials: A review. J Ind Text 2018;48:333–360. https://doi.org/10.1177/1528083717690613.

[11] Pott PP, Schwarz MLR, Gundling R, Nowak K, Hohenberger P, Roessner ED. Mechanical properties of mesh materials used for hernia repair and soft tissue augmentation. PLoS One 2012;7:1–10. https://doi.org/10.1371/journal.pone.0046978.

[12] Deeken CR, Lake SP. Mechanical properties of the abdominal wall and biomaterials utilized for hernia repair. J Mech Behav Biomed Mater 2017;74:411–427. https://doi.org/10.1016/j.jmbbm.2017.05.008.

[13] Crawford DL, Phillips EH. Laparoscopic repair and groin hernia surgery. Surg Clin North Am 1998;78:1047–1062. https://doi.org/10.1016/S0039-6109(05)70368-6.

[14] Yang Z, Wu G. Effects of soft segment characteristics on the properties of biodegradable amphiphilic waterborne polyurethane prepared by a green process. J Mater Sci 2020;55:3139–3156. https://doi.org/10.1007/s10853-019-04237-6.

[15] Lee KY, Mooney DJ. Alginate: Properties and biomedical applications. Prog Polym Sci 2012;37:106–126. https://doi.org/10.1016/j.progpolymsci.2011.06.003.

[16] Cobb WS, Burns JM, Peindl RD, Carbonell AM, Matthews BD, Kercher KW, Heniford BT. Textile analysis of heavy-weight, mid-weight and light-weight polypropylene mesh in a porcine ventral hernia model. J Surg Res 2006;136:1–7. https://doi.org/10.1016/j.jss.2006.05.022.

[17] Coda A, Lamberti R, Martorana S. Classification of prosthetics used in hernia repair based on weight and biomaterial. Hernia 2012;16:9–20. https://doi.org/10.1007/s10029-011-0868-z.

[18] Förstemann T, Trzewik J, Holste J, Batke B, Konerding MA, Wolloscheck T, Hartung C. Forces and deformations of the abdominal wall-A mechanical and geometrical approach to the linea alba. J Biomech 2011;44:600–606. https://doi.org/10.1016/j.jbiomech.2010.11.021.

[19] Junge K, Klinge U, Prescher A, Giboni P, Niewiera M, Schumpelick V. Elasticity of the anterior abdominal wall and impact for reparation of incisional hernias using mesh implants. Hernia 2001;5:113–118. https://doi.org/10.1007/s100290100019.

[20] Zhu LM. Mesh implants: An overview of crucial mesh parameters. World J Gastrointest Surg 2015;7:226-236. https://doi.org/10.4240/wjgs.v7.i10.226.

[21] Cobb WS, Peindl RM, Zerey M, Carbonell AM, Heniford BT. Mesh terminology 101. Hernia 2009;13:1–6. https://doi.org/10.1007/s10029-008-0428-3.

[22] Domínguez-Robles J, Mancinelli C, Mancuso E, García-Romero I, Gilmore BF, Casettari L, Larrañeta E, Lamprou DA. 3D printing of drug-loaded thermoplastic polyurethane meshes: A potential material for soft tissue reinforcement in vaginal surgery. Pharmaceutics 2020;12:63-79. https://doi.org/10.3390/pharmaceutics12010063.

[23] Hou X, Zheng W, Kodur V, Sun H. Effect of temperature on mechanical properties of prestressing bars. Constr Build Mater 2014;61:24–32. https://doi.org/10.1016/j.conbuildmat.2014.03.001.

[24] Jezupors A, Mihelsons M. The analysis of infection after polypropylene mesh repair of abdominal wall hernia. World J Surg 2006;30:2270–2278. https://doi.org/10.1007/s00268-006-0130-5.

[25] McHugh SM, Collins CJ, Corrigan MA, Hill ADK, Humphreys H. The role of topical antibiotics used as prophylaxis in surgical site infection prevention. J Antimicrob Chemother 2011;66:693–701. https://doi.org/10.1093/jac/dkr009.

Chapter 7

A-WBPU bioinks for 3D bioprinting of scaffolds for cartilage regeneration

CHAPTER 7 – A-WBPU bioinks for 3D bioprinting of scaffolds for cartilage regeneration

7. Alginate-WBPU bioinks for 3D bioprinting of scaffolds for cartilage regeneration

7.1. Aim of the chapter

The aim of this chapter is the development of bioinks composed of alginate and waterborne polyurethane for the fabrication of scaffolds for cartilage regeneration through 3D printing technology.

In the previous chapter, A-WBPU based inks showed proper rheological properties for extrusion 3D printing. Besides, the subsequent 3D printed meshes presented mechanical strength provided by the alginate and high elasticity and resilience given by the WBPU. These mechanical characteristics are also present in mature articular cartilage, suggesting that they could be good support materials for cartilage tissue engineering.

On the other hand, as explained in Chapter 1, 3D bioprinting allows the creation of functional 3D constructs containing living cells, enabling *in situ* tissue formation. In particular, the articular cartilage tissue is only formed by a type of cells named chondrocytes and, for the formation of neo-tissue, it is necessary the fabrication of complex scaffolds that can host these cells and thus, mimic the original tissue. However, chondrocyte cultures in stiff 3D architectures can lead to de-differentiation of the cells towards hypertrophic phenotypes. Hence, chondrocyte-laden constructs should present proper strength and elasticity to avoid cellular de-differentiation.

Therefore, in this chapter A-WBPU bioinks were developed and rheologically characterized. Their suitability for 3D bioprinting was analyzed, as well as the encapsulation and viability of the chondrocytes into the printed constructs. Moreover, *in vitro* cartilage formation and the absence of de-differentiated phenotypes were evaluated.

7.2. A-WBPU bioinks preparation and characterization

Five different ink formulations were prepared from alginate powder and WBPU dispersion. In this case, alginate powder at 10 wt. % was first dispersed in chondrocyte expansion medium (DMEM:F-12 + 5 % FBS + 1 % Pen/Strep). Then, the alginate-culture medium were mixed with the WBPU dispersion, obtaining ink formulations with different alginate/WBPU proportions as it is shown in **Table 7.1,** obtaining 0.4, 0.8, 1.6, 3.2 and 6.4 wt. % alginate, respectively, in each formulation. Alginate and WBPU solutions were

previously autoclaved to be sterilized during 10 min at 121 ºC. Both materials were mixed in the biosafety cabinet using sterile syringes to extrude and mix the materials until homogenization, preserving sterile conditions. The obtained ink formulations were denoted as AX-WBPU, being X the alginate amount in respect to the total solid content in the formulation.

Table 7.1. *Summary of the developed A-WBPU ink formulations. Proportions of alginate + culture medium/WBPU weight and total solid content present in each formulation.*

Bioink formulation	Alginate + culture medium / WBPU (w/w)	Total solid content (wt. %)
A0.4-WBPU	4/96	40.4
A0.8-WBPU	8/92	40.8
A1.6-WBPU	16/84	41.6
A3.2-WBPU	32/68	43.2
A6.4-WBPU	64/36	46.4

7.2.1. Rheological characterization of A-WBPU inks

The suitability of the developed inks for 3D printing technology was evaluated by performing similar rheological assays than in the previous chapter. First, flow viscosity curves versus shear rate increase were performed (**Figure 7.1 A**), showing the five inks shear-thinning behavior and thus, non-Newtonian characteristics. However, only A1.6-WBPU, A3.2-WBPU and A6.4-WBPU showed high viscosity at low shear rates. Moreover, as the alginate content increased in the formulations, viscosity values at zero shear rate increased, as it can be observed in **Table 7.2**. The non-Newtonian behavior of the A-WBPU ink formulations can be explained by comparing the experimental data with a power-law model (Eq. 3), as performed in previous rheological characterizations. Values of power-law index among 0.22 and 0.25 were obtained for all A-WBPU formulations (**Table 7.2**) indicating strong shear-thinning and non-Newtonian behavior in all cases. Consistency coefficient raised as the alginate content increased in the formulation (from 51.7 to 975.1 $Pa \cdot s^n$), and Pearson correlation coefficient, denoted strong correlation among the obtained experimental results and the power-law model (R^2>0.9).

Viscosity recovery tests were also carried out and the results are shown in **Figure 7.1 B**. The recovery percentages were calculated and the obtained values are summarized in

Table 7.2. All inks showed recovery percentages between 75 and 98 % after 60 seconds, indicating good shape fidelity properties of the materials after 3D printing.

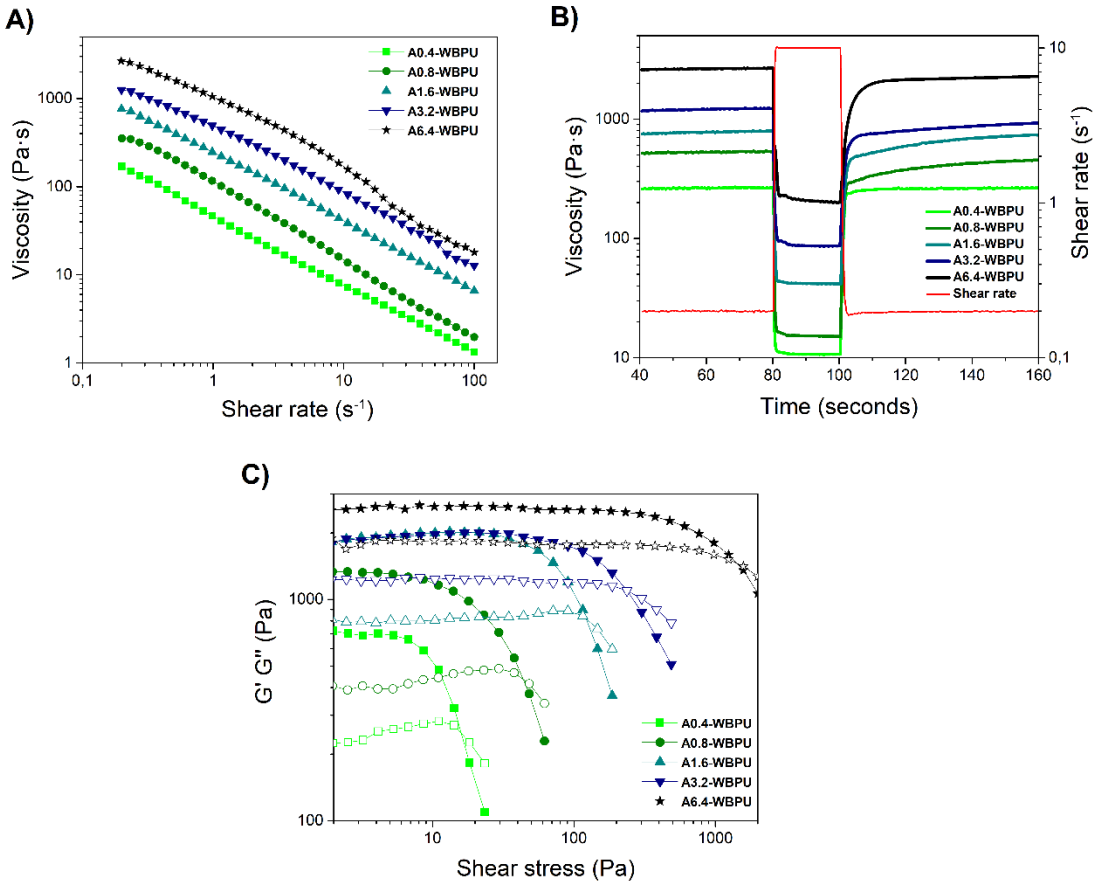

Figure 7.1. *Rheological characterization of the developed A-WBPU inks. A) Viscosity versus shear rate. B) Viscosity recovery tests. C) Storage modulus represented by solid symbols and the loss modulus represented by open symbols, versus an increasing shear stress.*

Table 7.2. *Viscosity measured at 0.2 s^{-1}, power-law index, consistency coefficient, Pearson correlation coefficient, viscosity recovery percentages after 60 sec, G' in the LVR and yield point values.*

Bioink formulation	Viscosity (Pa·s)	n	K (Pa·s^n)	R^2	Recovery (%)	G' in LVR (Pa)	Yield point (Pa)
A0.4-WBPU	184 ± 20	0.22	51.72	0.99	97.0 ± 1.0	770 ± 123	19 ± 4
A0.8-WBPU	325 ± 13	0.22	106.27	0.93	87.0 ± 1.0	1357 ± 62	43 ± 2
A1.6-WBPU	786 ± 37	0.21	241.61	0.99	91.1 ± 2.7	1950 ± 74	123 ± 1
A3.2-WBPU	1220 ± 54	0.25	458.27	0.96	75.8 ± 0.1	1944 ± 22	241 ± 4
A6.4-WBPU	2668 ± 2	0.24	975.14	0.92	84.8 ± 1.2	2488 ± 122	1407 ± 30

Viscoelastic characteristics of the A-WBPU inks were studied by oscillatory sweep tests. Storage modulus and loss modulus versus shear stress are shown in **Figure 7.1 C**. The five A-WBPU bioink formulations showed always G' above G'' in the LVR, indicating solid-like behavior and elastic characteristics. The G' values in LVR of the different formulations are related with the shape fidelity after printing [1] (**Table 7.2**). The increase in G' values of A-WBPU inks from 770 ± 123 to 2488 ± 122 Pa suggested that the 3D printed samples could retain the shape when compared to values within a printability window ranging from 647 to 4000 Pa reported in the literature [2,3]. A0.4-WBPU and A0.8-WBPU formulations presented suitable viscoelastic characteristics despite the low viscosity values observed in the previous experiments. As the shear stress increased, the values of G' values drop below G'' acquiring a viscous and liquid-like behavior [4]. The yield point values increased from 19 to 1407 Pa as the alginate content did in the A-WBPU formulations, thus increasing the force needed to extrude the material through the nozzle during 3D printing process [5].

Rheological characterization results showed that the addition of alginate-culture medium to the WBPU dispersion allows achieving desirable characteristics for 3D printing, increasing the viscosity and viscoelastic properties, as observed in the previous chapter. The developed A-WBPU inks reached proper viscosity, shear-thinning behavior and the viscoelasticity required for a suitable 3D printing process and shape retention of the obtained scaffolds.

7.2.2. Cell encapsulation into A-WBPU bioinks

After the rheological characterization, the ability of cell encapsulation into the A-WBPU bioinks was evaluated. Bioink droplets with a volume of 40 µL containing a cell density of $2 \cdot 10^6$ cell·mL^{-1} were 3D printed, Ca^{2+} crosslinked for 5 min and cultured for 24, 72 h and 7 days (**Figure 7.2**). The crosslinking of the scaffolds is an important point to ensure proper encapsulation of the cells in the form, creating a suitable environment for the cells to grow and perform their specific functions [6,7]. The ionic interactions among carboxylic groups present in the alginate as well as in WBPU particles with Ca^{2+} created a proper network that allowed nutrient exchange without compromising cell viability [8].

After harvesting the droplets at the different time points, cell number counting and cytotoxicity tests were performed in order to determine the cell viability in the developed bioink formulations.

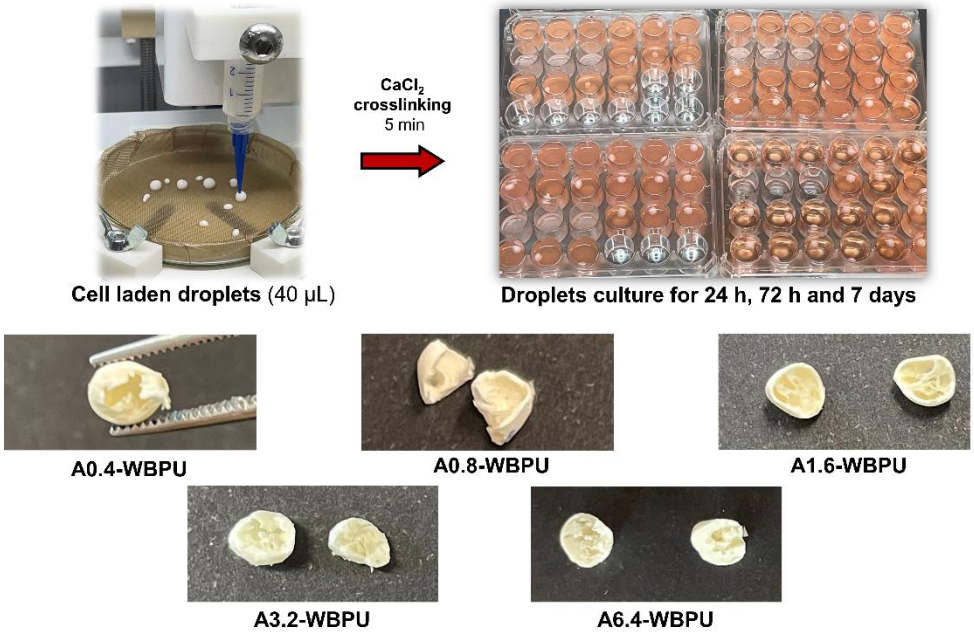

Figure 7.2. *Images of cell-laden droplets obtaining process and culture in expansion medium for 24, 72 h and 7 days. Down images represented freeze-dried droplets of each formulation after 7 days of culture.*

During the culture process, it was observed that A0.4-WBPU, A0.8-WBPU and A1.6-WBPU droplets were not able to preserve their integrity, leaching the material from the inner part to the culture medium. This suggests that the bioinks with less alginate content were not effectively crosslinked and did not maintain the full integrity of the scaffold during the whole experiment. The different droplets were freeze-died to observe the inner part of the samples after 7 days of culture and pictures are shown in **Figure 7.2** (down images). A3.2-WBPU and A-6.4-WBPU presented a compact internal structure as opposed to A0.4-WBPU, A0.8-WBPU and A1.6-WBPU, in which only the envelope could be detected, demonstrating that formulations with higher alginate content presented proper shape retention capacity.

The cell viability of the droplets was tested by means of DNA quantification and lactate dehydrogenase (LDH) release cytotoxicity assays (**Figure 7.3**). The results of the cell number quantification assays are shown in **Figure 7.3 A.** As can be observed, the initial number of cells per droplet ($8 \cdot 10^4$ cells) remained unchanged after 24 hours of culture in all cases. However, after 72 h and 7 days of culture, the cell number in the droplets with the less alginate content dropped due to the matrix disintegration. The cells lost their scaffolding and were probably released into the culture medium along with the liquid-like support materials. The cell number in the A3.2-WBPU and A6.4-WBPU droplets remained constant over the 7 days of experiment.

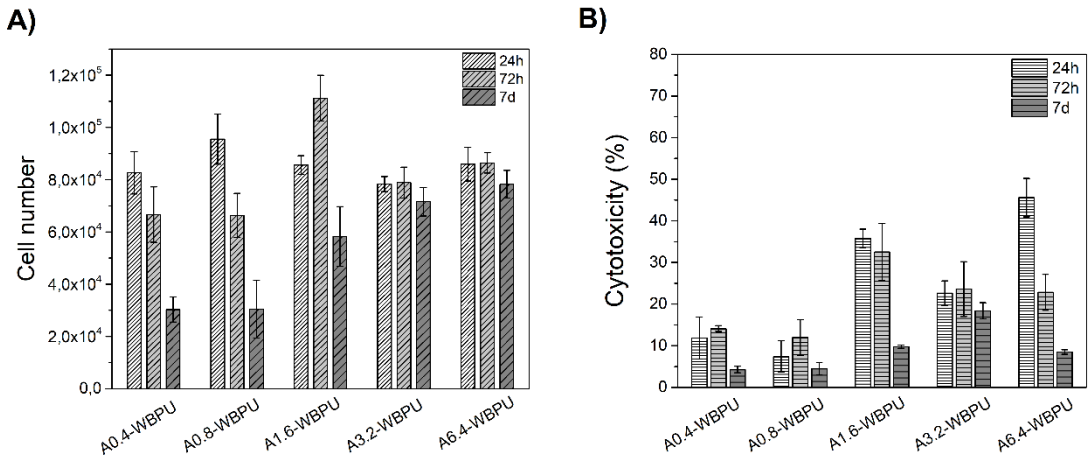

Figure 7.3. *Graphical representation of A) cell number and B) cytotoxicity of the droplets from the different A-WBPU formulations after 24, 72h and 7 days of culture.*

LDH release to the culture medium was used as a measure of cytotoxicity (**Figure 7.3 B**). The obtained results were normalized against a negative control, which presented the initial number of $8 \cdot 10^4$ cells, treated with lysis buffer. These results revealed that the higher alginate content in the formulation, the higher volume of LDH released probably due to the higher viscosity of these bioinks. The extrusion process of the high viscosity bioinks could result in cell crushing and thus, the release of LDH to the culture medium. It has been reported that bioprinting of hydrogels with high viscosity compromises cell integrity due to the high shear rates needed during the extrusion process [9], phenomenon that could have occurred in this case for high alginate content bioinks. As demonstrated in previous chapters, the alginate as well as the WBPU dispersion employed for these experiments presented a biocompatible character. Therefore, the cytotoxicity values detected in the culture medium of 35.77 ± 2.24 %, 22.6 ± 3 % and 45.59 ± 4.6 % for A1.6-WBPU, A3.2-WBPU and A6.4-WBPU formulations, respectively, after 24 h were not be caused by the materials itself, but for the extrusion process of the encapsulated cells. However, as it was demonstrated by the quantification of DNA, this slight crushing effect during 3D printing is not crucial for global cell viability in these higher alginate content bioinks due to the constant cell number presented for at least one week of culturing.

After rheological characterization, measurement of cell viability and encapsulation efficiency in the developed A-WBPU bioinks, it was observed that only A3.2-WBPU and A6.4-WBPU formulations presented proper structural integrity and cell viability after a week immersed in culture media. Moreover, these formulations presented better rheological properties such as high viscosity and viscoelasticity to be 3D printed and retain the desired shape compared to those with less alginate content. Therefore, A3.2-

WBPU and A6.4-WBPU formulations were selected as the most suitable to perform experiments of *in vitro* cartilage formation.

7.3. 3D Bioprinting of A-WBPU scaffolds and *in vitro* cartilage formation

7.3.1. 3D bioprinting of chondrocyte-laden constructs

In order to achieve successful chondrogenic tissue restoration, it is necessary to fabricate support scaffolds that present adequate mechanical properties to withstand the loads applied in the articular joint areas [10]. The mechanical properties of the A-WBPU meshes studied in the previous chapter revealed that increasing the alginate content in the formulation contributes to increased mechanical strength, on the one hand, and that WBPU provides elasticity and resilience properties, on the other hand, which are similar characteristics to those observed in mature articular tissue [11,12]. Therefore, those observations suggest that the selected A3.2-WBPU and A6.4-WBPU formulations with high alginate content would behave as suitable support materials for chondrogenic restoration, mimicking articular cartilage tissue.

The scaffolds for *in vitro* cartilage regeneration assays were manufactured by 3D bioprinting technique. A3.2-WBPU and A6.4-WBPU bioinks were loaded with a chondrocyte density of $2 \cdot 10^6$ cell·mL^{-1} and thereafter, the cell-laden formulations were 3D printed following a specific CAD model. The design of the scaffolds is crucial to ensure proper nutrient and oxygen diffusion, chemical exchange and waste removal among cells and the environment, avoiding chondrocyte de-differentiation [13–15]. It is important to provide a proper grid morphology to the constructs as these structure not only provide good communication with the environment, but also modulate the mechanical properties as well as the differentiation potential of the cells [16–18]. In this case, the scaffold architecture chosen for these experiments presented a square hole (strand distance) of 1.5 mm with a deposition of the material following a geometry of 90 – 0 º. After 3D bioprinting process, the scaffolds were crosslinked for 5 min with a 0.1 M $CaCl_2$ solution to achieve functional cell-laden constructs (**Figure 7.4**). The scaffolds were incubated during 14 and 28 days in basal (maintenance) and differentiation media containing growth factors and specific biochemicals that lead to chondrogenic phenotypes, to test whether the employed materials are able to promote cell adhesion, proliferation and tissue formation, avoiding de-differentiation.

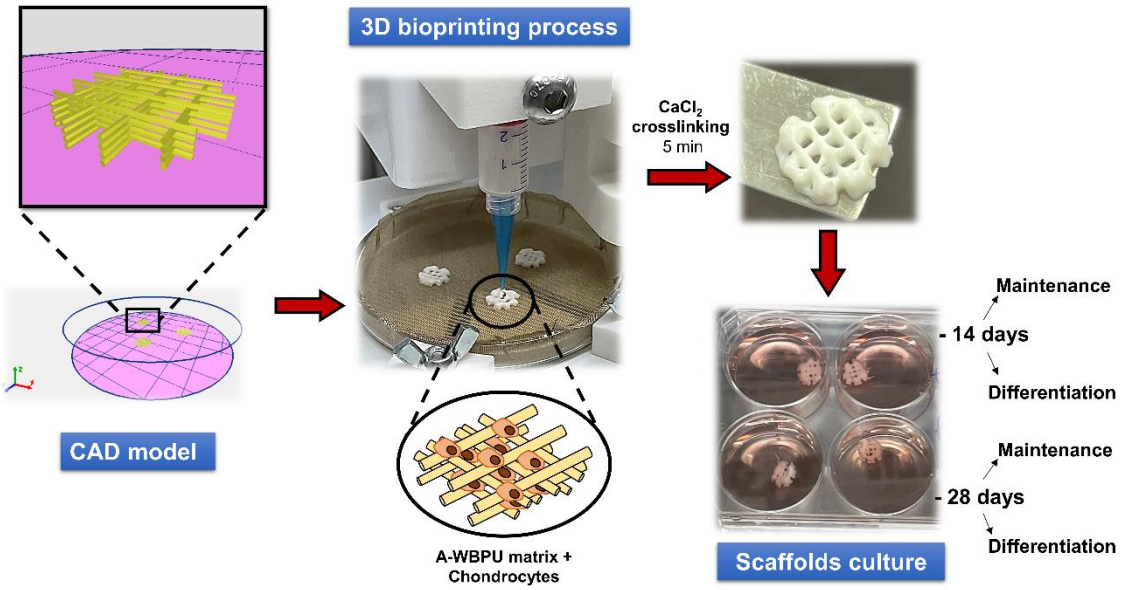

Figure 7.4. *3D bioprinting process of A3.2-WBPU and A6.4-WBPU formulations: from CAD model to functional cell-laden scaffolds. Printed scaffolds were cultured during 14 and 28 days in basal (maintenance) and differentiation media.*

7.3.2. Scaffolds characterization and *in vitro* cartilage formation

After 14 and 28 days of incubation, the scaffolds were harvested and morphologically characterized. SEM images presented in **Figure 7.5** and **Figure 7.6** revealed that all scaffolds from both A3.2-WBPU and A6.4-WBPU presented structural integrity, without material leaching out of the constructs along the experiment (left columns). Chondrocytes were found throughout the scaffolds, presenting spherical morphologies, typical from this phenotype [19]. The cells appeared embedded in the material, sometimes by pairs, similarly to the lacunae found in the native tissue. Besides, the presence of cells in all scaffolds suggested that these materials did not affect cell viability for longer periods of incubation, performing as suitable constructs for chondrocytes support. Moreover, the design of the scaffolds was adequate to promote nutrient exchange with the media and thus, cell survival. There were no visual differences in the number of cells between both formulations, time points or culturing conditions, since large and close groups of chondrocytes were not observed in any case, suggesting that no proliferation or only slight proliferation occurred.

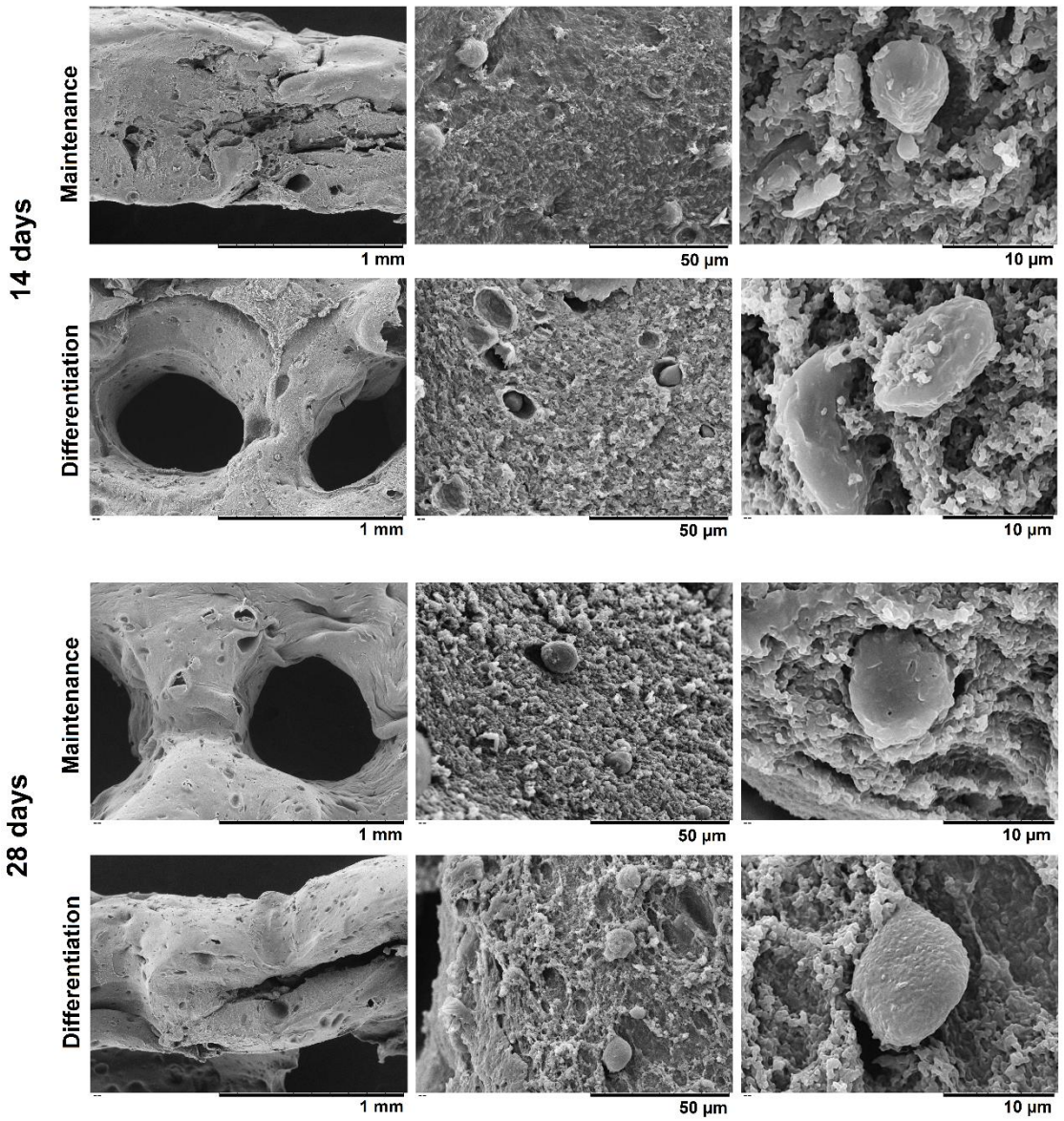

Figure 7.5. *SEM images of A3.2-WBPU scaffolds after 14 and 28 days of culture in maintenance and differentiation media. Magnifications of x100 (left column), x1500 (middle column) and x6000 (right column) were applied.*

The cells were mostly located inside of the scaffolds, as it can be observed in the images (middle and right columns). However, after the dehydration process needed for SEM, the original structure of the constructs was lost due to the water removal and the subsequent shrinkage after the treatment.

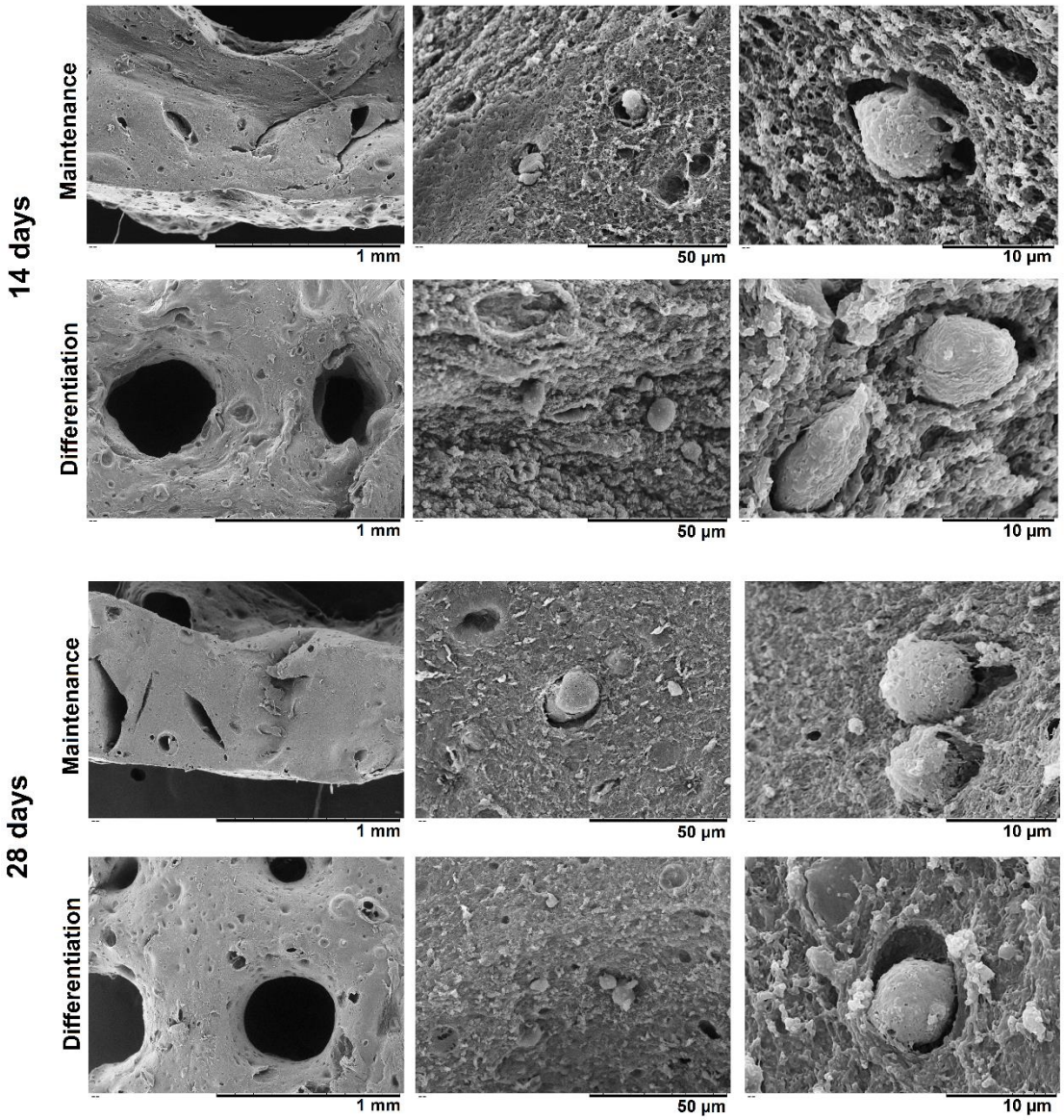

Figure 7.6. *SEM images of A6.4-WBPU scaffolds after 14 and 28 days of culture in maintenance and differentiation media. Magnifications of x100 (left column), x1500 (middle column) and x6000 (right column) were applied.*

After SEM analysis, the total DNA content into the scaffolds was determined (**Figure 7.7**). Samples after 24 h of culture were also analyzed as a control. Values of $6 \cdot 10^4 \pm 1 \cdot 10^2$ cells and $6.7 \cdot 10^4 \pm 1.6 \cdot 10^3$ cells per scaffold for A3.2-WBPU and A6.4-WBPU, respectively, were measured at 24 h. However, after 14 days of incubation the number of cells decreased in maintenance and differentiation conditions for both formulations. This could be caused by cell crushing effect during the bioprinting, being more accentuated in A6.4-WBPU scaffolds, as it was previously observed in droplets analysis. The number of cells in A3.2-WBPU after 14 days in maintenance and differentiation media presented values of $5.2 \cdot 10^4 \pm 1.3 \cdot 10^3$ and $5.1 \cdot 10^4 \pm 1.4 \cdot 10^3$, respectively, while in

A6.4-WBPU the values for cell number were $5.8 \cdot 10^4 \pm 4.4 \cdot 10^3$ and $5.3 \cdot 10^4 \pm 4 \cdot 10^3$ cells per scaffold in maintenance and differentiation media respectively.

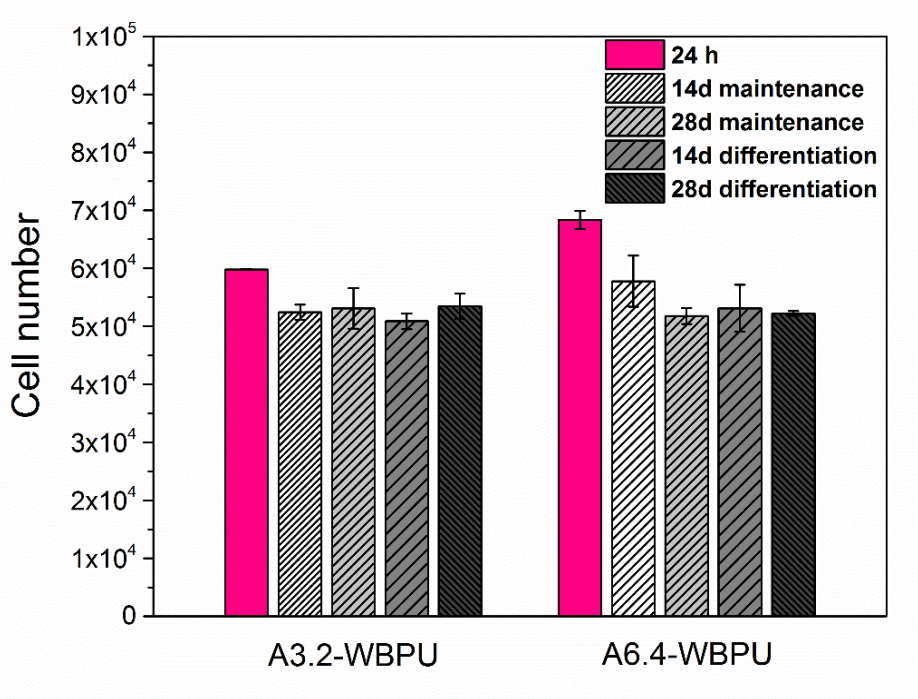

Figure 7.7. *Cell number after 24 h, 14 and 28 days of culture in maintenance and differentiation conditions from A3.2-WBPU and A6.4-WBPU scaffolds.*

After 28 days of incubation, the values remained constant for both formulations and conditions. For A3.2-WBPU values were $5.3 \cdot 10^4 \pm 3.5 \cdot 10^3$ and $5.3 \cdot 10^4 \pm 2.2 \cdot 10^3$ cells per scaffold in maintenance and differentiation medium, respectively, and values of $5.2 \cdot 10^4 \pm 1.4 \cdot 10^3$ and $5.2 \cdot 10^4 \pm 4 \cdot 10^2$ cells in A6.4-WBPU formulation.

In conclusion, chondrocytes embedded in A3.2-WBPU and A6.4-WBPU matrices were not able to proliferate, although their viability were not compromised at least during 28 days of incubation, confirming the previous observations in SEM images.

In the studies carried out by Martinez-Avila et al. [20], chondrocyte-laden cellulose-alginate constructs with a density of $20 \cdot 10^6$ cell·mL^{-1} before printing showed a significant proliferation after 14 and 28 days of culture, suggesting that the higher loaded cells the higher increment in their number along incubation time. In other study carried out by Hung et al. about chondrocyte-laden in WBPU constructs [21], also a significant increment of cell number after 14 days of incubation was informed, starting from $5 \cdot 10^7$ cell per mL of material. High cell densities loaded into the materials will be translated into higher proliferation rates due to the presence of very close groups of cells, creating a

suitable environment in which growth factors and other chemical cues are exchanged among them, increasing cell proliferation rates [22].

Chondrogenic cells present in mature cartilage tissue usually do not have proliferative capacity, but their main function is the maintenance of tissue homeostasis by means of the synthesis of specific extracellular matrix, which contains mainly large amounts of glycosaminoglycan (GAG) and collagen II [23,24]. Sulfated GAG molecules allow water retention in their structure, being the responsible of the osmotic pressure generated into the tissue [25]. Collagen II forms a structured network with fibers in different orientations and providing mechanical strength [26]. The deposition of these molecules are the main characteristic of the chondrocytes and the core of the mechanical properties of the mature articular cartilage [27].

In cartilage tissue regeneration, the seeded chondrocytes should be able to synthesize and deposit these molecules to form functional and mature tissue. However, when chondrocytes are *in vitro* expanded in 3D cultures, it could lead to de-differentiation of the cells towards hypertrophic phenotypes characterized by a deposition of higher concentrations on osteogenic markers such as collagen I [28,29]. The evaluation of the GAGs presence in the developed scaffolds would inform about the capacity of these chondrocytes to form functional neo-tissue in the 3D constructs, similar to the native one [30,31].

Optical images of histological Safranin-O staining, which is a marker for GAG, from cultured A3.2-WBPU and A6.4-WBPU scaffolds during 28 days are shown in **Figure 7.8**. In these images, GAGs deposition was hardly observed, in neither maintenance nor differentiation conditions, probably due to the small thickness of the histological slides. However, the original structure of the scaffolds could be appreciated. The cryosectioning technique of the samples allowed preserving the internal structure where cells were embedded. A-WBPU matrices were observed as pink and blue stained structures and chondrocytes are detected as stained blue circles (cytoplasm) with black nuclei located into the structure indicated by red circles.

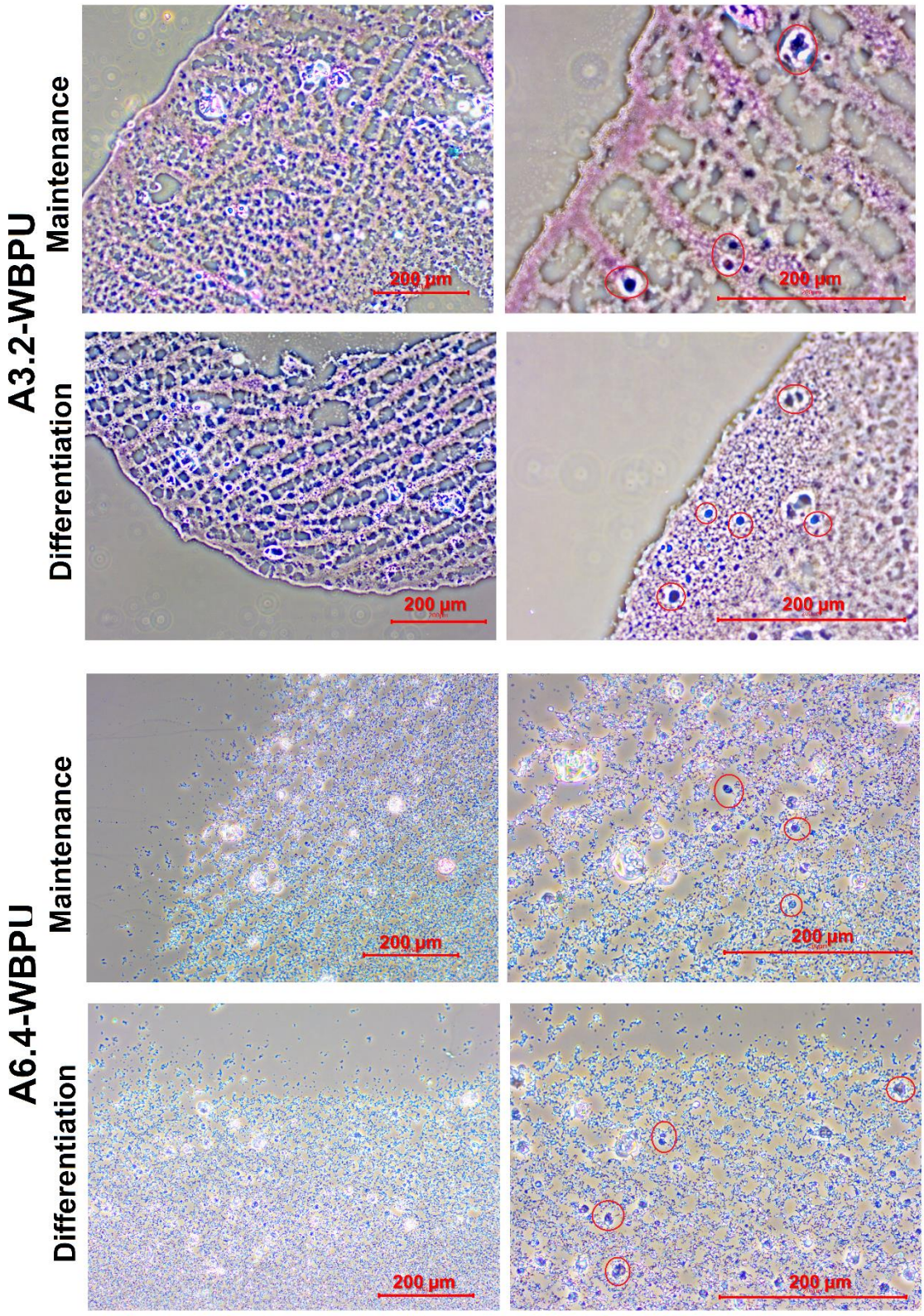

Figure 7.8. *Safranin-O staining images (with fast green and Weigert's Iron Hematoxylin solutions as counter stains) after 28 days of culture in maintenance and differentiation conditions from A3.2-WBPU and A6.4-WBPU scaffolds. Magnifications of 10x (left column) and 20x (right column). Cells are denoted by red circles.*

The GAG deposition was also analyzed quantitatively after 14 and 28 days of culture, and the obtained results are shown in **Figure 7.9 A.**

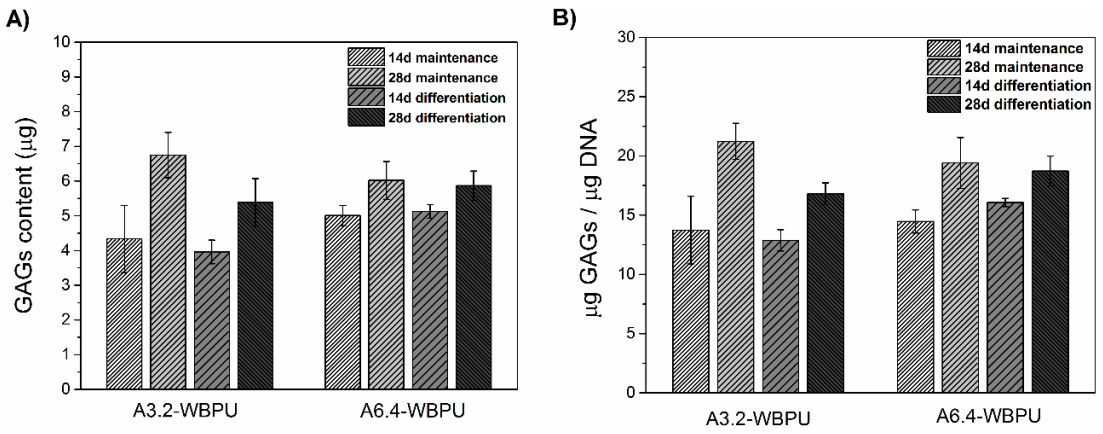

Figure 7.9. *A) GAGs deposition and B) normalized GAGs content after 14 and 28 days of incubation in maintenance and differentiation media from A3.2-WBPU and A6.4-WBPU chondrocyte-laden constructs.*

After 14 days of incubation, GAG content was similar in maintenance and differentiation conditions from both A3.2-WBPU and A6.4-WBPU scaffolds, presenting values from 4 and 5 µg per sample, respectively. However, after 28 days, the amount of GAGs increased, reaching values around 6 µg per sample in both formulations and conditions. This suggest that the de-differentiation phenomena of these chondrocytes did not occur due to the similar levels of GAGs observed in both maintenance and differentiation conditions. The GAG content was normalized versus the total DNA content and the obtained values are shown in **Figure 7.9 B.** After 14 of culture, A3.2-WBPU scaffolds showed values of 13.7 ± 2.8 and 12.9 ± 0.9 µg of GAGs per µg of DNA for maintenance and differentiation conditions, respectively. A6.4-WBPU scaffolds showed values of 14.5 ± 1 and 16 ± 0.3 µg of GAGs per µg of DNA for maintenance and differentiation, respectively. Further, after 28 days of incubation, A3.2-WBPU constructs contained values of 21.2 ± 1.5 and 16.8 ± 0.9 µg GAGs per µg of DNA in maintenance and differentiation conditions, respectively, while A6.4-WBPU scaffolds presented values of 19.4 ± 2.1 and 18.7 ± 1.2 µg of GAGs per µg of DNA. The fact that GAG normalized values to DNA increased during the culture period is in accordance with the observations reported in the literature [32].

In general, high polymer concentrations can inhibit matrix formation of embedded cells [33,34]. However, this affirmation was not in accordance with the concentrations evaluated in this study, since A6.4-WBPU presented values of GAGs content in general

higher than formulation with lower alginate content. In other studies, the authors also observed that the higher solid content in the formulation the higher GAGs deposition [32].

The observed GAGs content into the developed constructs suggest that the A-WBPU bioinks are able to promote specialized ECM synthesis, leading to the maintenance of chondrocyte phenotype at least during 28 days of culture.

The presence of collagen deposition in the scaffolds after 28 days of culture was analyzed through histological staining. Hematoxylin & Eosin and Masson's Trichrome staining were performed, and the optical images are shown in **Figure 7.10** and **Figure 7.11**, respectively. Histological staining techniques allow the visualization of principal cell structures stained with different components depending on their chemical character [35]. Hematoxylin stains specifically acid cell structures (purple) such as ribosomes and nucleus, whereas Eosin stains basic cell parts (pink-orange) such as cytoplasm, collagen and other structural molecules [36]. In the optical images from all formulations and conditions after 28 days of incubation (**Figure 7.10**), chondrocytes can be detected distributed along the surface sometimes in small groups (red circles), as it was previously observed. Purple stained circles represented cell structures such as the nucleus and in some cases cytoplasm, whereas other structural molecules were visible as orange-pink parts surrounding the nucleus.

Masson's Trichrome staining (**Figure 7.11**) represents collagen fibers and connective tissues specifically in blue-green, while the nucleus appears stained in dark brown and cytoplasm in pink [37]. Basic cell structures can also be appreciated in Masson's Trichrome images, with groups of chondrocytes appearing close one another in all formulations and conditions (red circles), but no collagen fibers (blue-green) are detected surrounding the cells. This suggest that the deposition of this structural molecule is not present or not appreciated in these histological slides probably due to the small thickness of the samples. In the images for both staining, the original porosity and the structure of the scaffolds can also be appreciated due to material highlighting by the different stains. No visual marked differences were detected among maintenance and differentiation conditions in each case, nor between both A-WBPU formulations.

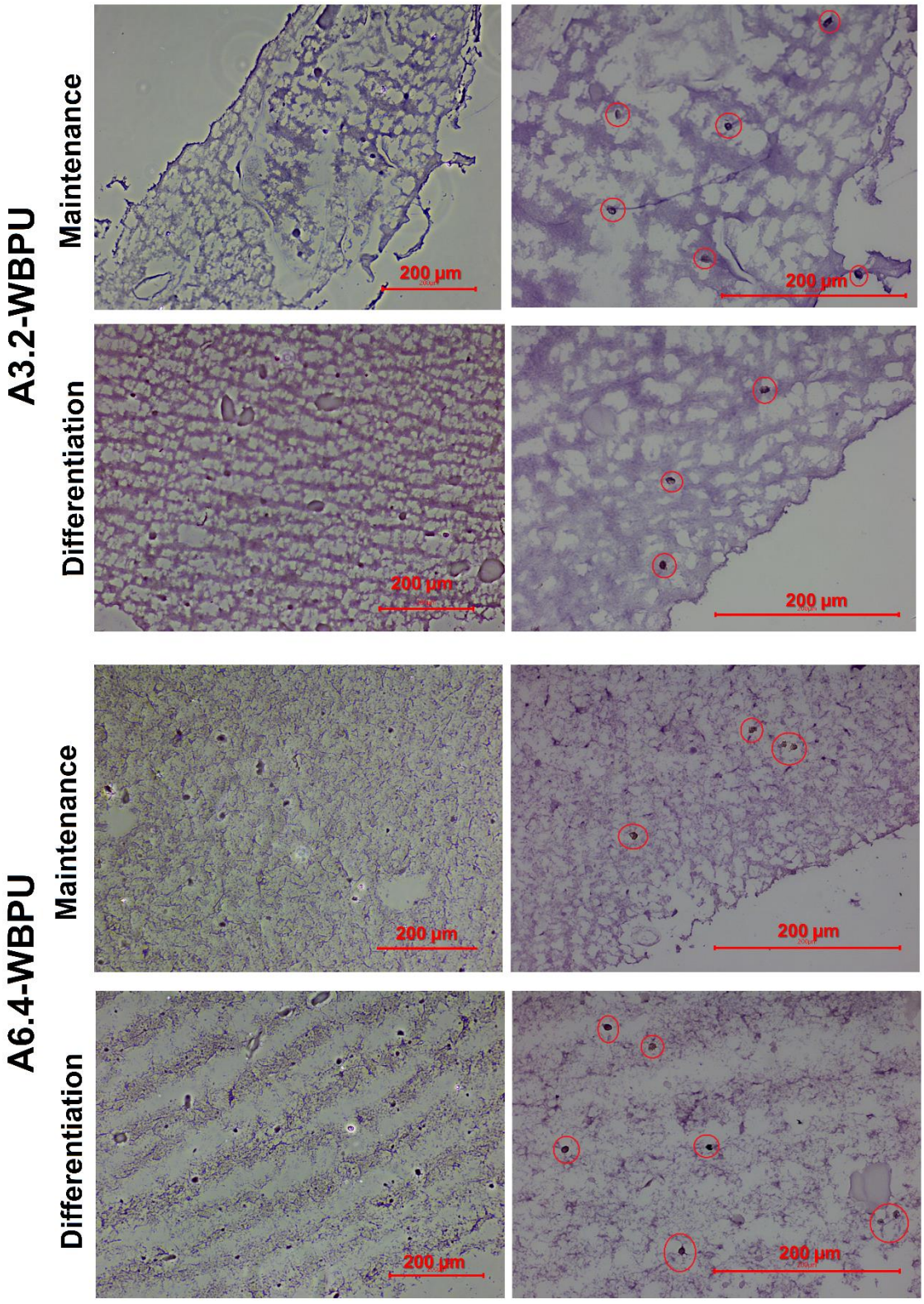

Figure 7.10. *Hematoxylin & Eosin staining images after 28 days of culture in maintenance and differentiation conditions from A3.2-WBPU and A6.4-WBPU scaffolds. Magnifications of 10x (left column) and 20x (right column). Cells are denoted by red circles.*

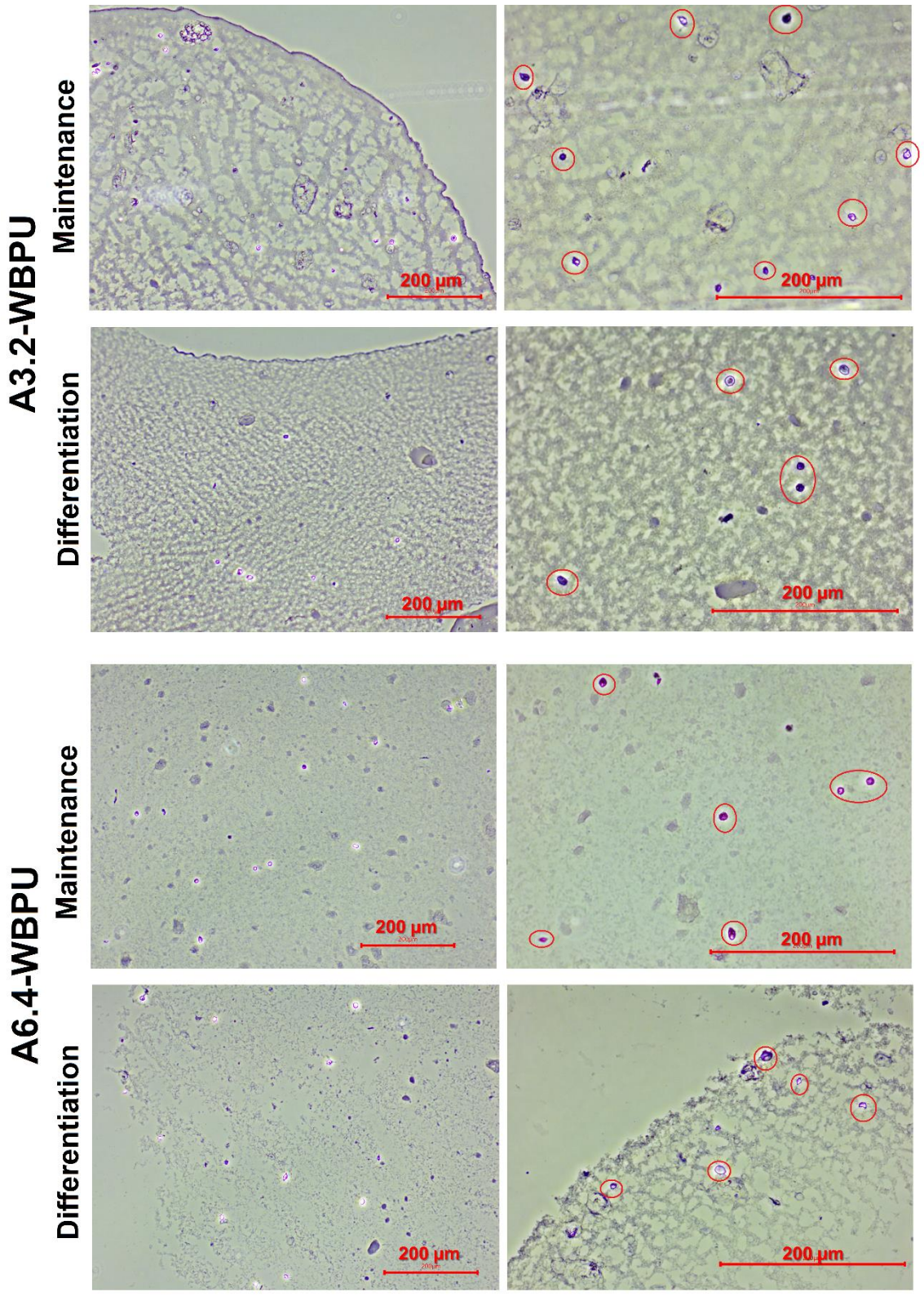

Figure 7.11. *Masson's Trichrome staining images after 28 days of culture in maintenance and differentiation conditions from A3.2-WBPU and A6.4-WBPU scaffolds. Magnifications of 10x (left column) and 20x (right column). Cells are denoted by red circles.*

To support histological results, the analysis of gene expression by RT-qPCR from A3.2-WBPU and A6.4-WBPU scaffolds cultured during 28 days in maintenance and differentiation conditions was performed. Chondrocytes from mature articular cartilage are characterized by larger expression of collagen II, aggrecan (ECM proteoglycan), transcription factor Sox-9 (responsible for chondrocyte differentiation) and low expression levels of collagen I [38–40]. This characteristic phenotype is the responsible of the mechanical properties of articular cartilage tissue [41]. When chondrocytes are cultured and expanded in 2D or in stiff 3D scaffolds, there is an increase in cell spread area, formation of actin filaments and larger synthesis of collagen I fibers, giving rise to de-differentiation of the cells towards hypertrophic phenotypes [30,42]. Therefore, expression (fold increase) of Sox9 Col1 and Col2 compared to monolayer controls was determined and the results are shown in **Figure 7.12.** ACAN (aggrecan) gene expression was also analyzed, but not relative expression was detected in neither scaffolds nor controls, and therefore the data are not reflected in the graphical results.

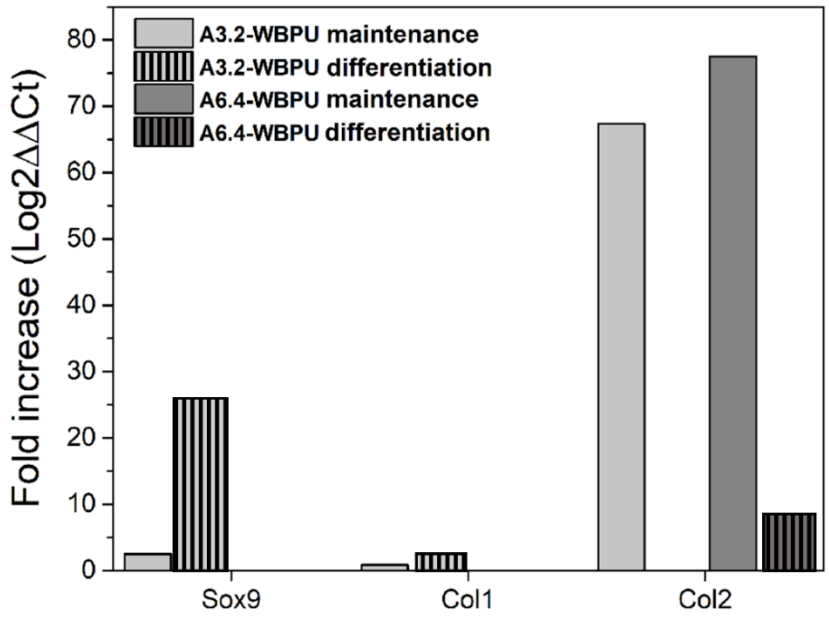

Figure 7.12. *Gene expression analysis from A3.2-WBPU and A6.4-WBPU scaffolds harvested after 28 of incubation in maintenance and differentiation conditions. Analysis of Sox9, collagen I (Col1) and collagen II (Col2) expression (fold increase) in the 3D scaffolds compared to 2D controls.*

The analysis revealed irregular expression patterns for all formulations and conditions, probably due to the low amount of mRNA extracted from scaffolds. However, collagen II was upregulated approximately 70-fold for A3.2-WBPU and A6.4-WBPU scaffolds in maintenance conditions, much higher than collagen I that was upregulated 0.9-fold and

2.5-fold for A3.2-WBPU scaffold in maintenance and differentiation conditions, respectively, in respect to monolayer controls. A6.4-WBPU scaffolds in differentiation condition also showed upregulation of 8.4-fold for collagen II, while no expression for collagen I was detected in this formulation.

Sox9 transcription factor was only upregulated in A3.2-WBPU scaffolds, showing 2.5-fold and 26-fold in maintenance and differentiation conditions, respectively. Values of 35-fold, 20-fold and 2-fold are reported in the literature [21] for Sox9, Col2 and Col1 relative expression, respectively, in polyurethane-hyaluronic acid scaffolds with a density of $2.5 \cdot 10^5$ cells after 14 days of culture. This suggests that with higher initial cell number in the scaffolds, the mRNA extracted would have been higher, enabling a better detection of all studied markers.

The gene expression analysis suggested that the embedded chondrocytes in A3.2-WBPU and A6.4-WBPU scaffolds after 28 days of culture synthesized typical chondrogenic markers, corroborating the absence of de-differentiated phenotypes. However, A3.2-WBPU scaffolds showed, in general, higher chondrogenic expression than A6.4-WBPU constructs, suggesting that the high viscosity and stiffer mechanical character of this formulation might lead to slight de-differentiation.

7.4. Conclusions

In this study, the fabrication of 3D bioprinted scaffolds from biocompatible A-WBPU bioinks and their potential application for cartilage tissue regeneration was carried out.

Five bioinks with different amounts of alginate were developed and characterized, demonstrating that those with the highest alginate content showed higher viscosity, viscoelasticity and shape retention, as well as capacity to maintain their structural integrity and the cell viability along a week of incubation. Therefore, the formulations with the highest alginate contents were selected as the most suitable to perform experiments of *in vitro* cartilage tissue formation.

Regarding the 3D bioprinting process, a grid architecture for the printed constructs was chosen demonstrating that this shape was able to provide suitable nutrient and signaling exchange for cell survival during at least 28 days of culture. Cell number and scaffolds integrity remained constant along the experiment, as it does in mature articular tissue. The evaluation of specialized ECM deposition (GAGs) showed an increment over time after 28 days, suggesting that the laden chondrocytes remained in a differentiated

phenotype, without the necessity of the growth factors provided by the differentiation medium.

Histological evaluation of the scaffolds after 28 days of culture did not show collagen I fibers deposition, indicating that the chondrocytes did not change to hypertrophic and de-differentiated phenotypes. To support histological results, gene expression analysis was performed, showing high expression of collagen II and low expression of collagen I, demonstrating the presence of chondrogenic phenotypes into the bioprinted scaffolds after 28 days of incubation. However, the lower expression in A6.4-WBPU constructs suggested that the high viscosity and stiffer mechanical character of this formulation might lead to slight de-differentiation compared to A3.2-WBPU scaffolds.

Therefore, A3.2-WBPU bioink and subsequent chondrocyte-laden scaffolds are able to maintain differentiated phenotypes capable to synthesize specialized ECM and thus, appearing to be potential candidates for *in vitro* regeneration of articular cartilage tissue.

7.5. References

[1] Vadillo J, Larraza I, Calvo-correas T, Gabilondo N, Derail C, Eceiza A. Design of a waterborne polyurethane–urea ink for direct ink writing 3d printing. Materials (Basel) 2021;14:1–13. https://doi.org/10.3390/ma14123287.

[2] Bendtsen ST, Quinnell SP, Wei M. Development of a novel alginate-polyvinyl alcohol-hydroxyapatite hydrogel for 3D bioprinting bone tissue engineered scaffolds. J Biomed Mater Res - Part A 2017;105:1457–1468. https://doi.org/10.1002/jbm.a.36036.

[3] Hsieh FY, Lin HH, Hsu SH. 3D bioprinting of neural stem cell-laden thermoresponsive biodegradable polyurethane hydrogel and potential in central nervous system repair. Biomaterials 2015;71:48–57. https://doi.org/10.1016/j.biomaterials.2015.08.028.

[4] Abouzeid RE, Khiari R, Beneventi D, Dufresne A. Biomimetic mineralization of three-dimensional printed alginate/TEMPO-oxidized cellulose nanofibril scaffolds for bone tissue engineering. Biomacromolecules 2018;19:4442–52. https://doi.org/10.1021/acs.biomac.8b01325.

[5] Chen H, Xie F, Chen L, Zheng B. Effect of rheological properties of potato, rice and corn starches on their hot-extrusion 3D printing behaviors. J Food Eng 2019;244:150–158. https://doi.org/10.1016/j.jfoodeng.2018.09.011.

[6] Rutz AL, Hyland KE, Jakus AE, Burghardt WR, Shah RN. A multimaterial bioink method for 3D printing tunable, cell-compatible hydrogels. Adv Mater 2015;27:1607–1614. https://doi.org/10.1002/adma.201405076.

[7] Suntornnond R, An J, Chua CK. Bioprinting of Thermoresponsive Hydrogels for Next Generation Tissue Engineering: A Review. Macromol Mater Eng

2017;302:1–15. https://doi.org/10.1002/mame.201600266.

[8] Kirillova A, Yeazel TR, Asheghali D, Petersen SR, Dort S, Gall K, Becker ML. Fabrication of biomedical scaffolds using biodegradable polymers. Chem Rev 2021;121:11238–11304. https://doi.org/10.1021/acs.chemrev.0c01200.

[9] Blaeser A, Duarte Campos DF, Puster U, Richtering W, Stevens MM, Fischer H. Controlling shear stress in 3D bioprinting is a key factor to balance printing resolution and stem cell integrity. Adv Healthc Mater 2016;5:326–333. https://doi.org/10.1002/adhm.201500677.

[10] Camarero-Espinosa S, Rothen-Rutishauser B, Weder C, Foster EJ. Directed cell growth in multi-zonal scaffolds for cartilage tissue engineering. Biomaterials 2016;74:42–52. https://doi.org/10.1016/j.biomaterials.2015.09.033.

[11] Liao IC, Moutos FT, Estes BT, Zhao X, Guilak F. Composite three-dimensional woven scaffolds with interpenetrating network hydrogels to create functional synthetic articular cartilage. Adv Funct Mater 2013;23:5833–5839. https://doi.org/10.1002/adfm.201300483.

[12] Boere KWM, Visser J, Seyednejad H, Rahimian S, Gawlitta D, van Steenbergen MJ, Dhert, WJ, Hennink WE, Vermonden T, Malda J. Covalent attachment of a three-dimensionally printed thermoplast to a gelatin hydrogel for mechanically enhanced cartilage constructs. Acta Biomater 2014;10:2602–2611. https://doi.org/10.1016/j.actbio.2014.02.041.

[13] Szychlinska MA, D'Amora U, Ravalli S, Ambrosio L, Di Rosa M, Musumeci G. Functional biomolecule delivery systems and bioengineering in cartilage regeneration. Curr Pharm Biotechnol 2019;20:32–46. https://doi.org/10.2174/1389201020666190206202048.

[14] Gonçalves AM, Moreira A, Weber A, Williams GR, Costa PF. Osteochondral tissue engineering: The potential of electrospinning and additive manufacturing. Pharmaceutics 2021;13:1-51. https://doi.org/10.3390/pharmaceutics13070983.

[15] Wang Y, Bella E, Lee CSD, Migliaresi C, Pelcastre L, Schwartz Z, Boyan B, Mota A. The synergistic effects of 3-D porous silk fibroin matrix scaffold properties and hydrodynamic environment in cartilage tissue regeneration. Biomaterials 2010;31:4672–4681. https://doi.org/10.1016/j.biomaterials.2010.02.006.

[16] Byrne DP, Lacroix D, Planell JA, Kelly DJ, Prendergast PJ. Simulation of tissue differentiation in a scaffold as a function of porosity, Young's modulus and dissolution rate: Application of mechanobiological models in tissue engineering. Biomaterials 2007;28:5544–5554. https://doi.org/10.1016/j.biomaterials.2007.09.003.

[17] Sharma B, Elisseeff JH. Engineering structurally organized cartilage and bone tissues. Ann Biomed Eng 2004;32:148–159. https://doi.org/10.1023/B:ABME.0000007799.60142.78.

[18] Gao J, Ding X, Yu X, Chen X, Zhang X, Cui S, Shi J, Chen J, Yu L, Chen S, Ding J. Cell-free bilayered porous scaffolds for osteochondral regeneration fabricated by continuous 3D-printing using nascent physical hydrogel as ink. Adv Healthc

Mater 2021;10:1–13. https://doi.org/10.1002/adhm.202001404.

[19] Hutmacher DW. Scaffolds in tissue engineering bone and cartilage. Biomaterials 2000;21:2529–2543. https://doi.org/10.1016/S0142-9612(00)00121-6.

[20] Martínez Ávila H, Schwarz S, Rotter N, Gatenholm P. 3D bioprinting of human chondrocyte-laden nanocellulose hydrogels for patient-specific auricular cartilage regeneration. Bioprinting 2016;1–2:22–35. https://doi.org/10.1016/j.bprint.2016.08.003.

[21] Hung KC, Tseng CS, Dai LG, Hsu SH. Water-based polyurethane 3D printed scaffolds with controlled release function for customized cartilage tissue engineering. Biomaterials 2016;83:156–168. https://doi.org/10.1016/j.biomaterials.2016.01.019.

[22] Bidarra SJ, Barrias CC, Granja PL. Injectable alginate hydrogels for cell delivery in tissue engineering. Acta Biomater 2014;10:1646–1662. https://doi.org/10.1016/j.actbio.2013.12.006.

[23] Camarero-Espinosa S, Rothen-Rutishauser B, Foster EJ, Weder C. Articular cartilage: From formation to tissue engineering. Biomater Sci 2016;4:734–767. https://doi.org/10.1039/c6bm00068a.

[24] Lotz M, Loeser RF. Effects of aging on articular cartilage homeostasis. Bone 2012;51:241–248. https://doi.org/10.1016/j.bone.2012.03.023.Effects.

[25] Maroudas A, Muir H, Wingham J. The correlation of fixed negative charge with glycosaminoglycan content of human articular cartilage. Biochim Biophys Acta - Gen Subj 1969;177:492–500. https://doi.org/10.1016/0304-4165(69)90311-0.

[26] Responte DJ, Natoli RM, Athanasiou KA. Collagens of articular cartilage: Structure, function, and importance in tissue engineering. Crit Rev Biomed Eng 2007;35:363–411. https://doi.org/10.1615/CritRevBiomedEng.v35.i5.20.

[27] Cohen NP, Foster RJ, Mow VC. Composition and dynamics of articular cartilage: Structure, function, and maintaining healthy state. J Orthop Sports Phys Ther 1998;28:203–215. https://doi.org/10.2519/jospt.1998.28.4.203.

[28] Camarero-Espinosa S, Tomasina C, Calore A, Moroni L. Additive manufactured, highly resilient, elastic, and biodegradable poly(ester)urethane scaffolds with chondroinductive properties for cartilage tissue engineering. Mater Today Bio 2020;6:1-12. https://doi.org/10.1016/j.mtbio.2020.100051.

[29] Darling EM, Athanasiou KA. Rapid phenotypic changes in passaged articular chondrocyte subpopulations. J Orthop Res 2005;23:425–432. https://doi.org/10.1016/j.orthres.2004.08.008.

[30] Camarero-Espinosa S, Calore A, Wilbers A, Harings J, Moroni L. Additive manufacturing of an elastic poly(ester)urethane for cartilage tissue engineering. Acta Biomater 2020;102:192–204. https://doi.org/10.1016/j.actbio.2019.11.041.

[31] Li F, Truong VX, Fisch P, Levinson C, Glattauer V, Zenobi-Wong M, Thissen H, Forsythe JS, Frith, JE. Cartilage tissue formation through assembly of microgels containing mesenchymal stem cells. Acta Biomater 2018;77:48–62.

https://doi.org/10.1016/j.actbio.2018.07.015.

[32] Mouser VHM, Melchels FPW, Visser J, Dhert WJA, Gawlitta D, Malda J. Yield stress determines bioprintability of hydrogels based on gelatin-methacryloyl and gellan gum for cartilage bioprinting. Biofabrication 2016;8:035003-035015. https://doi.org/10.1088/1758-5090/8/3/035003.

[33] Seliktar D. Designing cell-compatible hydrogels for biomedical applications. Science 2012;336:1124–1128. https://doi.org/10.1126/science.1214804.

[34] Bryant SJ, Anseth KS. Hydrogel properties influence ECM production by chondrocytes photoencapsulated in poly(ethylene glycol) hydrogels. J Biomed Mater Res 2002;59:63–72. https://doi.org/10.1002/jbm.1217.

[35] Veuthey T, Herrera G, Dodero VI. Dyes and stains: from molecular structure to histological application. Front Biosci 2014;19:91–112.

[36] Thompson JH, Richter WR. Hematoxylin-Eosin staining adapted to automatic tissue processing. Stain Technol 1960;35:145–148. https://doi.org/10.3109/10520296009114731.

[37] Garvey W. Modified elastic tissue-Masson trichrome stain. Stain Technol 1984;59:213–216. https://doi.org/10.3109/10520298409113858.

[38] Tchetina E V, Squires G, Poole AR. Increased type II collagen degradation and very early focal cartilage degeneration is associated with upregulation of chondrocyte differentiation related genes in early human articular cartilage lesions. J Rheumatol 2005;32:876–886.

[39] Mazor M, Lespessailles E, Coursier R, Daniellou R, Best TM, Toumi H. Mesenchymal stem-cell potential in cartilage repair: An update. J Cell Mol Med 2014;18:2340–2350. https://doi.org/10.1111/jcmm.12378.

[40] Koelling S, Kruegel J, Irmer M, Path JR, Sadowski B, Miro X, Miosge N. Migratory chondrogenic progenitor cells from repair tissue during the later stages of human osteoarthritis. Cell Stem Cell 2009;4:324–335. https://doi.org/10.1016/j.stem.2009.01.015.

[41] García-Carvajal ZY, Garciadiego-Cázares D, Parra-Cid C, Aguilar-Gaytán R, Velasquillo C, Ibarra C, Castro-Carmona JS. Cartilage tissue engineering: The role of extracellular matrix (ECM) and novel strategies. Regen. Med. Tissue Eng., InTech; 2013. https://doi.org/10.5772/55917.

[42] Bhattacharjee M, Coburn J, Centola M, Murab S, Barbero A, Kaplan DL, Martin I, Ghosh S. Tissue engineering strategies to study cartilage development, degeneration and regeneration. Adv Drug Deliv Rev 2015;84:107–122. https://doi.org/10.1016/j.addr.2014.08.010.

Chapter 8

General conclusions, future works and scientific contributions

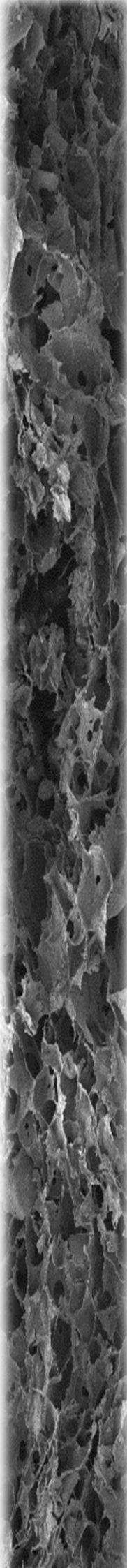

CHAPTER 8 - General conclusions, future works and scientific contributions

8. General conclusions, future works and scientific contributions

8.1. General conclusions

The aim of this work was the development of biomaterial inks and bioinks suitable for extrusion 3D printing technology composed of alginate, WBPU and cellulose nanoentities and the fabrication of scaffolds with suitable characteristics and potential applicability in precision medicine and healthcare industry. With this purpose, different polymeric blends and single-component ink formulations were developed and characterized. Finally, the assessment of the obtained scaffolds for drug delivery and tissue engineering applications, among others, were carried out.

Regarding the single-component inks, the formulation containing 10 wt. % of EnCNC represents the minimum solid content needed to achieve high viscosity and proper viscoelastic properties for extrusion 3D printing, while only the A-Ca formulation with 10 % of gelation degree presented suitable rheological characteristics for 3D printing compared to the formulations with higher or lower crosslinking degrees. Scaffolds 3D printed with both monocomponent inks showed porosity, high mechanical properties and cell proliferation after freeze-drying process, characteristics that make them potential candidates for tissue engineering applications. Moreover, both EnCNC and A-Ca porous scaffolds exhibited rapid *in vitro* drug release, demonstrating to be optimal materials for drug delivery systems.

Developed A-CNF ink formulations with CNF contents above 3 wt. % showed shear-thinning behavior and suitable viscoelastic properties for extrusion 3D printing technology. In order to manufacture tailor-made drug delivery systems for controlled release, hydrophobic and hydrophilic drug models were loaded in A-CNF ink formulations, showing good integration into A-CNF matrices and proper 3D printing performance. *In vitro* delivery experiments demonstrated that freeze-dried scaffolds, which presented a porous structure, could facilitate the release of hydrophobic drugs that present low solubility in physiological conditions, while Ca^{2+} crosslinking/air-dried compact tablets would delay the administration of hydrophilic drugs during longer periods, avoiding their rapid elimination from the body and thus, the need of high doses.

With the purpose of manufacturing alternative and customizable hernia mesh implants, different biomaterial inks made of alginate and WBPU were developed and characterized, showing all good properties for extrusion 3D printing. A $CaCl_2$ coating was applied to the 3D printed meshes as physical reinforcement, obtaining implants classified as partially-absorbable, heavyweight meshes with very large pores, presenting transparency and isotropic behavior that could facilitate their implantation. The analysis

of the mechanical properties revealed that the mesh implants with 6 wt. % of alginate and Ca^{2+} coat were the most suitable for hernia repair due to their ability to support the physiological stresses of small and inguinal hernias, recovering their original shape after physiological movements. Moreover, antibiotic-loaded meshes showed a suitable *in vitro* release of the drug, which would suppose a strategy to avoid post-surgical infection complications and a future mesh replacement.

Finally, *in situ* neo-cartilage formation was evaluated in 3D bioprinted chondrocyte-laden scaffolds constituted by alginate and WBPU. Cell number and scaffolds structure remained constant along the experiment, while the synthesis of specialized ECM (GAGs) increased with time until 28 days of incubation, suggesting that the laden chondrocytes remained in a differentiated phenotype. Besides, expression analysis of specific genes was performed, demonstrating the presence of chondrogenic phenotypes in the A-WBPU bioprinted constructs with 3.2 % of alginate, with these bioprinted scaffolds being potential candidates for *in vitro* cartilage tissue regeneration.

8.2. Future works

Based on the results obtained in this thesis work, the following ideas and research lines are proposed as future works:

- *The assessment of EnCNC scaffolds for bone tissue regeneration applications*. The outstanding mechanical properties and the macroporous network obtained after freeze-drying suggest that EnCNC scaffolds will perform as suitable supporting material for bone tissue regeneration. Osteoconductive and osteoinductive properties of these scaffolds should be evaluated. Besides, active molecules such as specific growth factors and calcium phosphate could be loaded into the biomaterial ink for further osteogenesis induction.

- *The development of bioinks based on alginate-Ca^{2+} for skin tissue regeneration*. Due to the observed cell proliferative capacity of the alginate-Ca matrices in preliminary assays carried out in this thesis work, fibroblast and keratinocytes would be loaded in the developed alginate-Ca inks for 3D bioprinting of cell-laden scaffolds. The capacity to form functional neo-tissue *in vitro* in the printed constructs should be extensively analyzed. In addition, alginate could be functionalized by linking RGD peptides in their structure to improve cell adhesion properties.

- *The assessment in vivo of the capacity of targeted drug delivery from the loaded A-CNF scaffolds.* The ability of hydrophobic and hydrophilic drugs release from freeze-dried and crosslinked compact dosage forms in animal models should be evaluated to corroborate the conclusions obtained *in vitro.*

- *The evaluation in vivo of the 3D printed A-WBPU+Ca mesh implants for hernia repair.* Mesh implantation capacity and subsequent hernia recovery in animal models should be analyzed as preclinical studies to ensure its potential application for the healing of human abdominal or groin hernia conditions. Moreover, the antibiotic-release capacity of the printed meshes in the wound site should be evaluated *in vivo* to corroborate the absence of mesh infection during recovery time.

- *The optimization of the cell concentration loaded into the A-WBPU bioinks for cartilage tissue regeneration*. Based on the experiments carried out in this thesis work about *in vitro* cartilage formation, an increase of the number of chondrocytes laden in the bioinks would be translated in higher GAGs and collagen II deposition and thus, larger amount of specialized neo-tissue formation.

8.3. Scientific contributions

The publications and contributions to conferences derived from this research work are detailed below:

8.3.1. Publications

Authors: Raquel Olmos-Juste, Borja Alonso-Lerma, Raúl Pérez-Jiménez, Nagore Gabilondo, Arantxa Eceiza

Title: 3D printed alginate-cellulose nanofibers based patches for local curcumin administration

Journal: Carbohydrate Polymers

Year: 2021

Impact factor: 10.723 (JCR 2021)

Rank: Polymer Science 3/90 (JCR 2021)

Applied Chemistry 4/72 (JCR 2021)

Organic Chemistry 2/56 (JCR 2021)

Authors: Raquel Olmos-Juste, Olatz Guaresti, Tamara Calvo-Correas, Nagore Gabilondo, Arantxa Eceiza

Title: Design of drug-loaded 3D printing biomaterial inks and tailor-made pharmaceutical forms for controlled release

Journal: International Journal of Pharmaceutics

Year: 2021

Impact factor: 6.510 (JCR 2021)

Rank: Pharmacology & pharmacy 40/279 (JCR 2021)

Authors: Raquel Olmos-Juste, Sheila Olza, Nagore Gabilondo, Arantxa Eceiza

Title: Tailor-made 3D printed meshes of alginate-waterborne polyurethane as suitable implants for hernia repair

Journal: Macromolecular Bioscience

Year: 2022

Impact factor: 5.859 (JCR 2021)

Rank: Polymer Science 11/90 (JCR 2021)

Materials Science, Biomaterials 15/44 (JCR 2021)

Biochemistry & Molecular Biology 78/296 (JCR 2021)

Authors: Raquel Olmos-Juste, Garazi Larrañaga-Jaurrieta, Sandra Ramos-Diez, Sandra Camarero-Espinosa, Nagore Gabilondo, Arantxa Eceiza

Title: Novel alginate-waterborne polyurethane 3D bioprinted scaffolds for articular cartilage tissue engineering

Year: 2022 (submitted to Journal of Materials Chemistry B)

Authors: Raquel Olmos-Juste, Borja Alonso-Lerma, Leire Barandiaran, Raul Perez-Jimenez, Nagore Gabilondo, Arantxa Eceiza

Title: Enzymatically obtained CNC ink for 3D printing and its biomedical applications

Year: 2022 (in process)

Authors: Raquel Olmos-Juste, Nagore Gabilondo, Arantxa Eceiza

Title: Extrusion 3D printing ink based on pre-crosslinked alginate for biomedical applications

Year: 2022 (in process)

- **Collaborations**

Authors: Borja Alonso-Lerma, Leire Barandiaran, Lorena Ugarte, Izaskun Larraza, Antonio Reifs, Raquel Olmos-Juste, Nerea Barruetabeña, Iban Amenabar, Rainer Hillenbrand, Arantxa Eceiza, Raúl Perez-Jimenez

Title: High performance crystalline nanocellulose using an ancestral endoglucanase

Journal: Communications Materials

Year: 2020

Impact factor: N/A (JCR 2021)

Rank: Material Science, Multidisciplinary 82/414 (based on JCI in JCR 2021)

Authors: Leire Barandiaran, Borja Alonso-Lerma, Antonio Reifs, Izaskun Larraza, Raquel Olmos-Juste, Alba Fernandez-Calvo, Ylenia Jabalera, Arantxa Eceiza, Raúl Perez-Jimenez

Title: Enzymatic upgrading of nanochitin using an ancient lytic polysaccharide monooxygenase

Journal: Communications Materials

Year: 2022

Impact factor: N/A (JCR 2021)

Rank: Material Science, Multidisciplinary 82/414 (based on JCI in JCR 2021)

8.3.2. Conferences

Authors: Raquel Olmos-Juste, Borja Alonso-Lerma, Raúl Pérez-Jiménez, Nagore Gabilondo, Arantxa Eceiza

Title: 3D printed alginate-cellulose nanofibers based patches for local curcumin administration

Conference: 4th International Conference on Advanced Polymer Materials and Nanocomposites

Contribution: Oral presentation

Year: 2021

Place: Aveiro, Portugal

Authors: Raquel Olmos-Juste, Olatz Guaresti, Tamara Calvo-Correas, Nagore Gabilondo, Arantxa Eceiza

Title: Design of drug-loaded 3D printing biomaterial inks and tailor-made pharmaceutical forms for controlled release

Conference: GEP-SLAP 2022

Contribution: Oral presentation

Year: 2022

Place: Donostia - San Sebastián, Spain

- **Collaborations**

Authors: Ainara Saralegi, Tamara Calvo-Correas, Lorena Ugarte, Julen Vadillo, Izaskun Larraza, Oihane Echeverria, Raquel Olmos-Juste, Stefano Torresi, Eider Mendiburu, Arantxa Eceiza

Title: New biobased polyurethane materials

Conference: GEP-SLAP 2022

Contribution: Oral presentation

Year: 2022

Place: Donostia - San Sebastián, Spain

Annexes

ANNEXE I - List of tables

Chapter 1. Introduction

Chapter 2. Materials and methods

Chapter 3. Characterization of alginate, WBPU and cellulose nanoentities

Chapter 4. Single-component inks for 3D printing and its biomedical applications

Chapter 5. Alginate-CNF inks for 3D printing and drug-loaded scaffolds for controlled release

Chapter 6. A-WBPU inks for 3D printing of tailor-made mesh implants for hernia repair

Chapter 7. Alginate-WBPU bioinks for 3D bioprinting of scaffolds for cartilage regeneration

ANNEXE II – List of figures

Chapter 1. Introduction

Chapter 3. Characterization of alginate, WBPU and cellulose nanoentities

Chapter 4. Single-component inks for 3D printing and its biomedical applications

Chapter 5. Alginate-CNF inks for 3D printing and drug-loaded scaffolds for controlled release

Chapter 6. A-WBPU inks for 3D printing of tailor-made mesh implants for hernia repair

Chapter 7. Alginate-WBPU bioinks for 3D bioprinting of scaffolds for cartilage regeneration

ANNEXE III – List of abbreviations

3D printing	Three-dimensional printing
^{13}C NMR	Carbon nuclear magnetic resonance
A	Alginate
ACAN	Aggrecan
AFM	Atomic force microscopy
API	Active pharmaceutical ingredients
BCS	Biopharmaceutics Classification System
CAD	Computer-aided design
cDNA	Copy deoxyribonucleic acid
Clph	Chloramphenicol
CNC	Cellulose nanocrystals
CNF	Cellulose nanofibers
CT	Computed tomography
Cur	Curcumin
DAPI	4′,6-Diamidino-2-phenylindole
DIW	Direct ink writing
DMEM	Dulbecco's modified Eagle medium
DMMB	1,9-Dimethylmethylene blue
DMSO	Dimethyl sulfoxide
DNA	Deoxyribonucleic acid
DSC	Differential scanning calorimetry
ECM	Extracellular matrix
EMA	European Medicines Agency
EnCNC	Enzymatic cellulose nanocrystals

FBS	Fetal bovine serum
FDA	Food and Drug Administration
FDM	Fused deposition modelling
FTIR	Fourier transform infrared spectroscopy
G	α-L-Guluronic acid
GAG	Glycosaminoglycan
GAPDH	Glyceraldehyde-3-phosphate dehydrogenase
GO	Graphene oxide
HA	Hyaluronic acid
HEK	Human embryonic kidney
HMDS	Hexametyldisilazane
IPTG	Isopropyl β-D-1-thiogalactopyranoside
ITS	Insulin transferrin selenium
LB	Luria-Bertani medium
LDH	Lactate dehydrogenase
LSM	Laser-scanning microscope
LVR	Linear viscoelastic region
M	β-D-Mannuronic acid
MRI	Magnetic resonance imaging
mRNA	Messenger ribonucleic acid
OCT	Optimal cutting temperature
PBS	Phosphate buffer saline
PCR	Polymerase chain reaction
PEG	Polyethylene glycol
Pen/Strep	Penicillin-streptomycin
PEO	Polyethylene oxide

PLGA	Poly-lactic-co-glycolic acid
PP	Polypropylene
PU	Polyurethane
RGD	Arginine-glycine-asparagine
RNA	Ribonucleic acid
RT	Reverse transcriptase
RT-qPCR	Real-time quantitative polymerase chain reactions
SEM	Scanning electron microscopy
SD	Swelling degree
TGA	Thermogravimetric analysis
UV	Ultraviolet
WBPU	Waterborne polyurethane
XRD	X-ray diffraction

ANNEXE IV – List of symbols

2θ	Reflectance angle
A	Area
Av	Viscometric constant
G’	Storage modulus
G’’	Loss modulus
K	Flow consistency index
Kv	Viscometric constant
L	Perimeter
Mw	Molecular weight
n	Power-law index
[η]	Intrinsic viscosity
η	Viscosity
Pr	Printability index
R^2	Pearson correlation coefficient
τ	Shear stress
Tan δ	Tangent of phase angle
T_0	Initial degradation temperature
Td	Maximum degradation temperature
Tg	Glass transition temperature
Wt.	Solid content
$\dot{\gamma}$	Shear rate
λ	Incident radiation wavelength
ΔΔCt	Difference in cycle threshold value